APPLIED COMPUTATIONAL ELECTROMAGNETICS SOCIETY JOURNAL

May 2021
Vol. 36 No. 5
ISSN 1054-4887

The ACES Journal is abstracted in INSPEC, in Engineering Index, DTIC, Science Citation Index Expanded, the Research Alert, and to Current Contents/Engineering, Computing & Technology.

The illustrations on the front cover have been obtained from the research groups at the Department of Electrical Engineering, The University of Mississippi.

MAY 2021 REVIEWERS

Zsolt Badics
Alireza Baghai-Wadji
Ayman Elboushi
Ibrahim Elshafiey
Nunzia Fontana
Andrey Grigoriev
Srividhya K.
Maokun Li
Qingya Li
Si Li
Yongwei Li
Tu-Lu Liang
Angelo Liseno
Peyman Mahouti
Mikhail Manuilov
Ronald Marhefka
Truong Khang Nguyen
Li Ning
Ernest Okon
Mauro Parise
Hassan Ragheb
Luis Ramirez
Jimmy Roden
Daniel Rodriguez Prado
Vince Rodriguez
Katherine Siakavara
Christopher Trueman
Luong Truong
Chao-Fu Wang
Lu Wang
Ping Wang
Zhonggen Wang
Shihyuan Yeh
Qingsheng Zeng
Bo Zhu

THE APPLIED COMPUTATIONAL ELECTROMAGNETICS SOCIETY JOURNAL

Vol. 36 No. 5 May 2021

TABLE OF CONTENTS

On the Possibility of Using ULF/ELF Electromagnetic Waves from Undersea Cables to Detect Airplanes Submerged in the Ocean

Dallin R. Smith [1] and Jamesina J. Simpson [2]

[1] Air Force Research Labs
Albuquerque, NM 87117, USA
dallin@afrlnewmexico.com

[2] Department of Electrical and Computer Engineering
University of Utah, Salt Lake City, UT 84112, USA
jamesina.simpson@utah.edu

Abstract ─ The loss of Malaysian Flight on March 8, 2014, and the subsequent lengthy search for the aircraft highlights the need for an effective detection system for locating airplanes that have crashed into the ocean. The goal of this paper is to test the feasibility of detecting submerged airplanes using ultra-low frequency and/or extremely-low frequency electromagnetic signals generated by undersea cables located along the bottom of the ocean. The proposed detection system is tested using three-dimensional finite-difference time-domain (FDTD) modeling of the cable source, ocean water, ground, and submerged object (aircraft). The perturbation caused by the object is obtained for different positions of the object relative to the cable source. The magnitude of the perturbation is compared to the expected background level for a depth of 3 km into the ocean. A sensor array is proposed for detecting objects within several km of the cable.

Index Terms ─ Airplane, extremely-low frequency, FDTD, ocean, ultra-low frequency.

I. INTRODUCTION

Malaysian Flight 370 (MH370) took off at 12:42 AM on March 8, 2014, and disappeared from air-traffic control secondary radar 39 minutes later. Later, a study of primary radar data indicated that MH370 flew off course for more than an hour after the aircraft was dropped from the secondary radar. Subsequently, an even later investigation of satellite data indicated that the aircraft continued to fly at high speeds and at a high altitude for six hours after it disappeared from secondary radar. Ultimately it is believed to have crashed into the Indian Ocean [1].

The inability to locate the MH370 aircraft brings to light the challenge of finding a (reasonably sized) metallic airplane in the ocean. Sonar may sometimes be used when the target of interest is sufficiently noisy. Alternatively, over short ranges, magnetic anomaly detectors may be employed [2]. In general, electromagnetic detection is not used due to the high attenuation rate of electromagnetic waves in the conductive ocean. With an average electrical conductivity of ~3.3 S/m, the skin depth of the ocean is just 27 m at 100 Hz, and it is even shallower at higher frequencies. Note that the average depth of the ocean is ~3.5 km.

The possibility of conducting remote-sensing studies in the ocean using frequencies below 100 Hz in the ultra-low frequency (ULF: < 3 Hz) and extremely low frequency (ELF: 3 Hz – 3 kHz) range opens up new detection possibilities because of the increased skin depth. These frequencies have been previously considered (e.g. [3-9]). However, most of these studies focused on electromagnetic sources located on land or in the air region above the ocean [3-8]. One study investigated electromagnetic propagation between source and receiver antennas both located in seawater, however frequencies of 100 kHz and 14 MHz were used, which provided ranges of just 300 m [9].

In this Paper, the feasibility of using subsea cables as a source of ULF/ELF electromagnetic waves for remote-sensing of the oceans is considered for the first time. The motivation for using subsea cables is as follows: (1) they already exist in many locations around the world, and (2) they are electrically long, even at ULF/ELF, due to the shortening of electromagnetic wavelengths in the ocean.

With respect to (1), sub-sea cables are extensively utilized for international communication purposes, with over 400 cables in operation around the world that collectively span over 1.2 million km. Additionally, there are many older cables no longer in service but still located along the ocean floor. In most cases, the undersea cables are simply laid on the ocean floor. Closer to shore, cables may be buried under the seabed for protection.

Concerning (2) above, the electromagnetic

Submitted On: March 10, 2021
Accepted On: April 25, 2021
https://doi.org/10.47037/2020.ACES.J.360501

wavelength at a frequency of 10 Hz is shortened from ~30 Mm in the air to just 548 m in the ocean. At 0.1 Hz, the wavelength is shortened from ~3,000 Mm in the air to 5.48 km in the ocean. As a result, long undersea cables are expected to radiate much more efficiently at the bottom of the ocean compared to a comparable antenna located in the air or on land. For example, the Navy's ELF transmitter, having two 22.5-km long lines over land in Wisconsin and Michigan and having a third line over land in Michigan that was 50 km long, was known to have very poor radiation efficiency at 76 Hz until it was turned off in 2004 [10].

The goal of this paper is to computationally test the feasibility of using undersea cables as a source in a ULF/ELF remote-sensing system used to detect airplanes submerged in the ocean. Three-dimensional finite-difference time-domain (FDTD) [11, 12] models are used to model a realistic bathymetry, the cable source, the resulting ULF/ELF propagation, and the scattering caused by the object (airplane). First, the remote-sensing system is tested at multiple frequencies in the ULF/ELF band to determine an optimal operating frequency. Subsequently, the object is moved around in the vicinity of the cable to examine the total field perturbation caused by the object.

Section II describes the first FDTD model (Model #1) that is used to obtain the optimal operating frequency. Section III discusses the possibility of detecting the object and analyzes the results relative to the background noise level and measurement capabilities of present-day magnetometers. Section IV studies the effect of the ocean floor. Section V describes a second FDTD model (Model #2) that that is equivalent to Model #1 but extends over a larger area, is more computationally efficient, and includes a more realistic bathymetry. Section VI presents results from Model #2 with the aircraft located on the ocean floor at various distanced from the undersea cable, and then also results for the aircraft elevated above the ocean floor (representing it sinking). Section VII summarizes and concludes the Paper.

II. FDTD MODEL DESCRIPTION

The first FDTD model (called Model #1) is used to find the optimal operating frequency by comparing the propagation attenuation rate of the scattered fields from the object with the background noise level and magnetometer sensitivity level. Model #1 extends 5 km in the X-, Y-, and Z-directions and has a grid resolution of 15 m in each Cartesian direction. This grid resolution is sufficiently high to account for the wavelengths and skin depth of the modeled electromagnetic waves ranging from 0.1 to 100 Hz.

As shown on the left side of Fig. 1, the top half of the grid in the Z-direction consists of ocean water having a conductivity of $\sigma = 3.3$ S/m and a relative permittivity of $\varepsilon_r = 81$. The bottom half of the grid models the ground having a conductivity of $\sigma = 0.01$ S/m (a conductivity for ground under the ocean as obtained from [13]) and a relative permittivity of $\varepsilon_r = 15$. Thus, in Model #1, the ground is assumed to be flat. Both the ground and ocean are homogeneous in the XY plane.

We note that in cold, deep ocean water, the conductivity of the ocean is ~2.5 S/m, and that in warmer surface ocean water, the conductivity is ~6 S/m [14]. Since this work is focused on ULF propagation in colder, deeper ocean waters (but not the deepest parts of the ocean), we used a value of $\sigma = 3.3$ S/m. The impact of accounting for the varying ocean conductivity in an FDTD model that extends from more than 2 km below the surface of the ocean and up into the atmosphere is presented in Fig. 12 of [4]. As expected, higher ocean conductivity values increase the attenuation of the ULF waves.

The undersea cable source is assumed to have a sinusoidal current of frequency 0.1, 1, 10, or 100 Hz with an amplitude of $I = 10$ mA. The cable is modeled as an infinitely-long current density source immediately above the ground, as shown in Fig. 1. Specifically, the cable source is modeled along a string of electric field components oriented in the X-direction (E_x) and across the entire length of the grid. Periodic boundary conditions (PBC) are used on the -X and +X edges of the grid to make the cable infinitely long in the X-direction. This is implemented by copying the last layer of updated, tangential electric field values on the +X side of the grid to the first layer of stored (not updated) electric field values on the -X side of the grid:

$$E_t(1,:,:) = E_t(imax,:,:). \quad (1)$$

This is performed immediately after the $E_t(imax,:,:)$ components are updated. Also, the magnetic fields are copied in the reverse direction; the first layer of updated tangential magnetic fields on the -X side of the grid are copied to the +X side of the grid:

$$H_t(imax,:,:) = H_t(1,:,:). \quad (2)$$

This is performed immediately after the $H_t(1,:,:)$ components are updated.

When the object is added to the grid, however, the periodic boundaries in the X-direction cause the object to be modeled as a periodic array in the X-direction. Therefore, the FDTD grid is extended over a considerable distance in the X-direction (5 km) to allow sufficient attenuation of the electromagnetic scattering from the mirrored objects, so that they do not influence the calculation of the scattered fields from the primary object of interest.

The other edges of the grid in the Y- and Z-directions employ surface impedance boundary conditions (SIBC)

to save computational space for each material. The Beggs method is used to formulate the SIBC for the ocean ground and ocean water [15], where the tangential electric fields on the same side of the boundary as the FDTD grid are updated using:

$$\vec{E}_t(n\Delta t) = \eta_2\left[\hat{n} \times \overrightarrow{H_t}(n\Delta t)\right] - \sum_{i=1}^{L} A_i(n\Delta t), \quad (3)$$

where n is the time step number, Δt is the time step increment, η_2 is the impedance of the ocean/ground boundary, L denotes the number of first-order rational functions used in the approximation (a value of 6 was used),

$$A_i(n\Delta t) = p_{i1}\left[\hat{n} \times \overrightarrow{H_t}(n\Delta t)\right] + p_{i2}\left[\hat{n} \times \overrightarrow{H_t}((n-1)\Delta t)\right] + p_{i3}\, A_i((n-1)\Delta t), \quad (4)$$

and

$$p_{i1} = \eta_2 \frac{C_i}{\omega_i}\left[1 + (e^{-a\omega_i \Delta t} - 1)/(\Delta a \omega_i)\right], \quad (5)$$

$$p_{i2} = \eta_2 \frac{C_i}{\omega_i}\left[\frac{1}{(\Delta t a \omega_i)} - e^{-a\omega_i \Delta t}\left(1 + 1/(\Delta t a \omega_i)\right)\right], \quad (6)$$

$$p_{i3} = e^{-a\omega_i \Delta t}, \quad (7)$$

where $a = \sigma_2/\varepsilon_2$, and the six values used for C_i and ω_i are provided in Table 1 of Ref. [15]. Please see Ref. [15] for more details. Additional simulations not shown here demonstrate that extending the grid out further in the X-, Y-, and Z-directions does not alter the results for the primary object of interest.

The object has a conductivity of $\sigma = \mathbf{1} \times \mathbf{10^7}$ S/m (on the same order as many metals) and resides on many electric field components in the shape of a cylinder with a diameter of 60 m and a length of 60 m.

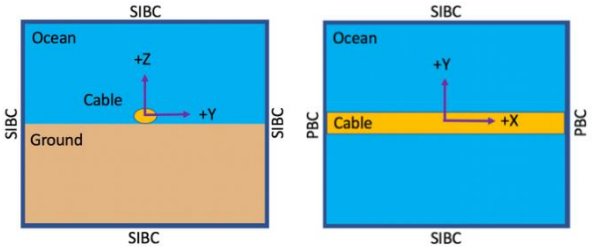

Fig. 1. Schematic diagram of Model #1 without the object. On the left is a view of the YZ-plane at the center of the FDTD grid in the X-direction. The diagram shows the ocean (blue), ground below the ocean (light brown), and the cable (yellow cylinder) located just above the ocean floor. PBCs are utilized on the X-direction edges of the grid, and SIBCs are used on the other four edges of the grid. On the right is a view of the XY-plane just above the ground and through the center of the cable.

III. DETECTABILITY AND FREQUENCY STUDY

A. Scattering calculation

To determine the optimal operating frequency for the remote-sensing system, the scattering from the object is first obtained for different cable source frequencies. Model #1 is run with no object. Then it is re-run with the object located horizontally away from the cable source at a distance of 2 km (on the ground). Several possible operating frequencies are tested to compare the scattering attenuation rates away from the object. Specifically, 0.1, 1, 10, and 100 Hz are tested. For each frequency, the simulation is run for a different number of time steps to ensure that steady-state conditions are reached all the way out to the edges of the grid. For example, the 100 Hz source is run for 25 wavelengths compared to just half of a wavelength for the 0.1 Hz source.

The scattering from the object is obtained by comparing the results from the simulation having the objects vs. the simulation without the object. Specifically, the total magnetic density field perturbation, ΔB, at any position of interest (X, Y, Z) is obtained from (8) by calculating the difference between the total magnetic flux density from the simulation having the object (B^{Obj}) vs. the simulation without the object ($B^{\text{No O}}$):

$$\Delta B(X,Y,Z) = B^{\text{Obj}}(X,Y,Z) - B^{\text{No Obj}}(X,Y,Z), \quad (8)$$

where

$$B^{\text{Obj}}(X,Y,Z) = \sqrt{\begin{aligned}&\left(B_X^{\text{Obj}}(X,Y,Z)\right)^2 \\ &+\left(B_Y^{\text{Obj}}(X,Y,Z)\right)^2 \\ &+\left(B_Z^{\text{Obj}}(X,Y,Z)\right)^2,\end{aligned}} \quad (9)$$

and

$$B^{\text{No Obj}}(X,Y,Z) = \sqrt{\begin{aligned}&\left(B_X^{\text{No O}}(X,Y,Z)\right)^2 \\ &+\left(B_Y^{\text{No O}}(X,Y,Z)\right)^2 \\ &+\left(B_Z^{\text{No O}}(X,Y,Z)\right)^2.\end{aligned}} \quad (10)$$

All of the ΔB results are plotted on a log base 10 scale according to:

$$\Delta B_{\log}(X,Y,Z) = \log_{10}(|\Delta B(X,Y,Z)|). \quad (11)$$

B. Background Noise Level (BNL) and Detection Limit (DL)

To investigate the feasibility of using the remote-sensing system in a real-world scenario, the field perturbations caused by the object are compared to the background noise level (BNL) to see how far away an object may be detected at each frequency. Figure 2 displays the magnetic background noise level over a wide range of frequencies in the air region of the Earth-ionosphere waveguide [16]. Figure 2 shows measured data along with a fitted curve.

According to Snell's Law, any electromagnetic wave propagating in the air region will propagate nearly perfectly downward in the ocean after crossing the air-ocean interface. Thus, the background noise level at

depth in the ocean may be obtained by taking the BNL in the air and attenuating it according to plane wave theory with depth in the ocean. Table 1 provides the BNL for the magnetic flux density in the air region and then also the corresponding attenuated magnetic flux density at a depth of 3 km below the ocean surface (roughly the average depth of the ocean). The scaling law equation from [16] (see the caption for Fig. 2) provides the BNL in the air assuming the receiver bandwidth is equal to the center frequency of the source.

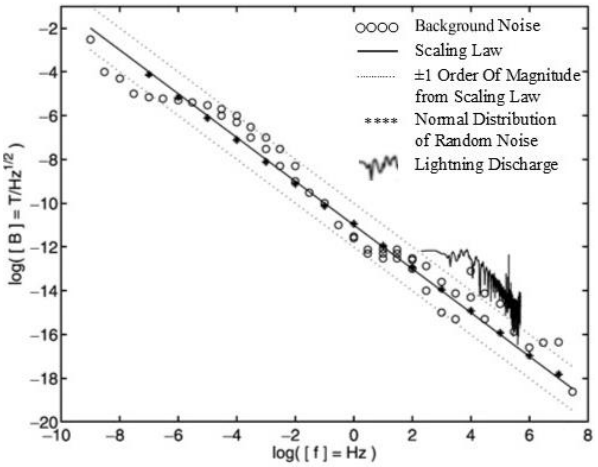

Fig. 2. The measured magnetic field spectrum of the background noise from ~10-9 Hz to ~107 Hz (circles) which can be approximated by the scaling law (solid line) B = B0(f0/f) where B0 ≈ 10−11 T/Hz1/2, f0 = 1 Hz is a scaling constant, and f is the frequency of the magnetic field. The measured magnetic field exhibits deviations from the scaling law by ∼±1 order of magnitude across the entire frequency range (dotted lines). The scaling law is simulated in the frequency range from 10−7 Hz to 107 Hz with a persistent normal distributed random noise process (stars) and exhibits an excellent agreement with the scaling law. The noisy solid line is measured data from a lightning discharge. (Courtesy of Ref. [16]).

Table 1: Background noise levels at different frequencies

Frequency	BNL in the Air Region	BNL at 3 km Depth in the Ocean
0.1 Hz	0.316 nT	0.0117 nT
1.0 Hz	1.00e-2 nT	2.04e-7 nT
2.0 Hz	3.55e-3 nT	8.01e-10 nT
10.0 Hz	3.16e-4 nT	3.28e-19 nT
100.0 Hz	1.00e-5 nT	5.07e-53 nT

To investigate the feasibility of using the remote-sensing system in a real-world scenario, the field perturbations caused by the object are compared to the sensitivity of a sensor that may be used. For this study, a superconducting quantum interference device (SQUID) magnetometer is considered for detecting the perturbation. SQUID sensors are based on superconducting loops containing alternating current Josephson junctions. The SQUID is inductively coupled to a resonant tank circuit, and the effective inductance of the tank circuit changes depending on the external magnetic field, thus changing the resonant frequency of the tank circuit. SQUIDS have been used in oil exploration, mapping tectonic faults, biomedical imaging, and in military applications [18]. SQUIDs are known to have a detection limit (DL) on the order of $fT/\sqrt{Hz}$ [17]. In Table 2 is listed the range of source frequencies and the associated DL for a SQUID magnetometer.

Table 2: Detection limit for SQUID magnetometers at different frequencies

Frequency	Detection Limit (DL)
0.1 Hz	3.1e-6 nT
1.0 Hz	1.0e-6 nT
10.0 Hz	3.1e-7 nT
100.0 Hz	1.0e-7 nT

C. Results

The BNL and DL values are now compared with the FDTD-calculated perturbations caused by the object. In Fig. 3, the scattering from the object at each source frequency is plotted in the Y-direction along a line through the center of the object (at X = 0, Z = 0). The object is placed at Y = 2 km away from the cable on the ground (at X = 0, Z = 0). The cable source is assumed to carry 10 mA. At each frequency, a horizontal line indicates the larger of the two values obtained from Table 1 (BNL) or Table 2 (DL) are plotted (so, the BN level is indicated for 0.1 Hz, and the DL level is indicated for 1, 10, and 100 Hz). For the object to be detectable, the scattered total magnetic density caused by the object must be above the corresponding horizontal line.

Examining the results in Fig. 3, at 1, 10, and 100 Hz the scattering from the object is detectable above the BNL and DL at distances away from the object. However, the scatterings at 100 Hz are only detectable within a few hundred meters of the object, and the scatterings at 10 Hz are detectable at distances of < 1 km. Thus, ~1 Hz is determined to be an optimal frequency for detecting a 60-m diameter and 60-m long object on the ocean floor.

Considering the values in Tables 1 and 2 and the results in Fig. 3, the detectability of the object may be improved if: (1) the cable source can carry more than 10 mA; or (2) more sensitive magnetometers may be employed.

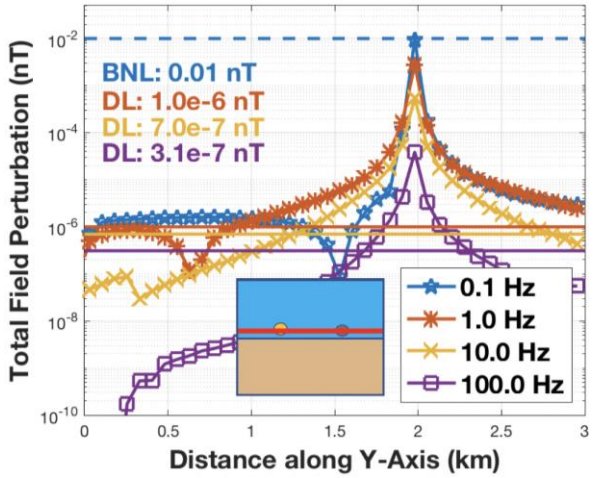

Fig. 3. Scattered total magnetic flux density from the object located at Y = 2 km and at the different source frequencies. Also included is a horizontal line indicating the larger of the two values obtained from Tables 1 and 2 at each frequency: the background noise level (BNL, shown as a dashed horizontal line) at a depth of 3 km in the ocean or the detection limit (DL, shown as a solid horizontal line) of a SQUID magnetometer.

IV. OCEAN FLOOR

Before different positions of the object are considered, Model #1 is used to study the effect of the ocean floor on the detectability of the object. The ocean floor is expected to play a role in the electromagnetic propagation from the cable source and the scattering from the object, since both the cable and object of interest are located directly on the ocean floor.

For this study, the same Model #1 is rerun at 1 Hz as for the results in Fig. 3, except that the ground is removed and it is replaced with ocean (it is an all-ocean model). Figure 4 superimposes the difference in the total magnetic flux densities at 1 Hz from Fig. 3 (with ground) with the corresponding results obtained from the two all ocean simulations (run with and without the object). As shown in Fig. 4, the ground plays a huge role in the total scattered magnetic flux densities when the source and scattering object are on the ground.

V. MODEL #2

A lower-resolution model (Model #2) is now used to perform simulations at the optimal frequency of 1 Hz. Model #2 is the same as Model #1 except for three changes:

(1) The grid resolution is 60 m in each Cartesian direction rather than 15 m. This 60-m resolution is still sufficient to capture the size of the object, the 1.7 km electromagnetic wavelength, and the 275 m skin depth at 1 Hz in the ocean, but it relaxes the computational requirements.

(2) Model #2 covers a larger spatial region, namely 7.4, 10.8, and 9.0 km in the X-, Y-, and Z-directions, respectively. This allows the object to be placed at further distances from the cable.

(3) The object size remains the same, but only one electric component (E_x) is used to model the object at the lower grid resolution.

Models #1 and #2 have been shown to provide identical results for the 1 Hz result shown in Fig. 3 (not shown here).

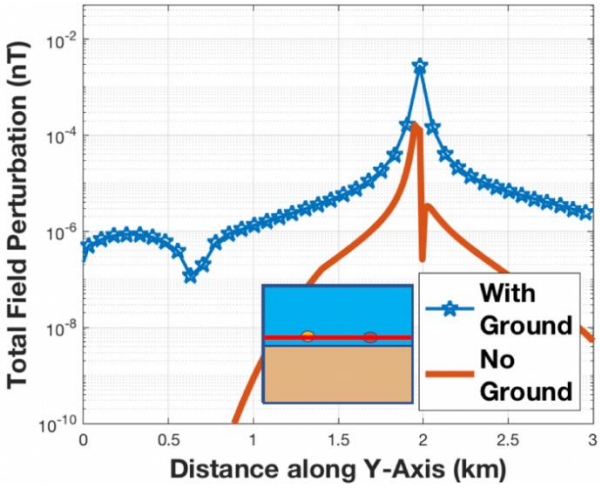

Fig. 4. Scattered total magnetic flux density from the object located at Y = 2 km and at 1 Hz for Model #2 (including the ground as in Fig. 3) and then for the case wherein the ground is replaced with ocean (an all-ocean model). The ground causes a significant amount of reflection allow more scattering from the object.

VI. SCATTERING

Model #2 is now used to obtain scatterings from the object located at different positions relative to the cable source. A realistic bathymetry is added for the ocean floor. Figure 5 displays the 2D and 1D plots of the bathymetry added to Model #2. The bathymetry data is a survey off the eastern coast of the U.S. The data is directly from the NOAA National Centers for Environmental Informational website (U.S. Coastal Relief Model Vol. 21). To obtain the perturbation from the scattering object, two sets of simulations are run as in Section III: the model is run with the object and then without the object. Equations (8) and (11) are used to

[1] https://www.ngdc.noaa.gov/mgg/coastal/grddas02/html/gna37075.htm

calculate the perturbation as the object is placed at various locations in the model.

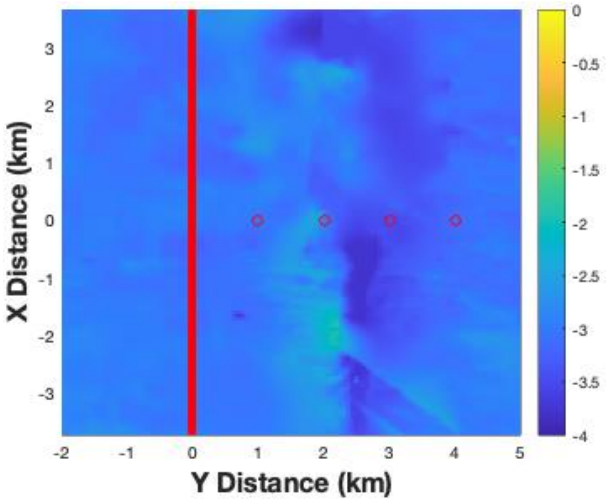

(a)

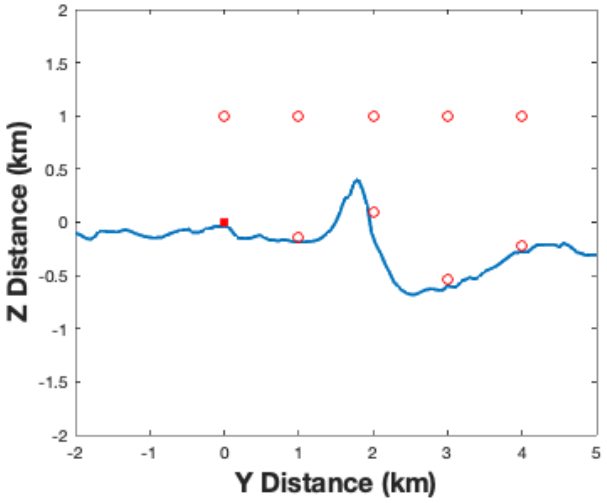

(b)

Fig. 5. (a) 2D top view of the bathymetry used in Model #2. The color scale refers to the elevation depth from the ocean surface. The red line represents where the cable source is located. The red circles illustrated where the scattering object is located for each simulation. (b) Is a 1D plot extending through the cable and scattering object locations of (a) in order to show in more detail the variance of the ocean floor.

Figure 6 illustrates the steady-state magnetic flux density values at 1 Hz (maximum magnetic flux densities achieved over all time steps at each grid cell). As expected, the 1 Hz wave attenuates faster in the ocean ($Z \geq 0$ km) than in the ground ($Z < 0$ km) due to the higher conductivity of the ocean. Also seen in Fig. 6 is that the much lower attenuation rate in the hill to the right of the cable makes up for the relatively high reflection coefficient between the ocean/ground and ground/ ocean interfaces. Also, there is diffraction around the hill. This means that there are higher amplitudes observed in the ocean on the far side of the hill relative to when there is a flatter ground (as on the left side of the cable).

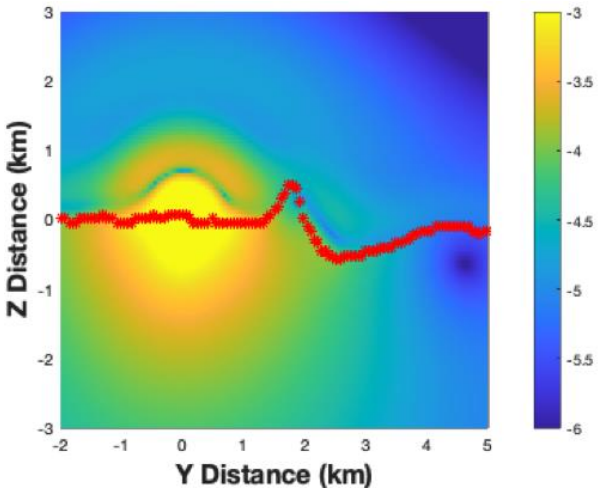

Fig. 6. A YZ-plane of the grid at X = 0 of the steady-state total magnetic flux density amplitudes with no object present plotted on a log base 10 scale. The cable source is located at (Y=0, Z=0). The units are in nanoTelsa. The red markers indicate the ocean floor.

A. Object on the ground

For the first simulation, the object is placed on the ocean floor at a distance of 1 km from the cable source. The simulation with the object is rerun three more times, with the object moved each time in 1 km increments away from the source until it reached 4 km (when the object is at Y = 2, the simulation scenario matches that of Fig. 3). Figure 7 shows the placement of the object for each of these four simulations.

Figure 8 shows a YZ-plane of total magnetic density field perturbation values at X = 0 on a log scale as calculated from (11) with the cable source at (Y=0, Z=0) km and the object at (X=0, Y=1, Z=0) km. The presence of the object is clearly visible, as well as the interaction of the scattering caused by the object with the ground and cable.

Figures 9 – 11 plot the total magnetic density field perturbation on a log scale as calculated by (11) for all four positions of the object along the ground. Figure 9 plots the perturbation along the Y-direction at X = 0 and Z = 0. As expected, the peak amplitude of $\Delta B_{\log}$ decreases as the object is moved further from the cable source. Comparing the magnitudes of the four peaks in Fig. 9, as well as additional simulations for a flat ground, the presence of the hill does not diminish the detectability of the object (at 1 km vs. further distances). Also, note that the electromagnetic wavelength in the

ocean water at 1 Hz is just 1.7 km, so when the object is at a distance of 1 km, it is in the near field of the cable.

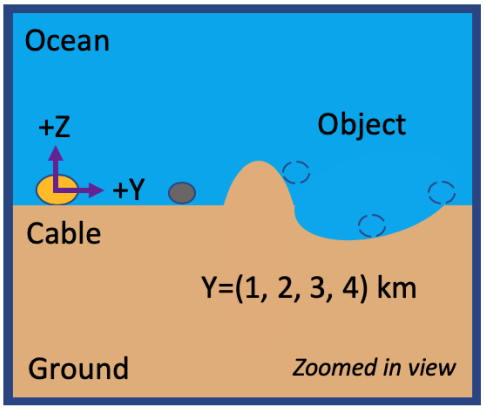

Fig. 7. Zoomed-in diagram illustrating where the object (gray and dashed circles) is placed in each simulation. In four separate simulations, the object is placed on the ocean floor starting 1 km away from the cable and then it is moved further away in increments of 1 km. The object is represented by grey and dashed circles to indicate that only a single object is included in each simulation.

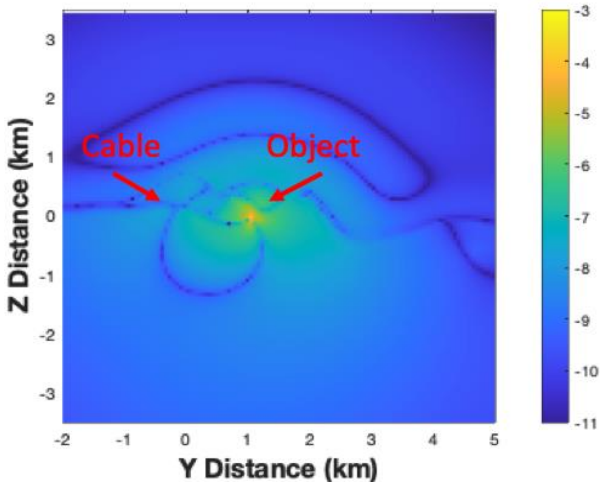

Fig. 8. A YZ-plane at X = 0 of $\Delta B_{\log}$ as calculated by Eq. 2. The object is placed at (X=0, Y=1, Z=0) km, and the cable is at (Y=0, Z=0) km in the image. The units are in nanoTesla. Note that the color scale is the same as in Fig. 6.

Figure 10 plots the perturbation along the X-direction at Z = 0 and through the center of the object. The background noise level (BNL) and magnetometer sensitivity limit (SL) from Tables 1 and 2 are plotted for comparison. Finally, Fig. 11 plots $\Delta B_{\log}$ along the Z-direction at X = 0 and through the center of each object. Negative Z positions correspond to positions in the ground.

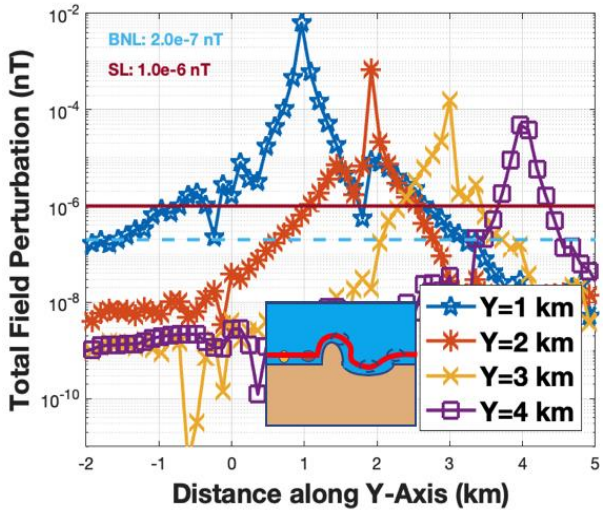

Fig. 9. Zoomed-in 1-D plots of $\Delta B_{\log}$ from four separate FDTD simulations with the object at distances of 1, 2, 3, and 4 km away from the cable source in the Y-direction and immediately above the ground. The values are plotted along the Y-direction along the red line shown in the diagram inset. The legend Y values correspond to the location of the object. The dash (BNL) and solid (SL) lines are the background noise level and sensor limits.

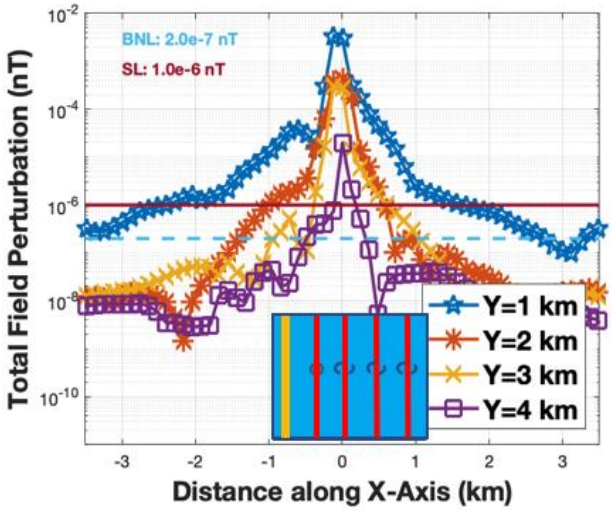

Fig 10. Same as Fig. 9, but now plotted along the X-direction at Y = 1, 2, 3, and 4 km and Z = 0 km. The legend Y values correspond to the location of the object.

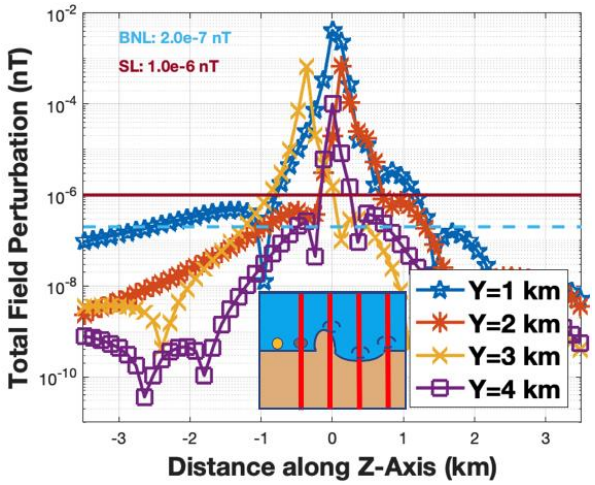

Fig. 11. Same as Fig. 9, but now plotted along the Z-direction at Y = 1, 2, 3, and 4 km and at X = 0 km. The legend Y values correspond to the location of the object.

B. Object 1 km above the ground

Following the same procedure as in Section A, Model #2 is now rerun with the object elevated 1 km above the ocean floor. First, the object is placed immediately above the cable source. The simulation with the object is then rerun four more times, with the object moved in 1 km increments horizontally away along the Y-direction. Figure 12 shows the placement of the object for each of these five simulations.

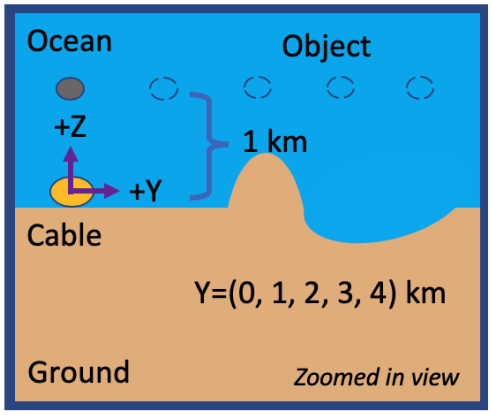

Fig. 12. Zoomed-in diagrams illustrating where the object (gray and dashed circles) is placed in each simulation. On the right side, in five separate simulations, the object is placed 1 km above the ocean floor. The object is initially positioned directly above the source and then it is moved horizontally away in the Y-direction in increments of 1 km. The object is represented by grey and dashed circles to indicate that only a single object is included in each simulation.

Figures 13 and 14 plot the total magnetic density field perturbation on a log scale as calculated by (11) for all five positions of the object. Figure 13 plots $\Delta B_{\log}$ along the Z-direction at X = 0 and through the center of each object. Figure 14 plots the perturbation along the Y-direction at X = 0 and Z = 1 km. Again, as expected, the peak amplitude of $\Delta B_{\log}$ decreases as the object is moved farther from the cable source.

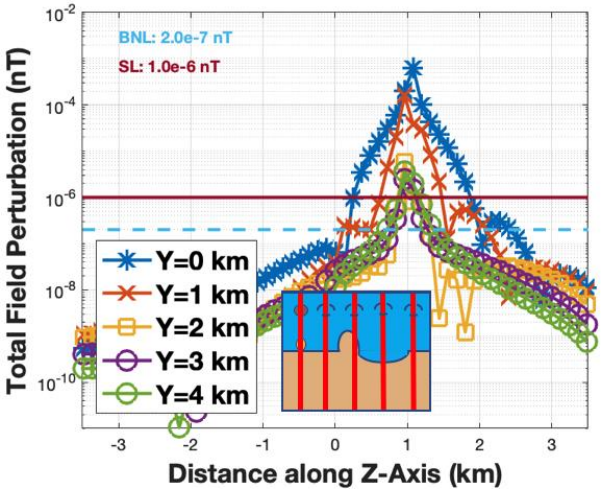

Fig. 13. Zoomed-in view of $\Delta B_{\log}$ from five separate FDTD simulations with the object 1 km above the ground and 0, 1, 2, 3, and 4 km away from the source in the Y direction. The values are recorded in the Z-direction along the red lines of the diagram inset. The legend Y values correspond to the location of the object and Y-position of the recorded data. The dash (BNL) and solid (SL) lines are the background noise level and sensor limits.

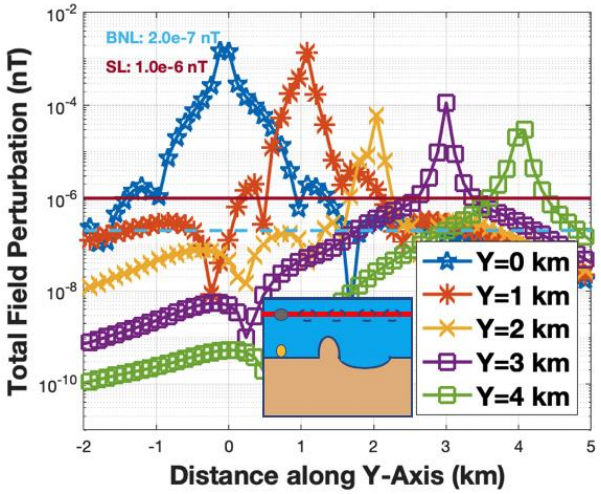

Fig. 14. Same as Fig. 13, but now along the Y-direction at X = 0 and Z = 1 km. The legend Y values correspond to the location of the object. The dash (BNL) and solid (SL) lines are the background noise level and sensor limits.

C. Discussion

The results in Sections A and B are now used to design a possible detection system. Using an undersea cable operating with 10 mA and at a frequency of 1 Hz, the object on the ground is observed to be detectable at distances of at least 4 km from the cable source. From Fig. 9, sensors would need to be placed at 1 km increments on the ground away from the cable in the Y-direction in order to detect the scatterings from the object above the BNL and the DL of the sensor. From Fig. 10, the sensors would also need to be in 1 km increments in the X-direction at Y distances up to 2 km, but then every ~500 meters between 2 and 4 km. The possible sensor array that accounts for the results from both Figs. 9 and 10 is shown in Fig. 15. Each sensor location would have one 3-axis SQUID magnetometer.

The above analysis assumes the object is parallel to the cable. The spacing of the sensor array may need to be closer to 500 meters at all distances from the cable and in both the X- and Y-directions if the object is always oriented perpendicularly to the cable.

From Fig. 13, none of the (sinking) objects 1 km above the ground are detectable on the ground, however, it would be possible to detect the sinking objects 1 km above the ground using sensors floating 1 km above the ocean floor. Therefore, this detection system is ideal for sunken airplanes and ships that lay on the ocean floor.

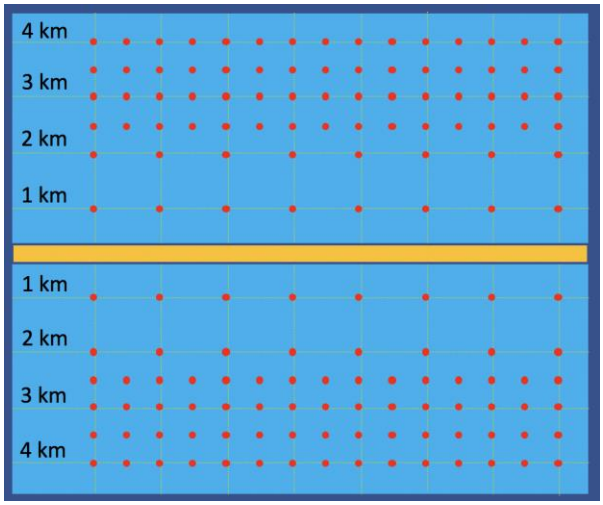

Fig. 15. Proposed sensor array for sensors (red circles) located on the ground and used to detect objects on the ground or located a relatively short distance above the ground.

IV. CONCLUSION

Remote sensing of airplanes that have crashed into the ocean is challenging due to the short skin depth of the electromagnetic fields, especially at frequencies above 100 Hz. In this Paper, a remote-sensing system is proposed that would involve three steps: (1) a subsea cable would be used to generate electromagnetic waves at 1 Hz; (2) the electromagnetic waves from the source would propagate in the ocean water and scatter off of objects (submerged airplanes modeled as being 60 m long and having a diameter of 60 m), thereby perturbing the background magnetic fields; and (3) the scatterings off of the objects would be detected by an array of sensors (spaced 1km apart closer to the cable and 500 further away from the cable) on the ocean floor. This proposed remote-sensing system would detect any of the sunken metallic objects within at least 4 km horizontally away from the cable. Note, however, that the spacing of the sensors may need to be slightly adjusted when the ocean conductivity in the vicinity of the sensors is different than the assumed 3.3 S/m used in this Paper (i.e., the sensors may be spaced farther apart when the ocean conductivity is lower than 3.3 S/m).

3-D FDTD models were used to design this remote-sensing system. Specifically, they were used to obtain the total magnetic flux density field perturbation from the object located at various distances and positions from the cable. The total field perturbation was extracted by running the model first without and then with the object. The FDTD models were also used to determine the optimal operation frequency for the remote-sensing system (1 Hz), which provides detection capabilities over the largest distances from the source and also permits the sensors to be located as far apart as possible. A separate simulation showed that for objects located on the ground, the presence of the ground improves the detectability of the object.

The FDTD-calculated scatterings caused by the object were compared with the expected background noise level of the magnetic flux density in the ocean. They were also compared with the sensitivity of a SQUID magnetometer. For the object to be detectable, the magnitude of the scatterings would need to be above the BNL and DL of the sensor. Detectability could possibly be improved by separately analyzing the magnitude of each Cartesian component of the magnetic flux density with the expected background noise level. Detectability could also be improved by increasing the current carried by the cable, and by using more sensitive sensors.

It is expected that the scatterings from an object would be dependent on its size. For this study, the object that was modeled is 60 meters in diameter and in length. Larger objects should generate larger scatterings and should be detectable at farther distances from the cable and with sensors spaced farther apart. Smaller objects would be expected to generate smaller scatterings. Future work could investigate the effect of having different sized objects.

ACKNOWLEDGMENT

The authors gratefully acknowledge the Center for

High Performance Computing (CHPC) at the University of Utah for providing supercomputing resources.

REFERENCES

[1] K. S. Yee, "Numerical solution of initial boundary value problems involving Maxwell's equations in isotropic media," *IEEE Trans. Antennas Propagat.*, vol. AP-14, pp. 302-307, 1966.

[2] W. Langewiesche, "What really happened to Malaysia's missing airplane," *The Atlantic*, July 2019.

[3] T. R. Clem, "Superconducting magnetic gradiometers for underwater target detection," *Nav. Eng. J.*, vol. 110, no. 1, pp. 139-149, Jan. 1998.

[4] R. W. P. King, "Lateral electromagnetic waves from a horizontal antenna for remote sensing in the ocean," *IEEE Trans. Antennas Propagat.*, vol. 37, pp. 1250-1255, Oct. 1989.

[5] D. R. Smith, S. Burns, J. J. Simpson, and S. M. Ferone, "FDTD modeling of scattered ultra-low frequency electromagnetic waves from objects submerged in the ocean," *IEEE Trans. Antennas Propagat.*, vol. 64, pp. 2534-2541, 2019.

[6] R. W. P. King, "Propagation of a low-frequency rectangular pulse in seawater," *Radio Science*, vol. 28, pp. 299-307, June 1993.

[7] R. W. P. King and S. S. Sandler, "The detection of dielectric spheres submerged in water," *IEEE Trans. Geosci. Remote Sens.*, vol. 30, pp. 892-896, Sept. 1992.

[8] R. W. P. King, "The propagation of a Gaussian pulse in seawater and its application to remote sensing," *IEEE Trans. Geosci. Remote Sens.*, vol. 31, no. 3, pp. 595-605, May 1993.

[9] M. Birsan, "Remote Sensing of 3-D conducting objects in a layered medium using electromagnetic surface waves," *IEEE Geosci. and Remote Sens. Let.*, Papers 4(4), pp. 561-565, 2007.

[10] M. Siegel and R. W. P. King, "Electromagnetic propagation between antennas submerged in the ocean," *IEEE Trans. Antennas Propagat.*, vol. 4, pp. 507-513, 1973.

[11] "Extremely Low Frequency Transmitter Site, Clam Lake, Wisconsin," (PDF). *Navy Fact File. United States Navy. 28 June 2001. Retrieved 17 February 2012 – via Federation of American Scientists.*

[12] S. Yee, "Numerical solution of initial value problems involving Maxwell's equations in isotropic media," *IEEE Trans. Antenna Propag.*, vol. 17, pp. 585-589, 1966.

[13] A. Taflove and S. Hagness, "Electrodynamics Entering the 21st Century" in C*omputational Electrodynamics: The Finite Difference Time-Domain Method*, 3rd ed., Norwood, MA, USA: Artech House, 2005.

[14] P. Bannister, "ELF propagation update," *IEEE J. Oceanic Eng.*, vol. OE-9, no. 3, pp. 179-188, 1984.

[15] S. Maus, "Electromagnetic ocean effects," in *Encyclopedia of Geomagnetism and Paleo-magnetism*, New York, NY, USA: Springer, 2007, pp. 740-742.

[16] J. Beggs, "Finite-difference time-domain implementation of surface impedance boundary condition," *IEEE Trans. Antenna Propag.*, vol. 40, no. 1, Jan. 1992.

[17] M. Füllekrug and A. C. Fraser-Smith, "The earth's electromagnetic environment," *Geophys. Res. Letts.*, 38, L21807, 2011. Doi: 10.1029/2011GL049572, 2011.

[18] M. Buchner, K. Hofler, B. Henne, V. Ney, and A. Ney, "Tutorital: Basic principles, limits of detection and pitfalls of highly sensitive SQUID magnetometry for nanomagnetism and spintronics," *J. Appl. Phys.*, 124, 161101, 2018.

[19] E. Mendenhall, "Shifting grounds: Scientific and technological change and international regimes for the ocean and outer space," *Ph.D. Dissertation*, Submitted to Johns Hopkins University, June 2017.

Dallin R. Smith received the B.S. in Physics from Brigham Young University, Provo, UT, USA, in 2016, and the M.S. and Ph.D. degrees in Electrical Engineering from the University of Utah, Salt Lake City, UT, USA, in 2019 and 2020, respectively. He is a Research Engineer in the Geospace Environment Impacts and Application Branch with the Space Vehicles Directorate, Air Force Research Laboratory, Albuquerque, NM, USA.

Jamesina J. Simpson received the B.S. and Ph.D. degrees in Electrical Engineering from Northwestern University, Evanston, IL, USA, in 2003 and 2007, respectively. She is an Associate Professor in the Electrical and Computer Engineering Department, University of Utah, Salt Lake City, UT, USA. Her research lab encompasses the application of the full-vector Maxwell's equations finite-difference time-domain (FDTD) method to electromagnetic wave propagation spanning 15 orders of magnitude across the electromagnetic spectrum. In particular, her group specializes in electromagnetic wave propagation within the global Earth-ionosphere waveguide. She received a 2010 National Science Foundation CAREER award, the 2012 IEEE AP-S Donald G. Dudley, Jr. Undergraduate Teaching Award, the 2017 URSI Santimay Basu Medal, and the 2020 IEEE AP-S Lot Shafai Mid-Career Distinguished Achievement Award.

Near-to-Far Field Transformation in FDTD: A Comparative Study of Different Interpolation Approaches

Ravi C. Bollimuntha[1], Mohammed F. Hadi[2], Melinda J. Piket-May[1], Atef Z. Elsherbeni[2]

[1]Department of Electrical, Computer and Energy Engineering
University of Colorado Boulder, Boulder, CO 80309, USA
ravi.bollimuntha@colorado.edu, mjp@colorado.edu

[2]Department of Electrical Engineering
Colorado School of Mines, Golden, CO 80401, USA
mhadi@mines.edu, aelsherb@mines.edu

Abstract—Equivalence theorems in electromagnetic field theory stipulate that farfield radiation pattern/scattering profile of a source/scatterer can be evaluated from fictitious electric and magnetic surface currents on an equivalent imaginary surface enclosing the source/scatterer. These surface currents are in turn calculated from tangential (to the equivalent surface) magnetic and electric fields, respectively. However, due to the staggered-in-space placement of electric and magnetic fields in FDTD Yee cell, selection of a single equivalent surface harboring both tangential electric and magnetic fields is not feasible. The work-around is to select a closed surface with tangential electric (or magnetic) fields and interpolate the neighboring magnetic (or electric) fields to bring approximate magnetic (or electric) fields onto the same surface. Interpolation schemes available in the literature include averaging, geometric mean and the mixed-surface approach. In this work, we compare FDTD farfield scattering profiles of a dielectric cube calculated from surface currents that are obtained using various interpolation techniques. The results are benchmarked with those obtained from integral equation solvers available in the commercial packages FEKO and HFSS.

Index Terms— Bistatic RCS, Equivalence theorem, FDTD, Field interpolation, Near-to-farfield transformation, Total-field/Scattered-field (TF/SF).

I. INTRODUCTION

Equivalence theorems come very handy in efficiently calculating farfields from a radiating source or a scatterer. Extending the problem space to include the farfield region is not often computationally feasible due to time and memory costs involved. Instead, the nearfields in the form of fictitious surface currents on equivalent surface are used to calculate the farfield magnetic and electric vector potentials A and F [1]. These vector potentials are then used to obtain either radiation pattern in case of sources or radar cross section (RCS) in case of scatterers. The equivalent surface fully encloses the sources/scatterers, and small enough to keep the computational costs in budget. The whole process, called near-to-farfield transformation (NTFF), requires calculation of unknown nearfields on an equivalent surface using analytical or numerical methods depending on the problem at hand. Nearfields of complex scattering structures, such as an airplane or a vessel, can only be solved numerically using techniques such as FDTD, method of moments (MoM) and finite element method (FEM).

In FDTD, one peculiar aspect about choosing the equivalent surface is that it is not possible for any single closed surface to house both the tangential electric (E) and magnetic (H) nearfields that are used to calculate surface currents J_s and M_s. The reason being, the E and H fields are not co-located in the FDTD grid (staggered in space along all three dimensions). This makes it necessary to interpolate fields from neighboring Yee cells in order to bring E and H (and thereby J_s and M_s) onto the same surface.

Arithmetic averaging has been widely used in the literature [2–4] to interpolate and bring fields onto the same surface in the FDTD grid. Use of geometric mean [5] for interpolation is also demonstrated to yield better results for 2D scattering problems. Another radical method called the mixed-surface approach [6], that does not involve any interpolation, is also shown to perform better for strong backward-scattering problems. In

Submitted On: June 28, 2019
Accepted On: April 17, 2021

https://doi.org/10.47037/2020.ACES.J.360502

this work, we compare the bistatic RCS of a dielectric cube, obtained in FDTD using aforementioned interpolation techniques, with those obtained from integral equations solvers in commercial packages FEKO and HFSS-IE. A cube scatterer, that snaps to the electric field FDTD grid, is chosen to avoid artifacts of stair-casing in the FDTD-calculated RCS. In FEKO and HFSS-IE, the planewave source is used to illuminate the scatterer in a particular direction. In FDTD, we use the perfect total-field/scattered-field (TF/SF) technique [7–10] for planewave illumination of scatterer. The TF/SF technique used is perfect in the sense that the spurious field leakage into the scattered field region is essentially nonexistent. Moreover, it is possible to launch planewave in almost any arbitrary direction.

Frequency domain NTFF transformation is used to obtain farfield scattering profile (to be exact, bistatic radar cross section, RCS), in the three planes XY, XZ and YZ, of the dielectric cube at a single frequency. This involves applying DFT (Discrete Fourier Transform) to the time-domain surface currents (on the entire equivalent surface) to obtain frequency domain currents at the desired frequency. These frequency domain currents are then used to calculate RCS at the desired frequency.

II. LEAKAGE-FREE TF/SF TECHNIQUE FOR A PLANEWAVE SOURCE IN FDTD

In TF/SF formulation, the FDTD problem space is divided into two regions: a total-field (TF) region and a scattered-field (SF) region. The interface between the two regions is used to introduce planewave sourcing conditions that excite fields inside the TF region. This is also an application of equivalence principle, that equivalent sources are used here to recreate fields *inside* a volume bounded by a closed surface.

Exciting planewaves using TF/SF formulation involves two steps [7–10]: 1) propagate a planewave, exploiting its one dimensional nature, along an auxiliary 1D FDTD grid. 2) Use the fields computed on the auxiliary 1D grid to enforce source conditions, in the form of consistency corrections to the main grid update equations, at the interface between the TF and SF regions. These consistency corrections act as equivalent source conditions and excite the planewave in the TF region of the main grid.

If the fields on the 1D grid undergo the same numerical dispersion as that of the main grid, it is possible to perfectly confine the planewave to the TF region, without any leakage into SF region. The above condition is satisfied, as shown by [9], when $\frac{p_x \Delta x}{m_x} = \frac{p_y \Delta y}{m_y} = \frac{p_z \Delta z}{m_z} = \Delta r$ (the rational angle condition), where $p_x = \cos\phi_{inc} \sin\theta_{inc}$, $p_y = \sin\phi_{inc} \sin\theta_{inc}$, and $p_z = \cos\theta_{inc}$. The angles θ_{inc} and ϕ_{inc} specify the direction of propagation of incident planewave. m_x, m_y, and m_z are some integers (all even or all odd), and Δr is 1D grid spacing.

If we intend to excite a planewave that propagates along certain direction θ_{inc} and ϕ_{inc}, then we choose some integers that roughly satisfy the following:

$$\phi_{inc} = \tan^{-1}\frac{m_y}{m_x},\ \theta_{inc} = \cos^{-1}\frac{m_z}{\sqrt{m_x^2 + m_y^2 + m_z^2}}, \quad (1)$$

which are directly derived from the rational angle condition. Larger integers can be chosen to finely resolve the angle of incidence.

The unique feature of this process is every field location of the main grid can be mapped onto a 1D grid (along the unit propagation vector of the planewave) and vice-versa. This allows us to collapse the very 3D FDTD update equations into a 1D form, thereby ensuring the fields on the 1D grid undergo the same numerical dispersion as that of the main 3D grid. This in turn ensures that the spurious leakage into SF region is negligible (as low as $-320\ dB$ or at machine precision), as mentioned earlier.

The polarization of the planewave is defined by E_ϕ and E_θ, for example if $E_\theta = 1$ & $E_\phi = 0$, the planewave will be theta-polarized. The polarization coefficients of the electric and magnetic fields in the X, Y and Z directions are given by [4]:

$$\begin{aligned}
E_{inc,x} &= [E_\theta \cos(\tilde{\theta}_{inc}) \cos(\tilde{\phi}_{inc}) - E_\phi \sin(\tilde{\phi}_{inc})] f(t),\\
E_{inc,y} &= [E_\theta \cos(\tilde{\theta}_{inc}) \sin(\tilde{\phi}_{inc}) + E_\phi \cos(\tilde{\phi}_{inc})] f(t),\\
E_{inc,z} &= -E_\theta \sin(\tilde{\theta}_{inc}) f(t),\\
H_{inc,x} &= \frac{-1}{\eta_0}[E_\phi \cos(\tilde{\theta}_{inc}) \cos(\tilde{\phi}_{inc}) + E_\theta \sin(\tilde{\phi}_{inc})] f(t),\\
H_{inc,y} &= \frac{-1}{\eta_0}[E_\phi \cos(\tilde{\theta}_{inc}) \sin(\tilde{\phi}_{inc}) - E_\theta \cos(\tilde{\phi}_{inc})] f(t),\\
H_{inc,z} &= \frac{1}{\eta_0} E_\phi \sin(\tilde{\theta}_{inc}) f(t),
\end{aligned} \quad (2)$$

where the function $f(t)$ is a time-series having a suitable profile for FDTD simulations that rises smoothly from zero or negligible value, such as sufficiently delayed Gaussian or modulated Gaussian pulses. The above coefficients are useful when hard-sourcing few initial grid points, to initiate the planewave on the auxiliary 1D grid of the TF/SF formulation [10]. Numerical angles (with a $\tilde{}$, i.e. $\tilde{\theta}_{inc}$ and $\tilde{\phi}_{inc}$) are used to calculate these coefficients. For the relationship between numerical angles and those given in equation (1), refer to [8].

III. NTFF EQUIVALENT SURFACE FIELD INTERPOLATION TECHNIQUES

The equivalent surface, on which near-to-farfield transformation is performed, is placed in the scattered field region as shown in Fig. 1. The scattered fields on

this equivalent surface are used to calculate surface currents, that are used in the surface integrals to calculate vector potentials. However, a single equivalent surface will not house both the tangential magnetic and electric fields (or surface currents), because of the staggered field locations in FDTD grid, as shown in Fig. 2.

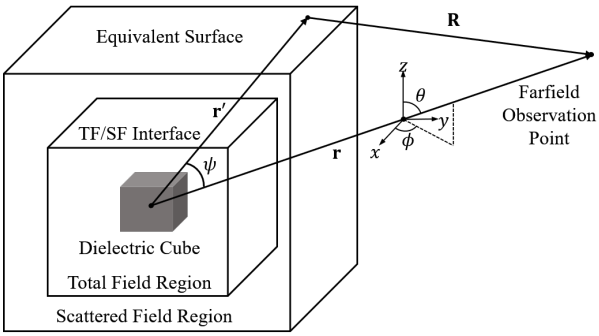

Fig. 1. Schematic of the FDTD problem space, showing the dielectric scatterer, TF/SF regions and the Equivalent surface.

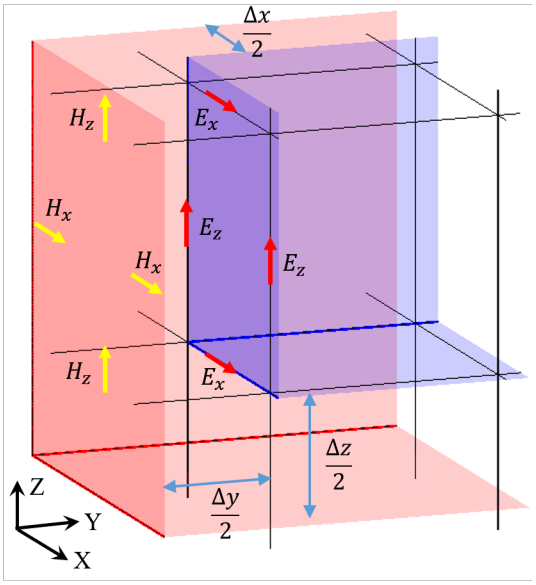

Fig. 2. The tangential electric and magnetic fields on two separate surfaces, red and blue.

One of the techniques to bring the surface currents (J_s and M_s) on to the same surface is to interpolate electric and magnetic fields using arithmetic average. Average of four H fields and two E fields (time-domain fields) brings currents onto the same surface and to the same location, as demonstrated in [4]. This is shown in Fig. 3. Discrete Fourier transform (DFT) is applied on the time-domain average to obtain frequency-domain current components, at the desired frequencies. These frequency-domain currents are obtained at discrete locations, covering all the six faces of the equivalent surface.

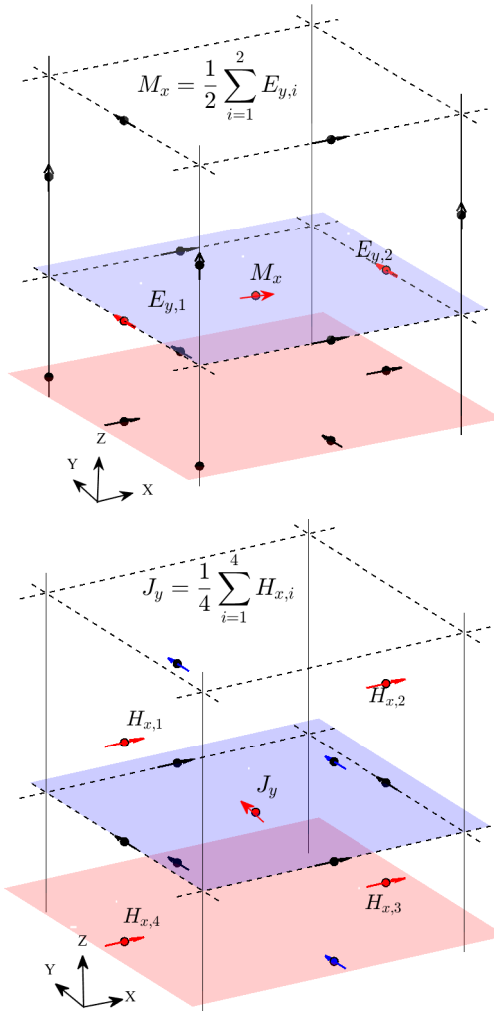

Fig. 3. Top: Average of two electric field components highlighted red gives magnetic current component M_x. Bottom: Average of four magnetic field components highlighted red gives electric current component J_y.

Geometric mean interpolation is another technique that can also be performed on the same fields as used by arithmetic averaging, shown in Fig. 3. However, a different sequence of steps is followed. First, the DFT is applied on the four time-domain H fields and the two time-domain E fields at the desired frequencies, and then the geometric mean of the complex-valued frequency-domain currents are obtained at all the discrete locations of the equivalent surface. Directly applying geometric mean on time-domain fields would force us to take the square root and fourth root of negative real values. Applying DFT first and then taking the geometric mean

would help avoid this.

While taking the geometric mean of complex numbers, the following pitfall needs to be avoided. The phases (angles of complex numbers) range between $[-\pi, \pi]$ in computational software by default. The angles that are less than $-\pi$ (such as -1.1π and -1.5π) are automatically wrapped-up by 2π (so that -1.1π becomes 0.9π and -1.5π becomes 0.5π). This makes it difficult to interpolate angles (phases) to compute geometric mean of complex numbers, since averaging the angles that are combination of wrapped-up and those that are not produces inconsistent results. This is essentially the conundrum involved in choosing the correct root while taking n^{th} root of product of n complex numbers, i.e. the geometric mean of n complex numbers. One solution to this problem is to first detect if there are any phase wraps (negative angles wrapped to positive angles) among the angles of complex numbers that we are trying to take the geometric mean of. If there aren't any phase wraps, simply use the average of phases of the complex numbers to calculate geometric mean. If there are phase wraps, we need to subtract h multiples of 2π from sum of the phases before taking the average of phases. Here, h is the number of positive phases among the complex operands for geometric mean. This allows the complex geometric mean to correctly bisect the angle between the two/four complex operands.

Geometric mean approach theoretically produces no nearfield error while interpolating fields of a planewave. This can be shown using a simple example: consider the four H fields in the bottom portion of Fig. 3. The position vectors of these four field locations starting with bottom left location and going in anti-clockwise direction are $(x, y + \frac{1}{2}\Delta y, z), (x + \Delta x, y + \frac{1}{2}\Delta y, z), (x + \Delta x, y + \frac{1}{2}\Delta y, z + \Delta z), (x, y + \frac{1}{2}\Delta y, z + \Delta z)$. Also, consider a free space planewave propagating in arbitrary direction represented in frequency domain form: $e^{-\jmath \mathbf{k}\cdot\mathbf{r}}$, here $\mathbf{k}$ is propagation vector and $\mathbf{r}$ is position vector. If we want to interpolate the planewave at the location of J_y shown in bottom portion of Fig. 3 using the geometric mean of four H fields mentioned above, we obtain:

$$
\begin{aligned}
&exp\Big(\jmath\mathbf{k}\cdot\frac{1}{4}[(x + x + \Delta x + x + \Delta x + x)\,\mathbf{a}_x \\
&+ (y + \frac{1}{2}\Delta y + y + \frac{1}{2}\Delta y + y + \frac{1}{2}\Delta y + y + \frac{1}{2}\Delta y)\,\mathbf{a}_y \\
&+ (z + z + z + \Delta z + z + \Delta z)\,\mathbf{a}_z]\Big) \\
&= exp\left(\jmath\mathbf{k}\cdot[(x + \frac{1}{2}\Delta x)\mathbf{a}_x + (y + \frac{1}{2}\Delta y)\mathbf{a}_y + (z + \frac{1}{2}\Delta z)\mathbf{a}_z]\right),
\end{aligned}
\tag{3}
$$

that is exactly the same as can be obtained by substituting the position vector $(x + \frac{1}{2}\Delta x, y + \frac{1}{2}\Delta y, z + \frac{1}{2}\Delta z)$ of J_y in the planewave representation.

Another technique to overcome the staggered-nature of planes containing tangential currents in FDTD for performing near-to-farfield transformation is mixed-surface approach introduced in [6]. Similarities exist between mixed-surface approach and TF/SF formulation. For example, the fictitious surface currents introduced at the TF/SF interface in the TF/SF formulation, in the form of consistency corrections to the FDTD update equations, where they excite equivalent planewave fields *inside* the total field region, required no interpolation. This mixed-surface approach is a dual of the TF/SF formulation, in the sense that it also does not use field interpolation to launch equivalent farfields *outside* the equivalent surface.

During the consistency corrections to the electric field in TF/SF formulation, for example, we add or subtract incident magnetic field to the right hand side of the update equation. This is analogous to placing a magnetic field-generated electric surface current at the electric field location, i.e. shifting the location of electric surface current from the location of its associated magnetic field. Similarly, the location of magnetic surface current is changed from the location of its associated electric field. This mixing of field and current locations, when applied to near-to-farfield transformation, is referred the Mixed-Surface approach [6].

The implementations of the mixed-surface approach is shown in equations (4) and Fig. 4:

$$
\begin{aligned}
\mathbf{N} &= \oiint_{S_h} \hat{\mathbf{n}} \times \mathbf{H}|_{S_h} e^{\jmath k\hat{\mathbf{r}}\cdot\mathbf{r}'_e} dS' = \oiint_{S_h} \mathbf{J}_s|_{S_e} e^{\jmath k\hat{\mathbf{r}}\cdot\mathbf{r}'_e} dS', \\
\mathbf{L} &= -\oiint_{S_e} \hat{\mathbf{n}} \times \mathbf{E}|_{S_e} e^{\jmath k\hat{\mathbf{r}}\cdot\mathbf{r}'_h} dS' = \oiint_{S_e} \mathbf{M}_s|_{S_h} e^{\jmath k\hat{\mathbf{r}}\cdot\mathbf{r}'_h} dS',
\end{aligned}
\tag{4}
$$

where S_e and S_h represent two surfaces on which the tangential electric and magnetic fields are present, respectively, in FDTD grid. When evaluating the surface integral for $\mathbf{N}$ using the magnetic fields on S_h, the surface electric currents caused by the magnetic fields ($\mathbf{J}_s = \hat{\mathbf{n}} \times \mathbf{H}$) are assumed to be placed on S_e. Therefore, the distance (between the reference point, i.e. the center of the volume enclosed by equivalent surface, and the current location on S_e) r'_e is used in the exponential inside integral.

Similarly, when evaluating the surface integral for $\mathbf{L}$ using the electric fields on S_e, the surface magnetic currents caused by the electric fields ($\mathbf{M}_s = -\hat{\mathbf{n}} \times \mathbf{E}$) are assumed to be placed on S_h. Thus, the distance r'_h is used in the exponential term inside integral. Finally, a separate-surface approach, that does not involve any mixing of field and current location and similar to mixed-surface approach in all other aspects, is implemented.

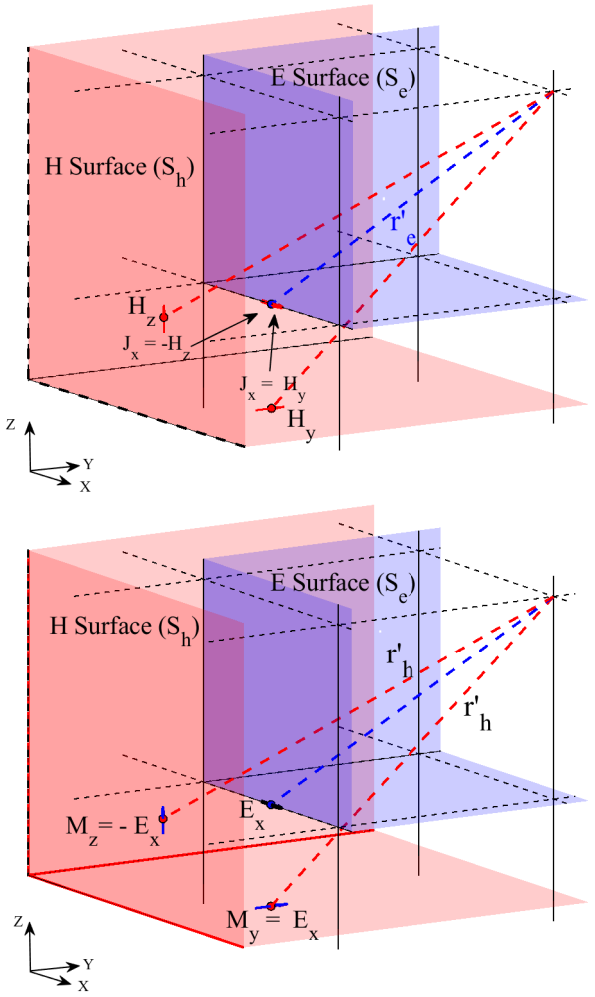

Fig. 4. Top: Magnetic field-produced electric currents are placed on S_e. Bottom: Electric field-produced magnetic currents are placed on S_h.

IV. FREQUENCY DOMAIN NEAR-TO-FARFIELD TRANSFORMATION IN FDTD

The frequency domain near-to-farfield projection is defined in terms of vector potential functions **A** and **F** in equations (5):

$$\mathbf{A}(\hat{\mathbf{r}},\omega) = \frac{\mu_0 e^{-jkR}}{4\pi R}\oiint_S \mathbf{J}_s(\mathbf{r}',\omega)e^{jk\hat{\mathbf{r}}\cdot\mathbf{r}'}dS' = \frac{\mu_0 e^{-jkR}}{4\pi R}\mathbf{N},$$
$$\mathbf{F}(\hat{\mathbf{r}},\omega) = \frac{\epsilon_0 e^{-jkR}}{4\pi R}\oiint_S \mathbf{M}_s(\mathbf{r}',\omega)e^{jk\hat{\mathbf{r}}\cdot\mathbf{r}'}dS' = \frac{\epsilon_0 e^{-jkR}}{4\pi R}\mathbf{L}. \tag{5}$$

The above equations are functions of frequency and farfield position unit vector $\hat{\mathbf{r}}$ along **r** shown in Fig. 1. The unit vector also represents farfield angles θ and ϕ. The closed surface integral is over the equivalent surface, and the frequency domain currents $\mathbf{J}_s$ and $\mathbf{M}_s$ (complex-valued) are functions of position on the equivalent surface (represented by primed position vector $\mathbf{r}'$ shown in Fig. 1) and the frequency. R is the magnitude of the vector $\mathbf{R} = \mathbf{r} - \mathbf{r}'$, also shown in Fig. 1.

The auxiliary vectors **N** and **L** in equations (5), that represent only the surface integrals, are then used to calculate the θ and ϕ components of electric field, given by equations (6):

$$E_\theta(\theta,\phi,\omega) = -\frac{je^{-jkR}}{4\pi R}\Big(L_\phi + \eta_0 N_\theta\Big),$$
$$E_\phi(\theta,\phi,\omega) = \frac{je^{-jkR}}{4\pi R}\Big(L_\theta - \eta_0 N_\phi\Big). \tag{6}$$

Similarly, the θ and ϕ components of RCS are given by equations (7):

$$RCS_\theta(\theta,\phi,\omega) = \frac{k^2}{8\pi\eta_0 P_{inc}}\Big|L_\phi + \eta_0 N_\theta\Big|^2,$$
$$RCS_\phi(\theta,\phi,\omega) = \frac{k^2}{8\pi\eta_0 P_{inc}}\Big|L_\theta - \eta_0 N_\phi\Big|^2, \tag{7}$$

where k and η_0 are the free-space wave-number and the intrinsic impedance, respectively. The surface integration in equations (5) are carried as discrete summations (Riemann sum). And, P_{inc} is the power density of the incident planewave, given by $P_{inc} = \frac{1}{2\eta}\left(E_\theta^2 + E_\phi^2\right)\cdot|F(\omega)|^2$. Here $F(\omega)$ is the Fourier transform of time-series $f(t)$, defined in equations (2), sampled at the desired frequency ω. The θ and ϕ components of the auxiliary vectors **N** and **L** are defined by equations (8) [4]:

$$N_\theta = \oiint_S \Big(J_x\cos(\theta)\sin(\phi) + J_y\cos(\theta)\sin(\phi) - J_z\sin(\theta)\Big)e^{jkr'\cos(\psi)}dS',$$
$$N_\phi = \oiint_S \Big(-J_x\sin(\phi) + J_y\cos(\phi)\Big)e^{jkr'\cos(\psi)}dS',$$
$$L_\theta = \oiint_S \Big(M_x\cos(\theta)\sin(\phi) + M_y\cos(\theta)\sin(\phi) - M_z\sin(\theta)\Big)e^{jkr'\cos(\psi)}dS',$$
$$L_\phi = \oiint_S \Big(-M_x\sin(\phi) + M_y\cos(\phi)\Big)e^{jkr'\cos(\psi)}dS'. \tag{8}$$

V. ERROR COMPARISON WITHOUT A SCATTERER

As a way to benchmark the accuracy of the above interpolation schemes, an empty region (no-scatterer) is illuminated by a planewave using discrete planewave technique with TF/SF formulation described earlier. Then, the farfields are obtained from the nearfields which are

interpolated using different schemes dealt with in the previous section, and compared. Since the fields in the scattered-field region for this case are down to the machine precision, the equivalent surface to perform NTFF transformation is placed inside the total-field region. As one might expect, the no-scatterer case should ideally result in zero farfield. Any electric farfield based on equation (6) observed is an error (the noise floor). Errors can be because of: numerical dispersion inherent in FDTD, approximations in calculation of J_s and M_s, discrete surface integration, discretization in space and time, and truncation of fields (finite word length).

Although this work does not attempt to separate the above mentioned error types, the farfield error caused by the error in approximating (interpolating) the nearfield surface currents J_s and M_s is the main differentiator. This is because, all the other error contributors mentioned above are identical for all the interpolation techniques. Therefore, it is expected that the interpolation scheme that gives minimum farfield performs better than the rest in terms of accuracy. The above interpolation schemes are compared for three different simulation parameters: resolution of the FDTD grid, incident angle of the planewave, and size of the equivalent surface.

A. Resolution sweep

Figure 5 shows how different interpolation schemes compare for different resolution of the grid. The vertical axis is the maximum of $\sqrt{|E_\theta|^2+|E_\phi|^2} \cdot \Delta t$ in dB observed across angles in the farfield principal planes (XY, XZ, and YZ planes). Here Δt is the FDTD discretization time step. The horizontal axis is the grid resolution in terms of cells per wavelength. The frequency at which the farfields are calculated is 2 GHz.

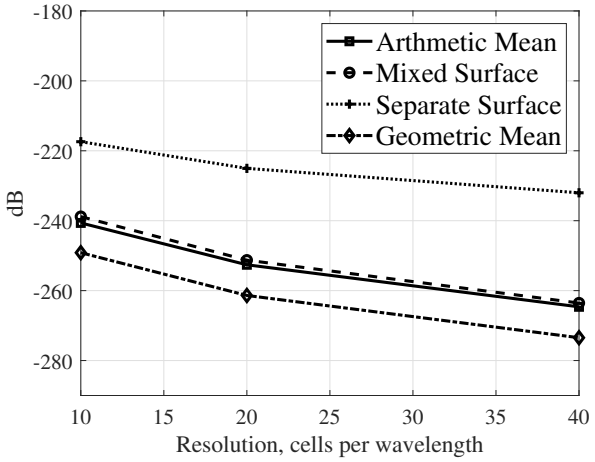

Fig. 5. Maximum farfield error in dB for different grid resolutions.

On the other hand, Fig. 6 shows average of $\sqrt{|E_\theta|^2+|E_\phi|^2} \cdot \Delta t$ observed across angles in the farfield principal planes.

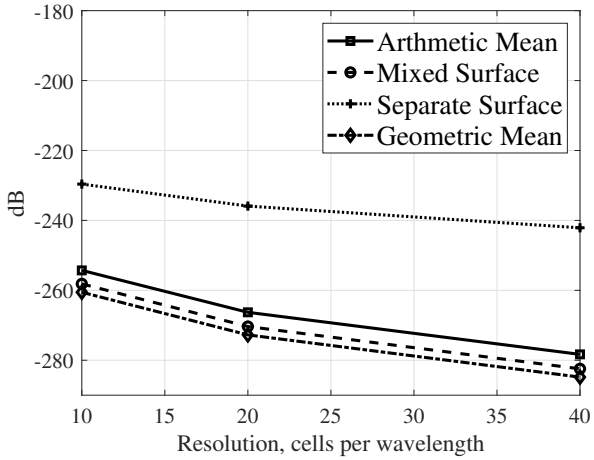

Fig. 6. Average farfield error in dB for different grid resolutions.

The incident angle for the planewave is $\phi_{inc} = 35.5^0, \theta_{inc} = 38^0$ and the size of equivalent surface is $(1\lambda)^3$. As expected, the farfield error decreases with increase in resolution as the dicretization errors in FDTD get minimized when the grid gets finer. The geometric mean approach produces the lowest farfield as one might expect because it interpolates the nearfields exactly as shown in section III, closely followed by arithmetic and mixed-surface approaches, followed by distant separate surface approach.

B. Incident angle sweep

Figures 7 and 8 show how maximum and average errors compare for different interpolation schemes at different incident angles of the planewave. The vertical axis is the same as described before and the horizontal axis specifies the θ_{inc} direction of the planewave while the $\phi_{inc} = 23.2^0$. The size of the equivalent surface is $(5\lambda)^3$ and the grid resolution is 10 cells per wavelength. The frequency at which the farfields are calculated is 2 GHz. The trend suggests that as incident planewave direction gets close to the axes directions ($\theta_{inc} = 0, 90^0$), the farfield errors increase. This could be because of FDTD numerical dispersion errors becoming worse for waves propagating along the axes directions as demonstrated in [11].

C. Equivalent surface size sweep

Figures 9 and 10 show how maximum and average errors compare for different interpolation schemes for different equivalent surface sizes. The vertical axis is same as described before and the horizontal axis specifies the size of equivalent surface as multiple of λ in $6(n\lambda)^2$.

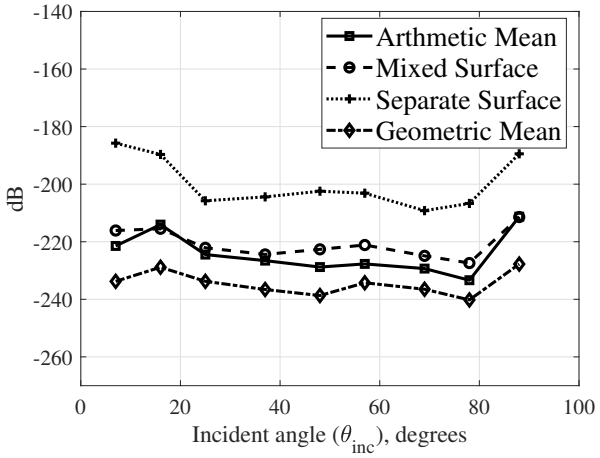

Fig. 7. Maximum farfield error in dB for different planewave incident angles.

The incident angle for the planewave is $\phi_{inc} = 35.5^0$, $\theta_{inc} = 38^0$, and the grid resolution is 10 cells per wavelength. The frequency at which the farfields are calculated is 2 GHz. Again, the geometric mean performs best, while arithmetic and mixed-surface approaches perform better than separate surface approach.

As expected, the farfield errors increase as size of equivalent surface increases. This is because, the phase errors in FDTD accumulate more as the wave travels in the grid longer and longer. All the above comparisons show that the geometric mean, mixed surface and arithmetic mean interpolation schemes perform consistently and considerably better when compared to the separate surface approach. Importantly, the geometric mean approach produces minimum farfield error, and the arithmetic & mixed surface approach produce similar errors.

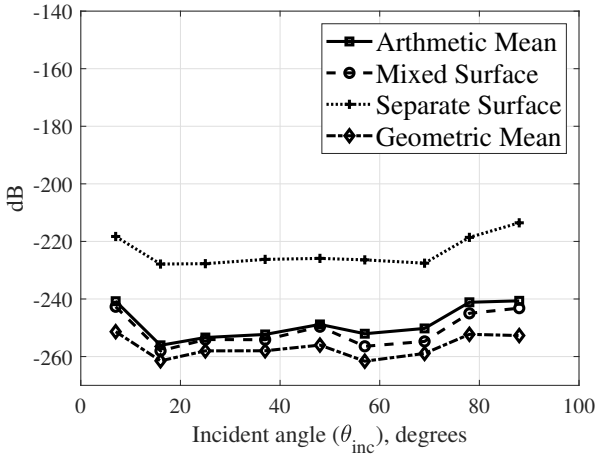

Fig. 8. Average farfield error in dB for different planewave incident angles.

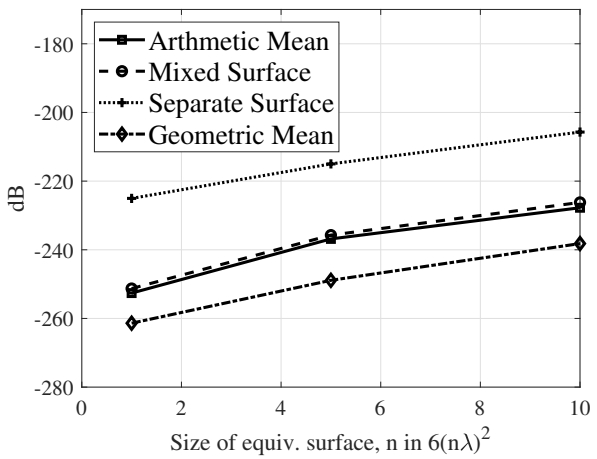

Fig. 9. Maximum farfield error in dB for various equivalent surface sizes.

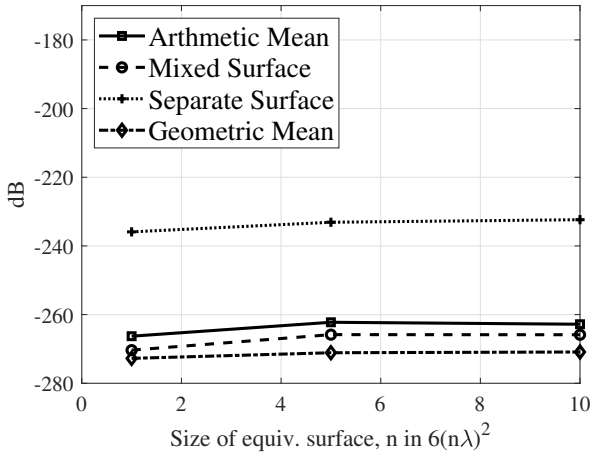

Fig. 10. Average farfield error in dB for various sizes of equivalent surface.

VI. BISTATIC RCS COMPARISON FOR A DIELECTRIC CUBE

To further validate the performance of different FDTD interpolation schemes, the bistatic RCS of a dielectric cube ($\epsilon_r = 5, \mu_r = 1$) is calculated at a single frequency of 1 GHz. This FDTD farfield scattering profile is compared with those obtained from integral equation solvers available in FEKO and HFSS.

The auxiliary vectors **N** and **L** in equations (5), that represent only the surface integrals, are used to calculate the θ and ϕ components of RCS, given by equations (7). The dielectric cube of size $\lambda/2$ on each side (at 1 GHz) is illuminated with a planewave incident at $\theta_{inc} = 38.0^0$ and $\phi_{inc} = 35.5^0$. This incident angle is rendered by the choice of integers (m_x,m_y,m_z) as (7,5,11) in the perfect TF/SF formulation described in the initial sections. These angles in FDTD indicate the direction of planewave propagation (direction of propagation

vector). Contrary to this, HFSS and FEKO would require the direction the planewave comes from (opposite to the direction of propagation vector). Consequently, the planewave arrival angles, $\theta_{arrival} = 180 - \theta_{inc}$ and $\phi_{arrival} = 180 + \phi_{inc}$, are used in these solvers. The time-profile of the theta-polarized planewave is a modulated Gaussian pulse, with frequency spectrum centered around 1 GHz.

The RCS results from the four interpolation schemes of interest –arithmetic averaging, geometric mean, mixed-surface, separate-surface approach– are compared with RCS profiles obtained from FEKO-MoM and HFSS-IE in Fig. 11.

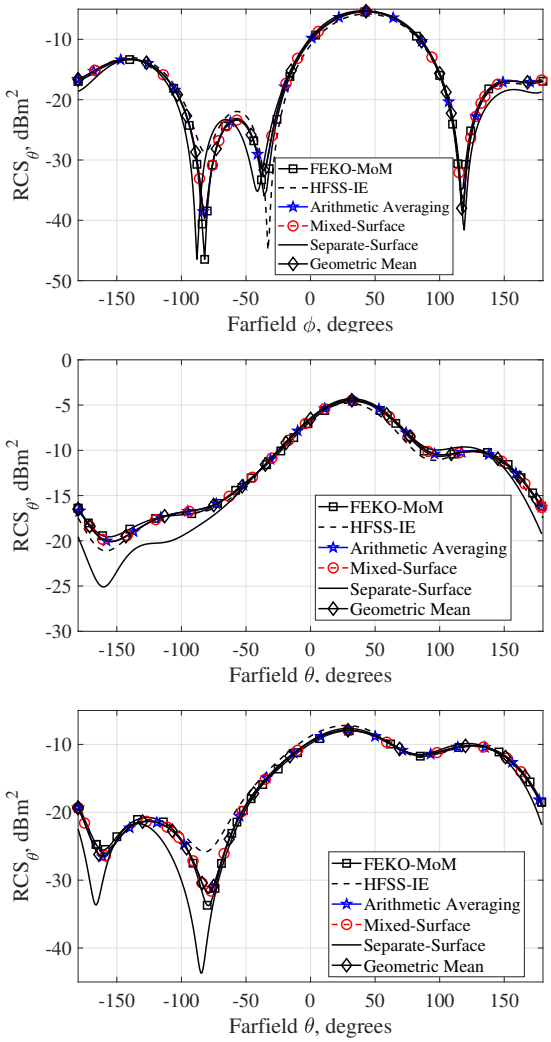

Fig. 11. The θ component of bistatic RCS in different farfield planes (XY, XZ and YZ respectively).

These figures show that the geometric mean, mixed surface and arithmetic averaging schemes match very close to each other and to at least one integral equation solution (FEKO in this case) confirming the clear advantage they have over the separate surface approach. Here, the FDTD grid resolution used is 40 cells/wavelength at 1 GHz. Also, only RCS_θ is shown on the three farfield principal planes as the RCS_ϕ results do not deviate from each other to a perceivable degree. The absorbing boundary condition used is Convolutional Perfectly Matched Layer (CPML) for the simulations involving dielectric cube. The CPML depth is 10 cells and there is a 10-cell gap between NTFF equivalent surface and CPML. The dielectric cube case is presented as a practical case to show how the errors in the FDTD NTFF formulation manifest themselves in RCS for different interpolation schemes, while keeping all other conditions (including type of ABC and distance to ABC) exactly same. No significant difference is observed between FDTD results (obtained using geometric mean, arithmetic averaging, mixed-surface approaches) and MoM-based FEKO results as shown in this section.

VII. SUMMARY AND CONCLUSION

Four interpolation approaches (arithmetic averaging, mixed-surface, geometric mean and separate surface scheme) for performing the frequency-domain near-to-farfield transformation in 3D FDTD are compared in terms of their baseline farfield errors and bistatic RCS for a dielectric cube. The planewave is excited in the FDTD grid using the error-free total-field/scatterd-field technique. To establish the baseline for farfield error comparison, nearfields without any scatterer in the total-field region are transformed to farfields. In this comparison, the geometric mean interpolation produces minimum farfield error as expected, followed by competing arithmetic averaging and mixed surface approaches, while the separate surface approach produces maximum error. Also, the FDTD RCS profiles calculated using geometric mean, arithmetic averaging and mixed-surface approaches for a dielectric cube match very close with that calculated using integral equation technique.

REFERENCES

[1] C. A. Balanis, *Advanced Engineering Electromagnetics*. New York: John Wiley, 1989.

[2] R. J. Luebbers, K. S. Kunz, M. Schneider, and F. Hunsberger, "A Finite-Difference Time-Domain Near Zone to Far Zone Transformation," *IEEE Trans. Antennas Propag.*, vol. 39, no. 4, pp. 429–433, Apr. 1991.

[3] M. J. Barth, R. R. McLeod, and R. W. Ziolkowski, "A Near and Far-Field Projection Algorithm for Finite-Difference Time-Domain Codes," *J. Electromagn. Waves Appl.*, vol. 6, no. 1, pp. 5–18, 1992.

[4] A. Z. Elsherbeni and V. Demir, *The Finite Difference Time Domain Method for Electromagnetics*

with MATLAB Simulations, 2nd ed., ACES Series on Computational Electromagnetics and Engineering, SciTech Publishing Inc. an Imprint of the IET. Edison, NJ, 2015.

[5] D. J. Robinson and J. B. Schneider, "On the use of the geometric mean in FDTD near-to-far-field transformations," *IEEE Trans. Antennas Propag.*, vol. 55, no. 11, pp. 3204–3211, Nov. 2007.

[6] T. Martin, "An improved near- to far-zone transformation for the finite-difference time-domain method," *IEEE Trans. Antennas Propag.*, vol. 46, no. 9, pp. 1263–1271, Sep. 1998.

[7] T. Tan and M. Potter, "1-D multipoint auxiliary source propagator for the total-field/scattered- field FDTD formulation," *IEEE Antennas Wirel. Propag. Lett.*, vol. 6, pp. 144–148, 2007.

[8] M. F. Hadi, "A Versatile Split-Field 1-D Propagator for Perfect FDTD Plane Wave Injection," *IEEE Trans. Antennas Propag.*, vol. 57, no. 9, pp. 2691–2697, Sep. 2009.

[9] T. Tan and M. Potter, "FDTD Discrete Planewave (FDTD-DPW) Formulation for a Perfectly Matched Source in TFSF Simulations," *IEEE Trans. Antennas Propag.*, vol. 58, no. 8, pp. 2641–2648, Aug. 2010.

[10] R. C. Bollimuntha, M. F. Hadi, M. J. Piket-May, and A. Z. Elsherbeni, "Dispersion optimised plane wave sources for scattering analysis with integral based high order finite difference time domain methods," *IET Microwaves, Antennas Propag.*, vol. 10, no. 9, pp. 976–982, 2016.

[11] A. Taflove and S. Hagness, *Computational Electrodynamics: The Finite-Difference Time-Domain Method, 3 ed.* Boston, MA: Artech House, 2005.

A Physics-based Transient Simulation and Modeling Method for Wide-frequency Electrical Overstress Including ESD

Ke Xu, Xing Chen, and Zhenzhen Chen

College of Electronics and Information Engineering
Sichuan University, Chengdu, Sichuan 610065, China
xingc@live.cn

Abstract ─ Circuits design that meets various IEC electrical overstress (EOS) standards is still a challenge, for that different kinds of EOS are at different frequency bands. In this paper, a physics-based transient simulation and modeling method is proposed, which can simulate wide-frequency EOS including electrostatic discharge (ESD) and AC characteristics. In this method, the physical model is used to characterize the nonlinear semiconductor devices in the finite-difference time-domain (FDTD)-SPICE co-simulation. Moreover, the modeling and physical parameters extraction method of the ESD protect devices, the transient voltage suppressor diode, is demonstrated. Taking an EOS protection circuit for example, it is modeled and simulated by the proposed method. Moreover, the circuit is also simulated by the widely-used System-Efficient ESD Design (SEED) method, in which the TVS diode is modeled based on 100 ns Transmission Line Pulse (TLP) measurements. The experiments show that both this method and SEED method can characterize the IEC system-level ESD behaviors well. However, the error of the SEED is about 219.2% at 10 MHz AC characteristics, but the maximum error of the proposed method is only 7.8%. Hence, compared with the widely-used SEED method, this method is more accurate when characterizing the EOS event during AC operation and switching.

Index Terms ─ Electric overstress, electrostatic discharge (ESD), transient simulation, wide-frequency.

I. INTRODUCTION

An electrical device suffers an EOS event when a maximum limit for either the voltage across, the current through, or power dissipated in the device is exceeded [1]. EOS causes immediate damage or malfunction, or latent damage resulting in an unpredictable reduction of its lifetime. The worldwide survey results show greater than 20% of total failures being EOS-related or 30% of total electrical failures being EOS-related [2]. The accurate simulation of EOS events enables the design of reliable protection on the first attempt and avoids the need for repeated design optimization tests [3]. The root causes leading to EOS include ESD [4], switching or alternating current (AC) applications [5, 6], and so on.

Among the simulation of EOS events, system-level ESD simulation is widely-concerned and well-studied. The SEED methodology is widely used for system-level ESD design. The SEED emphasizes the analysis of the interaction between the quasi-static I–V curve of a vulnerable protection element. Li *et al.* model and simulates transient response of a keypad backlight LED circuit in a smartphone under IEC 61000-4-2 excitation [7]. Scholz *et al.* present a TLP and HMM tests-based methodology which combines on-wafer characterization and transient simulation for the system-level ESD protection design [8, 9]. Wei *et al.* adopt SEED method to analyze interactions between external ESD protection device and the on-chip ESD protection circuit in a high-speed USB3.x IO circuit [10]. However, these studies only concern the ESD responses. That is to say, the accuracy for simulating other kinds of EOS root cause events is not validated, such as AC characteristics. Because a circuit or product must meet all kinds of EOS qualifications, and the accurate simulation of AC characteristics is essential for characterizing the EOS event during AC operation and switching.

Moreover, an accurate model of transient voltage suppressor (TVS) devices is critical to decide if the protection solutions are overdesigned or failed in the EOS tests. In the existing studies, the ESD protection components models are built by various methods. Zhang *et al.* use Hardware Description Language to describe the TLP-based behavioural model [11, 12]. Li *et al.* model the ESD protection devices by consisting of several compact model elements to accurately simulate the device behaviours under ESD stress conditions [13]. Pan *et al.* develop a physics-based model to model the conductivity modulation under an ESD stress [14]. Meng *et al.* present a piecewise-linear model with transient relaxation to describe the nonlinear transient characteristics of ESD protection devices [15]. But the models in these existing studies have only been validated by simulating responses to system-level IEC 61000-4-2 pulses, and the responses during AC operation are not

Submitted On: February 12, 2021
Accepted On: April 17, 2021
https://doi.org/10.47037/2020.ACES.J.360503

simulated and validated.

In this paper, we adopt physics-based field-circuit co-simulation to realize the EOS simulation. In this method, the physical model is used to characterize the nonlinear semiconductor devices, because physical models show great advantages in analyzing the circuits over wide frequencies [16, 17] and wide power ranges [18, 19]. The physics-based circuit simulation solves the carrier transport equations to model the semiconductor devices, and then the semiconductor devices' numerical physical model is incorporated into an equivalent-model based circuit simulation to analyze the whole circuits. Then the lumped circuit simulation is hybridized with the FDTD simulation by interfacing EM (electromagnetic) field quantities with lumped-element quantities at each timestep. The main feature that distinguishes this method from the field-circuit coupling methods [20, 21] is the physical modeling method of semiconductor devices. The main feature that distinguishes this method from the physical model-based methods [22, 23] is that this method involves electromagnetic computation. Moreover, the modeling and physical parameters extraction method of the ESD protect devices, the transient voltage suppressor diode, is demonstrated. Finally, taking an ESD protection circuit for example, it is modeled and simulated by the proposed method and also the widely-used SEED method.

II. SYSTEM-LEVEL EOS SIMULATION METHOD

In the physics-based system-level EOS simulation method, the simulation model is divided into two parts, the full-wave part, and the nonlinear-circuit part. In each timestep, the EM simulation and circuit simulation are coupled by an FDTD-SPICE linking method.

In the linear full-wave part, such as distributed electromagnetic structure such as the PCB circuit and the air around the circuit, the FDTD method [24] is used to solve Maxwell's equations, as (1-2):

$$\nabla \times \mathbf{E} = -\mu \frac{\partial \mathbf{H}}{\partial \mathrm{t}}, \tag{1}$$

$$\nabla \times \mathbf{H} = \mathbf{J} + \varepsilon \frac{\partial \mathbf{E}}{\partial \mathrm{t}}. \tag{2}$$

In the nonlinear circuit solving part, the physical model-based lumped circuit simulation is used to solve the circuit responses. Specifically, the Newton-Raphson method is used to solve Kirchhoff's current equation, as in (3). According to Kirchhoff's current equation, the sum of all currents leaving a node is zero. Assume that a circuit element is located between *(k-1)*th and *k*th node, the relationship between its current I_j and node voltage U_k and U_{k-1} is described in (4):

$$\sum I_j = 0, \tag{3}$$

$$I_j = \psi(U_k, U_{k-1}). \tag{4}$$

Hence, each element in the nonlinear circuit is characterized by the voltage-current relationship. For a relatively simple circuit element, such as a resistor or a capacitance, the relationship in (4) can be obtained by the analytic equation. For a critical semiconductor device, to obtain its voltage-current relationship in (4), it is modeled by the drift-diffusion physical model, as the equation group (5-9) [25]. The semiconductor device physical model is adopted to characterize the nonlinear semiconductor devices, and used to characterize the behaviours of the electric field, electron concentration, and hole concentration inside the nonlinear semiconductor devices. The physical model is selected because it is more applicable for simulating devices in high voltage and large current operations [19]. The voltage-current relationship of the semiconductor device can be obtained by solving the discrete equations of (5-9) in time domain by the finite difference method:

$$\mathbf{J}_{\mathrm{n}} = qD_{\mathrm{n}}\nabla n - q\mu_{\mathrm{n}} n\nabla\varphi, \tag{5}$$

$$\mathbf{J}_{\mathrm{p}} = -qD_{\mathrm{p}}\nabla p - q\mu_{\mathrm{p}} p\nabla\varphi, \tag{6}$$

$$\partial n/\partial t = q^{-1}\nabla\cdot\mathbf{J}_{\mathrm{n}} + G - R, \tag{7}$$

$$\partial p/\partial t = -q^{-1}\nabla\cdot\mathbf{J}_{\mathrm{p}} + G - R, \tag{8}$$

$$\nabla\cdot(\varepsilon_s\nabla\varphi) = q(n - p + N_A - N_D). \tag{9}$$

Equation (5) and (6) are current equations for electrons and holes in a semiconductor, equation (7) and (8) are continuity equations for electron and hole, equation (9) is Poisson's equation. J_n and J_p are the electron and hole current densities, q is the electronic charge, D_n and D_p are the hole and electron diffusion coefficients, n and p are the electron and hole density respectively, μ_n and μ_p are the hole and electron mobility respectively, φ is the electric potential, t is time, ε_s is the permittivity of the semiconductor material, R is electron-hole recombination rate, G is electron-hole generation rate, N_A is acceptor impurity concentration, and N_D is donor impurity concentration.

For the simulation of the TVS diode in this work, the ohmic contacts are implemented as boundary conditions. Hence, the electron concentration, hole concentration, and potential on the surface can be expressed as equations (10-12),

$$n_{\mathrm{s}} = 0.5\cdot[N_D - N_A + \sqrt{(N_D - N_A)^2 + 4n_{ie}^2}, \tag{10}$$

$$p_{\mathrm{s}} = \frac{n_{ie}^2}{n_{\mathrm{s}}}, \tag{11}$$

$$\varphi_{\mathrm{s}} = V_{\mathrm{s}} - \ln p_{\mathrm{s}}, \tag{12}$$

where n_{s}, p_{s}, φ_{s}, n_{ie} are the electron concentration, hole concentration, potential, and Intrinsic carrier concentration on the surface, respectively.

The initial values of the electron concentration, hole concentration, and potential affect the solving time and whether convergence can be achieved. Here, the dc initial value at N type doping zone is as:

$$n = N(x), \tag{13}$$

$$p = \frac{1}{N(x)}, \tag{14}$$

$$\varphi = \ln N(x). \tag{15}$$

The initial value at P type doping zone is as:

$$n = -\frac{1}{N(x)}, \tag{16}$$

$$p = -N(x), \tag{17}$$

$$\varphi = -\ln[-N(x)]. \tag{18}$$

After calculating the dc solution, the dc solution is used in the AC analysis as initial values.

By using the boundary condition (10-12) and initial value (13-15), the equations (5-9) are solved, so that the voltage-current relationship of the semiconductor device can be obtained.

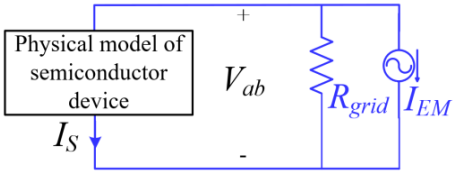

Fig. 1. The parallel circuit formed in FDTD-SPCIE linking procedure.

The FDTD-SPICE linking method [26] is used to couple the EM simulation and nonlinear circuit simulation. By discretization and transforming, equation (2) can be transformed into:

$$V_{ab}^{n+1} = [(I_x^{n+1})_{EM} - I_{sx}^{n+1}](R_x^{n+1})_{grid}, \tag{19}$$

where I_{EM}, R_{grid}, and I_S can equivalently form a parallel lumped circuit, as shown in Fig. 1. R_{grid} and I_{EM} are the equivalent circuit model of the distributed electromagnetic structure; I_S is the current through the semiconductor device. In the FDTD-SPICE linking procedure, I_{EM} and R_{grid} are calculated and used to characterize the effect of the "field" to "circuit" firstly. Then they are passed to the nonlinear circuit solving part, and the formed parallel circuit is calculated by the physical model-based lumped circuit simulation. Hence, the current through the semiconductor device I_S can be obtained. I_S characterizes the influence of the "circuit" to "field. Then the electric field is updated using I_S at the location where the semiconductor device is located. In this way, the physical-model circuit simulation and FDTD field simulation are integrated into a unified scheme. The specifics of this method can be found in previous work [27].

III. TVS DIODE PHYSICAL MODEL

The TVS diode is modeled by the diode chip's physical model and the package's equivalent circuit model, as shown in Fig. 2.

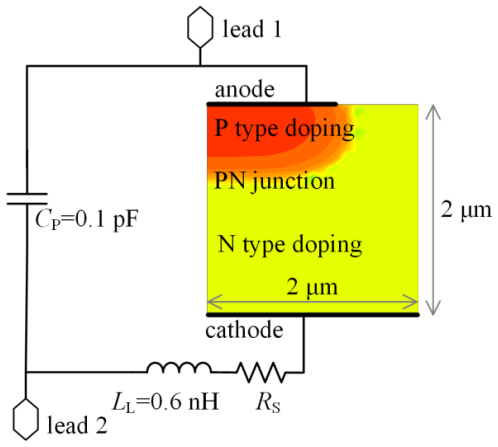

Fig. 2. TVS diode chip's physical model and package's equivalent circuit model.

In the package's equivalent circuit model, C_P represents the package capacitance, and L_L represents the lead inductance. To obtain the values of the two package circuit elements, the small-signal scattering parameters of two TVS diode circuits are measured. The TVS diode microstrip circuits are shown in Fig. 3. In the circuit of Fig. 3 (a), the TVS diode is connected between the centre of the microstrip line and a grounding via. In the circuit of Fig. 3 (b), the TVS diode is connected among the gap of the microstrip line. For the two circuits, the left and right end of the microstrip is port 1 and port 2, respectively. To measure the scattering parameters, the two ports are connected to vector network analyser Agilent N5230A through SMA connectors. Using the genetic algorithm, the value of C_P and L_L are adjusted, so that the simulated scattering parameters can fit the measured ones well.

To compute the scatting parameters of the limiter, a unit amplitude modulated Gaussian pulse is injected to the input port 1 as excitation, the reflection waveform at input port 1, and transmitter voltage waveform at output port 2 are calculated to obtain $|S_{11}|$ and $|S_{21}|$ respectively. The extracted value of C_P is 0.1 pF, and the extracted value of L_L is 0.6 nH. The measured and simulated $|S_{11}|$ and $|S_{21}|$ of the two circuits are shown in Fig. 4 (a) and 4 (b), respectively. The discrepancy at lower frequencies in $|S_{21}|$ of Fig. 4 (b) is due to the imperfect extracted component values.

(a) (b)

Fig. 3. Microstrip circuit: (a) with a series TVS diode, and (b) with a parallel TVS diode.

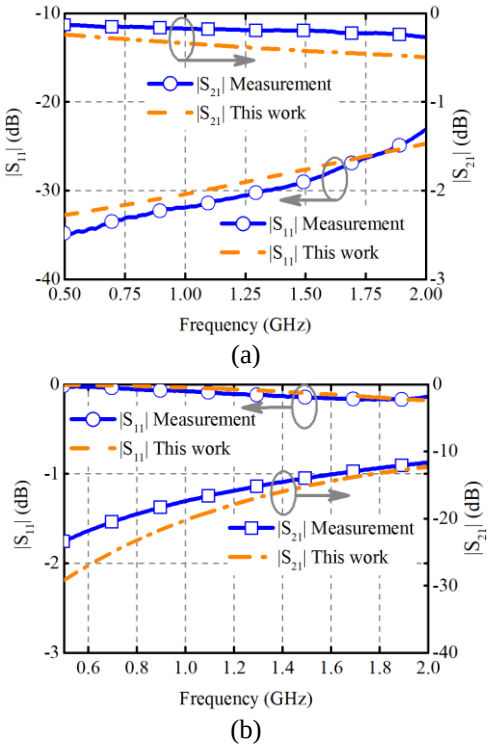

Fig. 4. Scattering parameters of TVS diode microstrip circuit: (a) series connection, and (b) parallel connection.

As shown in Fig. 2, the TVS diode chip is a P-N semiconductor junction, which is a linearly-graded junction. Hence, the unknown physical parameters that need to be extracted include P type doping concentration N_A, N type doping concentration N_D, P-N junction area A, and the substrate resistance R_S.

The physical parameters of the diode are extracted from the measurement results. The breakdown voltage of TVS diode V_{BR} is 6.8V, which is decided by the P type and N type doping concentration. Hence, the doping concentration is extracted from the value of V_{BR} based on the genetic algorithm. N_A is 8.0e15 /cm^3, and N_D is 1.2e18 /cm^3. Moreover, based on the measured DC I-V curve, the junction area A and the substrate resistance R_S are extracted, which are 0.3 mm^2 and 0.25 Ω, respectively. The simulation is based on a 2-D rectangle model, and its width is 2 μm. Hence, we need to multiply the calculated current value from the 2-D model by 1.5e5 times, so that the real diode current can be obtained.

By using the model and extracted physical parameters of the diode chip, the DC I-V curve is simulated, which agrees well with the measured curve, as shown in Fig. 5. The DC I-V curve is simulated by solving semiconductor equations (5-9).

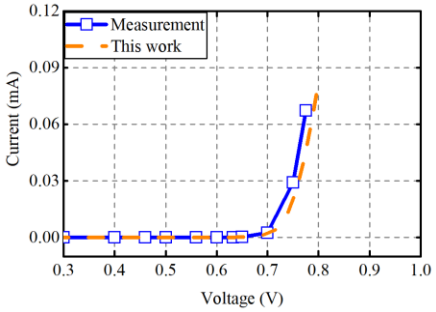

Fig. 5. Simulated and measured forward DC I-V curves.

IV. THE SEED SIMULATION METHOD

In white paper 3, the Industry Council on ESD target levels proposed the SEED methodology [2], which is used for the design of off-chip ESD protection solutions meeting system-level ESD specifications. When an IEC61000-4-2 discharge is applied to an external pin on the system board, the main ESD current flows directly to the ground through the on-board TVS, but some current will enter a connected IC. To prevent damage to the IC, it is important to assess the amount of current which may enter the IC and the associated voltage across the connected IC circuitry. Hence, it is clear that the design of on-chip ESD protection and on-board system level protection cannot be performed separately. By using the SEED method, the TLP curves of the on-chip and off-chip ESD protection devices are captured and compared. Then estimate the current and voltage operating point of the external pin for an ESD discharge event, and judge if it is outside the SOA. Hence, we can know if additional off-chip devices are required to obtain the desired system-level protection level.

To model and simulate the ESD protection circuit by SEED method, the TVS diode is modeled by both the TLP test results and the datasheet. Using the modeling method in [7], the model has two parts, as shown in Fig. 6. The factory-provided SPICE model is for nominal current conditions. The two voltage-controlled resistances are to mimic the high-current TLP I-V behaviour. Diode 2 was used as a unidirectional switch to separate the positive and negative pulse injections. Diode 1 defines the TLP I-V characteristics of the TVS diode under negative pulses applied to its cathode. Diode 3 and the switch determined the positive TLP I-V characteristics. The measured and simulated 100 ns TLP I-V curves by this model are shown in Fig. 7. The simulated curve agrees well with the measured TLP curve.

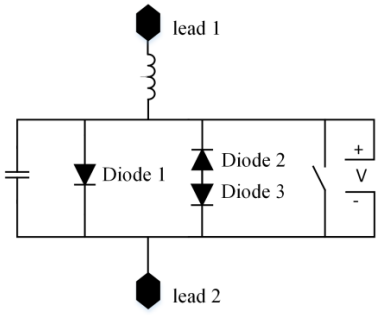

Fig. 6. TVS diode SPICE model.

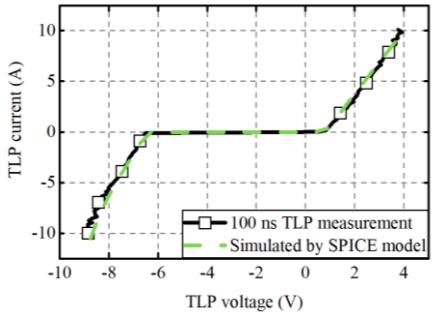

Fig. 7. TVS diode SPICE model simulation TLP results.

V. SIMULATION AND MEASUREMENT RESULTS

To validate the simulation method, a typical EOS protection circuit is simulated and measured, as shown in Fig. 8. In the circuit, a 50 Ω microstrip line is the EOS transmission path. The left end of the line is the EOS discharge point. The right end is connected to a load resistance and an SMA connector, which is connected to an oscilloscope to observe the voltage waveform. Moreover, a commercial TVS diode is a protection component and connected between the microstrip centre and a grounded via. The modeling method of each circuit element is as follows. Moreover, the ESD generator is modeled by its equivalent circuit model [7], as shown in Fig. 9. This model is selected because it can characterize the effect of load impedance and simulate efficiently.

Various responses of this circuit are simulated by the proposed method and the SEED method, including DC I-V curves, system-level ESD discharge responses, and AC characteristics. The simulated results are compared with the measured results.

The reverse DC I-V curves simulated by solving semiconductor equations (5-9) in this work, SEED method, and the measured ones are shown in Fig. 10. The simulated curve by this work shows that the breakdown voltage is 6.8V, which is consistent with the measured results. There is error between the simulated steepness of the I-V curve after the breakdown by this work and the measurement ones, because that the semiconductor equations (5-9) don't include the heat equation, so that the heat generation and its influence on the current have not been simulated. The breakdown voltage simulated by the SEED method is 6.5 V, which is slightly different with the measured results. The error from the SEED is due to the TLP measurement error.

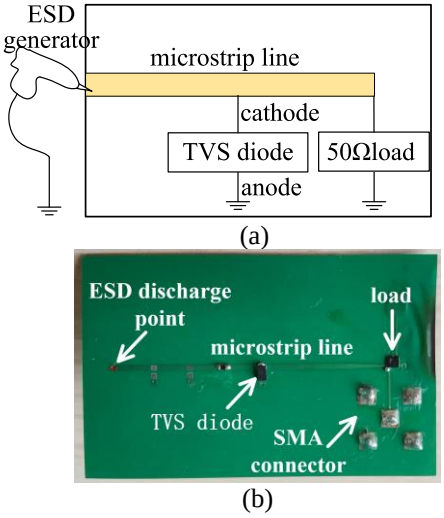

Fig. 8. EOS protection circuit: (a) circuit diagram and (b) circuit prototype.

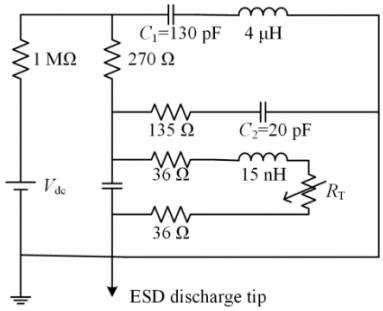

Fig. 9. ESD generator equivalent circuit.

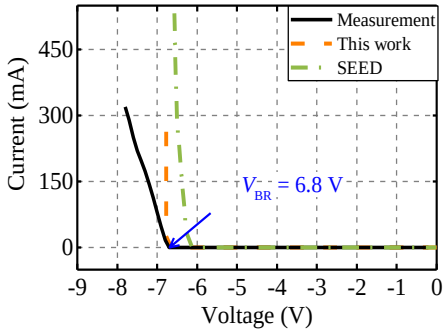

Fig. 10. Reverse DC I-V curves of the TVS diode.

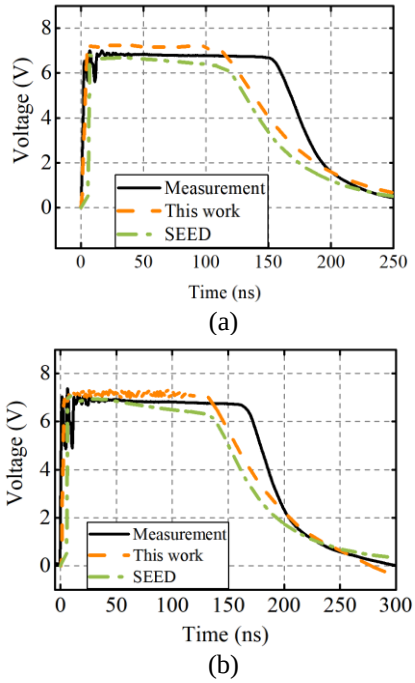

Fig. 11. Voltage waveforms of load when ESD pulse discharges. (a) 0.5 kV ESD pulse discharges. (b) 1 kV ESD pulse discharges.

As shown in Fig. 11, the system-level IEC61000-4-2 ESD discharge responses are also simulated and measured. In each simulation timestep, the voltage value is calculated by using the equivalent circuit in Fig. 9, and is applied to the discharge point in the EOS protection circuit. Then the voltage across the TVS diode at this timestep is obtained by the proposed method. The calculation process is repeated until the last timestep. The voltage waveforms across the TVS diode are also measured. In comparison with the measurement, the simulated voltage clamping time is a little shorter, which is caused by the imperfect generator model and measurement error. But the proposed method and the SEED method both can characterize the clamping behaviours of the TVS diode well. Specifically, when the pulse amplitude is 0.5 kV, the measured voltage is 6.82 V at 50 ns. The simulated voltage by this work is 7.17 V with error of 5.0%, as shown in Fig. 11 (a). When the pulse amplitude is 1 kV, the measured voltage is 6.91 V at 50 ns, and the simulated voltage by this work is 7.23 V with error of 4.6%, as shown in Fig. 11 (b).

Figure 12 shows the simulated and measured AC voltage waveforms across the load at different frequencies. When calculating the AC characteristics, the input signal is defined as a sine wave with amplitude of 1 V at different working frequencies. As shown in Fig. 12 (a) and 12 (b), the diode shows the characteristic of rectification at low frequencies. Namely, it has low resistance in one direction and has high resistance in the opposite direction. Both the proposed method and the SEED method can characterize the voltage waveforms at 1 kHz and 2 kHz. However, as the working frequency increases, the voltage waveforms across the diode don't show the "rectification" characteristics. As shown in Fig. 12 (c) and 12 (d), the voltage waveforms become nearly sinusoidal. Meanwhile, the maximize voltages are 0.56 V and 0.29 V at 5 MHz and 10 MHz, respectively. Namely, its amplitude decreases with the frequency increases. Compared with measured results, the proposed physics-based system-level EOS simulation method agrees well with the measurement results, and can characterize these AC nonlinear behaviours well. The maximum relative error values of the simulated curves by the proposed method in Fig. 12 (c) and 12 (d) are 0.34% and 7.8%, respectively. The proposed method can accurately characterize the TVS diode impedance characteristics at a wider frequency range, because the TVS diode is modeled by its physical model, which solves the semiconductor equations. However, the maximum relative error values of the simulated curves by the SEED method are 65.5% and 219.2%, respectively. The SEED method is inaccurate at 5 MHz and 10 MHz, because the TVS diode is modeled by its TLP tests, which is equivalent to a nonlinear resistance and cannot characterize the reactance characteristics of the TVS diode. It indicates that the SEED method cannot characterize nonlinear AC characteristics, which can lead to totally wrong voltage calculations when characterizing the EOS events during AC operation and switching.

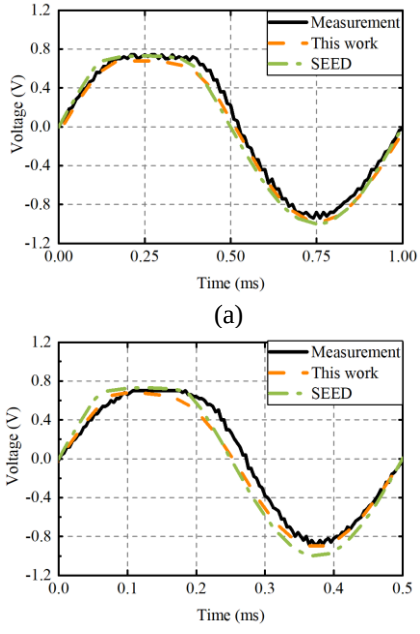

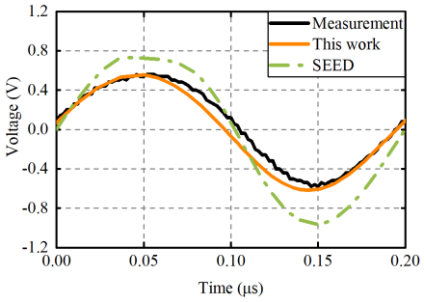

(c)

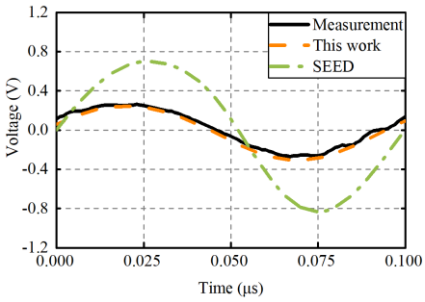

(d)

Fig. 12. AC voltage waveforms of the load at different frequencies: (a) 1 kHz, (b) 2 kHz, (c) 5 MHz, and (d) 10 MHz.

VI. CONCLUSION

This paper adopts a physics-based transient simulation and modeling method to simulate wide-frequency electric overstress. The method is the semiconductor device's physical model-based FDTD-SPICE co-simulation. Moreover, the modeling method of the TVS diodes is introduced. The experiments show that the proposed method can characterize the EOS protection circuit accurately, including DC, AC, and system-level ESD responses. Compared with the widely-used SEED method, this method can characterize nonlinear AC characteristics more accurately. This method shows advantages in designing a product that can immune from EOS.

ACKNOWLEDGMENT

This work was supported by Civil Aerospace Technology Research Project (D010201).

REFERENCES

[1] S. H. Voldman, *Electrical Overstress (EOS): Devices, Circuits and Systems*. John Wiley & Sons, pp. 1-29, Oct. 2013.

[2] R. Ashton, F. Bahrenberg, J. Dunnihoo, P. Design, and C. Duvvury, "White Paper 4 Understanding Electrical Overstress-EOS. Industry Council on ESD Target Levels," pp. 14-15, Sep. 2016.

[3] C.H. Diaz, S. Kang, and C. Duvvury, "Circuit-level electrothermal simulation of electrical overstress failures in advanced MOS I/O protection devices," *IEEE Trans. Comput.-Aided Des. of Integr. Circuits Syst.*, vol. 13, no. 4, pp. 482-493, Apr. 1994.

[4] J. E. Vinson, and J. J. Liou, "Electrostatic discharge in semiconductor devices: An overview," *Proc. IEEE*, vol. 86, no. 2, pp. 399-420, Feb. 1998.

[5] U. Choi, F. Blaabjerg, and K. Lee, "Study and handling methods of power IGBT module failures in power electronic converter systems," *IEEE Trans. Power Electron.*, vol. 30, no. 5, pp. 2517-2533, May 2015.

[6] R. Baburske, F. Niedernostheide, J. Lutz, H. Schulze, E. Falck, and J. G. Bauer, "Cathode-side current filaments in high-voltage power diodes beyond the SOA limit," *IEEE Trans. Electron. Devices*, vol. 60, no. 7, pp. 2308-2317, June 2013.

[7] T. Li, V. Pilla, Z. Li, J. Maeshima, H. Shumiya, K. Araki, and D. J. Pommerenke, "System-level modeling for transient electrostatic discharge simulation," *IEEE Trans. Electromagn. Compat.*, vol. 57, no. 6, pp. 1298-308, Aug. 2015.

[8] M. Scholz, S. H. Chen, G. Vandersteen, D. Linten, G. Hellings, M. Sawada, and G. Groeseneken, "Comparison of system-level ESD design methodologies—Towards the efficient and ESD robust design of systems," *IEEE Trans. Device Mater. Reliab.*, vol. 13, no. 1, pp. 213-222, Dec. 2012.

[9] M. Scholz, S. Thijs, S. H. Chen, A. Griffoni, D. Linten, M. Sawada, G. Vandersteen, and G. Groeseneken, "System-level ESD protection of high-voltage tolerant IC pins—A case study," *ESD-Forum*, Tagungsband, 12, pp. 87-94, Jan. 2011.

[10] P. Wei, G. Maghlakelidze, J. Zhou, H. Gossner, and D. Pommerenke, "An application of system level efficient ESD design for highspeed USB3.x interface," *Electr. Overstress/Electrost. Discharge Symp., Reno*, NV, pp. 1-10, Sep. 2018.

[11] F. Zhang, C. Wang, F. Lu, Q. Chen, C. Li, X. Wang, D. Li, and A. Wang, "A full-chip ESD protection circuit simulation and fast dynamic checking method using SPICE and ESD behavior models," *IEEE Trans. Comput.-Aided Des. Integr. Circuits Syst.*, vol. 38, no. 3, pp. 489-498, Mar. 2019.

[12] L. Wang, R. Ma, C. Zhang, Z. Dong, F. Lu, and A. Wang, "Behavior modeling for whole-chip HV ESD protection circuits," *IEEE Int. Symp. Power Semicond. Devices ICs*, pp. 182-184, June 2014.

[13] H. Li, M. Miao, Y. Zhou, J. A. Salcedo, J. Hajjar, and K. B. Sundaram, "Modeling and simulation of comprehensive diode behavior under electrostatic discharge stresses," *IEEE Trans. Device Mater. Reliab.*, vol. 19, no. 1, pp. 90-96, Mar. 2019.

[14] Z. Pan, D. Schroeder, S. Holland, and W. H. Krautschneider, "Understanding and modeling of diode voltage overshoots during fast transient ESD events," *IEEE Trans. Electron Devices*, vol. 61, no.

8, pp. 2682-2689, Aug. 2014.
[15] K. Meng, R. Mertens, and E. Rosenbaum, "Piecewise-linear model with transient relaxation for circuit-level ESD simulation," *IEEE Trans. Device Mater. Reliab.*, vol. 15, no. 3, pp. 464-466, Sep. 2015.
[16] J. Grajal, V. Krozer, E. Gonzalez, F. Maldonado, and J. Gismero, "Modeling and design aspects of millimeter-wave and submillimeter-wave Schottky diode varactor frequency multi-pliers," *IEEE Trans. Microwave Theory Tech.*, vol. 48, no. 4, pp. 700-711, Apr. 2000.
[17] J. V. Siles and J. Grajal, "Physics-based design and optimization of Schottky diode frequency multipliers for terahertz applications," *IEEE Trans. Microwave Theory Tech.*, vol. 58, no. 7, pp. 1933-1942, June 2010.
[18] Z. Pan, S. Holland, D. Schroeder, and W. H. Krautschneider, "Understanding the mechanisms of degradation and failure observed in ESD protection devices under system-level tests," *IEEE Trans. Device Mater. Reliab.*, vol. 10, no. 2, pp. 187-191, Dec. 2010.
[19] C. Mukherjee, B. Ardouin, J. Y. Dupuy, V. Nodjiadjim, M. Riet, T. Zimmer, F. Marc, and C. Maneux, "Reliability-aware circuit design methodology forbeyond-5G communication systems," *IEEE Trans. Device Mater. Reliab.*, vol. 17, no. 3, pp. 490-506, May 2017.
[20] A. Hosseinbeig, O. H. Izadi, S. Solanki, T. D. Lingayat, B. P. Subramanya, A. K. Vaidhyanathan, J. Zhou, and D. Pommerenke, "Methodology for analyzing ESD-induced soft failure using full-wave simulation and measurement," *IEEE Trans. Electromagn. Compat.*, vol. 61, no. 1, pp. 11-19, Feb. 2018.
[21] R. Myoung, B. S. Seol, and N. Chang, "System-level ESD failure diagnosis with chip-package-system dynamic ESD simulation," *Electr. Overstress/ Electrost. Discharge Symp.*, pp. 1-10, Sep. 2014.
[22] M. D. Ker and S. F. Hsu, "Physical mechanism and device simulation on transient-induced latch up in CMOS ICs under system-level ESD test," *IEEE Trans. Electron Devices*, vol. 52, no. 8, pp. 1821-1831, July 2005.
[23] M. Scholz, A. Shibkov, S. H. Chen, D. Linten, S. Thijs, M. Sawada, G. Vandersteen, and G. Groeseneken, "Mixed-mode simulations for power-on ESD analysis," *Electr. Overstress/Electrost. Discharge Symp. Proc.*, pp. 1-9, Sep. 2012.
[24] K. S. Yee, "Numerical solution of initial boundary value problems involving Maxwell's equations in isotropic media," *IEEE Trans. Antennas Propagat.*, vol. AP-14, pp. 302-307, May 1966.
[25] S. M. Sze and K. K. Ng, *Physics of Semiconductor Devices*. John Wiley & Sons, pp. 62-63, Mar. 2007.
[26] W. Sui, *Time-domain Computer Analysis of Non-linear Hybrid Systems*. CRC Press, Oct. 2018.
[27] K. Xu, X. Chen, and Q. Chen, "Non-quasi-static effects simulation of microwave circuits based on physical model of semiconductor devices," *Appl. Comput. Electromagn. Soc. J.*, vol. 35, no. 9, pp. 992-998, Sep. 2020.

Ke Xu received the B.S. degree in Electronics and Information Engineering from Sichuan University, Chengdu, China, in 2013. She is currently pursuing the Ph.D. degree in Radio Physics at the same university. Her research interests include computational electromagnetics and semiconductor device simulation.

Xing Chen received the Ph.D. degree in Biomedical Engineering from Sichuan University, Sichuan, China, in 2004, respectively. He is currently a Professor with the College of Electronics and Information Engineering, Sichuan University. His research interests include antenna, numerical methods applied in electromagnetics, and parallel computation.

Zhenzhen Chen was born on May 6, 1992 in Jiangxi, China. He is pursuing his Ph.D. degree in Radio Physics at Sichuan University. His research is mainly focused on computational electromagnetics and antenna design.

A Second-Order Stabilized Control Volume Finite Element Method for Self-Heating Effects Simulation of Semiconductor Devices based on Triangular Elements

Da-Miao Yu, Xiao-Min Pan*, and Xin-Qing Sheng

Center for Electromagnetic Simulation
Beijing Institute of Technology, Beijing, 100081, China
*xmpan@bit.edu.cn

Abstract ─ A second-order control volume finite element method combined with the multiscale flux approximation (CVFEM-MS) based on triangular elements is proposed to numerically investigate the self-heating effects of semiconductor devices. The multiscale fluxes are combined with a selected set of second-order vector basis functions to stabilize the discretization of carrier continuity equations with respect to triangular elements. Numerical results reveal that the proposed method is robust and accurate, even on the mesh of low-quality, where the detrimental impacts caused by the severe self-heating on the terminal currents can be obviously observed for a bipolar transistor model.

Index Terms ─ CVFEM-MS, self-heating effects, semiconductor devices, triangular element.

I. INTRODUCTION

Nowadays, self-heating effects simulation plays a vital role in the design of modern high-performance semiconductor devices, because of the miniaturization and integration of electron devices, as well as the newly developed device architectures such as silicon-on-insulator (SOI) transistors, FinFETs and resistive random access memory (RRAM) [1-3].

Physically, the carrier transport in semiconductor devices can be described by the drift-diffusion equation [1-6]. To deal with the strong advection effects, many discretization schemes based on Scharfetter-Gummel (S-G) upwinding were employed to enhance the stability and to ease the requirement of a mesh of high quality, such as the finite volume S-G (FVSG) method and the control volume finite element with S-G upwinding method (CVFEM-SG) [2-8]. In these methods, an analytically derived one-dimensional solution is utilized to generate an exponential type of upwinding. Nevertheless, due to the additional diffusion originating from the classical S-G upwinding, the above methods can only deliver first-order accuracy, which limits their ability to resolve the interior and boundary layers. To overcome this limitation, many schemes were proposed, such as the streamline-upwind Petrov-Galerkin method (SUPG), the spectral element time-domain (SETD) method, and the local discontinuous Galerkin (LDG) method [9-13]. But these methods have their own limitations. For example, the choice of stability parameters in the SUPG is problem dependent; the SETD is based on quadrilateral/hexahedron grids; and the auxiliary variables related to fluxes are introduced to generate a larger system in the LDG.

Recently, a parameter-free second-order control volume finite element method combined with multiscale flux approximation (CVFEM-MS) was proposed [14]. The quadrilateral elements were employed and the currents were interpolated by second-order quadrilateral edge elements with fluxes of second-order accuracy. It has been proved that the additional diffusion can be effectively suppressed. Generally, triangular elements are more versatile than quadrilateral ones in modeling complex structures. It is thus important to study CVFEM-MS on triangular meshing. Therefore, in this work, we implement the CVFEM-MS with respect to triangular elements to solve drift-diffusion equations. Different from the case of quadrilateral elements, the number of vector basis functions are more than what are required to expand the currents within an element. A special form of second-order curl-conforming vector basis functions is developed to remove the redundancy without affecting the stabilization.

The rest of the paper is organized as follows. The employed thermodynamic model is presented in Section II, and the discretization scheme is discussed in detail in Section III. The simulation results are presented and discussed in Section IV and the conclusions are finally drawn in Section V.

II. PHYSICAL MODEL

The thermodynamic drift-diffusion model is utilized in this paper to simulate the self-heating effects. The employed equations can be written as [5,6],

Submitted On: November 13, 2020
Accepted On: April 29, 2021

https://doi.org/10.47037/2020.ACES.J.360504

$$-\nabla\cdot\varepsilon\nabla\psi = q\left(p-n+N_d^+-N_a^-\right), \tag{1}$$

$$q\frac{\partial n}{\partial t}-\nabla\cdot\mathbf{J}_n = -q\left(U_n-G_n\right), \tag{2}$$

$$q\frac{\partial p}{\partial t}+\nabla\cdot\mathbf{J}_p = -q\left(U_p-G_p\right), \tag{3}$$

$$\rho C\frac{\partial T}{\partial t}-\nabla\cdot\kappa\nabla T = Q, \tag{4}$$

where q is the elementary charge, ε is permittivity, ψ, n, p and T are electric potential, electron densities, hole densities and lattice temperature respectively; N_d^+ and N_a^- are doping concentrations; $\mathbf{J}_{n/p}$ denote electron/hole current densities; $G_{n/p}$ and $U_{n/p}$ are generation and recombination rates corresponding to electrons/holes; ρ, $C$and κ are, respectively, mass density, specific heat capacity and thermal conductivity. Q is the generated heat power, which is defined as [5,12]:

$$Q = \left(\mathbf{J}_n+\mathbf{J}_p\right)\cdot\mathbf{E}+\left(U-G\right)\left(E_g+3k_BT\right), \tag{5}$$

where E_g is the energy gap, k_B is the Boltzmann constant, $U=(U_n+U_p)/2$ and $G=(G_n+G_p)/2$.

In the above model, the electric currents $\mathbf{J}_{n/p}$ are given as in [5],

$$\mathbf{J}_n = qn\mu_n\mathbf{E}+qD_n\nabla n+qnD_n^{\mathrm{T}}\nabla T, \tag{6}$$

$$\mathbf{J}_p = qp\mu_p\mathbf{E}-qD_p\nabla p-qpD_p^{\mathrm{T}}\nabla T, \tag{7}$$

where $\mu_{n/p}$, $D_{n/p}$ and $D_{n/p}^T$ are the mobilities, diffusion coefficients and thermal diffusion coefficients of electron/holes respectively, and $\mathbf{E}$ is the electric field. According to the Einstein relation, the diffusion coefficients are connected with the mobilities $D_{n/p}=k_BT\mu_{n/p}/q$ and the coefficients for thermal diffusion are given by $D_{n/p}^T=D_{n/p}/2T$.

III. OUR DISCRETIZATION SCHEME

The main difficulty in the numerical simulation of the above model is the accurate and stable discretization of equations (2) and (3). The performance of the widely used FVSG method depends on the mesh quality [3]. To ease the requirement on the mesh quality, CVFEM-SG was proposed [8], but it can only deliver first-order accuracy due to the additional artificial diffusion originating from the classical S-G upwinding. Recently, a second-order accurate scheme, denoted as CVFEM-MS, was developed on the quadrilateral meshing [14]. Considering that triangular elements are more suitable in modeling the complex structures, CVFEM-MS on the triangular meshing is developed to discretize equations (2) and (3) in this paper. Besides, the Galerkin finite element method based on second-order nodal basis functions is utilized to discretize equations (1) and (4), which has been detailed in many textbooks. Different from what was discussed in [14] for quadrilateral elements, this work defines the second-order accurate multiscale edge currents in terms of triangular elements to avoid unphysical oscillations in carrier continuity equations by the so-called multiscale flux approximation.

A. Second-order basis functions with respect to triangular elements

This subsection discusses the choice of the second-order basis functions with respect to triangular elements to construct the MS currents. To this end, a general drift-diffusion equation is considered, which can be written as:

$$\begin{aligned}\frac{\partial n}{\partial t}+\nabla\cdot\mathbf{J} &= -R,\\ \mathbf{J} &= D\nabla n-\mathbf{F}n,\end{aligned} \tag{8}$$

where n is carrier density, R is net recombination rate, D and $\mathbf{F}$ are diffusion coefficient and drift coefficient respectively, and $\mathbf{J}$ is the scaled current density which is scaled by the elementary charge q.

Based on the conformal triangular meshing, the configuration of a given interpolation point $\mathbf{x}_i$, its control volume C_i and the intersection points $\mathbf{m}_i$ on the control volume boundary edges can be defined, as sketched in Fig. 1 (a). The integration operation over (8) in terms of the control volume C_i for point $\mathbf{x}_i$ yield:

$$\frac{\partial}{\partial t}\int_{C_i} n d\Omega+\int_{\partial C_i}\hat{n}\cdot\mathbf{J}d\Gamma = -\int_{C_i} R d\Omega, \tag{9}$$

where ∂C_i and $\hat{n}$ are the boundary and the associated outward normal vector respectively.

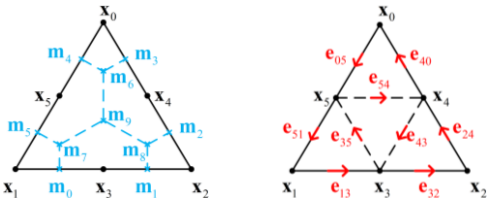

(a) Partition of control volumes (b) Subedges

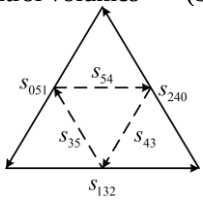

(c) Element segments

Fig. 1. Notations used in the discretization.

In the second-order CVFEM, the carrier densities n are interpolated by second-order Lagrangian nodal basis functions, while the current densities $\mathbf{J}$ are written as:

$$\mathbf{J} = \sum\nolimits_{e_{ij}}^{\text{subedges}}\mathbf{N}_{ij}J_{ij}, \tag{10}$$

where J_{ij} are the tangential current components on the subedge midpoints and $\mathbf{N}_{ij}$ are the second-order curl-conforming vector basis functions corresponding to the subedges $\mathbf{e}_{ij}$. As illustrated in Fig. 1 (b), the subedges $\mathbf{e}_{ij}$ with respect to triangular patches are defined by triangle vertices or midpoints of element segments. If the commonly used set of vector basis functions [15] are employed, it is not trivial to construct the suitably stabilized currents corresponding to the face basis functions because the face interpolation point is located at the barycenter of triangle. This is the reason why we give up the well-defined basis functions in [15]. Similar to what was done in [16], the midpoints of the subedges are chosen as the interpolation points, thus the basis functions have the form:

$$\begin{aligned}
&\mathbf{N}_{13}=\mathbf{W}_{12}\left(2L_1-0.5\right)l_{132},\ \mathbf{N}_{32}=\mathbf{W}_{12}\left(2L_2-0.5\right)l_{132},\\
&\mathbf{N}_{24}=\mathbf{W}_{20}\left(2L_2-0.5\right)l_{240},\ \mathbf{N}_{40}=\mathbf{W}_{20}\left(2L_0-0.5\right)l_{240},\\
&\mathbf{N}_{05}=\mathbf{W}_{01}\left(2L_0-0.5\right)l_{051},\ \mathbf{N}_{51}=\mathbf{W}_{01}\left(2L_1-0.5\right)l_{051},\\
&\mathbf{N}_{54}=4\mathbf{W}_{12}L_0l_{132},\mathbf{N}_{43}=4\mathbf{W}_{01}L_2l_{051},\mathbf{N}_{35}=4\mathbf{W}_{20}L_1l_{240},
\end{aligned} \tag{11}$$

where $\mathbf{W}_{ij}=L_i\nabla L_j-L_j\nabla L_i$ and tangential components of these functions at associated interpolation points are normalized by the lengths of segments s_{ijk}.

As revealed in [15], the number of curl-conforming vector basis functions to reach the second-order accuracy for a triangle element is 8. In contrast, (11) defines 9 basis functions. It is obvious that one of them is redundant. The reason lies in that the three basis functions corresponding to $\mathbf{e}_{54}$, $\mathbf{e}_{43}$ and $\mathbf{e}_{35}$ are not independent. A common way to remove the redundancy is to discard one of them, as in [15]. However, this method cannot offer accurate result for our applications according to our numerical experiments in Section IV. To solve the problem, we establish nine equations by integrating (10) over the subedges:

$$\sum_{e_{ij}} J_{ij}\int_{e_{ij}}\mathbf{N}_{ij}\cdot\hat{e}_{ij}\mathrm{d}s=\int_{e_{ij}}\mathbf{J}\cdot\hat{e}_{ij}\mathrm{d}s. \tag{12}$$

The right-hand side of (12) can be approximated analytically through the currents on the subedges, whose detailed discussion will be given in the next subsection. In short, the interpolation quantities J_{ij} can be obtained by solving (12). Since the matrix system of (12) is singular due to the redundancy of basis functions, we employ the Moore-Penrose pseudoinverse to solve it.

B. CVFEM-MS with respect to triangular elements

As shown in Fig. 1 (c), there are two types of segments in the triangle. Accordingly, two types of tangential current expressions should be defined. Similar to what was done in [14], for segments connecting three points s_{ijk}, the multiscale current can be written as:

$$\begin{aligned}
J_{ij}&=\frac{D_{ijk}}{l_{ijk}/2}\left(n_j-n_i\right)-F_{ijk}\frac{n_i+n_j}{2}+\frac{D_{ijk}}{l_{ijk}}q_{ijk}\Psi(-q_{ijk})\left(n_i-2n_j+n_k\right),\\
J_{jk}&=\frac{D_{ijk}}{l_{ijk}/2}\left(n_k-n_j\right)-F_{ijk}\frac{n_j+n_k}{2}+\frac{D_{ijk}}{l_{ijk}}q_{ijk}\Psi(q_{ijk})\left(n_i-2n_j+n_k\right),
\end{aligned} \tag{13}$$

where the indices $ijk\in\{132,240,051\}$, D_{ijk} and F_{ijk} are average diffusion coefficients and average drift coefficients over the segment s_{ijk}, l_{ijk} is the segment length, $\Psi(x)=\left(\coth x+1\right)\left(x\coth x-1\right)/x$, and $q_{ijk}=F_{ijk}l_{ijk}/4D_{ijk}$.

For the segments connecting only two points as shown in Fig. 1 (c), the tangential currents have no counterparts in [14] due to the employment of the triangle elements. Here, the classical S-G approximation is used:

$$\begin{aligned}
J_{ij}=&\frac{D_{ij}}{l_{ij}}\left(n_j-n_i\right)-F_{ij}\frac{n_i+n_j}{2}\\
&+\frac{D_{ij}}{l_{ij}}\left(p_{ij}\coth p_{ij}-1\right)\left(n_j-n_i\right),
\end{aligned} \tag{14}$$

where the indices $ij\in\{54,35,43\}$, D_{ij} and F_{ij} are average diffusion coefficients and average drift coefficients over the segment s_{ij}, and $p_{ij}=F_{ij}l_{ij}/2D_{ij}$.

Similar to that in [14], the third term in the right-hand side of (13) makes the numerical diffusion weaker compared with the case of the traditional first-order S-G current. Our proposed method is thus expected to resolve the interior and boundary layer better than the CVFEM-SG scheme for triangular elements, which will be illustrated later by numerical results in Fig. 3. However, the first-order S-G current (14) is used in (12), resulting in a relative larger numerical diffusion compared with the original CVFEM-MS for quadrilateral elements. Further study should be carried out to remedy it.

Finally, the matrix form of (9) can be written as:

$$\left[M\right]\{\dot{n}\}+\left[K\right]\{n\}=\{b\}, \tag{15}$$

where $\left[M\right]$ is the mass matrix, $\left[K\right]$ is the stiffness matrix, and the $\{b\}$ is the right-hand side vector. Employing the Backward Euler (BE) method, the time evolution equation is written as:

$$\left(\left[M\right]+\Delta t\left[K\right]\right)\{n\}_{t+\Delta t}=\left[M\right]\{n\}_t+\Delta t\{b\}_{t+\Delta t}, \tag{16}$$

where Δt is the time step.

In this work, Gummel iteration is employed to solve the coupled nonlinear equations. The equations for electrical properties are firstly solved self-consistently to calculate the carrier and current distributions. Subsequently, the heat generation rate is evaluated according to equation (5). The temperature-dependent parameters for electric potentials and carrier densities

are then updated through the obtained temperature distribution. In the above process, the proposed method is employed to handle the carrier continuity equations, while the Poisson equation for electric potentials and heat equation for temperatures are discretized by second-order classical nodal FEM.

IV. RESULTS AND DISCUSSIONS

The validity and the numerical stability of the developed algorithm are validated here. Numerical experiments on the electrothermal characteristics of the bipolar transistor are also presented to show the performance of the developed method on the low-quality mesh. In the computations, each single equation is solved by the multifrontal sparse direct solver MUMPS [17]. Since all computations can be finished in short time, we will not detail the CPU time in what follows.

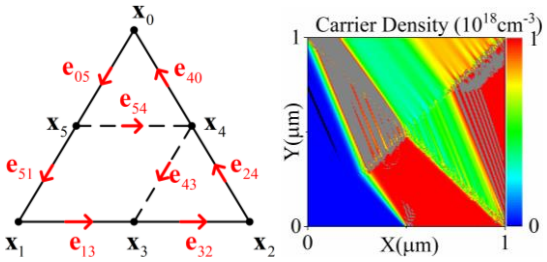

(a) $\mathbf{N}_{35}$ is removed (b) The numerical results

Fig. 2. The basis functions remained after removing one basis function, and the profile of n of equation (8) obtained by using these basis functions to expand the currents.

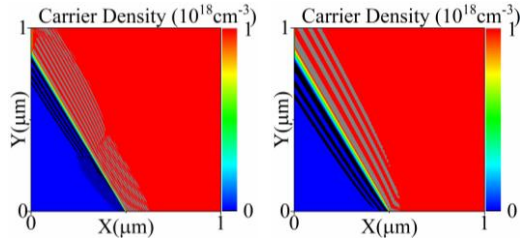

(a) 2nd-order SUPG-FEM (b) Quadrilateral CVFE-MS

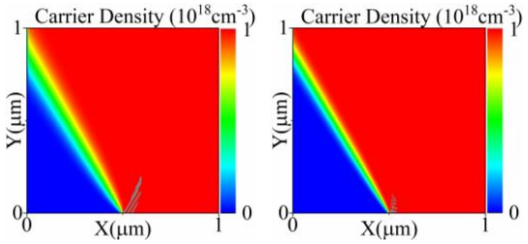

(c) Triangular CVFE-SG (d)The proposed method

Fig. 3. The n of equation (8) obtained from different schemes. In all the figures, the overshoots and undershoots are highlighted in gray and black respectively. Note that the SUPG-FEM results are obtained by COMSOL.

We begin with a homogeneous test problem to examine qualitatively the performance of the proposed method for the carrier continuity equations by setting $R = 0\ \mathrm{cm}^{-3}\cdot\mathrm{s}^{-1}$ where coefficients and boundary conditions of (8) are pre-specified. In particular, less-diffusive effect is considered by setting $D = 1\times10^{-5}\ \mathrm{cm}^{2}\cdot\mathrm{s}^{-1}$. The advective velocity and the boundary conditions are given by:

$$\mathbf{F} = \left(-\sin\pi/6, \cos\pi/6\right)\ \mathrm{cm}\cdot\mathrm{s}^{-1},$$

and

$$n = \begin{cases} 0, & \Gamma_L \cup \left(\Gamma_B \cap \{x \le 0.5\mu\mathrm{m}\}\right) \\ 1\times10^{18}\,\mathrm{cm}^{-3}, & \Gamma_T \cup \Gamma_R \cup \left(\Gamma_B \cap \{x \ge 0.5\mu\mathrm{m}\}\right) \end{cases},$$

where the problem domain $\Omega = [0,1\mu\mathrm{m}]\times[0,1\mu\mathrm{m}]$; Γ_T, Γ_B, Γ_L and Γ_R denote respectively the top, bottom, left and right boundary of Ω. As stated in [14], the exact solution of this problem is bounded between 0 and 1, and has an internal layer corresponding to the discontinuity at the boundary. The performance of our proposed method to deal with the singular matrix system of (12) is compared with the naive manner by removing one of the three interior basis functions.

In naive computation, $\mathbf{N}_{35}$, as depicted in Fig. 2 (a), is removed and the associated numerical result is given in Fig. 2 (b). Apparently, tremendous unphysical oscillations appear. The similar numerical instability can be also observed when other two interior basis functions are deleted respectively. Clearly, the singularity of the matrix system of (12) cannot be overcome through deleting the redundant basis functions directly.

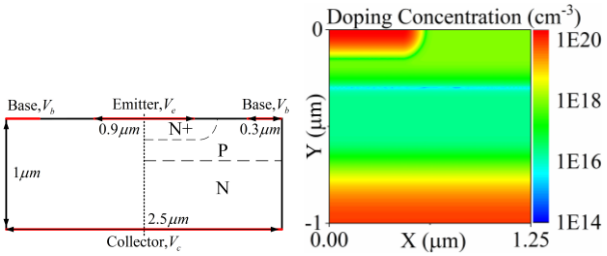

(a) Schematic of the device (b) Net doping profile

Fig. 4. The sketch of the bipolar transistor and the net doping profile in the right side of the device.

Figure 3 compare the results obtained from different schemes for the homogeneous test problem. The unstructured grid is generated by SUPG-FEM in COMSOL with the maximum edge length 0.01. The comparison indicates that the proposed method resolves the internal layer accurately. However, compared with the CVFEM-MS with quadrilateral elements, our scheme produces a wider internal layer due to the larger numerical diffusion. The reason for it has been discussed in Section III.B. One positive effect of the larger

diffusion is that the unphysical oscillations in our method are confined at the boundary discontinuity, as shown in Fig. 3. In contrast, such oscillations in SUPG-FEM and quadrilateral CVFEM-MS methods propagate along the crosswind direction.

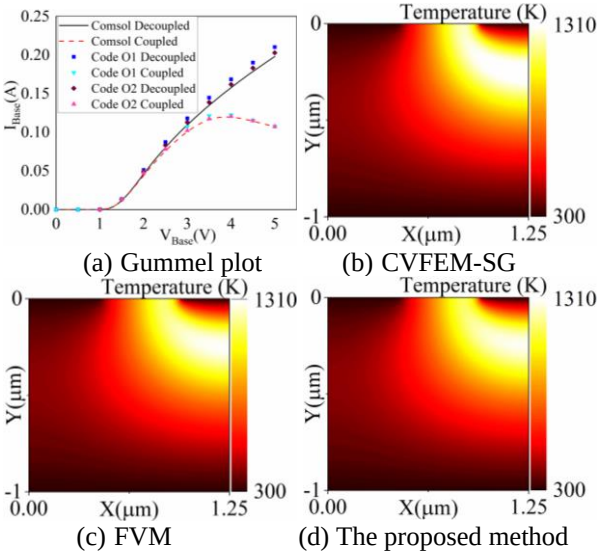

Fig. 5. The gummel plot for a base bias of $V_{\text{base}} \in [0, 5\text{V}]$, and the temperature distributions at $V_{\text{base}} = 5\text{V}$.

In the following, a more complicated model, e.g., a bipolar transistor is employed to demonstrate the performance of the proposed method where the self-heating effects play an important role. The sketch of the example is given in Fig. 4 (a) and the doping profile is shown in Fig. 4 (b). The doping-dependent and temperature-dependent carrier mobilities are taken from [18], which can be written as:

$$\mu_n(T) = 88T_n^{-0.57} + \frac{1252T_n^{-2.33}}{1+\left(C/1.26\times10^{17}T_n^{2.4}\right)^{0.88T_n^{-0.146}}},$$

$$\mu_p(T) = 54.3T_n^{-0.57} + \frac{407T_n^{-2.33}}{1+\left(C/2.35\times10^{17}T_n^{2.4}\right)^{0.88T_n^{-0.146}}},$$

where $T_n = T/300$, C is the doping concentration. The Auger process plays a vital role in this simulation,

$$R_{\text{Auger}} = U - G = c_n n\left(np - n_i^2\right) + c_p p\left(np - n_i^2\right),$$

where n_i is the intrinsic carrier concentration, $c_n = 2.8\times10^{-31}\text{cm}^6\cdot\text{s}^{-1}$ and $c_p = 9.9\times10^{-32}\text{cm}^6\cdot\text{s}^{-1}$ are the Auger recombination coefficients. The thermal conductivity is $\kappa(T) = 354/(T-68)\,\text{W/cm}\cdot\text{K}$. In the computations, the emitter is grounded and the collector voltage V_c is set to 0.5 V. All the terminals are treated as ideal heat sink and the environment temperature is fixed at 300 K throughout the simulations.

As shown in Fig. 5 (a), the obtained temperature distributions by the developed simulator agree well with that generated by the COMSOL. The results show that the base currents depend heavily on self-heating effects. More specifically, the inhomogeneous temperature distribution leads to lower terminal currents, especially when the base voltage increases. According to the temperature profiles at $V_{\text{base}} = 5\text{V}$, a hot spot with 1300 K appears in the area between the base and the collector.

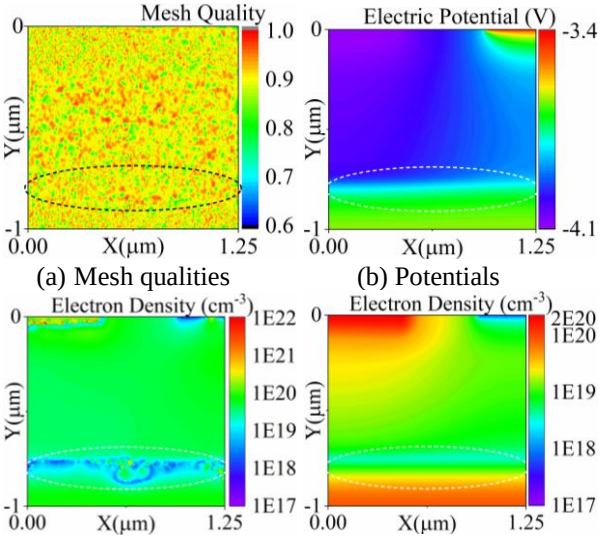

Fig. 6. Mesh qualities and the simulation results at $V_{\text{base}} = 1.8\text{V}$. An element is an obtuse triangle if its quality is less than 0.75, [19].

To study the performance of the proposed method with bad mesh quality, we generate a set of low-quality mesh with many randomly distributed obtuse triangles for the bipolar transistor example. The mesh, as shown in Fig. 6 (a), is generated by the Delaunay tessellation method provided in COMSOL. According to the maximum-angle-rule [19], an element is an obtuse triangle if its quality is less than 0.75. In the Newton solver of COMSOL, a sufficiently small step size $\Delta V_{\text{base}} = 0.1\text{V}$ is chosen and the solutions of previous steps are reused to improve its convergence. As highlighted in Fig. 6 (c), the Newton iteration failed to converge at $V_{\text{base}} = 1.8\text{V}$ due to the low quality of the mesh, whereas our method converges successfully. An abrupt variation of electron concentration caused by large electric potential gradients can be observed clearly from our results, as shown in Fig. 6 (d). In contrast, the obtuse triangles in the low-quality mesh makes the finite volume method employed in COMSOL solver fail in resolving such an internal layer, as depicted in Fig. 6 (c), and the resultant unphysical negative electron concentration densities lead to the divergence of Newton

iteration. In brief, our proposed method can resolve the internal layers successfully and deliver accurate results even when the mesh becomes low in quality.

V. CONCLUSION

A control volume finite element method equipped with the multiscale flux (CVFEM-MS) in terms of triangular elements is developed to simulate the self-heating effects on semiconductor devices by the thermodynamic drift-diffusion model. The qualitative numerical studies suggest that the proposed CVFEM-MS with respect to triangular elements is acceptably robust and accurate. The stability of our method is superior to the widely used finite volume method, especially on the low-quality mesh.

ACKNOWLEDGMENT

This work was supported in part by the NSFC under Grant 61771053, Grant U-1730102, and Grant 61421001.

REFERENCES

[1] M. Braccioli, G. Curatola, Y. Yang, E. Sangiorgi, and C. Fiegna, "Simulation of self-heating effects in different SOI MOS architectures," *Solid-State Electron.*, vol. 53, no. 4, pp. 445-451, Apr. 2009.

[2] F. Nasri, F. Echouchene, M. F. B. Aissa, I. Graur, and H. Belmabrouk, "Investigation of self-heating effects in a 10-nm SOI-MOSFET with an insulator region using electrothermal modeling," *IEEE Trans. on Electron Devices*, vol. 62, no. 8, pp. 2410-2415, Aug. 2015.

[3] G. Zhu, W. Chen, D. Wang, H. Xie, Z. Zhao, P. Gao, J. Schutt-Aine, and W. Yin, "Study on high-density integration resistive random access memory array from multiphysics perspective by parallel computing," *IEEE Trans. on Electron Devices*, vol. 66, no. 4, pp. 1747-1753, Apr. 2019.

[4] N. Bushyager, B. McGarvey, and E. M. Tentzeris, "Introduction of an adaptive modeling technique for the simulation of RF structures requiring the coupling of Maxwell's, mechanical, and solid-state equations," *Applied Computational Electromagn. Soc. J.*, vol. 17, no. 1, pp. 104-111, Mar. 2002.

[5] A. Amerasekera, M. Chang, J. A. Seitchik, A. Chatterjee, K. Mayaram, and J. Chern, "Self-heating effects in basic semiconductor structures," *IEEE Trans. on Electron Devices*, vol. 40, no. 10, pp. 1836-1844, Oct. 1993.

[6] R. E. Bank, D. J. Rose, and W. Fichtner, "Numerical methods for semi-conductor device simulation," *IEEE Trans. Electron Devices*, vol. 30, no. 9, pp. 1031-1041, Sept. 1983.

[7] P. Bochev and K. Peterson, "A parameter-free stabilized finite element method for scalar advection-diffusion problems," *Cent. Eur. J. Math.*, vol. 11, no. 8, pp. 1458-1477, May 2013.

[8] P. Bochev, K. Peterson, and X. Gao, "A new control volume finite element method for the stable and accurate solution of the drift-diffusion equations on general unstructured grids," *Comput. Methods Appl. Mech. Engrg.*, vol. 254, pp. 126-145, Feb. 2013.

[9] A. N. Brooks and T. J. R. Hughes, "Streamline upwind/Petrov-Galerkin formulations for convection dominated flows with particular emphasis on the incompressible Navier-Stokes equations," *Comput. Methods Appl. Mech. Engrg.*, vol. 32, no. 1, pp. 199-259, Sept. 1982.

[10] H. Bao, D. Ding, J. Bi, W. Gu, and R. Chen, "An efficient spectral element method for semiconductor transient simulation," *Applied Computational Electromagn. Soc. J.*, vol. 31, no. 11, pp. 1337-1342, Nov. 2016.

[11] F. Li, Q. H. Liu, and D. P. Klemer, "Numerical Simulation of high electron mobility transistors based on the spectral element Method," *Applied Computational Electromagn. Soc. J.*, vol. 31, no. 10, pp. 1144-1150, Oct. 2016.

[12] A. Cheng, S. Chen, H. Zeng, D. Ding, and R. Chen, "Transient analysis for electrothermal properties in nanoscale transistors," *IEEE Trans. Electron Devices*, vol. 65, no. 9, pp. 3930-3935, Sept. 2018.

[13] Y. Liu and C.-W. Shu, "Analysis of the local discontinuous Galerkin method for the drift-diffusion model of semiconductor devices," *Sci. China Math.*, vol. 59, no. 1, pp. 115-140, Jan. 2016.

[14] P. Bochev, K. Peterson, and M. Perego, "A multiscale control volume finite element method for advection-diffusion equations," *Int. J. Numer. Methods Fluids*, vol. 77, no. 11, pp. 641-667, Jan. 2015.

[15] R. D. Graglia, D. R. Wilton, and A. F. Peterson, "Higher order interpolatory vector bases for computational electromagnetics," *IEEE Trans. Antennas Propag.*, vol. 45, no. 3, pp. 329-342, Mar. 1997.

[16] A. Ahagon and T. Kashimoto, "Three-dimensional electromagnetic wave analysis using high order edge elements," *IEEE Trans. Magn.*, vol. 31, no. 3, pp. 1753-1756, May 1995.

[17] P. R. Amestoy, I. S. Duff, J. Koster, and J.-Y. L'Excellent, "A fully asynchronous multifrontal solver using distributed dynamic scheduling," *SIAM J. Matrix Anal. Appl.*, vol. 23, no. 1, pp. 15-41, April 2001.

[18] N. D. Arora, J. R. Hauser, and D. J. Roulston, "Electron and hole mobilities in silicon as a function of concentration and temperature," *IEEE Trans. Electron Devices*, vol. 29, no. 2, pp. 292-295, Feb. 1982.

[19] COMSOL Multiphysics Reference Manual, pp. 628-634, COMSOL Multiphysics® ver. 5.5. COMSOL AB, Stockholm, Sweden, 2019.

Orthogonally Integrated Hybrid Antenna for Intelligent Transportation Systems

Syedakbar Syedyusuff [1], Ramesh Subramaniam [2], and Ramya Vijay [3]

[1] Department of Electronics and Communication Engineering
K Ramakrishnan College of Technology, Trichy, Tamil Nadu 621 112, India
akbarkrct@gmail.com

[2] Department of Electronics and Communication Engineering
SRM Valliammai Engineering College, Kattankulathur, Chengalpattu, Tamil Nadu 603 203, India
rameshsvk@gmail.com

[3] RFCoE Lab, School of Electrical and Electronics Engineering
SASTRA Deemed University, Thanjavur, Tamil Nadu 613401, India
vijaramya@gmail.com

Abstract ─ The aim of this paper is to design an orthogonally integrated hybrid antenna to address 5G/Wi-Fi/C-V2X communication simultaneously in one device. The proposed antenna consists of three planar monopoles and a defected ground plane with a dimension of 55x30x1.2mm^3. High Frequency Structure Simulator (HFSS) is employed to design the proposed antenna, which resonates at three distinct frequencies 2.45 GHz (Wi-Fi), 3.5 GHz (5G), and 5.9 GHz. Further, the prototype antenna is fabricated and experimentally validated in comparing with simulation results. The excellent agreement among the simulation and measured results shows that the designed antenna operates simultaneously at 5G/Wi-Fi/C-V2X frequency bands and the isolation effects between the elements is less than 15dB.

Index Terms ─ C-V2X, defective ground, DGS, ECC, hybrid antenna, vehicular communication.

I. INTRODUCTION

Wireless communication is integral to life of common man that involves the necessity for public safety communication. Intelligent Transportation Systems (ITS) are a combination of cutting-edge information and communication technologies used in transportation and traffic management systems for safety improvement, efficiency, and sustainability of transportation networks; to minimize traffic congestion; and to enhance drivers' experiences. Intelligent Transport Systems (ITS) addresses these safety and environmental related issues by incorporating government bodies, universities, research organizations, and automotive industries [1]. Recent development in the vehicles are connected to each other through on-board-unit (OBU) and also with the road-side-unit (RSU) to communicate the information regarding the traffic for ITS. Cellular and transportation networks, in partnership, can deliver efficient smart transportation solutions through the way of providing safer pedestrians and bicycling conditions, reducing cut-through traffic, contribute to city-level traffic planning, pre-trip information and multi-modal choices Greening opportunities. Additionally, it ensures the safety during land travel. Figure 1 shows the different portfolios of communication in vehicular communication services.

Many researchers have addressed different types of antennas for vehicular communication which are surveyed and analyzed. Numerous solutions are proposed in the survey which addresses slot antennas, inverted F antennas, and printed monopole antennas with multiband operations for various vehicular applications. Stacked antennas are developed to operate in multiple frequencies and different structures of monopole were addressed [2-6]. Many multi-band frequency operating antennas and embedded antennas were evolved for mobile communication [7-12], it also impinges the challenges occur in the integrating multiband antennas in a smaller volume. In [13], planar inverted F antenna (PIFA) is integrated with "Y" shaped monopole antenna to obtain the multiband operation. In [14], author designed an antenna to address LTE and C-V2X. A three-dimensional antenna addressing GPS, LTE, WLAN, and DSRC is presented in [15-16]. In [17] integrated monopole antenna is proposed to operate at GPS and DSRC frequencies.

Submitted On: December 21, 2020
Accepted On: April 30, 2021

https://doi.org/10.47037/2020.ACES.J.360505

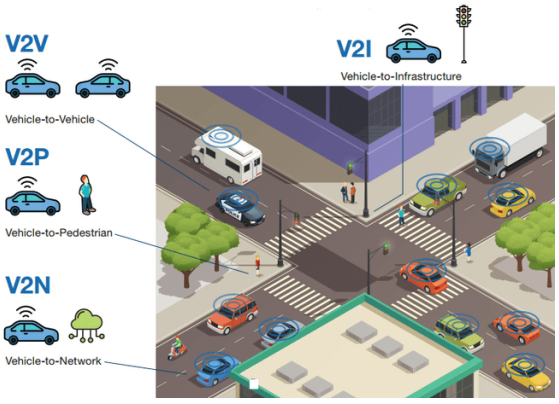

Fig. 1. Different types of V2X.

Many other multi-band antennas have been proposed for automotive applications including unmanned automotive vehicle [18-24] by that a good intelligent transportation system is evolved. Our innovative technology enables the connected transportation experience today. To be at the forefront of pioneering technologies from vehicle communications to precise positioning for the always connected.

For perfect intelligent transportation system, we have proposed an integrated planar monopole hybrid antenna which resonates at triple-bands addressing 5G/Wi-Fi/C-V2X communication simultaneously in a single device. Initially, the planar monopole antenna resonates at 2.4 GHz. Further, other antennas were integrated to operate on 5.9 GHz and 3.5 GHz. When each antenna element is placed closely located, another challenge nurtures the researcher is the isolation effect among elements. Various methods like defected ground structure (DGS), EBG structure, stubs, parasitic elements and novel 3D meta-material structures [12,25-28] to improve the isolation and capacity enhancement of vehicular antennas are found in the literature. In this proposed work, the monopole antennas are integrated orthogonally by that without incorporating any special methods to have better isolation among the antennas.

This research article is divided into multiple sections for clear explanation. Section I deals with a general introduction to this research work, Section II explains the design methodology, and Section III explains the result analysis of the proposed work followed by the conclusion.

II. DESIGN METHODLOGY

This work proposes a three port hybrid antenna with an overall dimensions of 30x55, which operates at three different frequencies to address 5G/Wi-Fi/C-V2X. The design of the antenna is evolved from a fundamental micro strip antenna substrate dimensions. A monopole antenna with λ/4 dimension inspired with meander line antenna is designed to operate at the lowest desired operating frequency. The single band (2.45 GHz) antenna is shown in Fig. 2.

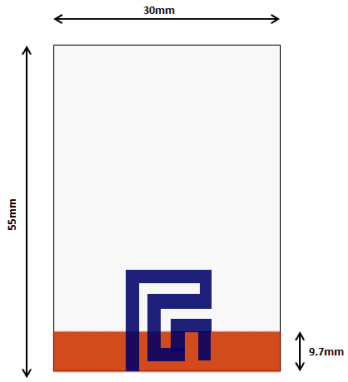

Fig. 2. Structure of single band antenna.

The ground plane length is chosen based on the parametric study and it is shown in Fig. 3. The designed antenna operates at 2.45 GHz. This band is aimed for Wi-Fi/V2I/Intra-vehicular applications. Another monopole antenna with λ/4 dimension is added to operate at the highest desired operating frequency. Figure 4 shows the structure of the antenna resonates at two bands simultaneously.

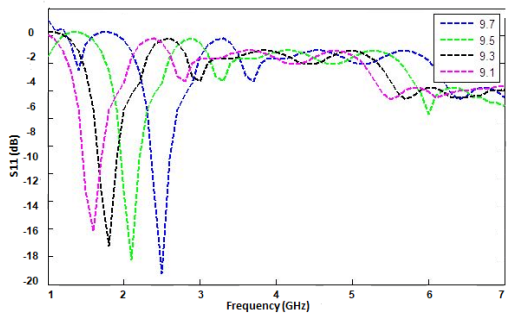

Fig. 3. Parametric analysis of single band antenna.

The antenna is placed orthogonal to the earlier one to achieve better isolation. This frequency is suitable for C-V2X applications. Figure 5 shows the performance of dual band antenna with the parametric analysis of second structure.

Furthermore, the monopole antenna with λ/4 dimension is added to operate at the 3.5 GHz operating frequency. This configuration provides tri-bands (2.45 GHz/3.5 GHZ/5.9 GHz) operation. The location of the three different monopole antenna in a same substrate, which comes under hybrid antennas. The antenna dimensions are optimized to provide a better impedance match at the desired tri-bands. Figure 6 shows the structure of the proposed hybrid antenna and Fig. 7 shows its return loss characteristics of hybrid antenna along with the parametric analysis of third antenna.

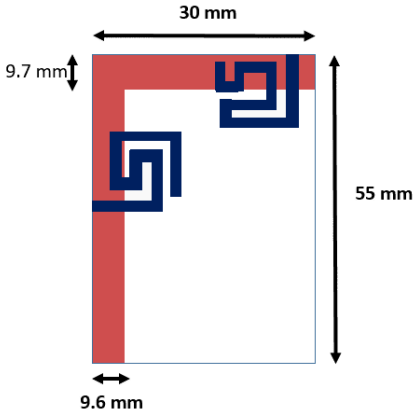

Fig. 4. Structure of dual band antenna.

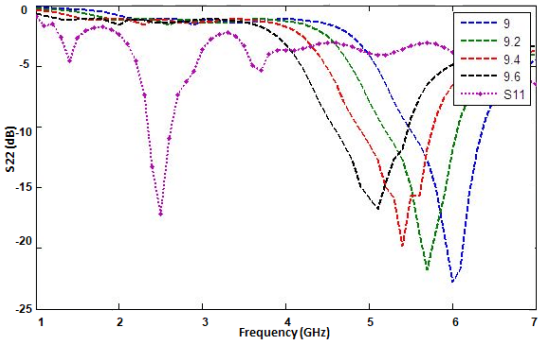

Fig. 5. S-Parameter of dual band antenna.

III. RESULTS AND DISCUSSION

The designed antenna is printed on 1.2 mm thickness FR4 substrate with the permittivity of 4.4, and loss tangent (d)=0.0009. Field Fox Vector Network Analyzer (N9952A) is been used to do near field measurements. Figure 8 and Fig. 9 shows the prototype of the designed antenna and measurement set-up.

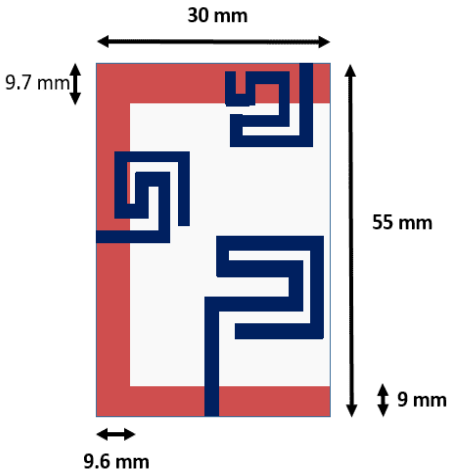

Fig. 6. Structure of Hybrid antenna.

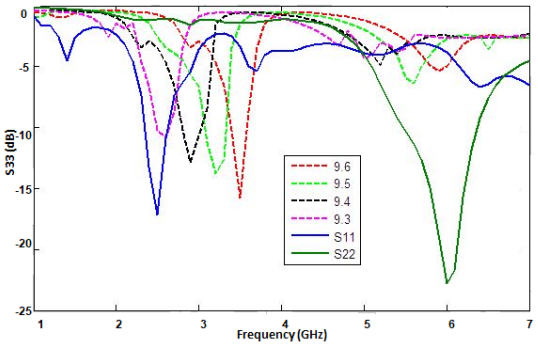

Fig. 7. Simulated and measured S-parameter of hybrid antenna.

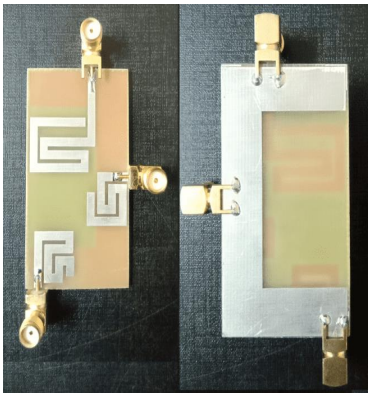

Fig. 8. Designed prototype.

A. S-parameters

Figure 9 shows the experimental setup of the measurement of S-parameter. Figure 10 shows the comparison of simulated and measured S-parameter characteristics of the proposed Tri-band integrated antenna. The graph reflects the excellent agreement between simulated and measured results.

Fig. 9. Measurement setup.

The Fig. 10 clearly specifies the inference that the proposed antenna has impedance bandwidth of 2.15 GHz to 3.05 GHz, 3.35 GHz to 3.75 GHz and 5.3 GHz

to 6.8 GHz. There is a variation between the simulated and measured impedance bandwidth. This may be due to prototyping error

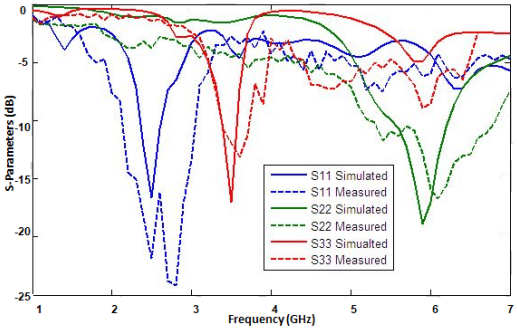

Fig. 10. Simulated and measured S-parameter results.

B. Isolation characteristics

Figure 11 shows the isolation characteristics comparison of the proposed antenna. The results show that isolation is greater than 15 dB at all desired bands. It conveys that there is a considerable amount of isolation among the ports, and the possibility of interference between the antennas are less.

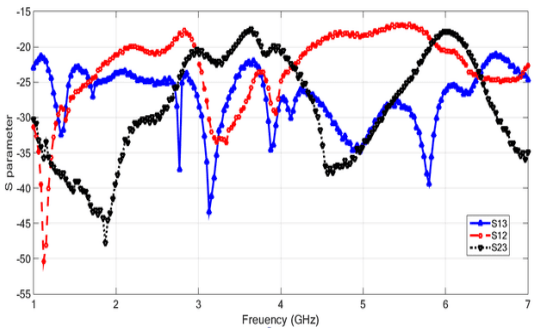

Fig. 11. Measured isolation effects of hybrid antenna.

C. Radiation pattern

Figure 12, shows the far field measurement setup of the tri-band antenna in the anechoic chamber. E field and H Field patterns of the proposed antenna are shown in the Fig. 13. It shows that the antenna has Omni-directional radiation pattern at the desired frequencies. It is observed that maximum of gain of 2.77 dB, 3.75 dB and 4.183 dB at 2.45 GHz, 3.5 GHz, and 5.9 GHz respectively.

The comparison between various antennas with proposed work is discussed in Table 1. It shows that the proposed work gives better gain with smaller dimension and proves the proposed work can be a better candidate as integrated antenna for vehicular communication.

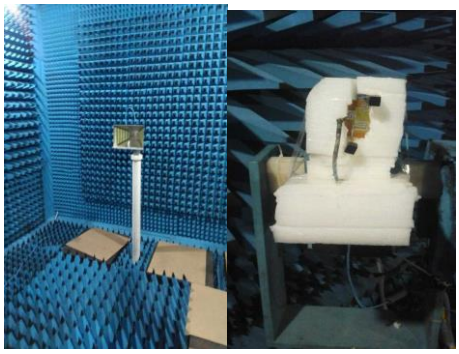

Fig. 12. Far field measurement setup.

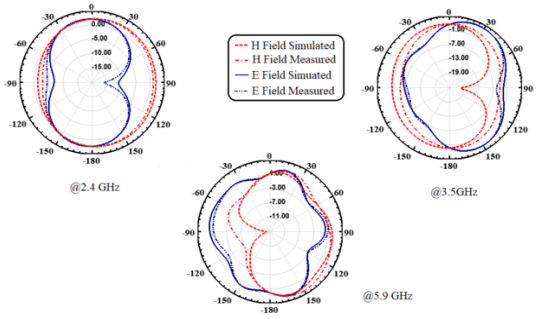

Fig. 13. Simulated and measured radiation pattern at tri-bands.

Table 1: Comparison among the different antennas and its performance

Reference Paper	Operating Frequency (GHz)	Dimensions (mm^2)	Gain (dB)
[5]	1.5, 2.4, 5.9	59.5x44.3	0.5 – 2.5
[6]	2.54, 3.5, 5.8	90 x 90	5
[7]	5.1 & 6.7	35 x 52.2	2.45
[15]	2.5, 3.5, 4.5, 5.5	50x50	0.75 – 4.15
Proposed work	2.45, 3.5, 5.9	55 x 30	2.77 3.75 4.18

D. Envelope correlation co-efficient

The envelope correlation co-efficient is essential parameter to analysis the different ports of the hybrid antenna. This parameter explains the correlation among the different antennas at various ports and lower the ECC means better performance of antenna. The value of ECC<0.5 is a desirable standard value for the hybrid system. The ECC is given by equation (1):

$$\rho_e = \frac{|S_{11}^{*}S_{12} + S_{21}^{*}S_{22}|^2}{\left(1-|S_{11}|^2-|S_{12}|^2\right)\left(1-|S_{22}|^2-|S_{12}|^2\right)}. \quad (1)$$

Table 2: ECC between different antennas

Freq (GHz)	Envelope Correlation Coefficient			
	Antenna 1,2	Antenna 2,3	Antenna 3,1	S_{11}
2.4	0.0374	0.00068	0.0319	-35dB
3.5	0.057	0.065	0.027	-18dB
5.9	0.0067	0.028	0.0026	-21dB

Table 2 explains the correlation between the various antennas. The ECC value is less than 0.1 over the different frequency ranges.

IV. CONCLUSION

The MIMO antenna is designed to address 5G/Wi-Fi/C-V2X for vehicular Communication is presented in this paper. The significant feature of the design approach is its compactness of total substrate dimension of 55 mm x 30 mm. There is good agreement between simulated and measured results on S-parameters, radiation patterns, gain and ECC Values. Further, it is observed that the inter port isolation is achieved below 15 dB among antenna elements in the hybrid structure. Thus, the proposed design is a suitable candidate for vehicular applications.

ACKNOWLEDGEMENT

The authors wish to acknowledge DST-FIST supporting facilities available in the department of Electronics & Communication Engineering, SRM Valliammai Engineering College and SASTRA-Keysight Centre for Excellence in RF System Engineering at SASTRA Deemed University for providing access and facilities to test and measure our Antenna module performance.

REFERENCES

[1] G. Dimitrakopoulos and P. Demestichas, "Intelligent transportation systems," *IEEE Vehicular Technology Magazine*, vol. 5, no. 1, pp. 77-84, 2010.

[2] T. Fujimoto and Tanaka, "An L-probe fed stacked rectangular micro-strip antenna combined with a ring antenna for triple band operation," *Progress in Electromagnetic Research,* vol. 37, pp. 1-13, 2013.

[3] T. Fujimoto and R. Nakanishi, "Stacked rectangular micro-strip antenna for triple band (GPS/VICS/ETC) operation," *Proceedings of IEEE International Symposium on Antennas and Propagation (AP-S URSI)*,Spokane, Washington, 2011.

[4] F. Ez-Zaki, H. Belahrach, and A. Ghammaz, "Broadband micro-strip antennas with cantor set fractal slots for vehicular communications," *International Journal of Microwave and Wireless Technologies*, vol. 13, no. 3, pp. 295-308, 2020.

[5] O.-Y. Kwon, R. Song, and B.-S. Kim, "A fully integrated shark-fin antenna for MIMO-LTE, GPS, WLAN and WAVE applications," *IEEE Transactions on Antenna and Wireless Propagation Letters*, vol. 17, no. 4, pp. 600-603, 2018.

[6] B. M. G. N. Alsath, H. Arun, Y. P. Selvam, M. Kanagasabai, S. Kingsly, S. Subbaraj, R. Sivasamy, S. K. Palaniswamy, and R. Natarajan, "An integrated tri-band/UWB polarization diversity antenna for vehicular networks," *IEEE Transactions on Vehicular Technology*, vol. 67, no. 7, pp. 5613-5620, 2018.

[7] S. Pahadsingh and S. Sahu, "Four port MIMO integrated antenna system with DRA for cognitive radio platforms," *AEU - International Journal of Electronics and Communications,* vol. 92, pp. 98-110, 2018.

[8] W. Lee, Y. K. Hong, J. J. Lee, J. Park, and W. M. Seong, "Omnidirectional low-profile multiband antenna for vehicular telecommunication," *Progress in Electromagnetic Research*, vol. 51, pp. 3-59, 2015.

[9] E. Irci, K. Sertel, and J. L.Volakis, "Miniature printed magnetic photonic crystal antennas embedded into vehicular platforms," *Applied Computational Electromagnetics Society Journal (ACES)*, vol. 26, pp. 109-115, 2011.

[10] S. Bandi, D. K. Nayak, B. T. P. Madhav, and A. Tirunagari, "Transparent circular monopole antenna for automotive communication," *Applied Computational Electromagnetics Society Journal (ACES)*, vol. 34, pp. 704-709, 2019.

[11] F. M. A. Haj-Ahmed and M. K. Abedel Azeez, "Design of a multi-band loop antenna for wireless communications: Simulation and analysis," *Journal of King Saud University - Engineering Sciences*, vol. 23, no. 1, pp. 67-73, 2011.

[12] K. Yu, Y. Li, and X. Liu, "Mutual coupling reduction of a MIMO antenna array using 3-D novel meta-material structures," *Applied Computational Electromagnetics Society Journal (ACES)*, vol. 33, pp. 758-763, 2018.

[13] M. Assa raj and S. Ramesh, "UWB MIMO antenna for interference reduction in wireless communications," *International Journal of Telecommunications and Radio Engineering*, vol. 76, pp. 107-122, 2017.

[14] H. Xu, H. Wang, S. Gao, H. Zhou, Q. Xu, and Y. Cheng, "A compact and low-profile loop antenna with six resonant modes for LTE smart phone,"

IEEE Transactions on Antennas Propagation, vol. 64, no. 9, pp. 3743-3751, 2016.

[15] W. Wang, Z. Zhao, Q. Sun, X. Liao, Z. Fang, K. Y. See, and Y. Zheng, "Compact quad element vertically-polarized high isolation wideband MIMO antenna for vehicular Base station," *IEEE Transactions on Vehicular Technology*, vol. 69, no. 9, pp. 10000-10008, 2020.

[16] M.-T. Wu and M.-L. Chuang, "Multi broadband slotted bow-tie monopole antenna," *IEEE Antennas Wireless Propagation Letter*, vol. 14, pp. 887-890, 2015.

[17] R. Vijay and T. R. Rao, "Penta-band linear tapered feed planar spiral antenna for vehicular communications," *International Journal of Microwave and Wireless Technologies*, vol. 9, pp. 1523-1532, 2017.

[18] M. G. N. Alsath and M. Kanagasabai, "A shared-aperture multiservice antenna for automotive communications," *IEEE Antennas Wireless Propagation Letter*, vol. 13, pp. 1417-1420, 2014.

[19] S. Singhal, "Feather-shaped super wideband MIMO antenna," *International Journal of Microwave and Wireless Technologies*, vol. 13, no. 1, pp. 94-102, 2020.

[20] H. Li, J. Xiong, and S. He, "A compact planar MIMO antenna system of four elements with similar radiation characteristics and isolation structure," *IEEE Antennas and Wireless Propagation Letters*, vol. 8, pp. 1107-1110, 2009.

[21] K. Wei, Z. Zhang, and Z. Feng, "Design of a coplanar integrated micro strip antenna for GPS/ITS applications," *IEEE Antennas and Wireless Propagation Letters*, vol. 10, pp. 458-461, 2011.

[22] Z. Ma, B. Ai, R. He, G. Wang, Y. Niu, M. Yang, J. Wang, Y. Li, and Z. Zhong, "Impact of UAV rotation on MIMO channel characterization for air-to-ground communication systems," *IEEE Transactions on Vehicular Technology*, vol. 69, no. 11, pp. 12418-12431, 2020.

[23] A. Kunwara, A. K. Gautamb and K. Rambabu, "Design of a compact U-shaped slot triple band antenna for WLAN/WiMAX applications," *International Journal of Electronics and Communications*, vol. 71, pp. 82-88, 2017.

[24] B. E. Abishek, A. Raaza, S. Ramesh, S. Jerritta, and V. Rajendran, "Circularly polarized circular slit planar antenna for vehicular satellite applications," *Applied Computational Electromagnetics Society Journal (ACES)*, vol. 34, pp. 1340-1345, 2019.

[25] J. Kowalewski, J. Eisenbeis, M. Tingulstad, Z. Kollar, and T. Zwick, "Design method for capacity enhancement of pattern-reconfigurable MIMO vehicular antennas," *IEEE Transaction on Antennas and Wireless Propagation Letters*, vol. 18, no. 12, pp. 2557-2561, 2019.

[26] J. Huang, C.-X. Wang, H. Chang, J. Sun, and X. Gao, "Multi-frequency multi-scenario millimeter wave MIMO channel measurements and modeling for B5G wireless communication systems," *IEEE Journal on Selected Areas in Communication*, vol. 38, no. 9, pp. 2010-2025, 2020.

[27] I. Gnanaharan and R. Anbazhagan, "Review on isolation techniques in MIMO antenna systems," *Advanced Electromagnetics*, vol. 7, no. 4, pp. 46-70, 2018.

[28] J. Xu, B. Lan, J. Zhang, C. Guo, and J. Ding, "A novel dual-band dual-polarized shared-aperture antenna with high isolation," *International Journal of Microwave and Wireless Technologies*, vol. 12, no. 7, pp. 652-659, 2020.

Syedakbar Syedyusuff received his bachelor degree in Electronics and Communication Engineering in the year 2009 at Mohamed Sathak Engineering College, Kilakarai, Master of Engineering in Optical Communication in the year 2011 at ACCET, Karaikudi. He is currently working as an Assistant Professor in the Department of Electronics & Communication Engineering, K. Ramakrishnan College of Technology, Tiruchirappalli since 2011. He is a member of ACES, IEEE APS, Life member in ISTE, SEMCE, BES. His research interest include Antenna, RF filters, Optical Communication.

Ramesh Subramanian received his B.E. in Electronics and Communication Engineering from University of Madras, M.Tech in Communication Engineering from VIT University, Vellore and received his Ph.D. degree on from SRM University, Chennai, in 2001, 2004 & 2015 respectively. He is currently, working as an Associate Professor in the Department of ECE, SRM Valliammai Engineering College, Chennai with experience of 16 years. He is a senior member of IEEE APS, Life member in IETE, ISTE, SEMCE, BES. He authored papers in reputed journals. His area of interest includes Antennas & Propagation and Wireless Communications. He is guiding research scholars in the field of antennas & RF Filter under Anna University, Chennai.

Ramya Vijay is an Assistant Professor of Electronics and Communication Engineering at SASTRA University, India, and has research passion on Radio Communications. She received her Ph.D. degree at SRM University, Chennai, Tamil Nadu, India. Her Ph.D. work is on design of Active Integrated Antennas for Vehicular Wireless Communications. She received best paper award in Antennas and RF Communications session of 30th GISFI Standardization Series Meeting and IEEE 5G meet. She is a member of IEEE, IET, BES, IETE and SDIWC. So far she has authored 7 papers in reputed SCI journals and 10 in various conferences. Her research interest include Antennas & its Applications, Broadband & Mobile Cellular Telecommunications.

Structural Optimization of an Optical 90 Degree Hybrid Based on a Weakly-guided 4×4 Multimode Interference Coupler Using a Parallelized Real-coded Micro-genetic Algorithm

Takashi Yasui, Jun-ichiro Sugisaka, and Koichi Hirayama

Faculty of Engineering
Kitami Institute of Technology, Kitami-shi, Hokkaido, 090-8507, Japan
yasui@mail.kitami-it.ac.jp, sugisaka@mail.kitami-it.ac.jp, hirakc@mail.kitami-it.ac.jp

Abstract ─ The optimal design of a 4×4 multimode interference (MMI) coupler as an optical 90° hybrid based on a weakly-guided optical waveguide was considered. Seven geometrical parameters of a 4×4 MMI coupler were optimized by a real-coded micro-genetic algorithm, and parallelized using a message-passing interface. The beam-propagation method was used to evaluate the fitness of the MMI coupler in the optimization process. The optimized 4×4 MMI coupler showed a common-mode rejection ratio greater than 28.9 dBe and a phase error less than 2.52° across a wavelength range of 1520 to 1580 nm, which satisfied typical system requirements. The optimization process was executed on a Beowulf-style cluster comprising five identical PCs, and its parallel efficiency was 0.78.

Index Terms ─ Beam-propagation method, finite element method, genetic algorithm, multimode interference coupler, optical waveguides, parallel computation.

I. INTRODUCTION

The optical 90° hybrid is a key component for demodulating optical signals in coherent transmission systems, and is considered to be a promising candidate for next-generation high-capacity optical transmission systems. Although some configurations for the waveguide-based 90° hybrids have been proposed [1,2] for photonic integrated circuits (PICs), those based on 4×4 multimode interference (MMI) couplers have attracted considerable attention because of their simple and compact structures [3,4,5]. These MMI-based 90º hybrids are based on high-index-contrast technologies such as silicon-on-insulator (SOI) [3,4] and InP [5] waveguides.

Silica is another attractive material for PICs because of its extremely low propagation loss, low coupling loss to single-mode fibers, and low polarization dependence, and is widely used in PICs. In general, the self-imaging theory [6], which relies on a parabolic distribution of effective indices of eigenmodes in the MMI section, is used to design MMI couplers. However, it is difficult to design accurate and high-performance MMI couplers based on weakly-guided waveguides, such as silica-based waveguides using the self-imaging theory is difficult. This is because that the parabolic distribution of the effective indices of eigenmodes in the MMI section cannot be assumed in weakly guided waveguides.

To realize high-performance MMI couplers based on weakly guided waveguides, structural optimization of MMI couplers using genetic algorithms (GAs) has been considered [7,8,9]. Wang et al. [7], and West and Honkanen [8] performed structural optimization of weakly-guided MMI couplers operating at a single wavelength. In their work, a simple GA and a mode propagation analysis were employed for the optimization and propagation analysis of optical waves, respectively. Yasui et al. [9] demonstrated the structural optimization of silica-based 2×2 MMI couplers operating at wavelengths ranging from 1520 to 1580 nm, which includes the C-band of optical transmission systems. A real-coded micro-GA, which is a combination of a real-coded GA and a micro-GA (μGA), was employed for the structural optimization, and the two-dimensional beam-propagation method (BPM) based on the finite element method (FE-BPM) [10,11] was used for the propagation analysis. The BPM analysis, which is a more accurate but time-consuming method, was executed 750 times for one optimization process.

In this study, we propose a parallelized optimization method based on a real-coded μGA. Two-dimensional FE-BPM was applied to the optimization of silica-based 4×4 MMI couplers as an optical 90º hybrid to satisfy typical system requirements [4,5]. A 4×4 MMI coupler optimized by the proposed method has a common-mode rejection ratio (CMRR) greater than 28.9 dBe and a phase error less than 2.52° across a wavelength range of 1520 to 1580 nm, which satisfies the system requirements. In addition, the excess loss remained less than 0.68 dB. The optimization process was executed on a Beowulf-style cluster [12], which comprised five identical PCs,

Submitted On: January 20, 2021
Accepted On: April 30, 2021
https://doi.org/10.47037/2020.ACES.J.360506

and its parallel efficiency was 0.78.

II. NUMERICAL METHODS

A. Parallelized μ GA

A μGA is a GA with a small population, (typically five), and reinitialization. It starts with a randomly generated population. The production of individuals in the next generation by a genetic operation is performed until nominal convergence is reached. Subsequently, a new population is generated by transferring the best individual in the converged population to the new one, followed by randomly generating the remaining individuals [9,13,14].

The flowchart of the proposed algorithm parallelized with the message passing interface (MPI) [15,16] is shown in Fig. 1. Let N_p be the population number, which is equal to the number of MPI processes. First, an initial random population is generated in process 0. The genes in the population are broadcast to all the processes. Second, in the *i*-th process, a BPM analysis is executed for a 4×4 MMI coupler represented by the *i*-th individual in the population, and its fitness is evaluated. Here, the two-dimensional FE-BPM [10,11] is utilized to an equivalent two-dimensional 4×4 MMI coupler obtained by the effective index method. After a barrier synchronization to ensure that all the processes have reached the same point in the code, all fitness values were gathered to process 0. Third, if a termination condition is satisfied then the optimization process is completed; otherwise, genes in the next generation are generated. Here, the individual with the largest fitness is carried to the next generation as the elite (elitist strategy). If nominal convergence is reached, the remaining $N_p - 1$ individuals in the next generation are randomly generated; otherwise, the remaining $N_p - 1$ individuals are produced by selection and crossover. The second and third procedures are repeated until the termination condition is satisfied.

B. Real-coded GA

In a real-coded GA, a chromosome is represented as a vector of floating-point numbers, in which the elements denote the values of the parameters to be optimized [17,18]. In this study, we denote the chromosome of the *i*th individual in the *g*th generation as:

$$x^{(g,i)} = (x_1^{(g,i)}, x_2^{(g,i)}, \ldots, x_N^{(g,i)}), \tag{1}$$

where *N* is the size of the chromosome.

For the selection and crossover, a binary tournament selection and the BLX-α strategy [9,17] were applied, respectively.

C. A brief review of FE-BPM

Herein, we briefly review the FE-BPM [10, 11]. We consider an optical wave propagating in the $+z$-direction in a two-dimensional planar optical waveguide uniform in the x-direction. From Maxwell's equations, we obtain the following wave equation:

$$\frac{\partial}{\partial y}\left(p\frac{\partial \Phi}{\partial y}\right) + \frac{\partial}{\partial z}\left(p\frac{\partial \Phi}{\partial z}\right) + k_0^2 q\Phi = 0, \tag{2}$$

where $\Phi = E_x$, $p = 1$, $q = n^2$ for the transverse electric (TE) modes, and $\Phi = H_x$, $p = 1/n^2$, $q = 1$ for the transverse magnetic (TM) modes, and n is the refractive index. Substituting the solution of the form:

$$\Phi(y,z) = \varphi(y,z)\exp(-jk_0 n_0 z), \tag{3}$$

into Eq. (2), we obtain the following equation for the slowly varying complex amplitude φ:

$$p\frac{\partial^2 \varphi}{\partial z^2} - 2jk_0 n_0 p\frac{\partial \varphi}{\partial z} + \frac{\partial}{\partial y}\left(p\frac{\partial \varphi}{\partial y}\right) + k_0^2(q - n_0^2 p)\varphi = 0. \tag{4}$$

Applying the finite-element method to the cross-section of the waveguide in the y-direction of Eq. (4), we obtain:

$$[M]\frac{d^2\{\varphi\}}{dz^2} - 2jk_0 n_0[M]\frac{d\{\varphi\}}{dz} + ([K] - k_0^2 n_0^2[M])\{\varphi\} = \{0\}, \tag{5}$$

where $\{\varphi\}$ is the global electric or magnetic field vector, and $[K]$ and $[M]$ are the finite-element matrices. Applying the Crank-Nicholson algorithm for the z-direction after introducing the Padé approximation [19] and the transparent boundary condition [20] to Eq. (5), we finally obtain the following fundamental equation of the BPM:

$$[A]_i\{\varphi\}_{i+1} = [B]_i\{\varphi\}_i, \tag{6}$$

where $[A]_i$ and $[B]_i$ are the beam-propagation matrices, and the subscripts i and $i+1$ denote the quantities related to the ith and $(i+1)$th propagation steps at $z = i\Delta z$ and $(i+1)\Delta z$, respectively, and Δz is the propagation step size. When an incident field $\{\varphi\}_0$ is given, the propagating field can be calculated by solving Eq. (6).

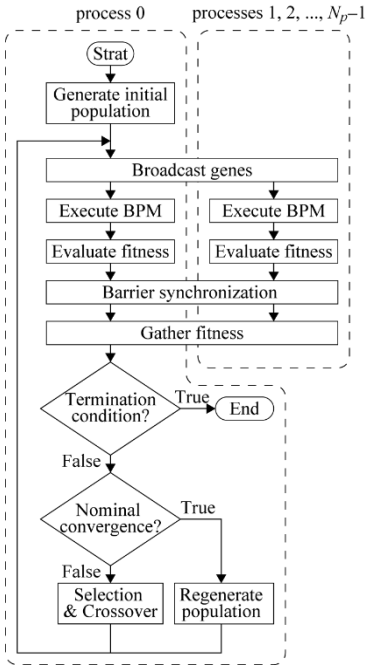

Fig. 1. Flow chart of the proposed parallelized μGA.

III. NUMERICAL MODEL

Figure 2 (a) shows a three-dimensional model of an optical 90° hybrid based on a 4×4 MMI coupler, whose core and cladding materials are ZrO_2-doped silica and silica, respectively. Let W and L be the width and length of the MMI section, respectively. The MMI has four input waveguides labeled $1, \ldots, 4$ and four output waveguides labeled $5, \ldots, 8$. We note that input waveguides 2 and 4 are not used for optical 90° hybrids [3]. The widths of the input and output waveguides were identical and equal to w. The positions of the centers of these waveguides are y_i $(i = 1, \ldots, 8)$. In addition, we assume $y_i = y_{i+4}$ for $i = 1, \ldots, 4$.

Figure 2 (b) shows an equivalent two-dimensional model, which is obtained using the effective index method, of a 4×4 MMI coupler. In this model, the refractive index of the core region is expressed as the effective index of a three-layer slab waveguide. The BPM analyses in the proposed method were performed for two-dimensional equivalent models.

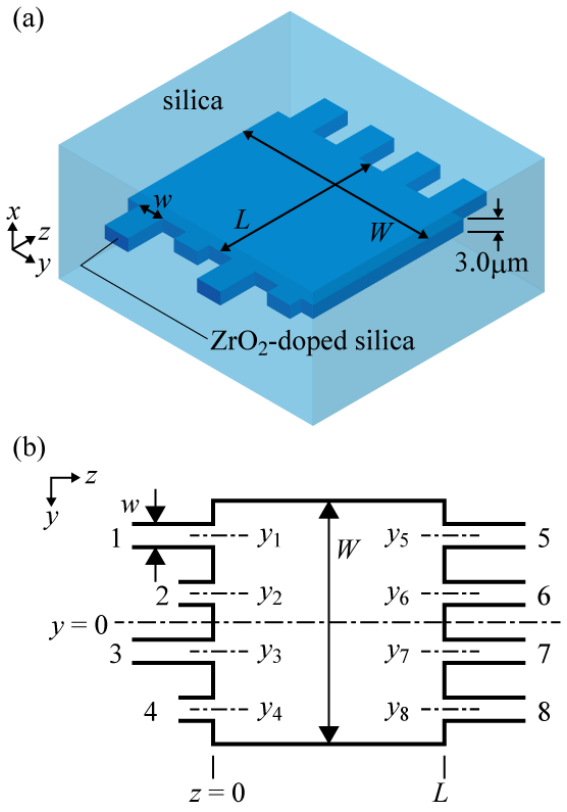

Fig. 2. Schematic structure of 4×4 MMI coupler for: (a) a three-dimensional model, and (b) an equivalent two-dimensional model.

The length of the MMI, L, and the positions of the input waveguides, y_i $(i = 1, \ldots, 4)$, are, respectively, given as follows:

$$L = \frac{3L_\pi}{4} + \Delta L, \tag{7}$$

and

$$y_i = \frac{2i - 5}{8} W + \Delta y_i, \tag{8}$$

where ΔL and Δy_i are the deviations of the length of the MMI and the positions of the center of the input waveguides, respectively. Here, L_π is the beat length in the MMI and is given by:

$$L_\pi = \frac{\pi}{\beta_0 - \beta_1}, \tag{9}$$

where β_0 and β_1 denote the propagation constants of the fundamental and first-order modes of the MMI, respectively [6].

To evaluate the fitness of a 4×4 MMI coupler, we define two properties of the coupler as follows: Let $I = \{1,3\}$, $O = \{5,6,7,8\}$, and Λ be sets of the input ports, output ports, and wavelengths for BPM analysis, respectively. Let $S_{ji}(\lambda)$ be the scattering parameter at $j \in O$ for the input from $i \in I$ at wavelength $\lambda \in \Lambda$. We define the imbalance $I_{B,i}(\lambda)$, and excess loss $X_{L,i}(\lambda)$ by the following equations, respectively:

$$I_{B,i}(\lambda) = -10 \log_{10} \left[\frac{\min \{ |S_{ji}(\lambda)|^2 | j \in O \}}{\max \{ |S_{ji}(\lambda)|^2 | j \in O \}} \right] \text{[dB]}, \tag{10}$$

and

$$X_{L,i}(\lambda) = -10 \log_{10} \left[\frac{\sum_{j \in O} |S_{ji}(\lambda)|^2}{P_{in}(\lambda)} \right] \text{[dB]}, \tag{11}$$

where $P_{in}(\lambda)$ denotes the input power. The fitness of a 4×4 MMI coupler expressed as an individual is evaluated as follows:

$$F = \exp \left\{ -\frac{1}{|I||\Lambda|} \times \sum_{i \in I} \sum_{\lambda \in \Lambda} [C_{IB} I_{B,i}(\lambda) + C_{XL} X_{L,i}(\lambda)] \right\}, \tag{12}$$

where $|I|$ and $|\Lambda|$ denote the number of elements in the sets I and Λ, respectively, and C_{IB} and C_{XL} are the weighting coefficients that determine the relative importance of $I_{B,i}(\lambda)$ and $X_{L,i}(\lambda)$, respectively.

IV. NUMERICAL RESULTS

We consider silica-based 4×4 MMI couplers as optical 90° hybrids. The operating wavelength ranged from 1520 to 1580 nm. The relative refractive index difference Δ, was 5.5% [21]. The wavelength-dependent refractive index of the cladding is given by the Sellmeier equation [22]: the thickness of the core was assumed to be 3.0 μm. The equivalent two-dimensional models obtained by the effective index method were analyzed using the BPM. The incident wave was assumed to be the TE-polarized fundamental mode of the input waveguides. The set of wavelengths used to evaluate the

fitness was $\Lambda = \{1520, 1550, 1580\ \text{nm}\}$. The values of β_0 and β_1 for Eq. (9) were evaluated at 1550 nm. The termination condition of the proposed GA was g = 50. The genes in a chromosome, which represent a 4×4 MMI coupler, and their search ranges are shown in Table 1. The coefficients in Eq. (12) are assumed as $C_{IB} = 1$ and $C_{XL} = 0.5$.

Table 1: Genes and their search ranges

j	$x_j^{(g,i)}$	$x_{j,min}$	$x_{j,max}$
1	W	20 μm	40 μm
2	ΔL	−10 μm	10 μm
3	w	2.3 μm	3.3 μm
4	Δy_1	−1 μm	1 μm
5	Δy_2	−1 μm	1 μm
6	Δy_3	−1 μm	1 μm
7	Δy_4	−1 μm	1 μm

The optimization processes were executed on a Beowulf-style cluster [12] comprise five identical PCs. Each PC had an Intel Core i7-8700 processor and a solid-state disk. The code for the proposed optimization was primarily developed in Python language with mpi4py [15], which is a Python library for MPI. From the Python code, a Fortran90 code for the BPM was executed on each process as a subprocess. The population of the GA N_p was assumed as 5; thus, each single process in Fig. 1 was assigned to one PC each.

The performance of an optical 90° hybrid is often quantified in terms of the CMRR and phase error. The CMRRs for the in-phase (I) and quadrature (Q) channels are, respectively, defined as:

$$\text{CMRR}_{I,i}(\lambda) = -20\log_{10}\left[\frac{||S_{5i}(\lambda)|^2 - |S_{8i}(\lambda)|^2|}{|S_{5i}(\lambda)|^2 + |S_{8i}(\lambda)|^2}\right]\text{[dBe]}, \quad (13)$$

and

$$\text{CMRR}_{Q,i}(\lambda) = -20\log_{10}\left[\frac{||S_{6i}(\lambda)|^2 - |S_{7i}(\lambda)|^2|}{|S_{6i}(\lambda)|^2 + |S_{7i}(\lambda)|^2}\right]\text{[dBe]}, \quad (14)$$

for the input from $i \in I$[4]. The phase error at the output port $j \in O$ with respect to output port 5 is defined as:

$$\Delta\varphi_j(\lambda) = \varphi_j(\lambda) - \varphi_5(\lambda) - (\tilde{\varphi}_j - \tilde{\varphi}_5). \quad (15)$$

Here, $\varphi_j(\lambda) = \angle S_{j3}(\lambda) - \angle S_{j1}(\lambda)$, and $\tilde{\varphi}_j$ (j = 5, ...,8) are the theoretical values of $\varphi_j(\lambda)$; in other words, $\tilde{\varphi}_5 = -45^\circ$, $\tilde{\varphi}_6 = 225^\circ$, $\tilde{\varphi}_7 = 45^\circ$, and $\tilde{\varphi}_8 = 135^\circ$ [3]. The typical system requirements of these values were CMRR ≥ 20 dBe and $|\Delta\varphi_j| \leq 5^\circ$ [4,5].

Figure 3 shows the characteristics of an optimized 4×4 MMI coupler obtained through trials, and the optimized parameters are summarized in Table 2. A CMRR greater than 28.9 dBe and a phase error less than 2.52° across the operation wavelength range, which satisfied the system requirements, were achieved. In addition, the excess loss remained less than 0.68 dB. Figure 4 shows the field distributions at the end of the 4×4 MMI coupler at wavelengths of 1520, 1550, and 1580 nm. A uniform field distribution among the output ports was realized, and thus, good values of CMRR were achieved. Conversely, we observed larger field distributions between two adjacent output waveguides, especially at wavelengths of 1520 and 1580 nm. This caused a larger excess loss at the shorter and longer sides of the operation wavelength range, as shown in Fig. 3 (c).

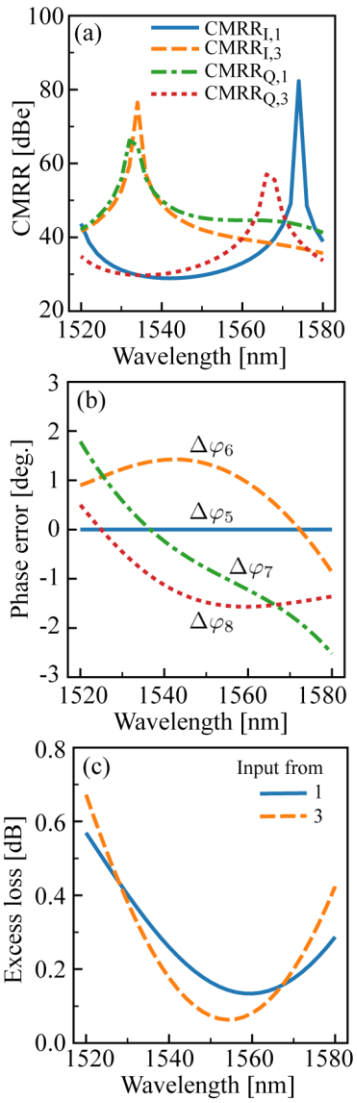

Fig. 3. Performance of an optimized 4×4 MMI coupler as an optical 90° hybrid: (a) CMRR, (b) phase error, and (c) excess loss.

The computational time of the optimization executed in parallel with five PCs was 330 s. Contrastingly, the total computational time of the BPMs in serial execution for all the individuals generated in the optimization

process was 1287 s. The speedup and parallel efficiency were 3.90, and 0.78, respectively. Here, the speedup is the ratio of the sequential to parallel execution times, and the parallel efficiency is equal to the speedup divided by the number of processes. The speedup or parallel efficiency was degraded by unbalanced computational loads in the BPM analyses, executed in parallel. This imbalance occurred, because the number of unknowns and propagation steps in the BPM analyses depended on the generated individuals in the optimization process.

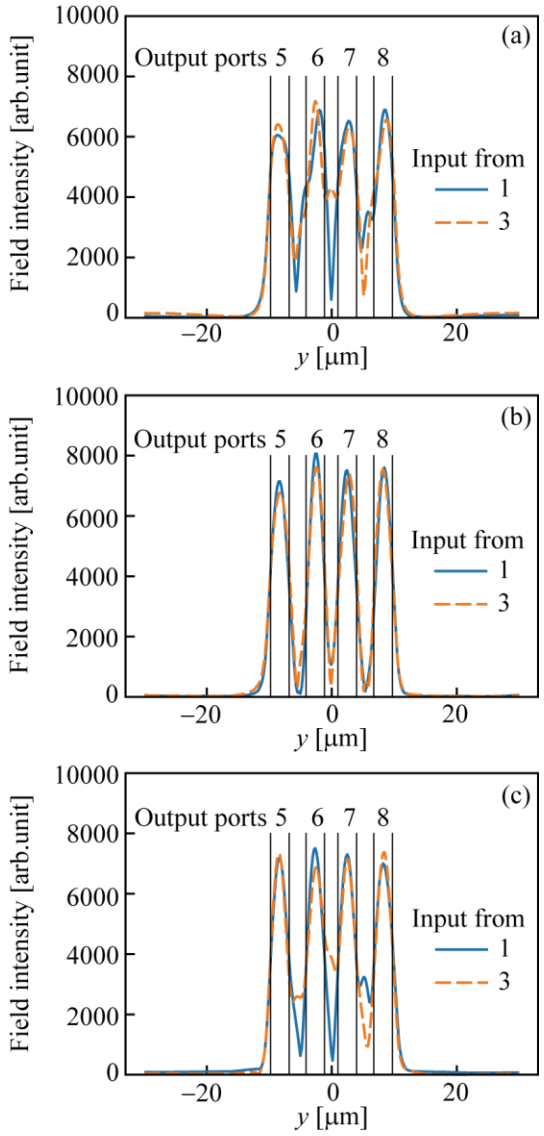

Fig. 4. Field distributions at the end of the optimized 4×4 MMI coupler at wavelengths of: (a) 1520, (b) 1550, and (c) 1580 nm. The boundaries of the output waveguides are also shown by thin solid lines.

Because of using the real-coded GA was used, the optimized structural parameters shown in Table 2 were more accurate than the typical fabrication tolerances, which were of the order of 0.1 μm for silica waveguides. To verify the influence of the fabrication tolerances on the optimized 4×4 MMI coupler, we subsequently carried out an FE-BPM analysis for a 4×4 MMI coupler having the parameters of the fabrication tolerance shown in Table 3. The results are shown in Table 4 and compared with those for the optimized model. Moreover, this model satisfies the typical system requirements of the CMRR and phase error. The excess loss is comparable to that of the optimized structure. We can see that the accuracy of the fabrication tolerance did not degrade the performance of the optimized device.

Table 2: The optimized structural parameters

Parameter	Value [μm]
W	20.606524
L	459
w	2.982606
y_1	−8.310509
y_2	−2.643767
y_3	2.471436
y_4	8.202657

Table 3: Structural parameters with the accuracy of fabrication tolerance

Parameter	Value [μm]
W	20.6
L	459
w	3.0
y_1	−8.3
y_2	−2.6
y_3	2.5
y_4	8.2

Table 4: Comparison of performance

Structural Parameters	Table 3	Table 2
CMRR [dBe]	≥ 28.9	≥ 28.9
Phase error [deg.]	≤ 2.46	≤ 2.52
Excess loss [dB]	0.63	0.68

V. CONCLUSIONS

In this study, we proposed a parallelized structural optimization method based on a real-coded μGA for weakly guided 4×4 MMI couplers for use as optical 90º hybrids. The proposed method was applied to a silica-based 4×4 MMI coupler with $\Delta = 5.5\%$. The optimized 4×4 MMI coupler showed a CMRR greater than 28.9 dBe and a phase error less than 2.52°, which satisfied the typical system requirements over the wavelength range of 1520 to 1580 nm. In addition, the excess loss remained less than 0.68 dB over the wavelength range. The optimization process was executed on a Beowulf-style

cluster comprises five identical PCs. As a result, the speedup and parallel efficiency of the optimization process were 3.90 and 0.78, respectively. A 4×4 MMI coupler with structural parameter values close to the optimized values within an accuracy of typical fabrication tolerance was also analyzed using the FE-BPM. This result is comparable to that of the optimized 4×4 MMI coupler.

ACKNOWLEDGMENT

This work was supported by JSPS KAKENHI (Grant Number JP19K11997). We would like to thank Editage (www.editage.com) for English language editing.

REFERENCES

[1] Y. Sakamaki, Y. Nasu, T. Hashimoto, K. Hattori, T. Saida, and H. Takahashi, "Reduction of phase-difference deviation in 90º optical hybrid over wide wavelength range," *IEICE Electron. Express*, vol. 7, no. 3, pp. 216-221, Feb. 2010.

[2] C. R. Doerr, D. M. Gill, A. H. Gnauck, L. L. Buhl, P. J. Winzer, M. A. Cappuzzo, A. Wong-Foy, E. Y. Chen, and L. T. Gomez, "Monolithic demodulator for 40-Gb/s DQPSK using a star coupler," *J. Lightw. Technol.*, vol. 24, no. 1, pp. 171-174, Jan. 2006.

[3] L. Zimmermann, K. Voigt, G. Winzer, K. Petermann, and C. M. Weinert, "C-band optical 90°-hybrids based on silicon-on-insulator 4×4 waveguide couplers," *IEEE Photon. Technol. Lett.*, vol. 21, no. 3, pp. 143-145, Feb. 2009.

[4] R. Halir, G. Roelkens, A. O.-Monux, and J. G. Wangüemert-Pérez, "High-performance 90º hybrid based on a silicon-on-insulator multimode interference coupler," *Opt. Lett.*, vol. 36, no. 2, pp. 178-180, Jan. 2011.

[5] J. S. Fandino and P. Munoz, "Manufacturing tolerance analysis of an MMI-based 90º optical hybrid for InP integrated coherent receivers," *IEEE Photon. J.*, vol. 5, no. 2, pp. 7900512-7900512, Apr. 2013.

[6] L. B. Soldano and E. C. M. Pennings, "Optical multi-mode interference devices based on self-imaging: Principles and applications," *J. Lightw. Technol.*, vol. 13, no. 4, pp. 615-627, Apr. 1995.

[7] Q. Wang, J. Lu, and S. He, "Optimal design of a multimode interference coupler using a genetic algorithm," *Opt. Commu.*, vol. 209, no. 1, pp. 131-136, Aug. 2002.

[8] B. R. West and S. Honkanen, "MMI devices with weak guiding designed in three dimensions using a genetic algorithm," *Opt. Express*, vol. 12, no. 12, pp. 2716-2722, June 2004.

[9] T. Yasui, J. Sugisaka, and K. Hirayama, "Structural optimization of silica-based 2×2 multimode interference coupler using a real-coded micro-genetic algorithm," *Progress in Electromagnetics Research M*, vol. 55, pp. 169-178, Apr. 2017.

[10] Y. Tsuji and M. Koshiba, "A finite element beam propagation method for strongly guiding and longitudinally varying optical waveguides," *J. Lightw. Technol.*, vol. 14, no. 2, pp. 217-222, Feb. 1996.

[11] T. Yasui, M. Koshiba, and Y. Tsuji, "A wide-angle finite element beam propagation method with perfectly matched layers for nonlinear optical waveguides," *J. Lightw. Technol.*, vol. 17, no. 10, pp. 1909-1915, Oct. 1999.

[12] M. El-Shenawee, C. M. Rappaport, D. Jiang, W. M. Melsei, and D. R. Kaeli, "Electromagnetics computations using the MPI parallel implementation of the steepest descent fast multipole method (SDFMM)," *Applied Computational Electromagnetics Society Journal*, vol. 17, no. 2, pp. 112-122, 2002.

[13] K. Krishnakumar, "Micro-genetic algorithms for stationary and non-stationary function optimization," *Proc. SPIE, Intelligent Control and Adaptive Systems*, vol. 1196, pp. 289-296, Feb. 1990.

[14] C. A. C. Coello and G. T. Pulido, "A micro-genetic algorithm for multiobjective optimization," *Lect. Notes Comput. Sci.*, vol. 1993, pp. 126-140, July 2001.

[15] W. Gropp, R. Thakur, and E. Lusk, *Using MPI-2: Advanced Features of the Message Passing Interface*, 2nd ed., Cambridge, MA, USA: MIT Press, 1999.

[16] L. D. Dalcin, R. R. Paz, P. A. Kler, and A. Cosimo, "Parallel distributed computing using python," *Advances in Water Resources*, vol. 34, no. 9, pp. 1124-1139, Sept. 2011.

[17] F. Herrera, M. Lozano, and J. Verdegay, "Real-coded genetic algorithms: Operators and tools for behavioural analysis," *Artificial Intelligence Review*, vol. 12, pp. 265-319, Aug. 1998.

[18] F. Zhang, K. Sonag, and Y. Fan, "Real-coded genetic algorithm with differential evolution operator for terahertz quasi-optical power divider/ combiner design," *Applied Computational Electromagnetcs Society Journal*, vol. 32, no. 10, pp. 888-894, Oct. 2017.

[19] G. R. Hadley, "Wide-angle beam propagation using Padé approximant operators," *Opt. Lett.*, vol.17, no.20, pp.1426-1428, Oct. 1992.

[20] G. R. Hadley, "Transparent boundary condition for beam propagation," *Opt. Lett.*, vol. 16, no. 9, pp. 624-626, May 1991.

[21] M. Takahashi, Y. Uchida, S. Yamasaki, J. Hasegawa, and T. Yagi, "Compact and low-loss coherent mixer based on high Δ ZrO_2-SiO_2 PLC," *J. Lightw. Technol.*, vol. 32, no. 17, pp. 3081-3088, Sept. 2014.

[22] K. Okamoto, *Fundamentals of Optical Waveguides*, 2nd ed., Cambridge, MA, USA: Academic Press, 2005.

Takashi Yasui graduated with the B.S. degree in Electronic Engineering from Fukui University, Fukui, Japan, in 1997, and the M.S. and Ph.D. degrees in Electronic Engineering from Hokkaido University, Sapporo, Japan, in 1999 and 2001, respectively. From 1999 to 2002, he was a Research Fellow of the Japan Society for the Promotion of Science. In 2002, he joined Fujitsu Ltd., Chiba, Japan. From 2004 to 2011, he was an Assistant Professor of the Department of Electronic and Control Systems Engineering, Shimane University, Matsue, Japan. Since 2011, he has been an Associate Professor of the Faculty of Engineering, Kitami Institute of Technology, Kitami, Japan. He has been engaged in research on wave electronics. Yasui is a member of the IEEE, the Optical Society of America (OSA), the Institute of Electronics, Information and Communication Engineers (IEICE) of Japan, and the Information Processing Society of Japan. In 2018, he was awarded the Excellent Paper Award from IEICE.

Jun-ichiro Sugisaka graduated with the B.E., M.E., and Ph.D. degrees in Optics and Photonics from the University of Tsukuba, Tsukuba, Japan, in 2005, 2007, and 2010, respectively. From 2008 to 2010, he was a research fellow at the Japan Society for the Promotion of Science. From 2010 to 2013, he joined the Center for Optical Research Education at Utsunomiya University, Utsunomiya, Japan, as a doctoral research fellow. From 2013 to 2019, he joined Kitami Institute of Technology as an Assistant Professor. Thenceforth, he has been an Associate Professor of Kitami Institute of Technology. His research interests are in photonic crystals, diffraction, scattering theory inverse problems, artificial intelligence, and computational electromagnetics. Sugisaka is a member of the Institute of Electronics, Information and Communication Engineers (IEICE) of Japan, the Japan Society of Applied Physics, IEEE, and the Optical Society of America. In 2018, he was awarded the Best Paper Award from the IEICE.

Koichi Hirayama received the B.S., M.S. and Ph.D. degrees in Electronic Engineering from Hokkaido University, Sapporo, Japan, in 1984, 1986 and 1989, respectively. In 1989, he joined the Department of Electronic Engineering, Kushiro National College of Technology, Kushiro, Japan. In 1992, he became an Associate Professor of Electronic Engineering at Kitami Institute of Technology, Kitami, Japan, and in 2004 he became a Professor. He has been interested in the analysis and optimal design of electromagnetic and optical waveguides. Hirayama is a senior member of IEEE. In 2018, he was awarded the Excellent Paper Award from IEICE.

Linear Pattern Correction Technique for Compensating the Effects of Mutual Coupling and Deformation in Wedge-Shaped Conformal Antenna Arrays

Adnan Tariq, Shahid Khattak, Hina Munsif, Sohail Razzaq, and Irfanullah*

Department of Electrical and Computer Engineering
COMSATS University Islamabad, Abbottabad Campus, Pakistan
*eengr@cuiatd.edu.pk

Abstract — In this paper, the effects of mutual coupling and antenna surface deformity in a conformal wedge-shaped antenna array are compensated using a linear pattern correction technique. The problem is formulated to reduce the absolute distance between the actual (simulated) and the desired radiation patterns and to allow for null positioning control. The individual field patterns for the antenna elements are deformed due to changes in mutual coupling and the conformal surface. The deformed patterns of the individual antennas for specific bend angles are stored as lookup tables and interpolated to get the desired radiation pattern at any arbitrary bend-angle. The problem is linearly and quadratically constrained at the null points and performance compared with unconstrained optimization. The proposed solution for diminishing the effect of mutual coupling and surface deformity is independent of main lobe direction, type of individual antenna, array geometry, and spacing between antenna elements. The closed-form results are validated through Computer Simulation Technology (CST) for the wedge-shaped deformed dipole antenna array. The results for the proposed scheme are also assessed with the traditional Open Circuit Voltage Method (OCVM) and show superior compensation for deformity and the mutual coupling effects in conformal beam-forming arrays in terms of main beam direction, position and depth of nulls.

Index Terms — Aerial platform, conformal antenna array, interpolation of patterns, least square estimation, mutual coupling compensation, radiation pattern correction.

I. INTRODUCTION

Modern 5G networks comprise heterogeneous systems overseeing massive data transfer capacities and with the high frequency of access points. In order to make these access points less noticeable to the natural eye, they would be required to conform in shape to everyday objects around us [1]. A conformal antenna array can be defined as an array that follows the surface of objects whose shape is defined by considerations other than electromagnetic [2].

Besides 5G wireless massive Multiple Input Multiple Output (MIMO) systems, spatial filtering achieved by conformal antenna array also has applications in radar, and target tracking [3]. Additionally, conformal antenna arrays can be used to replace numerous antennas protuberant from the surface of modern aircraft which are used for navigation, radar altimeter, instrument landing systems and various communication systems [1], [4]-[6] causing considerable mechanical strain and increased fuel ingestion. The need for conformal reception apparatuses is much higher for the large-sized openings that are required for capacities like military airborne observation radars and satellite correspondence [2].

The surfaces, on which the conformal antennas are mounted, may not be sturdy structures and are susceptible to physical deformation because of natural changes. This flexing of surfaces will make the original positions of the antenna component change, resulting in changes in steering vector and Mutual Coupling (MC) among them and producing the radiation pattern conduct entirely unreliable [7], [8]. The subsequent pattern alteration may shift the location of the main beam and loss of null points which minimizes the expected gain of the antenna array and may render any Signal-Not-of-Interest (SNOI) avoidance through the shaping of the radiation pattern. Researchers are, therefore, focusing on compensation techniques in order to accurately recovere the beam pattern and directivity of the antenna array to direct the nulls and the main beam to any wanted direction irrespective of the extent of the distortion of the conformal surface. Through defined employment of the broadside pattern and the nulls, with no power-driven movement of the antenna elements [2], high signal to noise plus interference ratio (SNIR) is attained.

The impact of MC on the wire antenna (monopole antenna, dipole antenna etc.) in an array can be demonstrated through variations in their input impedances. This idea was first introduced by Gupta in [9], where an impedance matrix was utilized to relieve the impact of MC in a planar array of dipole antennas. In [10], [11], this method was used for Direction of Arrival

Submitted On: January 14, 2021
Accepted On: April 18, 2021
https://doi.org/10.47037/2020.ACES.J.360507

(DOA) signal estimation and adaptive nulling of interference. Hui in [11] modelled the MC using impedance matrix based on estimated current distribution and it was shown that the new method for modelling MC performs better in terms of DOA estimation. Notwithstanding, the impedance matrix was assessed under the supposition that the antenna will not radiate while open-circuited in the Open-Circuit Voltage Method (OCVM), which limits this technique to wire antenna elements only.

Another technique called Linear Pattern Correction Method (LPCM) reduces the impacts of MC in antenna arrays through pattern adjustment by limiting the Mean Square Error (MSE) between the wanted and actual patterns [10]-[16]. The outcomes show that the complex excitations for array component assessed utilizing the LPCM are more powerful in alleviating the impacts of MC than OCVM [14],[19]. Since unconstrained LPCM attempts to decrease the MSE between actual and wanted patterns, its effect is less pronounced on patterns alongside directions where signal quality is low, i.e., along with null points.

In [17], the genetic algorithm is used to determine the optimum antenna element excitation for a conformal array. In [11], a framework for radiation pattern synthesis is developed using convex optimization theory in order to optimize dual-polarized conformal arrays. However, both these techniques exhibit higher complexity than LPCM and would bring only marginal performance gains.

In [3], [17], the phase compensation procedure is deployed to recovere the desired antenna array pattern for conformal antennas after incorporating the surface deformity and MC effect. In this method, the projection technique has been utilized to ascertain the measure of phase shift presented by every component in an array to arrive at the reference plane, which is then consolidated in the excitations to recovere the ideal pattern. No exertion has been done to recovere the nulls in this method and there is no control on the arrangement of sidelobes. In [15], the LPCM is implemented to deformed conformal antenna arrays utilizing the impedance matrix of the distorted antenna array acquired from [7]. Direct imperatives are additionally incorporated at the null points so as to govern their position and depth. This model when tried in CST for bigger deformations gives insufficient compensation. The radiation pattern compensation for conformal beamforming array with precise control at the desired direction is, therefore, an open research area and the focus of this paper.

In the introduced work, a practical procedure is created and tested for absolutely controlling the array pattern of deformed conformal antennas through constrained optimization of LPCM. Both the linear and quadratic constraints have been considered. The effect of varying mutual coupling due to deformation is compensated using pre-calculated separately evaluated antenna patterns at various bend angles. The technique is independent of inter-element spacing and antenna element type and has been tested successfully for different deformation angles through interpolation of patterns and for different main beam directions. Even though the strategy is just tested here for wedge-shaped surfaces, it is independent of the surface geometry as long as the position and direction of the individual antenna component are accurately characterized.

The remainder of the paper is organized as follows: In Section II, the problem is formulated. In Section III, the proposed solution for deformity and MC reduction is discussed. Section IV and V the results and their detailed analysis are presented. Section VI finally concludes the paper.

Notation: All matrices are shown in boldface capital letters (**E, A, V, etc.**), vectors are represented by boldface small-case letters (**w, b etc.**), while all the scaler quantities are represented as normal letters. $|\cdot|$ represents the absolute value and $\|\cdot\|$ represents the Euclidean norm.

II. PROBLEM FORMULATION

The physical layout of an N-dipole conformal antenna array mounted on a wedge shape surface, formed along the XZ-plane, is shown in Fig. 1. The antenna elements are equally divided on either side of the wedge with equal inter-element spacing d. The individual dipoles are oriented along Y-axis in order to increase the MC between them so that the effectiveness of the proposed algorithm can be better demonstrated. Bend angle Υ, between the surface of the wedge and X-axis, can be varied, resulting in pattern distortions due to change in antenna locations and orientations. This also affects the relative distances between the antenna elements and changes the MC.

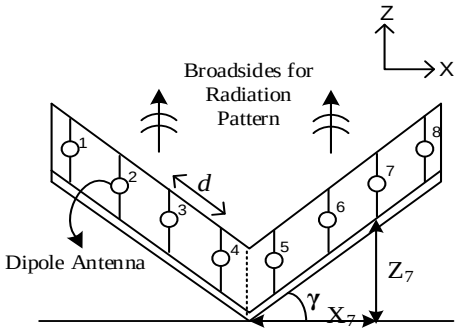

Fig. 1. A deformed wedge shape antenna array in XZ-plane with eight dipole antennas and a bend angle Υ.

The two planar wedge surfaces are considered inflexible and the deformity only occurs as the bend angle changes. The location of an individual element in antenna array along X and Z directions is measured by

the following equations respectively,

$$x_n(d,\Upsilon) = \left(-(N-1)\frac{d}{2} + (n-1)d\right)\cos(\Upsilon), \quad (1)$$
$$z_n(d,\Upsilon) = \left|\left(-(N-1)\frac{d}{2} + (n-1)d\right)\right|\sin(\Upsilon),$$

where $n = 1, \cdots, N$. The position of all the antennas along the Y direction is assumed fixed. A three-dimensional steering matrix is formed $\mathbf{V} \in \mathbb{C}^{[M\times J\times N]}$, with each element $v(m,j,n)$ given by:

$$v(\theta_m, \phi_j, n) = e^{-j\frac{2\pi}{\lambda}[x_n(sin\theta_m cos\phi_j) + y_n(sin\theta_m sin\phi_j) + z_n(cos\theta_m)]}, \quad (2)$$

where x_n, y_n and z_n is the location of the n^{th} element in the array, $\theta_m \in \{\theta_1, \ldots, \theta_M\}$ is the elevation steering angle and $\phi_j \in \{\phi_1, \ldots, \phi_J\}$ is the azimuth steering angle. *M* and *J* are the total numbers of elevation and azimuth angle points respectively.

Individual element patterns for dipole antennas are concatenated to form a three-dimensional matrix **P** such that $\mathbf{P} \in \mathbb{C}^{[\boldsymbol{M\times N\times J}]}$. The Array Pattern matrix **A** is given as the element-wise product of matrix **V** and **P**, i.e., $\mathbf{A} = \mathbf{V} \odot \mathbf{P}$. The field pattern **E** at any arbitrary angle θ_m and ϕ_j can be calculated as:

$$\mathbf{E}(\theta_m, \phi_j) = \mathbf{A}(\theta_m, \phi_j)\,\mathbf{w} \quad (3)$$

where **w** represent the complex excitations to the antenna elements. For succeeding analysis, ϕ_j has been presumed static and the resulting patterns have been observed for the elevation angle θ only.

When the bend angle Υ changes due to external conditions, the whole array pattern distorts due to changes in MC and steering matrix **V**. The problem is to adapt the weights **w** with changes in Υ so as to compensate for any radiation pattern errors due to distortion in the shape of the conformal surface.

III. PROPOSED SOLUTION

A. Procedure for compensation

The flowchart presented in Fig. 2 predicts the approach implemented for deformity compensation and reduction of the MC effect. Here, the deformity is defined as changes in the position of individual antennas elements as the $\boldsymbol{\Upsilon}$ changes. A single dipole antenna is designed in CST Studio Suite and desired array pattern $\mathbf{A}_{\text{des}} \in \mathbb{C}^{\boldsymbol{M\times N}}$ is shaped by the element-wise product of the concatenated isolated pattern of individual element (taken from CST Studio Suite) with the steering matrix ($\boldsymbol{V}$). The initial excitations $\mathbf{w}_{\text{i}}$ given to each array element are extracted by optimizing the pattern of the antenna that minimizes $\mathbf{w}_{\text{i}}$ while having the main beam and null points at the desired positions. The optimization problem is written as:

$$\min_{\mathbf{w_i}} \sum_{\text{i}} \|\mathbf{E}_{\text{des}}(\theta_{SB})\|, \quad \text{s.t.} \quad \mathbf{E}_{\text{des}}(\theta_{tar}) = 1, \quad \mathbf{E}_{\text{des}}(\theta_{null}) \le \epsilon, \quad (4)$$

where θ_{tar} and θ_{null} are the target and null directions respectively and ϵ is an arbitrary null depth. $\mathbf{E}_{\text{des}} = \mathbf{A}_{\text{des}}\mathbf{w}_{\text{i}}$ is the required field pattern. The constraints here ensure that null point positions are precisely defined, and nulls are of sufficient depth to test between the algorithms. The compensation algorithms require individual antenna patterns $\mathbf{P}_{\text{def}}$ incorporating the effect of deformation and MC, the desired pattern of array and location of the radiating antenna elements. It calculates the compensated weights $\mathbf{w}_{\text{c}}$, which mitigates the effect of deformity and MC. The compensated field pattern is given by $\mathbf{E}_{\text{c}}$.

B. OCVM and LPCM

OCVM is the most commonly cited technique for compensation of MC and deformity effect in conformal arrays with wired antennas. In OCVM, dimensionless normalized impedance matrix $\mathbf{Z}_{\text{c}}$ is used to compensate for the MC by taking the product of its inverse $\mathbf{Z}_{\text{c}}^{-1}$ and the open-circuited voltages $\mathbf{v}_{\text{oc}}$ as the terminal voltage $\mathbf{v}_{\text{T}} = \mathbf{Z}_{\text{c}}^{-1}\mathbf{v}_{\text{oc}}$ [9]. The closed-form expression for the impedances for wired antennas is obtained by assuming the antenna array as an N −port network as explained in [13]. For more complex antenna elements, the moments method is used for obtaining $\mathbf{Z}_{\text{c}}$. However, due to non-zero antenna current under open-circuit, $\mathbf{Z}_{\text{c}}$ fails to accurately model the antenna behaviour. This method, therefore, suffers from considerable error as the nulls are not only filled up but their positions are also shifted. For conformal antenna arrays, the situation gets even worse as the effect of small approximation errors for individual antennas is compounded as their patterns are combined with less than optimal phases and amplitudes. As a result, the final array pattern looks very different from the desired one.

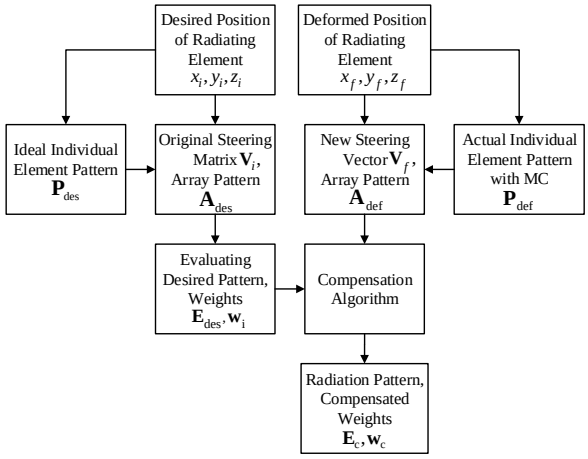

Fig. 2. The procedure adopted for compensating the effect of MC and surface deformity in conformal antenna arrays.

A more accurate procedure for alleviating the MC

and deformation impact from array pattern is the Linear Pattern Correction Method (LPCM) which attempts to limit the Euclidean separation among actual and ($\mathbf{E}_{\text{def}}$) and desired ($\mathbf{E}_{\text{des}}$) field patterns. It aims to reduce the Mean Square Error (MSE) between the simulated deformed and desired APs as shown in the equation,

$$\min_{\mathbf{w}_c} \sum_{\theta} \left\| \mathbf{A}_{\text{def}} \mathbf{w}_c - \mathbf{A}_{\text{des}} \mathbf{w}_i \right\|^2. \tag{5}$$

In [14], it has been observed that the distorted pattern is recovered through matrix **K** obtained as:

$$\begin{aligned} \mathbf{K} &= (\mathbf{A}_{\text{def}})^{\dagger} \mathbf{A}_{\text{des}}, \\ \mathbf{w}_c &= \mathbf{K}.\, \mathbf{w}_i, \\ \mathbf{E}_c &= \mathbf{A}_{\text{def}}\, \mathbf{w_c}, \end{aligned} \tag{6}$$

where † indicates the pseudoinverse and is defined as $(\mathbf{A}_{\text{def}})^{\dagger} = \mathbf{A}_{\text{def}}^{\text{H}}(\mathbf{A}_{\text{def}}\mathbf{A}_{\text{def}}^{\text{H}})^{-1}$. Here $\mathbf{A}_{\text{def}} \in \mathbb{C}^{\text{M}\times\text{N}}$ is the matrix containing defomed patterns of an individual element in array and $\mathbf{E}_c \in \mathbb{C}^{\text{M}\times 1}$ is the radiation pattern of corrected element patterns. The vector $\mathbf{w}_i$ contain the initial excitations used to obtain desired array pattern, and $\mathbf{w}_c$ contain the recovered excitations which compensate for MC and antenna deformity. It is suggested to use the individual antenna patterns obtained from CST at required bend angle ϒ values which are to be utilized as a lookup table for pattern compensation. As LPCM decreases the MSE between the patterns giving the same weight to all angles, the comparative error between the recovered pattern and desired one is much smaller at the main beam than the ones at the nulls. This is evident in the electric field radiation pattern plotted in dBs, where the nulls can be seen as shifted and the algorithm is shown to have little control over the depth of the nulls.

C. Linear and quadratic constrained LPCM

In order to precisely control the null depth and position, LPCM is modified by introducing either linear or quadratic constraints at those points on the pattern that needs to be recovered precisely.

In Linearly Constrained (LC) LPCM, the Euclidean distance between the simulated deformed pattern $\mathbf{E}_{\text{def}}$ and desired pattern $\mathbf{E}_{\text{des}}$ is minimized while constraining the pattern at some points (either null points or the peak sidelobe points) to find the compensated weights $\mathbf{w}_c$. The LC-LPCM optimization problem is written as:

$$\begin{aligned} \min_{\mathbf{w}_c} & \sum_{\theta} \left\| \mathbf{A}_{\text{def}} \mathbf{w}_c - \mathbf{A}\mathbf{P}_{\text{des}} \mathbf{w}_i \right\|^2, \\ \text{s. t.} \quad & \mathbf{A}_c \mathbf{w}_c = \mathbf{b}, \end{aligned} \tag{7}$$

where

$$\begin{aligned} \mathbf{A}\mathbf{P}_c &= [\mathbf{A}_{\text{def}}(\theta_1), \mathbf{A}_{\text{def}}(\theta_2) \cdots \mathbf{A}_{\text{def}}(\theta_q)]^{\text{T}}, \\ \mathbf{E}_{\text{des}} &= \mathbf{A}_{\text{des}} \mathbf{w}_i, \\ \mathbf{b} &= [\mathbf{E}_{\text{des}}(\theta_1), \mathbf{E}_{\text{des}}(\theta_2), \cdots, \mathbf{E}_{\text{des}}(\theta_q)]^{\text{T}}. \end{aligned} \tag{8}$$

Here, $\mathbf{A}_c \in \mathbb{C}^{\boldsymbol{q\times N}}$ is a matrix containing the q constraint vectors at desired constrained angles in the simulated deformed individual element pattern matrix and $\mathbf{b} \in \mathbb{C}^{\boldsymbol{q\times 1}}$ is a vector of q constraint points on desired array pattern. To find out the solution for (7) the objective function is expanded as:

$$\begin{aligned} \|\mathbf{A}_{\text{def}}\mathbf{w}_c - \mathbf{E}_{\text{des}}\|^2 = \mathbf{w}_c^{\text{H}}\mathbf{A}_{\text{def}}^{\text{H}}\mathbf{A}_{\text{def}}\mathbf{w}_c - \\ \mathbf{w}_c^{\text{H}}\mathbf{A}_{\text{def}}^{\text{H}}\mathbf{E}_{\text{des}} - \mathbf{E}_{\text{des}}^{\text{H}}\mathbf{A}_{\text{def}}\mathbf{w}_c + \\ \mathbf{E}_{\text{des}}^{\text{H}}\mathbf{E}_{\text{des}}\,. \end{aligned} \tag{9}$$

The Lagrangian of (7) is formed by:

$$\begin{aligned} \mathscr{L}(\mathbf{w}_c, \mu) = \mathbf{w}_c^{\text{H}}\mathbf{A}_{\text{def}}^{\text{H}}\mathbf{A}_{\text{def}}\mathbf{w}_c - \mathbf{w}_c^{\text{H}}\mathbf{A}_{\text{def}}^{\text{H}}\mathbf{F}_{\text{des}} - \\ \mathbf{A}_{\text{def}}\mathbf{w}_c + \mathbf{E}_{\text{des}}^{\text{H}}\mathbf{E}_{\text{des}} + \mu(\mathbf{A}_c\mathbf{w}_c - \mathbf{b}), \end{aligned} \tag{10}$$

where μ is the Lagrangian multiplier.

The closed-form solution for the above optimization problem is found by solving Karush-Kuhn-Tucker (KKT) conditions [18]. which are given as:

1. Primal Constraint: $\mathbf{A}_c\mathbf{w}_c - \mathbf{b} = 0$.
2. Dual Constraint: $\mu \geq 0$.
3. Complementary slackness: $\mu(\mathbf{A}_c\mathbf{w}_c - \mathbf{b}) = 0$.
4. The gradient of Lagrangian with respect to $\mathbf{w}_c$ vanishes:

$$\begin{aligned} \frac{\text{d}}{\text{d}\mathbf{w}_c}\mathscr{L}(\mathbf{w}_c, \mu) = 0 \\ 2\mathbf{w}_c^{\text{H}}\mathbf{A}_{\text{def}}^{\text{H}}\mathbf{A}_{\text{def}} - 2\mathbf{E}_{\text{des}}^{\text{H}}\mathbf{A}_{\text{def}} + \mu\mathbf{A}_c = 0. \end{aligned} \tag{11}$$

Rewriting third and fourth KKT conditions in matrix form give:

$$\begin{bmatrix} 2\mathbf{A}_{\text{def}}^{\text{H}}\mathbf{A}_{\text{def}} & \mathbf{A}_c \\ \mathbf{A}_c & 0 \end{bmatrix} \begin{bmatrix} \mathbf{w}_c \\ \mu \end{bmatrix} = \begin{bmatrix} 2\mathbf{E}_{\text{des}}^{\text{H}}\mathbf{A}_{\text{def}} \\ \mathbf{b} \end{bmatrix}. \tag{12}$$

The above system of linear equations is solved for $\mathbf{w}_c$ as:

$$\mathbf{w}_c = \mathbf{A}_c{}^{\dagger}\mathbf{b}. \tag{13}$$

The linear constraints reduce the search space so that the solution satisfying the constraint is the only possible solution. Consequently, the compensated pattern performs well at the null points (constraint points) but does not care for the rest of the radiation pattern. As a result, a higher side-lobe level at the edges, away from the constraint points, can be observed. The error performance of LC-LPCM, however, improves with increasing the number of constraints chosen at the point evenly spread over the radiation pattern. However, there is an upper limit on the maximum number of constraint points $q \leq N$.

The problem is therefore modified to Quadratically Constrained Quadratic Programming (QCQP), which is given as:

$$\begin{aligned} \min_{\mathbf{w}_c} & \sum_{\theta} \|\mathbf{A}_{\text{def}}\mathbf{w}_c - \mathbf{A}_{\text{des}}\mathbf{w}_i\|^2, \\ \text{s. t.} \quad & |\mathbf{A_c}\mathbf{w}_c - \mathbf{b}|^2 \leq \beta, \end{aligned} \tag{14}$$

here $0 \leq \beta \leq 1$ is a constraining factor, lower the value of β smaller the search space. Since closed form solution of QCQP do not exist, the Newton-Raphson method is used to solve for the above optimization problem. Quadratic constraint allows a good compromise, enabling the corrected pattern to follow the desired pattern more closely while at the same time ensuring that the desired null depths are achieved.

D. Using LUTs to reduce complexity and storage cost

In order to deal with the difficulty of evaluating the pattern of every element at different bend positions, lookup tables (LUTs) are used in computations in which these patterns are pre-calculated. Lookup table stores the patterns of each antenna element at all the combination of angles ϕ and θ, as well as for different bend angles Υ. The Electric field pattern illustrated in Fig. 3 changes with different bend angle Υ for the first array element.

Clearly, at any angle (θ), the behaviour changes regularly with Υ and in-between values can be evaluated with interpolation. Different combinations of $\Delta\Upsilon$ spacing and interpolation schemes are experimented with. It is found that the results generated with $\Delta\Upsilon = 5^o$ using cubic interpolation is reasonably accurate. The significant expense of figuring the individual array element pattern in the presence of MC and the effect of deformation occurred could be avoided by storing the simulated deformed pattern in LUTs for selected bend angles. The patterns at the rest of the flex angles can be accurately found through interpolation. Moreover, due to the geometric symmetry of the wedge-shaped conformal antennas only half of the patterns of the radiating element are required to be stored because in wedge shape the patterns of the elements are the flipped version of one another.

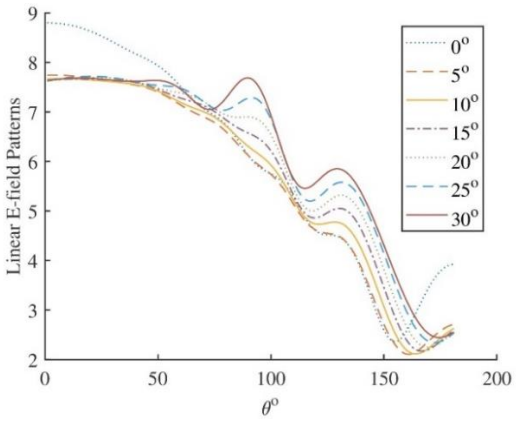

Fig. 3. Electric field pattern magnitude at different bend angles for the leftmost (1^{st}) array element in an 8 element wedge-shaped array at an inter-element spacing of 0.3λ.

IV. RESULTS AND DISCUSSIONS

Eight element dipole antenna arrays have been used for simulation and analysis purposes. Inter-element spacing is kept at 0.3λ, so that the effect of MC is pronounced and the effectiveness of the proposed algorithm in mitigating it can be clearly demonstrated. 3D EM analysis software (CST) is used for verification of the results. All the radiation patterns, such as desired, deformed coupled and the compensated one, are first evaluated in MATLAB and then validated through CST. Two types of patterns have been recovered: a broadside pattern having nulls at 30º and -30º and one with a steered the main beam towards 30º with nulls at 0º and 60º.

A. OCVM and unconstrained LPCM compensation

In Fig. 4 OCVM and unconstrained LPCM (UC-LPCM) compensation results are shown when an 8-element linear dipole array is deformed at 15º and 30º bend-angles. The desired field pattern as shown in Figs. 4 (a) and 4 (b) is the optimized one for the linear array minimizing the sidelobe level.

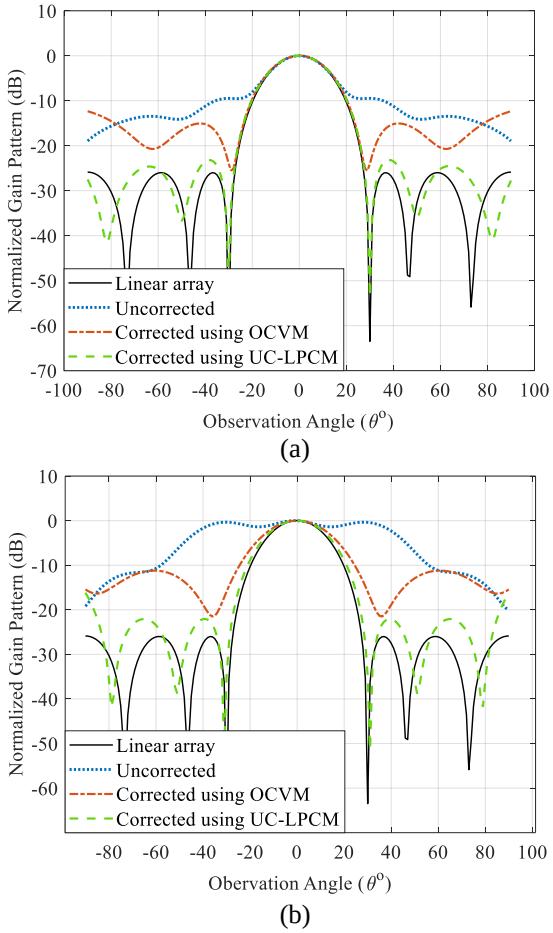

Fig. 4. OCVM and UC-LPCM compensation with the main beam at broadside for wedge shape dipole array at bend angles: (a) 15º and (b) 30º.

In OCVM, an impedance matrix is employed to find weights for deformed CBA for its pattern to approach the desired pattern. One can see in Fig. 4 (b) that OCVM is not very effective in compensating for deformation and the MC effect. In fact, at greater deformation, the impedance matrix fails to model the effect of these impairments and the compensated pattern is very different from the desired one. On the other hand, the pattern recovery is very good when using the UC-LPCM method for both small and medium deformation. The only

drawback is that the null positions have shifted by a few degrees and its depth is also gone up to around -40dB as against -60dB obtained for the desired pattern. Since UC-LPCM assigns the same weight to errors at all the angles, greater accuracy is exhibited at the peak values in the log domain representation. It is, therefore, evident from Fig. 4 that the peak to null power ratio of the compensated radiation pattern has been greatly compromised.

In Fig. 5, the results are presented for OCVM and LPCM compensation, however, the main beam is now shifted toward 30º. A wedge-shaped array is again flexed at 15º and 30º in Fig. 5 (a) and Fig. 5 (b) respectively.

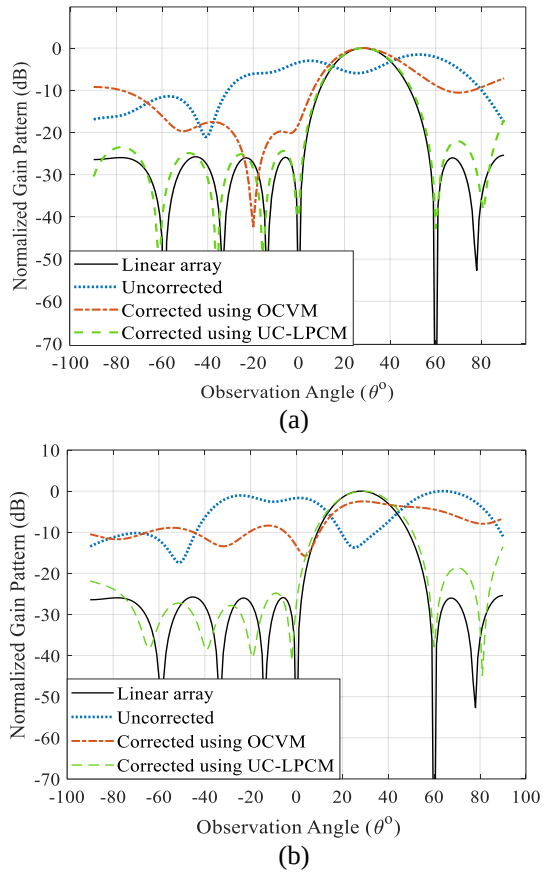

Fig. 5. OCVM and UC-LPCM compensation with the main beam centred at 30º for wedge shape dipole array at bend angles: (a) 15º and (b) 30º.

When the main beam is shifted from broadside to any other angle, OCVM fails completely to recover the pattern. It is evident that the nulls are completely lost and the sidelobe levels are higher than -10dB. The results indicate that the changed current distribution due to MC and deformation cannot be accurately modelled by the impedance matrix. The results improve considerably for unconstrained LPCM with the sidelobes dropping below -20dB. However, little control is exhibited on the position and depth of the null points.

The results of Figs. 4 and 5 shows that OCVM has limitations for pattern recovery of severely deformed wedge antennas. While the performance is bad along the broadside, it becomes worse when the main beam is steered away from it. On the other hand, UC-LPCM gives good pattern recovery for both broadside and the steered main beam, with good sidelobe suppression. The null position and its depth, however, is greatly compromised (>-40dB) for the steered main beam.

B. Linear and quadratically constrained LPCM

The algorithm works as long as the number of constraint points is less than the size of the array. To have a better trade-off between side-lobe level and nulls depth QC-LPCM results are presented, which shows the good recovery of constrained points as well as a lower side-lobe level. The search space for QC-LPCM is reduced to a hyperplane defined by the constraints. This results in a solution that gives a better trade-off between the null point recovery and the side-lobe levels.

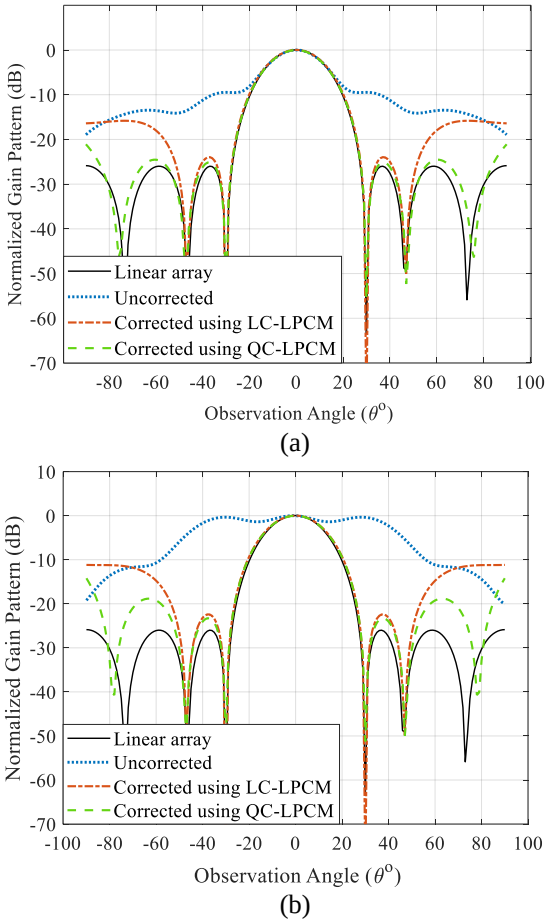

Fig. 6. LC-LPCM and QC-LPCM compensation with the main beam at broadside for wedge shape dipole array at bend angles: (a) 15º and (b) 30º.

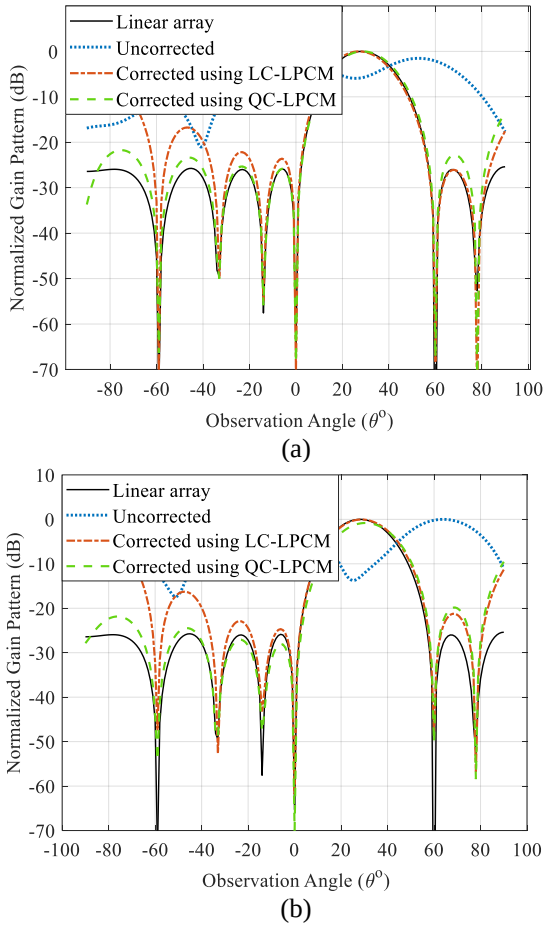

Fig. 7. LC-LPCM and QC-LPCM compensation with the main beam centred at 30º for wedge shape dipole array at bend angles: (a) 15º and (b) 30º.

In Figs. 6 and 7, only the peak point on the main beam and the first two nulls on either side of the main beam are constrained. Although the mean square error (MSE) is greater than the unconstrained LPCM as expected, the main lobe to null difference is better preserved in LC-LPCM and QC-LPCM.

C. Null depth comparison

The nulls approaching capability of the above-mentioned techniques are compared in Table 1. For broadside pattern, null at 30° and for steered main beam null at 0° has been considered for comparison and the desired null depth is assumed to be -60dB. Both LC-LPCM and QC-LPCM give the best null recovery and are better than UC-LPCM, especially for greater distortion levels.

D. Interpolation of patterns

In order to show the effect of interpolation, a case is considered in which radiation pattern for bend-angle $\Upsilon = 18°$is recovered through the interpolation of pre-stored individual element patterns in Fig. 3. $\Delta\Upsilon = 15°$ together with cubic interpolation is compared with UC-LPCM in Fig. 8 for pattern recovery. One can see that there is not much difference between compensated radiation patterns obtained from accurate pre-stored individual antenna patterns at 18° and the interpolated patterns. So interpolation can be used to reduce the storage data requirements of the proposed algorithm. However, the spacing between the bend angles $\Delta\Upsilon$ needs to be kept within a reasonable range for interpolation to be reliable, as the results deteriorate greatly if $\Delta\Upsilon > 10°$.

Table 1: Null depth comparison of pattern recovery techniques

Technique	Broadside		Main Beam at 30°	
	$\Upsilon = 15°$	$\Upsilon = 30°$	$\Upsilon = 15°$	$\Upsilon = 30°$
OCVM	-24dB	-15dB	-17dB	-13dB
UC-LPCM	-53dB	-34dB	-40 dB	-27 dB
LC-LPCM	-60dB	-60dB	-60dB	-60dB
QC-LPCM	-55dB	-51dB	-55dB	-52dB

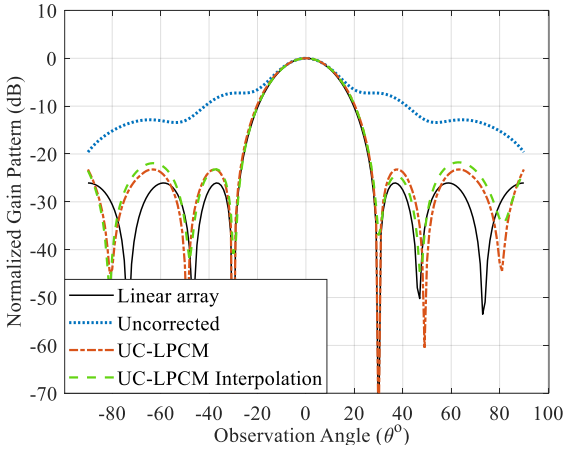

Fig. 8. Effect of interpolation for 18º wedge deformed dipole array.

V. GENERAL DISCUSSION

OCVM method is employed for the compensation of MC and the effect of surface deformity on the array radiation pattern. It is shown that only a partial broadside radiation patterns recovery is obtained, and the results for steered main-beam in directions away from broadside are not good at all. This is because the impedance matrix does not accurately model the effect of MC and deformation and the problem compounds away from the broadside.

Unconstrained linear pattern correction through least square error (LSE) was also used to recover the original pattern of the conformal wedge array. Although pattern recovery was very accurate with the lowest MSE between the desired and compensated radiation patterns, there is little control on the position and depth of the

nulls. As a result, the nulls are partially filled up (-40dB for broadside main-beam pattern) and displaced from the required value by a few degrees. This is one of the simplest methods to recover the desired array pattern with analytical closed-form expressions for calculating the compensated weights.

In order to achieve the maximum recovery at some points in patterns (such as nulls and side-lobe level points), LC-LPCM is investigated. Although the result is promising at constraint points, the algorithm exhibits no control at other points resulting in larger side-lobe levels. This behaviour is because of the search space becoming very limited with a small number of permissible solutions. QC-LPCM gives a better compromise by increasing the search space to hyper-surfaces formed by the constraints. Not only the nulls are recovered while maintaining a low side-lobe level, but a healthy gap between the main lobe and nulls is also obtained.

Since the proposed methods require pre-stored individual element radiation pattern to be available, the effect of pattern interpolation is also investigated in order to reduce the storage cost. It is shown that by using an appropriate bend-angle spacing as pre-stored interpolation points, radiation pattern could be recovered at any arbitrary bend angle with only a marginal performance loss.

VI. CONCLUSION

From the above discussion, one can conclude that patterns can be recovered for wedge-shaped deformation of antenna arrays at large flex angles (up to 30°) using the constrained LPCM techniques. The proposed techniques only require prior knowledge of individual element patterns of desired and deformed arrays and can be used for different types of resonators. It is shown that the proposed QC-LPCM and LC-LPCM algorithm had an increased peak to null power-ratio without unduly degrading the LSE. It was also shown that a few pre-stored individual antenna patterns can be used to give the desired pattern at any arbitrary bend-angle through interpolation.

ACKNOWLEDGEMENT

This work is supported by IGNITE (National Technology Fund), Ministry of IT and Telecom, Government of Pakistan via project no. ICTRDF/ TR&D/2015/04.

REFERENCES

[1] P. Chen, Y. Zhao, and C. Liu, "A novel adaptive wideband frequency invariant beamforming algorithm for conformal arrays," *18th International Radar Symposium (IRS)*, Prague, Czech Republic, pp. 1-10, Aug. 2017.

[2] L. Josefsson and P. Persson, *Conformal Array Antenna Theory and Design*. Wiley-IEEE Press, chapter-1, 2006.

[3] B. D. Braaten, S. Roy, S. Nariyal, M. A. Aziz, N. F. Chamberlain, Irfanullah, M. T. Reich, and D. E. Anagnostou, "A self-adapting flexible (SELFLEX) antenna array for changing conformal surface applications," *IEEE Transactions on Antennas and Propagation*, vol. 61, no. 2, pp. 655-665, Feb. 2013.

[4] J.-L. Guo and J.-Y. Li, "Pattern synthesis of conformal array antenna in the presence of platform using differential evolution algorithm," *IEEE Transactions on Antennas and Propagation*, vol. 57, no. 9, pp. 2615-2621, Sept. 2009.

[5] M. A. Aziz, S. Roy, L. A. Berge, Irfanullah, S. Nariyal, and B. D. Braaten, "A conformal CPW folded slot antenna array printed on a Kapton substrate," *6th European Conference on Antennas and Propagation (EUCAP)*, Prague, Czech Republic, pp. 159-162, Mar. 2012.

[6] R. C. Hansen, *Phased Array Antennas*. 2nd edition, John Wiley and Sons, Inc., New York, NY, chapter-7, 2009.

[7] C. A. Balanis, *Antenna Theory: Analysis and Design.* 4th edition, John Wiley & Sons, chapter-16, 2016.

[8] W. L. Stutzman and G. A. Thiele, *Antenna Theory and Design*. 3rd edition, John Wiley & Sons, chapter-8, 2012.

[9] I. J. Gupta and A. A. Ksienski, "Effect of mutual coupling on the performance of adaptive arrays," *IEEE Transactions on Antennas and Propagation*, vol. 31, no. 5, pp. 785-791, Sept. 1983.

[10] A. Tariq, M. Ayaz, W. Saif, S. Khattak, J. Kazim, Irfan ullah, and R. A. Bhatti, "LSE based radiation pattern compensation in wedge shaped deformed conformal antenna arrays," presented in *International Applied Computational Electromagnetics Society (ACES) Symposium*, Beijing, China, July 29-Aug. 1, 2018.

[11] H. T. Hui, M. E. Bialkowski, and H. S. Lui, "Mutual coupling in antenna arrays," *International Journal of Antennas and Propagation*, vol. 2010, 2 pages, 2010.

[12] P. Chakravorty and D. Mandal, "Radiation pattern correction in mutually coupled antenna arrays using parametric assimilation technique," *IEEE Transactions on Antennas and Propagation*, vol. 64, no. 9, pp. 4092-4095, Sept. 2016.

[13] P. Kumari, B. Chauhan, and S. Vijay, "Performance analysis of microstrip conformal antenna array and effect of mutual coupling for different curvature," *International Journal of Computer Applications*, vol. 135, no. 9, pp. 30-35, Feb. 2016.

[14] J. Nasir, M. H. Jamaluddin, M. R. Kamarudin, Irfanullah, Y.-C. Lo, and R. Selvaraju, "A four-element linear dielectric resonator antenna array for beamforming applications with compensation

of mutual coupling," *IEEE Access*, vol. 4, pp. 6427-6437, Oct. 2016.

[15] S. Lou, W. Wang, H. Bao, N. Hu, G. Ge, X. Hu, S. Qian, and C. Ge, "A compensation method for deformed array antennas considering mutual coupling effect," *IEEE Antennas and Wireless Propagation Letters*, vol. 17, no. 10, pp. 1900-1904, Oct. 2018.

[16] A. Tariq, Irfanullah, J. Kazim, M. Ayaz, A. Zaib, R. A. Bhatti, and S. Khattak, "Interpolation based radiation pattern correction in conformal beamforming arrays," *2nd World Symposium on Communication Engineering (WSCE)*, Nagoya, Japan, pp. 102-106, Dec. 2019.

[17] B. Ijaz, A. Sanyal, A. M-Radal, S. Roy, Irfanullah, M. T. Reich, D. Dawn, B. D. Braaten, N. F. Chamberlain, and D. E. Anagnostou, "Gain limits of phase compensated conformal antenna arrays on non-conducting spherical surfaces using the projection method," *IEEE International Conference on Wireless for Space and Extreme Environments*, pp. 1-6, Nov. 2013.

[18] G. Gordon and R. Tibshirani, *Karush-Kuhn-Tucker Conditions, Optimization*, 10-725/36-725, 2012.

A Frequency Reconfigurable Antenna based on Few Layer Graphene

Sheng-lan Wang, Jing-Song Hong, Yan Deng, and Zhi-jian Chen

Institute of Applied Physics
University of Electronic Science and Technology of China, Chengdu, 610054, China
wsl_0317@hotmail.com

Abstract ─ In this paper, a frequency reconfigurable antenna was presented. This antenna is made up of a square loop and a microstrip line with a gap, in which the few layer graphene (FLG) sheet is located to achieve frequency reconfigurable. FLG is likes a lumped resistor with resistance. And the surface impedance can be adjusted by applying a direct current bias voltage, which obtains two work modes that imitate switch. Additionally, the experimental evidence show the proposed frequency reconfigurable antenna can provide a tunable bandwidth.

Index Terms ─ Few layer graphene, frequency tunable, microstrip structure.

I. INTRODUCTION

Reconfigurable antenna, with its advantages of improving integration and space utilization, has been widely used in the modern wireless communication system. According to their functions, a reconfigurable antenna can be designed in resonant frequency, radiation pattern, and polarization. The method is usually achieved by switches, such as PIN diodes [1], varactor diodes [2], and micro-electromechanical systems (MEMS) [2].

Graphene, a flat monoatomic layer of carbon atoms distributed in a 2-D honeycomb like lattice, which has excellent electrical and thermal properties, will emerge as a leading material for communication technologies [3, 4]. And with changing the bias voltage across graphene, the resonant frequency of the antenna changes significantly [5, 6]. In Ref. [7], Huang et al. studied the performance of wearable antennas made of graphene ink from 1 to 5GHz. In Ref. [8], Rajni studied the wearable Graphene Based Curved Patch Antenna. However, the performance of antenna may be affected by bending. Fortunately, many scholars carry out some basic research on the optimal design method and radiation efficiency of the few layer graphene (FLG) [9, 10]. As experimental evidence in Ref. [11], it is verified that the application of a proper voltage through two bias tees changes the surface resistivity of FLG. In Ref. [12], analyze the optimization of the shorted microwave stub. Few layer graphene was synthesized by CVD deposition techniques, which the thickness less than 5 nm.

In this paper, a novel frequency reconfigurable antenna was presented. This antenna is made up of a square loop with a microstrip structure, in which the FLG sheet is set. This letter is structured as follows. Section II will introduce the design and analyze of the proposed antenna. And Section III will introduce the Fabrication and measurement of the proposed antenna.

II. ANTENNA DESIGN AND ANALYZE

A. Configuration of antenna

The geometry of the presented antenna is shown in the Fig. 1. The antenna has three layers, which are a ground plate, a dielectric substrate, and a radiation layer. As the Fig. 1 (a) shown was the front of antenna, which is the radiation layer. The radiation patch comprised a rectangular loop and a microstrip stub. The stub consists of two microstrip lines and an FLG, which is connected to the ground by a shorting pin. The gray part was the dielectric substrate. The dielectric substrate is Duride 5880 with h=1.6mm, $\varepsilon_r = 2.2$, $\tan\delta = 0.0009$. As the Fig. 1 (b) shown was the back of antenna, which is the ground plate. As shown in Fig. 1 (c), it is the voltage connection method on the FLG. One port of bias DC voltage connects the FLG sheet, the other port connects the ground of antenna.

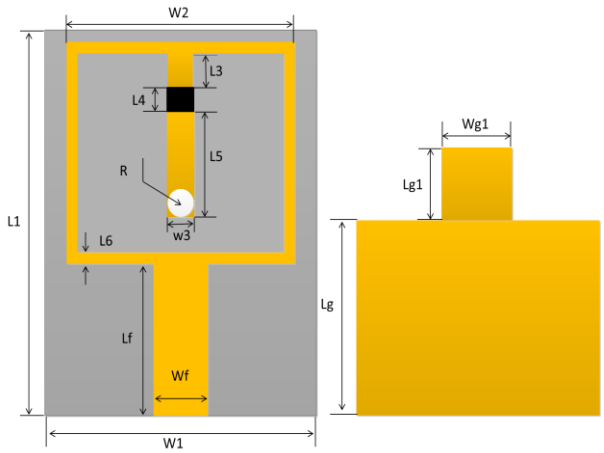

(a) (b)

Submitted On: November 28, 2018
Accepted On: June 28, 2019

https://doi.org/10.47037/2020.ACES.J.360508

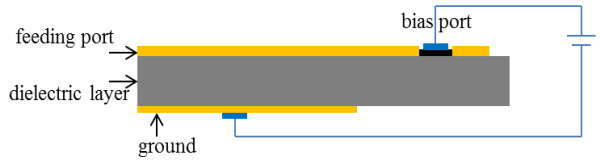

(c)

Fig. 1. Geometry of presented frequency tunable antenna: (a) the front geometry of antenna; (b) the back of geometry antenna; (c) the DC voltage connection method on the FLG. (L1=25, Lg=13, L2=11, Lg1=4.5, L3=1.5, W1=20, L4=0.7, W2=12, L5=4.5, W3=1, L6=0.6, Wf=4.8, Lf=13, Wg1=3.5) (unit: millimeter).

B. The analysis of frequency reconfigurable structure

Based on existing research on few layer graphene, the graphene flake can be modeled as an infinitely thin resistive flake with a sheet resistance ρ (Ω/sq), which is likes a lumped resistor with resistance. And:

$$R = \rho L_4 / W_3 . \quad (1)$$

R is the resistance of the FLG, L, and W is the length and width, ρ is the resistivity. According to the Ref (2), the ρ is 1360 (Ω/sq) when the DC voltage is loaded to 0 V (mode1), the ρ is 49.6 (Ω/sq) when the DC voltage is loaded to 5.5V (mode2).

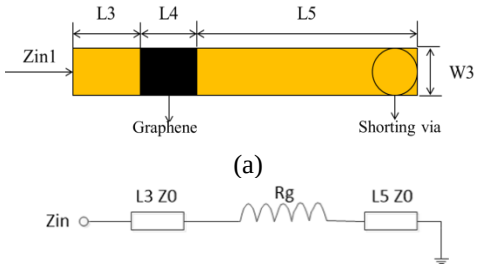

(a)

(b)

Fig. 2. The microstrip stub: (a) geometry of microstrip structure; (b) circuit equivalent model of microstrip structure.

The microstrip stub is shown in Fig. 2 (a). It includes microstrip line, graphene fleet and shorting via which connects the ground. As shown in Fig. 2 (b), the microstrip stub is equivalent to the transmission line circuit model. The input impedance of the transmission line can be calculated by formula (2):

$$Z_{inc} = Z_0 \frac{Z_L + jZ_0 \tan(\beta L)}{Z_0 + jZ_L \tan(\beta L)}, \quad (2)$$

$$Z_{in} = Z_0 \frac{\rho L_4 / W_3 + jZ_0 \tan(\beta L_3) + jZ_0 \tan(\beta L_5)}{Z_0 + \left(\rho L_4 / W_3 + jZ_L \tan\left(\beta L_5\right)\right)\tan\left(\beta L_3\right)}. \quad (3)$$

For this model, the input impedance Z_{in} of antenna can be obtained by two calculations of Equation (2). In Equation (3), Z_0 is the characteristic impedance of microstrip line, β is propagation constant. And the following conditions (4) should be met:

$$L_3 + L_4 + L_5 \le 10 . \quad (4)$$

In order to achieve the impedance matching of the entire antenna, the ranges of L3, L4, and L5 is initially estimated by equations (3) and (4) and (5).

C. Parameters optimization

According to the theoretical calculation results, several parameters optimization have been carried out to improve the performances of the proposed reconfigurable antenna. Because of the diverse combination of parameters, the better value was selected by multiple simulation optimization tests, and the simulation result of optimization was shown in Fig. 3. The simulation was completed by 3D electromagnetic simulation software HFSS17. Four parameters are optimized to improve bandwidth of mode1 and mode2. One of them is L_4, which represents the length of the graphene flake that connect with the microstrip line. Figure 3 (a) and Fig. 3 (b) intimate that with the variation of L_4 from 0.5mm to 0.9mm, in two modes, S11 achieves the best value at L_4=0.7mm. The other are W_3, L_3, and L_5, they represent the width and length of two microstrip line. Figures 3 (c)-(h) show that with the variation of W_3 from 0.8mm to 1.2mm, L_3 from 1mm to 3mm, and L_5 from 4mm to 6mm. Consider the balance of the two modes, the values of the three parameters were L_4 = 0.7mm, W_3 = 1mm, L_3 = 1.5mm and L_5 = 4.5mm respectively.

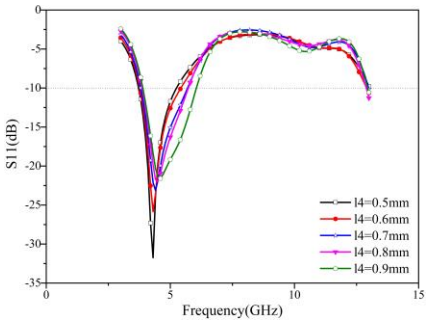

(a)

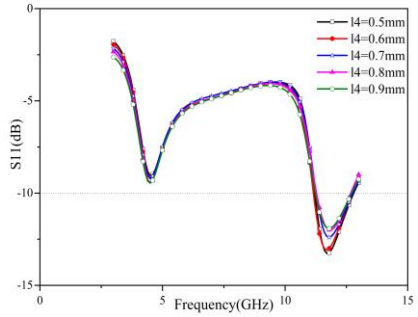

(b)

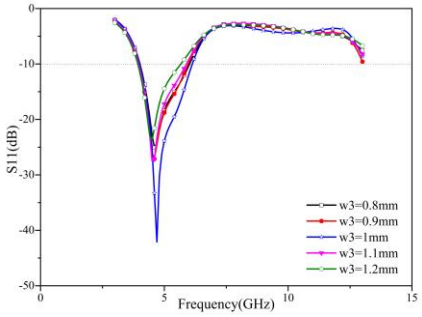

(c)

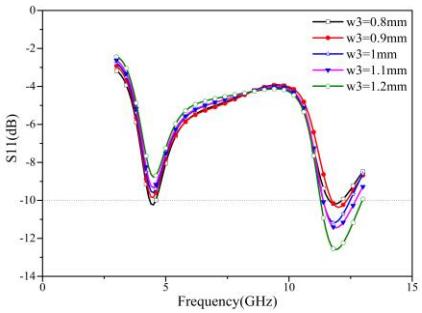

(d)

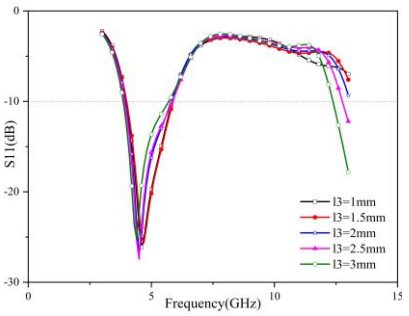

(e)

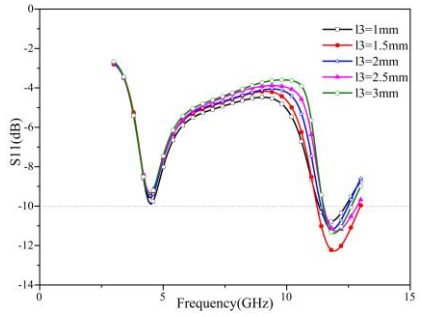

(f)

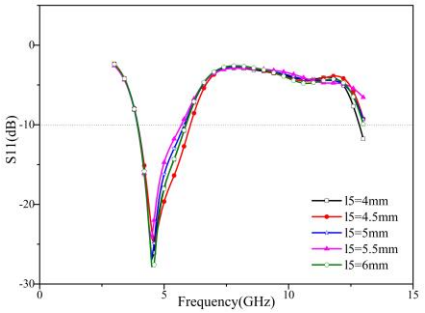

(g)

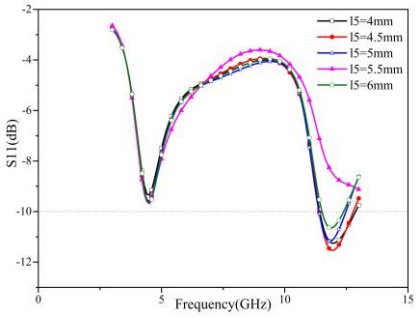

(h)

Fig. 3. The S11 of parameters optimization: (a) mode1, the variation of L4; (b) mode2, the variation of L4; (c) mode1, the variation of W3; (d) mode2, the variation of W3; (e) mode1, the variation of L3; (f) mode2, the variation of L3; (g) mode1, the variation of L5; (h) mode2, the variation of L5.

III. FABRICATION AND MEASUREMENT

A prototype of the frequency tunable antenna is shown in Fig. 4. The scattering parameter is measured using an Agilent N5230C vector network analyzer to analysis impedance matching. Because of the processing technology, the FLG sheet is large than the gap area. The simulated and measured scattering parameter is shown in Fig. 5. The measured resonance frequency is 4.9GHz (from 3.9GHz to 5.45GHz) in mode1 and 11.58GHz (from 11.1GHz to 12.75GHz) in mode2. The S-parameter in different modes verifies that it is feasible to achieve frequency reconfigurable.

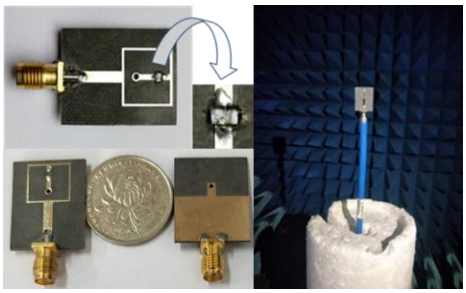

Fig. 4. The prototype of the proposed antenna.

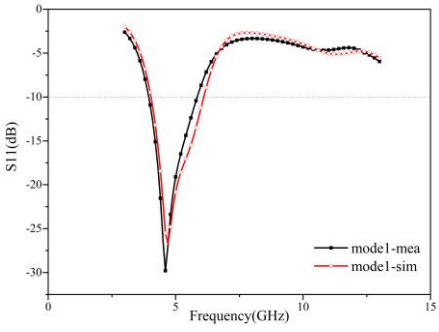

(a)

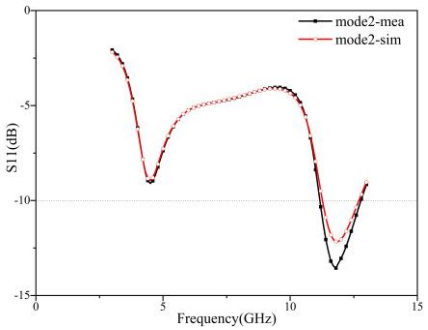

(b)

Fig. 5. Simulated and measured S-parameter of the proposed antenna: (a) mode1, simulated and measured S-parameter, and (b) mode2, simulated and measured S-parameter.

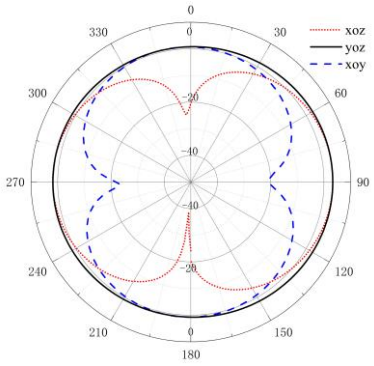

(a)

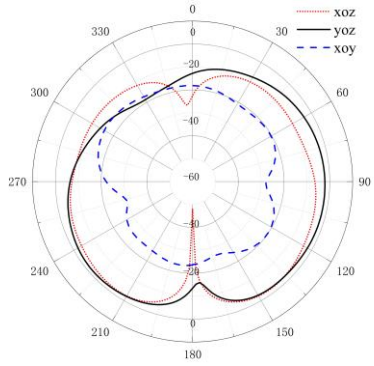

(b)

Fig. 6. Far filed radiation patterns of the proposed antenna: (a) mode1, measured radiation pattern at 4.9GHz, and (b) mode2, simulated radiation pattern at 11.6GHz.

Far filed radiation patterns of proposed antenna which was measured in the satimo OTA system as shown in Fig. 6. Figure 6 (a) was the measured radiation pattern at 4.9GHz of mode 1. Figure 6 (b) was simulated radiation pattern at 10.6GHz of mode 2. For both 4.9 GHz and 11.6 GHz, the antenna manifests a good performance in radiation patterns. Comparing the two radiation patterns, it is found that the changes in different modes were acceptable. The gain of the antenna is also improved of the mode 2. The 3D radiation patterns are shown following (Fig. 7). In mode 1, the maximum gain of the antenna is 2.71dB. In mode 2, the maximum gain of the antenna is 3.28dB. Compared to mode 1, 3D radiation patterns of mode 2 have some variations.

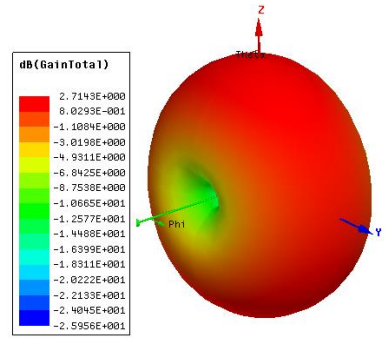

(a)

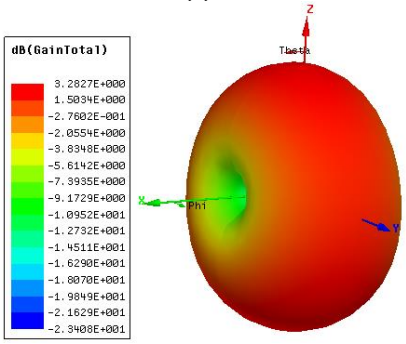

(b)

Fig. 7. 3D radiation patterns of antenna: (a) mode 1 3D radiation patterns, and (b) mode2 3D radiation patterns.

Efficiency of the proposed antenna was shown in Fig. 8. At 4.9 GHz, the efficiency of the antenna is 58%. At 11.6 GHz, the efficiency of the antenna is about 41%. The lower efficiency of the proposed antenna may be due to the smaller radiation area of rectangular loop. In mode 2, the electromagnetic wave radiation was affected to some extent, and the efficiency was also reduced.

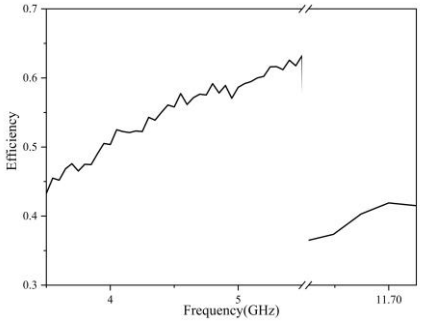

Fig. 8. Efficiency of the proposed antenna.

IV. CONCLUSION

This letter presents a frequency tunable antenna. It was made up of a square loop with a microstrip structure based on the few layer graphene, which the surface impedance can be adjusted by applying a direct current bias voltage. As experimental evidence, the resonant frequency of the antenna can be modified from 4.9GHz to 10.6GHz. The proposed frequency reconfigurable antenna may be great candidate for wireless communication system in the future.

REFERENCES

[1] I. Lim and S. Lim, "Monopole-like and boresight pattern reconfigurable antenna," *IEEE TAP*., 2013. doi: 10.1109/TAP.2013.2283926.

[2] L. Zhong, "A novel pattern-reconfigurable cylindrical dielectric resonator antenna with enhanced gain," *IEEE AWPL*, 2015. doi: 10.1109/LAWP.2015.2504127.

[3] I. Llatser, C. Kremers, A. Cabellos-Aparicio, J. M. Jornet, E Alarcon, and D. N. Chigrin, "Graphene-based nano-patch antenna for terahertz radiation," *Photonics and Nanostructures – Fundamentals and Applications*, 10, pp. 353-358, 2012. doi: 10.4236/anp.2014.33010.

[4] J. Perruisseau-Carrier, "Graphene for antenna applications: Opportunities and challenges from microwaves to THz," *2012 Loughborough Antennas & Propagation Conference*, 2012. doi: 10.1109/LAPC.2012.6402934.

[5] Z. Xu, X. Dong, and J. Bornemann, "Design of a reconfigurable MIMO system for THz communications based on graphene antennas," *IEEE TTHZ*, vol. 4, no. 5, Sep. 2014. doi: 10.1109/TTHZ.2014.2331496.

[6] M. Akbari, M. W. A. Khan, M. Hasani, and T. Bjorninen, "Fabrication and characterization of graphene antenna for low-cost and environmentally friendly RFID tags," *IEEE AWPL*, vol. 15, 2016. doi: 10.1109/LAWP.2015.2498944.

[7] R. Bala and R. Singh, "Wearable graphene based curved patch antenna for medical telemetry applications," *Applied Computational Electromagnetics Society*, 2016.

[8] X. Huang, T. Leng, M. Zhu, X. Zhang, J.-C. Chen, K.-H. Chang, M. Aqeeli, A. K. Geim, K. S. Novoselov, and Z. Hu, "Highly flexible and conductive printed graphene for wireless wearable communications applications," Scientific Reports, 2015. doi: 10.1038/srep18298.

[9] C. Núñez Álvarez, R. Chheung, and J. S. Thompson, "Performance analysis of hybrid metal–graphene frequency reconfigurable antennas in the microwave regime," *IEEE TAP*, vol. 65, no. 4, Apr. 2017. doi: 10.1109/TAP.2017.2670327.

[10] G. Deligeorgis, M. Dragoman, D. Neculoiu, and D. Dragoman, "Microwave propagation in graphene," *Phys. Rev. Lett*., vol. 95, pp. 073107-1–073107-3, 2009. doi:10.1063/1.3202413.

[11] L. Pierantoni, D. Mencarelli, M. Bozzi, R. Moro, S. Moscato, L. Perregrini, F. Micciulla, A. Cataldo, and S. Bellucci, "Broadband microwave attenuator based on few layer graphene flakes," *IEEE TMTT*, vol. 63, no. 8, Aug. 2015. doi: 10.1109/TMTT.

[12] 2015.2441062.

[13] M. Yasir, P. Savi, S. Bistarelli, A. Cataldo, M. Bozzi, L. Perregrini, and S. Bellucci, "A planar antenna with voltage-controlled frequency tuning based on few-layer graphene," *IEEE AWPL*, vol. 16, 2017. doi: 10.1109/LAWP.2017.2718668. CST Microwave Studio, ver. 2008, Computer Simulation Technology, Framingham, MA, 2008.

Sheng-lan Wang was born in Henan, China. She received her B.S. degree in Electronics Information and Engineering from Northwest A&F University, China, in 2016. She is now working toward her M.S. degree in Radio Physics from the University of Electronic Science and Technology of China (UESTC). Her research interests include antennas for wireless communication and the graphene application in antenna.

Jing-Song Hong received the B.S. degree in Electromagnetic from Lanzhou University, China, in 1991, and the M.S. and Ph.D. degrees in Electrical Engineering from the University of Electronic Science and Technology of China (UESTC), in 2000 and 2005, respectively. He is now a professor with UESTC. His research interest includes the use of numerical techniques in electromagnetic and the use of microwave methods for materials characterization and processing.

Yan Deng was born in Jiangsu, China. He received his B.S. degree in New Energy and Electronic Engineering from Yancheng Teaching University, China, in 2017. He is now working toward his M.S. degree in Radio Physics from the University of Electronic Science and Technology of China (UESTC). His research interests include antennas for wireless communication and microwave power transmission.

Zhi-jian Chen was born in Sichuan, China. He received his B.S. degree in School of Electronic Engineering from Chengdu University of Information Technology, China, in 2017. He is now working toward his M.S. degree in Radio Physics from the University of Electronic Science and Technology of China (UESTC). His research interests include antennas for wireless communication and metamaterial antennas.

Improved Configuration of Halbach Magnets with a Homogeneous Magnetic Field for Portable NMR Device

Yi-Yuan Cheng [1], Ming-Yang Su [2], Tao Hai [1], Ming Hui[3], Bao-lei Li [3], and Ling Xia [4]

[1] Department of Mechanical and Electrical Engineering
Nanyang Normal University, Nanyang, 473061, China
chengyy850@gmail.com, nytcht@163.com

[2] Department of Environmental Engineering
Henan Polytechnic Institute, Nanyang, 473000, China
sumingyang@foxmail.com

[3] Department of Physics and Electrical Engineering
Nanyang Normal University, Nanyang, 473061, China
huimingsn@163.com, bl_li@qq.com

[4] Department of Biomedical Engineering
Zhejiang University, Hangzhou, 310027, China
xialing@zju.edu.cn

Abstract ─ Halbach array magnets are widely used in portable nuclear magnetic resonance (NMR) devices that the homogeneity of the magnetic field generated by the array affects the imaging quality. In this paper, we propose some improvements to the construction of the Halbach magnets to enhance magnetic field uniformity. Using a Halbach array model comprising 16 magnets, all the calculations are based on 3D finite element method (FEM) analysis and optimized using the particle swarm optimization (PSO) algorithm. Comparisons of the results are shown to support the observations that the optimized and improved constructions can generate a more homogeneous magnetic field.

Index Terms ─ Halbach magnet, improved configuration, particle swarm optimization, portable NMR.

I. INTRODUCTION

Portable nuclear magnetic resonance (NMR) devices have been of interest since the early 1950s for well-logging [1]. With the development of permanent magnet materials such as Nd–Fe–B in the 1990s, new prospects have emerged for portable NMR applications [2]. The first portable magnetic resonance imaging (MRI) system was proposed for mouse studies in 1995 [3]. Portable NMR devices must be relatively small in size and light in weight, so most devices use permanent magnets instead of superconducting magnets, which generate relatively low magnetic field strengths but can be used in outdoor environments and offer numerous applications.

Halbach magnets are widely used in portable NMR systems and were first proposed by Klaus Halbach for high-energy accelerators [4]; they have also been used in other electromagnetic systems, such as motors, eddy current brakes, and mobile MRI units [5-9]. Halbach magnets have several advantages [10-11]: First, these magnets are composed of small permanent magnet blocks that generate strong and homogeneous fields. Second, they produce a transverse magnetic field distribution in an air gap, which allows the usage of solenoid coils for NMR applications. Moreover, the stray field is small, and the magnets can be produced easily and economically. In particular, Halbach magnets satisfy several of the requirements of portable NMR devices and can be widely used [12].

The Halbach magnet generates a static magnetic field that largely determines the final imaging quality. The ideal Halbach magnet is theoretically expected to provide a homogeneous field, but the inhomogeneities are unavoidable. In this study, we consider some improved constructions for the Halbach magnet array to produce a homogeneous magnetic field. The simulation model comprises an array of 16 magnets, and all calculations are based on 3D finite element method (FEM) analysis.

To obtain a more homogeneous magnetic field, the proposed method improves the construction of the Halbach magnet array and optimizes it. The optimization procedure is a nonlinear and nonconvex problem with

Submitted On: October 17, 2019
Accepted On: May 20, 2021

https://doi.org/10.47037/2020.ACES.J.360509

multipole points owing to the nonlinear characteristics of the ferromagnetic materials. The conventional optimization methods generally converge at local optima and may be suitable for convex problems with single extreme points, where it is difficult to find the global optima in the optimization problems of electromagnetic fields. Particle swarm optimization (PSO) [13] proposed by Eberhart and Kennedy in 1995 is used to optimize the improved construction of the Halbach array in this work; PSO is one of the recently developed intelligent global optimization methods that can handle many complex optimization problems in engineering and science [14-15].

II. THEORY AND MODEL

A. Theory

The ideal Halbach magnet array is also known as a magic ring and is an infinite long hollow cylinder made of a permanent magnet material; the magnetization characteristics change regularly and continuously along the cylinder. The ideal and homogeneous magnetic field inside the hollow cylinder is as shown in Fig. 1 (a). The magnetic field intensity B_0 [16] inside the ideal Halbach magnet array can be defined as:

$$B_x = B_r \ln \frac{r_{outer}}{r_{inner}},\ B_y \cong 0,\ B_z \cong 0, \tag{1}$$

where B_r is the remanence of the magnetic material, and r_{outer} and r_{inner} are the outer and inner radii of the cylindrical magnet. In the ideal state, the magnetic field components in the y- and z-directions can be considered to be approximately 0.

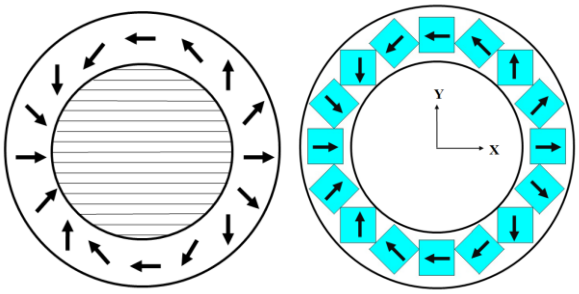

(a) (b)

Fig. 1. (a) Ideal halbach magnet; (b) mandhalas ring magnet.

In reality, the magnetization characteristics cannot change regularly and continuously along the cylinder, and the length of the magnet cannot be infinite; thus, inhomogeneities in the magnetic field cannot be avoided, which may influence the NMR image quality. Several Halbach array magnets made using discrete magnet blocks have been proposed and produced based on the theory of the ideal Halbach magnet. NMR-mandhalas [10], i.e., magnet arrangements for novel discrete Halbach layout, which are ring magnets, were proposed by Raich and Blumler in 2004, as shown in Fig. 1 (b); this structure is composed of 16 magnet blocks with the same sizes and magnetization characteristics. In this work, the 16-mandhalas ring magnet is used as the model for optimization.

The detailed theoretical description of the Halbach magnet array is as follows [8, 10, 17]. The Halbach magnet consists of permanent magnets with equal magnetizations that are oriented and positioned according to the analytic equations given below. There are two predetermined parameters for the exact geometry of the magnet arrangement: radius of the ring, r, and number of magnets, n. The position of each magnet is determined by its center (^cP_i), which is at a distance r from the origin, as shown in Fig. 2.

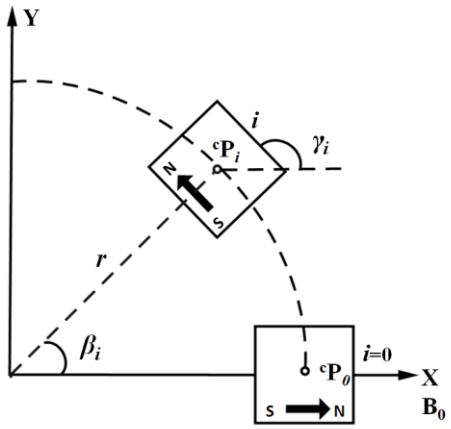

Fig. 2. Geometry of magnet coordinates.

The coordinates of the magnet centers are given as:

$$^cP_i = \begin{pmatrix} ^cx_i \\ ^cy_i \end{pmatrix} = r \begin{pmatrix} \sin\beta_i \\ \cos\beta_i \end{pmatrix}, \tag{2}$$

where $\beta_i = i\alpha$ for $i = 0, 1..., n\text{-}1$ and $\alpha = \frac{2\pi}{n}$.

Once the n magnets are spatially arranged, their size a is scaled such that the densest possible arrangement can be obtained. This results in the following coordinates for the corners of the i-th magnet:

$$\begin{aligned}
^1P_i &= \begin{pmatrix} ^1x_i \\ ^1y_i \end{pmatrix} = ^cP_i + \frac{a}{\sqrt{2}} \begin{pmatrix} \cos\xi_i \\ \sin\xi_i \end{pmatrix} \\
^2P_i &= \begin{pmatrix} ^2x_i \\ ^2y_i \end{pmatrix} = ^cP_i + \frac{a}{\sqrt{2}} \begin{pmatrix} -\sin\xi_i \\ \cos\xi_i \end{pmatrix} \\
^3P_i &= \begin{pmatrix} ^3x_i \\ ^3y_i \end{pmatrix} = ^cP_i + \frac{a}{\sqrt{2}} \begin{pmatrix} -\cos\xi_i \\ -\sin\xi_i \end{pmatrix} \\
^4P_i &= \begin{pmatrix} ^4x_i \\ ^4y_i \end{pmatrix} = ^cP_i + \frac{a}{\sqrt{2}} \begin{pmatrix} \sin\xi_i \\ -\cos\xi_i \end{pmatrix}
\end{aligned}, \tag{3}$$

where $\xi_i = \frac{\pi}{4} - 2\beta_i$.

From the above equations, we can determine the position and arrangement of each magnet, as shown in Fig. 3.

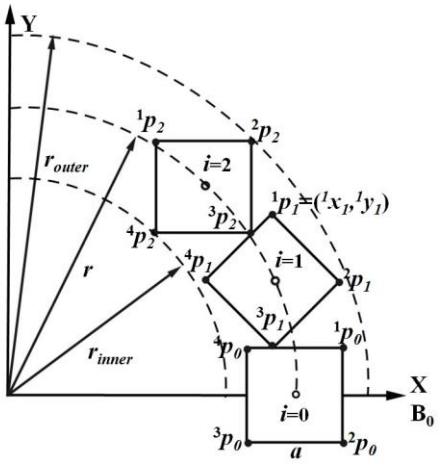

Fig. 3. Schematic representation of the magnet coordinates.

The magnet size, *a*, is given by:

$$a = 2r\Xi(\alpha), \tag{4}$$

where $\Xi(\alpha) = \frac{\cos\alpha - \sin\partial - \sqrt{2}\sin\left(\frac{\pi}{4} - 2\alpha\right)}{2\cos\left(\frac{\pi}{4} - 2\alpha\right) + \sqrt{2}}$.

The inner and outer radii are given by:

$$r_{inner} = r\left(1 - \sqrt{2}\Xi(\alpha)\right), \tag{5}$$

$$r_{outer} = r\left(1 + \sqrt{2}\Xi(\alpha)\right). \tag{6}$$

B. Initial Halbach array magnet model

Based on the above theory, we build the initial 3D half-Halbach array model with n = 16 magnet blocks of dimensions 22.2×22.2×200 mm^3. The radius is r = 70 mm, inner radius is r_{inner} = 54.3 mm, and outer radius is r_{outer} = 85.7 mm. The model is shown in Fig. 4, and each magnet is numbered consecutively for later use. The black arrows represent the direction of magnetization. The magnets are made from Nd–Fe–B (N40) permanent magnet material with a coercivity of 939,014.18 A/m and relative permeability of 1.085, assuming linear dependence between B and H. The orientation of the magnetic field, which unlike those of traditional superconducting magnets is perpendicular to the ring axis, defines the x-direction of the proposed reference system, while the z-axis is directed along the bore.

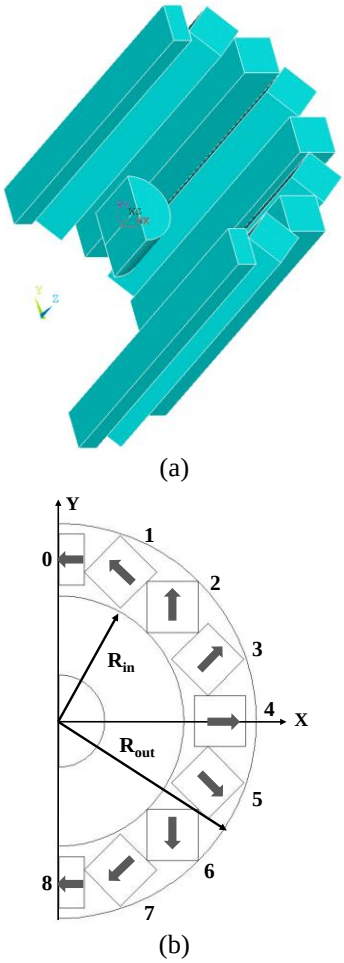

Fig. 4. 3D model (a) initial half; (b) cross section.

In the design of the magnet, we focused on high field homogeneity for the central part of the magnet, with a cylindrical volume of 20 mm diameter and 20 mm length. The field uniformity U is defined as:

$$U = \frac{B_{\max} - B_{\min}}{B_{avg}}, \tag{7}$$

where B_{min}, B_{max}, and B_{avg} are the respective minimum, maximum, and averaged magnetic flux densities of the grid elements in a cylindrical volume of 20 mm diameter and 20 mm length in the FEM calculations.

The 3D FEM analysis of the permanent magnet was carried out using ANSYS 14.0 (www.ansys.com) software, and a half model is considered here because of the symmetry of the model. The conditions of the air-field boundary in a long distance are set to zero flux, for a distance that is five times the height and the outer radius of the entire magnet. We choose the solid 117 type element in ANSYS for the edge-based FEM. The model is divided using a free tetrahedral mesh. Based on practical experience with meshing, to ensure reliability of calculations, the components of concern or

components with larger changes in the magnetic fields need be divided into smaller grids [18]; hence, a fine mesh is used in the center cylindrical imaging region. The magnets are divided into larger grids in regions other than the center imaging region, and the external air part is meshed using a slightly coarse grid.

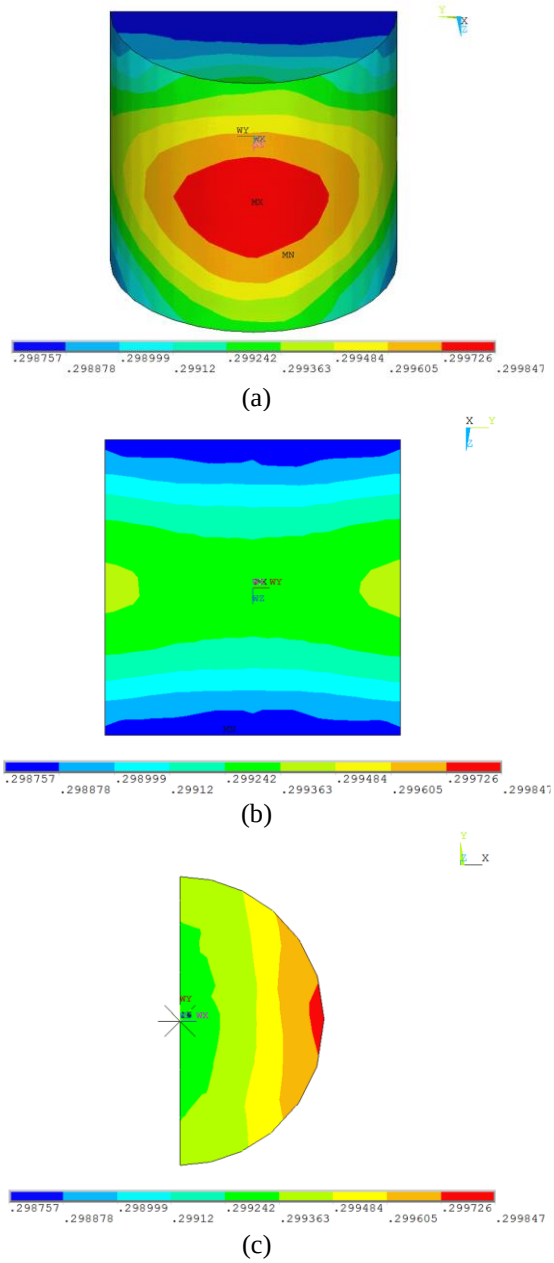

Fig. 5. The magnetic field distribution of the initial model: (a) the cylindrical volume; (b) the yz plane (x=0); (c) the xy plane (z=0).

For the initial model, a magnetic flux density of 0.2998 T and a field uniformity of 3393.88 parts per million (ppm; 10^{-6}) are obtained through ANSYS. Figure 5 shows the magnetic field distribution of the cylindrical volume at the center of the magnet. The homogeneity of the magnetic field at the imaging center is very important for ensuring good imaging quality, so an effective method should be used to improve the magnetic field in the initial magnet model.

III. IMPROVED CONFIGURATIONS

Based on the 2D simulation models reported in a previous work [19], two improved 2D constructions of Halbach magnet using PSO algorithm have been proposed. We extend these methods from the 2D model to the 3D model in this work, namely method 1 and method 2, as follows. The 2D models are based on the assumption that the z-direction is infinite; however, as the magnet has finite length with complex considerations in the 3D model, weaker magnetic fields may be observed at the ends of the cylindrical volume. The other methods will be taken into consideration for the finite length，such as stack structure, addition of shim units and so on.

A. Method 1: Changes to the sizes of the magnets

In theory, all the magnets are of the same size and have similar magnetization characteristics. If we change the sizes of some of the magnets, the magnetic field at the center will be changed. Because most of the magnets are rotated at a theoretical angle, we only consider magnets 0, 4, and 8, whose positions can be easily controlled, as shown in Fig. 6 (a); the additional parts are made of the same magnetic material as the original magnets. The magnet on the right has an increased thickness of W1, and the top and bottom magnets have thicknesses increased by W2. The values of W1 and W2 are obtained by optimization later.

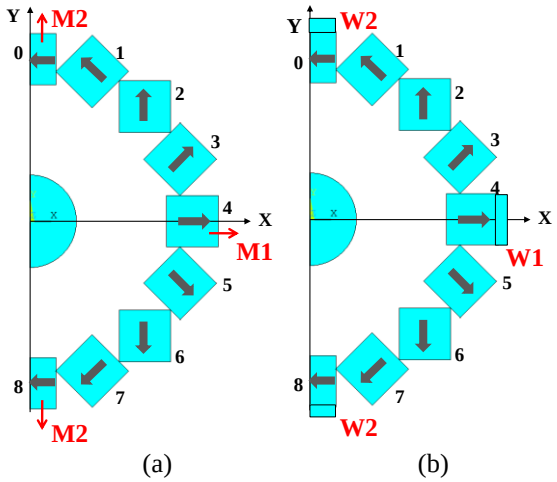

Fig. 6. Schematic cross section of: (a) changing the size of the magnets; (b) moving the position of the magnet towards outside.

B. Method 2: Moving the positions of the magnets

In another paper [12], it is noted that the "magic ring" is shifted outward by 5 mm from the center along the radius. If we want to change the magnetic field at the center, it can be achieved by moving the magnets outward or inward. Here, only the magnets numbered 0, 4, and 8 are considered as their positions can be easily controlled, as shown in Fig. 6 (b). A positive value of M1/M2 in Fig. 6 (b) implies moving outward, and a negative value implies moving inward. The values of M1 and M2 are determined by PSO, as shown later.

C. Method 3: Stack structure

The first two methods change only the radial distances of the magnets to improve the uniformity at the center of the magnetic field. However, when the model is extended to three dimensions, the axial direction must also be considered in addition to the radial direction. The most important problem with the 3D magnet model is that the imaging center has a weaker magnetic field at the ends but is stronger in the middle because of the finite length of the magnet. In a previous work [10], a stack structure also called as a "sandwich", was proposed comprising several short mandhala rings in the z-direction. The short mandhala rings are supported by an aluminum frame, with air gaps between the rings to ensure a more uniform magnetic field. Stacking more than six "magic rings" improves the field homogeneity within the stack but increases the weight and cost [20].

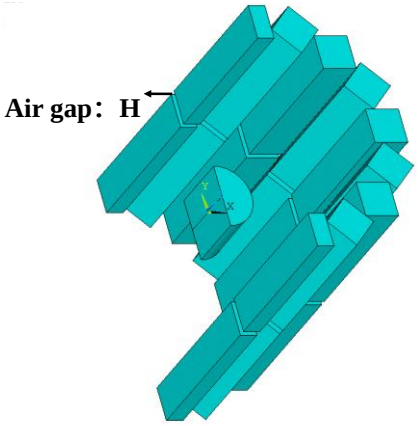

Fig. 7. Schematic representation of stack structure.

Considering the complexity of modeling, magnet weight, and manufacturing cost, we explore a two-ring stack structure where the magnet is divided into the upper and lower parts by an air gap of height H, as shown in Fig. 7. The stack structure can weaken the strength of the magnetic field in the middle, which will generate a more uniform field over the cylindrical volume.

D. Method 4: Addition of shim units

The weaker magnetic field at the ends of the magnet can be enhanced through adding some shim units to improve the uniformity of the center imaging volume. Two smaller rings with smaller magnets at the top and bottom of the cylinder are added to provide end-correction fields to offset the fall-off of the finite array in the z-direction [7, 21]. Because the magnet model used in this study is relatively small, we added eight shim units, four each at the top and bottom of the magnet. The positions of the four units are symmetrically distributed along the x and y axes, as shown in Fig. 8. The cross section of the shim unit is square, with a side length of 10 mm, height UAZ, and the positions (determined by DX and DY) optimized later. The material of the shim units is identical to that of the magnet, and the magnetization direction is same as those of the adjacent magnets.

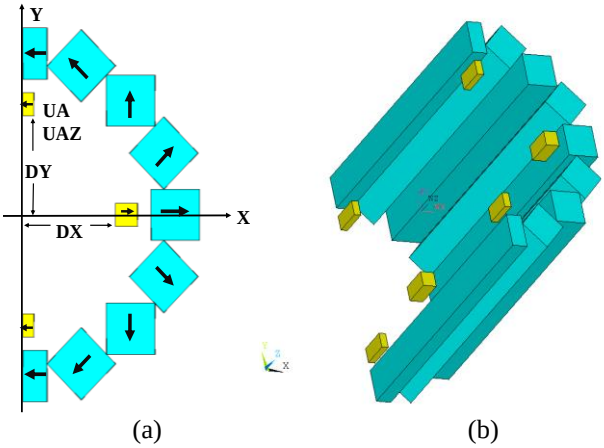

Fig. 8. Schematic representation of adding shim units: (a) cross-section; (b) half model.

E. Combination of several methods

The methods mentioned above are not mutually exclusive, so it is possible to optimize with a combination of these methods, e.g., combination of Methods 1 and 3, combination of Methods 2, 3, and 4. All the parameters in these methods can be optimized at the same time. By combining the optimizations of these methods, we hope to find a relatively optimal structure that can generate a uniform magnetic field in the imaging area.

IV. SIMULATION AND OPTIMIZATION

In this study, the 3D FEM analysis of permanent magnets is carried out using ANSYS (version 14.0, www.ansys.com). Owing to the symmetry of the magnet model, only a half model is considered. To obtain the homogeneous DSV, the parameters of the methods mentioned above are optimized using the PSO algorithm, which is programmed in MATLAB R2009b (The MathWorks, Natick, MA, USA). The optimized design parameters obtained by PSO are then used to calculate

the magnetic field of model. The optimized variables and constrains are listed in Table 1.

Table 1: Optimization variables and constraints

Methods	Optimization Variables	Constrains (mm)
Method 1: Change size	W1, W2	[0.2, 10]
Method 2: Move position	M1, M2	[-5, 5]
Method 3: Stack structure	H	[1, 5]
Method 4: Shim unit	DX, DY	[30, 45]
	UAZ	[5, 20]

In the PSO algorithm, we choose the uniformity of the cylindrical volume of 20 mm diameter and 20 mm length as the objective function and fitness of PSO. The optimization can be expressed as:

Minimize

$$U = \frac{B_{\max}\left(x_1, L, x_k\right) - B_{\min}\left(x_1, L, x_k\right)}{B_{avg}\left(x_1, L, x_k\right)}, \quad (8)$$

where x_1 to x_k are the optimization parameters or variables from the different methods listed in Table 1.

Based on the number of optimization parameters using the different methods, the population size of the PSO algorithm may differ. According to the rule that more parameters have a greater number of groups, the detailed population sizes of the different methods are shown in the Table 2 below. In addition, the number of iterations for the different methods is set to 100.

Table 2: Optimization parameters and population sizes

Methods	Optimized Parameters by PSO (mm)	Population Sizes
Method 1: Change size	W1, W2	20
Method 2: Move position	M1, M2	20
Method 4: Shim unit	DX, DY, UAZ	30
Method 1+3: Change size + Stack	W1, W2, H	30
Method 2+3: Move position + Stack	M1, M2, H	30
Method 3+4: Stack + Shim unit	DX, DY, UAZ, H	40
Method 1+3+4: Change size+Stack+Shim unit	DX, DY, UAZ	30
Method 2+3+4: Move position+Stack+Shim unit	DX, DY, UAZ	30

V. RESULTS

A. Results of Method 1, Method 2, Method 3 and Method 4

We provide the results of Method 3, i.e., the stack structure first. There is only one parameter in Method 3, and we calculate the magnetic field values for air gap values of H = 1, 2, 3, 4, 5, and 6 mm; these results are shown in Fig. 9.

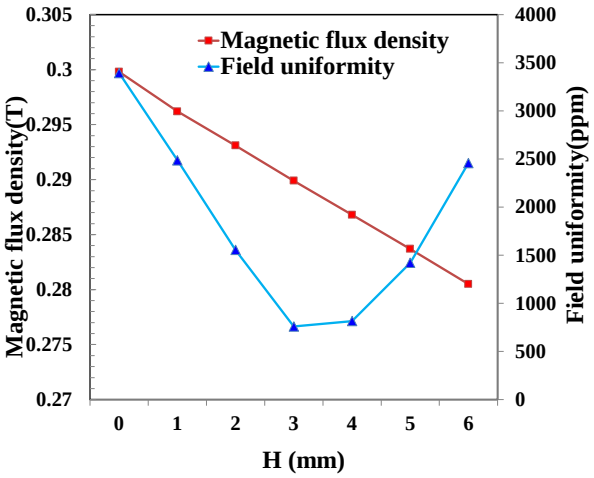

Fig. 9. The magnetic field with different air gaps in the stack structure.

The initial model with H = 0 mm is compared to the others. The strength of the magnetic field is weakened according to the increase in the gap height, and the uniformity is improved correspondingly; however, this air gap cannot be increased continuously. When the air gap is 3 mm, the magnetic field is most uniform, as shown in Fig. 10. These results show that the magnet with the stack structure can generate a more uniform magnetic field than the initial model, but the uniformity cannot meet the demands of imaging. We therefore combine the stack structure with other methods, and the optimization range of the air gap is restricted to the range of [1 mm, 5 mm] based on the results of optimization.

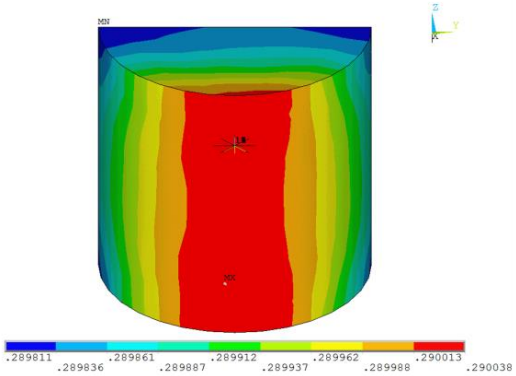

(a)

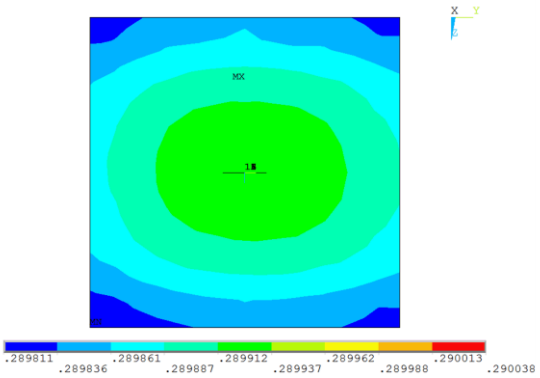

(b)

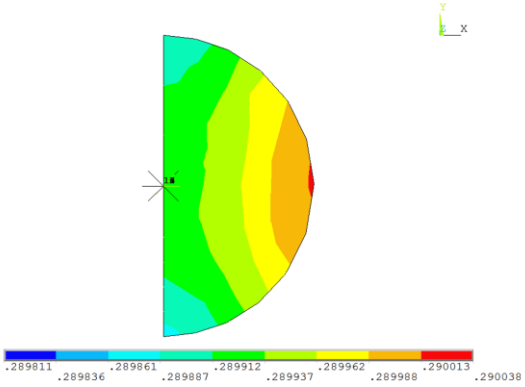

(c)

Fig. 10. The magnetic field distribution with H=3 mm air gap. (a) the cylindrical volume; (b) the yz plane (x=0); (c) the xy plane (z=0).

The parameters of Methods 1, 2, and 4 are optimized by iterative calculations of the PSO, and the comparisons are displayed in Table 3. From these results, we see that the uniformities of the obtained magnetic fields are much better than those when using the methods individually, especially in the combinations of Methods 1 and 2 with Method 3. The magnetic flux densities are observed to be weakened slightly owing to the air gap of the stack structure.

Table 3: Optimization results

Methods	Optimized Parameters by PSO (mm)	Magnetic Flux Density (T)	Field Uniformity (ppm)
Initial model	NULL	0.2988	3393.8817
Method 1: Change size	W1=1.7574 W2=6.5851	0.3077	2863.2789
Method 2: Move position	M1=-0.0221 M2=-3.8119	0.3063	2752.3956
Method 4: Shim unit	DX=42.6497 DY=33.6686 UAZ=19.8297	0.2998	2976.2469

B. Results of Methods 1+3, Methods 2+3, and Methods 3+4

The previous section presents the results of the four methods separately, and the uniformities of the magnetic field are marginally improved in each case. We therefore combine these methods for optimization, i.e., Method 3 with each of the other methods. Based on these combinations, an extra optimization parameter is added to Methods 1, 2, and 4, namely the height of the air gap, H, of the stack structure. After iterative calculation of the PSO, the obtained results are shown in Table 4.

Table 4: Optimization results

Methods	Optimized Parameters by PSO (mm)	Magnetic Flux Density (T)	Field Uniformity (ppm)
Initial half model	NULL	0.2988	3393.8817
Method 1+3: Change size + Stack	W1=2.0568 W2=4.2943 H=3.3908	0.2955	246.2565
Method 2+3: Move position + Stack	M1=-0.0532 M2=-1.2619 H=3.3229	0.2908	258.2889
Method 3+4: Stack + Shim unit	DX=35.8377 DY=36.9083 UAZ=19.3052 H=3.1307	0.2898	498.0765

C. Results of Methods 1+3+4 and Methods 2+3+4

Adding the shim units does not conflict with Methods 1+3 and 2+3; hence, we combined the addition of the shim units with the optimization models of Methods 1+3 and 2+3. The positions and heights of the shim units are optimized by PSO to obtain the final results shown in Table 5.

Table 5: Optimization results

Methods	Optimized Parameters by PSO (mm)	Magnetic Flux Density (T)	Field Uniformity (ppm)
Method 1+3+4: Change size+ Stack+Shim unit	DX=34.7569 DY=39.9797 UAZ=5.1494	0.2955	284.1458
Method 2+3+4: Move position+ Stack+Shim unit	DX=31.6021 DY=44.3450 UAZ=5.0169	0.2909	249.9071

From the results in Table 5, we can see that the magnetic field uniformity is not better but worse after adding the shim units, which is increased by about 40 ppm, so it's infeasible that adding the shim units to the improved configuration optimized by Method 1+3. Besides, the other improved configuration optimized by Method 2+3, generate a stronger and more uniform magnetic field after adding the shim units.

D. Comparisons of some results

(1) Comparisons of Weight

Beside the flux density and homogeneity, the mass of the magnet is an important design criterion, especially for portable applications. The density of the magnet material is known (Nd–Fe–B: $\rho = 7.5$ g·cm^{-3} as a reference), and we can estimate the weight of magnets roughly as a reference, as shown in Fig. 11. The weight estimations include only that of the permanent magnet material used in the model and not those of the support structures and other components used in the actual device.

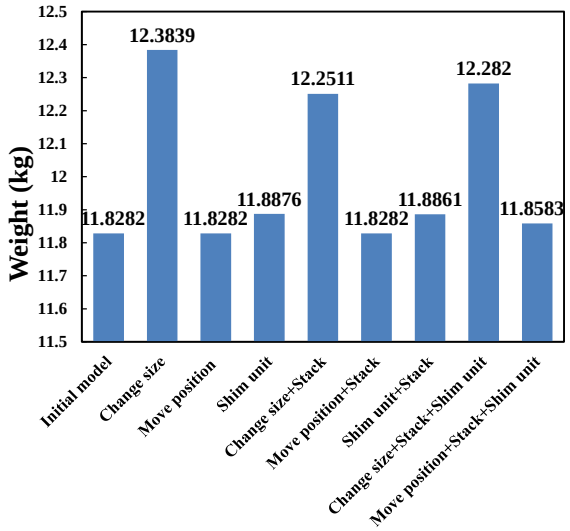

Fig. 11. Weight of the whole magnets model.

The weight of the permanent magnet material used in the initial whole magnet is about 11.8282 kg. Some methods do not change the weight of the magnet, such as the methods involving moving the position and the stack structure, because no extra material is added. However, weight increment is inevitable in the methods involving changing the size and adding the shim units; in particular, the weight increases more in the method of changing the size of the magnet (about 0.5 kg).

These calculations only consider the weight of the permanent magnet materials used in the model, but there are the mutual attractive and repulsive forces between the magnets in practice, so an external framework is needed to maintain the arrangement of the magnets. This framework must made of a light material, such as aluminum, to minimize the overall weight of the system.

(2) Comparisons of Three Combinations

Among the previous attempts at optimization, we choose the three most improved combinations of the Halbach magnet array that have better uniformities for imaging compared with the initial model. These are Methods 1+3, 2+3, and 2+3+4.

In the above work, we focused on the field density and uniformity in a cylindrical volume of 20 mm diameter and 20 mm length. Now, we calculate the magnetic field at the center of the ring for different cylindrical volumes. All these cylindrical volumes have the origin of the coordinate system as the center, and the diameters and heights are varied from 8 mm to 20 mm. We obtain the minimum, maximum, and average magnetic flux density from these calculations, and the statistical results are shown in Fig. 12.

The magnetic field of the initial model is as shown in Fig. 12 (a), and the average magnetic flux density is about 0.2993 T. The deviation over a small cylindrical volume is smaller, which means that the uniformity is better than that of a large cylindrical volume. The deviations over different cylindrical volumes are smaller for the three improved Halbach magnet arrays than those for the initial configuration, indicating that all three optimized methods generate more uniform magnetic fields. Compared to Fig. 12 (c), shim units are added in the configuration of Fig. 12 (d); thus, the average magnetic flux density increases.

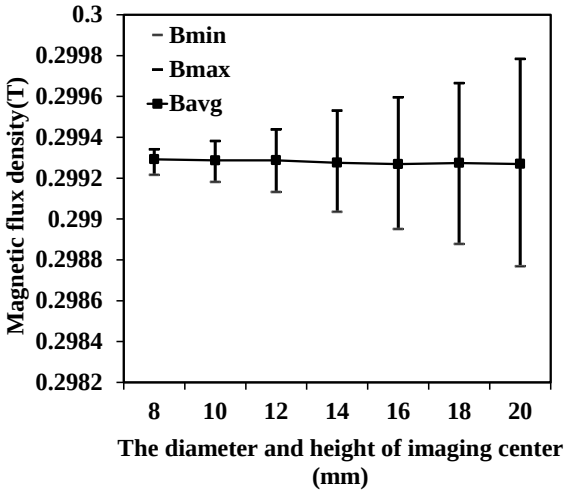

(a)

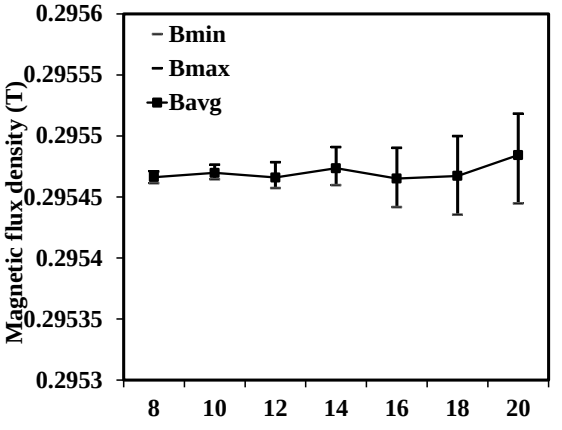

(b)

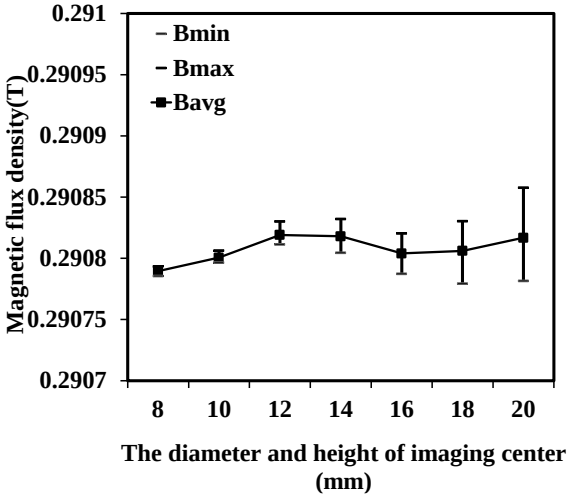

(c)

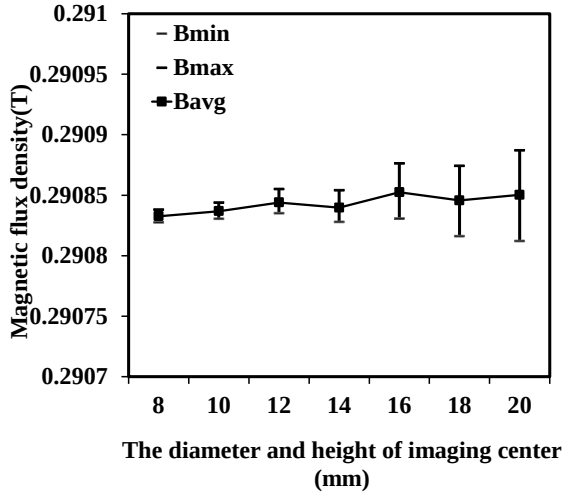

(d)

Fig. 12. The average magnetic flux density and standard deviation over different cylindrical volumes of the center imaging. (a) the initial model; (b) method 1+3: change size + stack; (c) method 2+3: move position + stack; (d) method 2+3+4: Move position + Stack + Shim unit.

There are no considerable differences among the three improved Halbach magnet arrays over different cylindrical volumes, as shown in Fig. 13. Here, we do not recommend the improved magnet with the shim units because the shim units involve uncertainties that affect the quality of the magnetic field, such as accuracies of location and size, magnetization characteristics, and so on. At the same time, the shim units occupy some of the inner space in the magnet, which will affect the arrangement of the gradient and radio frequency (RF) coils. In comparison, the other two improved Halbach magnet configurations have relatively simple structures and are recommended.

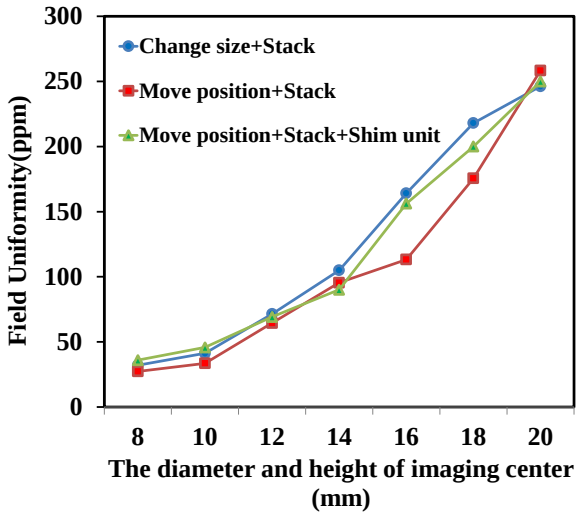

Fig. 13. The magnetic field uniformity over different cylindrical volumes.

VI. DISCUSSION AND CONCLUSION

In this study, a few different optimized configurations of the Halbach magnet array are proposed. Simulations were performed to validate the designs and show that the optimized constructions could significantly improve the magnetic field uniformity.

The design and optimization of the magnet are improved along the radial and axial directions at the same time. Method 1 involving changing the sizes of some of the magnets and Method 2 involving moving the positions of some of the magnets are extended from a 2D model to a 3D model along the radial direction. Method 3 involving the stack structure and Method 4 involving addition of shim units are based on the axial direction; hence, we combine these methods to obtain three improved configurations with low nonuniformities.

In the proposed optimized configurations, there are only two layers in the stack structure. More layers in the stack will generate more uniform magnetic fields, but these complex structures will have increased cost and more factors need to be controlled. Adding shim units should be carefully considered because the location and size as well as magnetization characteristics of the shim units might affect the accuracy of shimming directly. The design and simulations are based on improvement of configuration of the magnets that have more limitations, so shimming coils can be used for further improvement of the homogeneity, which is easier and more practical.

In future work, more comparisons can be performed using conventional optimization methods and PSO. In addition, improved configurations of the Halbach magnet array with homogeneous magnetic fields can be compared with other published results.

ACKNOWLEDGMENT

This work was supported in part by the National Natural Science Foundation of China under Grant No. 61701262, the scientific and technological project of Henan Province in China under Grant No. 182102310610, the key scientific research project in colleges of Henan Province in China under Grant No. 17A510016 and the special project of Nanyang Normal University in China under Grant No. ZX2016011.

REFERENCES

[1] D. E. Woessner, "The early days of NMR in the Southwest," *Concepts in Magnetic Resonance*, vol. 13, pp. 77-102, 2001.

[2] M. Sagawa, S. Fujimura, H. Yamamoto, Y. Matsuura, and K. Hiraga, "Permanent magnet materials based on the rare earth-iron-boron tetragonal compounds," *IEEE Transactions on Magnetics*, vol. 20, pp. 1584-1589, 1984.

[3] G. Eidmann, R. Savelsberg, P. Blümler, and B. Blümich, "The NMR MOUSE, a mobile universal surface explorer," *Journal of Magnetic Resonance*, Series A, vol. 122, pp. 104-109, 1996.

[4] K. Halbach, "Permanent magnets for production and use of high energy particle beams," *in Proceedings of the Eighth International Workshop on Rare Earth Cobalt Permanent Magnets and Their Applications*, Dayton, Ohio, pp. 103, May 1985.

[5] Z. Zhu and D. Howe, "Halbach permanent magnet machines and applications: A review," *IEE Proceedings-Electric Power Applications*, vol. 148, no. 4, pp. 299-308, 2001.

[6] W. Min, M. Zhang, Y. Zhu, B. Chen, G. Duan, J. Hu, and W. Yin, "Analysis and optimization of a new 2-D magnet array for planar motor," *IEEE Transactions on Magnetics*, vol. 46, pp. 1167-1171, 2010.

[7] E. Danieli, J. Mauler, J. Perlo, B. Blümich, and F. Casanova, "Mobile sensor for high resolution NMR spectroscopy and imaging," *Journal of Magnetic Resonance*, vol. 198, pp. 80-87, 2009.

[8] N. Doğan, R. Topkaya, H. Subaşi, Y. Yerli, and B. Rameev, "Development of Halbach magnet for portable NMR device," *Journal of Physics: Conference Series*, 153. 012047, 2009.

[9] C. W. Windt, H. Soltner, D. Dusschoten, and P. Blümler, "A portable Halbach magnet that can be opened and closed without force: The NMR-CUFF," *Journal of Magnetic Resonance*, vol. 208, pp. 27-33, 2011.

[10] H. Raich and P. Blümler, "Design and construction of a dipolar Halbach array with a homogeneous field from identical bar magnets: NMR Mandhalas," *Concepts in Magnetic Resonance Part B: Magnetic Resonance Engineering*, vol. 23, pp. 16-25, 2004.

[11] B. Hills, K. Wright, and D. Gillies, "A low-field, low-cost Halbach magnet array for open-access NMR," *Journal of Magnetic Resonance*, vol. 175, pp. 336-339, 2005.

[12] J. Chen and C. Xu, "An improved discrete configuration of a cylinder magnet for portable nuclear magnetic resonance instruments," *Journal of Applied Physics*, vol. 101, pp. 123926-123926, 2007.

[13] J. Kennedy and R. Eberhart, "Particle swarm optimization," *IEEE International Conference of Neural Networks*, Perth, Australia, pp. 1942-1948, 1995.

[14] M. AlRashidi and M. El-Hawary, "A survey of particle swarm optimization applications in electric power systems," *IEEE Trans. Evolutionary Computation*, vol. 13, pp. 913-918, 2009.

[15] J. Park, Y. Jeong, J. Shin, and K. Lee, "An improved particle swarm optimization for nonconvex economic dispatch problems," *IEEE Trans. Power Systems*, vol. 25, pp. 156-166, 2010.

[16] G. Moresi and R. Magin, "Miniature permanent magnet for table‐top NMR," *Concepts in Magnetic Resonance Part B: Magnetic Resonance Engineering*, vol. 19, pp. 35-43, 2003.

[17] H. Soltner and P. Blümler, "Dipolar Halbach magnet stacks made from identically shaped permanent magnets for magnetic resonance," *Concepts in Magnetic Resonance Part A*, vol. 36, pp. 211-222, 2010.

[18] Y. Y. Cheng, T. Hai, Y. B. Zheng, B. L. Li, and L. Xia, "Optimization and design of multi-ring pole pieces for small-sized permanent magnetic resonance imaging magnet," *Applied Computational Electromagnetics Society Journal*, vol. 33, no. 9, pp. 1026-1033, 2018.

[19] Y. Cheng, L. Xia, W. He, M. Zhu, and F. Liu, "Improved Halbach magnets by particle swarm optimization for mobile nuclear magnetic resonance systems," *in Ninth International Conference on Natural Computation, IEEE*, pp. 798-802, 2013.

[20] S. Anferova, V. Anferov, J. Arnold, E. Talnishnikh, M. A. Voda, K. Kupferschläger, P. Blümler, C. Clauser, and B. Blümich, "Improved Halbach sensor for NMR scanning of drill cores," *Magnetic resonance imaging*, vol. 25, pp. 474-480, 2007.

[21] C. Z. Cooley, J. P. Stockmann, B. D. Armstrong, M. Sarracanie, M. H. Lev, M. S. Rosen, and L. L. Wald, "Two‐dimensional imaging in a lightweight portable MRI scanner without gradient coils," *Magnetic Resonance in Medicine*, vol. 73, pp. 872-883, 2014.

Yi-Yuan Cheng was born in Henan, China, in 1985. She received her B.E. degree in Biomedical Engineering from South-Central University for Nationalities, Wuhan, China, in 2008, and received Ph.D. degree in Biomedical Engineering from Zhejiang University, Hangzhou, China, in 2015. She is currently working as a Lecturer in the Department of Mechanical and Electrical Engineering in Nanyang Normal University, Nanyang, China. Her main research interests include MRI, design and optimization of magnet, artificial intelligence and so on.

Ming-Yang Su was born in Henan, China, in 1984. He received his Bachelor degree of Engineering from Qingdao University of Science and Technology, Qingdao, China, in 2006 and Master degree from Qingdao University of Science and Technology in 2010. He is currently working as a Lecturer in Henan Polytechnic Institute, Nanyang, China. His main interests in materials research.

Tao Hai was born in Henan, China, in 1974. He received his Ph.D. degree in Signal and Information Processing from Harbin Engineering University, Harbin, China. He is currently working as a Lecturer in the Department of Mechanical and Electrical Engineering in Nanyang Normal University, Nanyang, China. His main research interests include signal processing, image processing and so on.

Ming Hui was born in Henan, China, in 1983. He received his Ph.D. degree in Communication and Information System from Ningbo University, Ningbo, China, in 2013. He is currently working as an Associate Professor in the Department of Physics and Electrical Engineering in Nanyang Normal University, Nanyang, China. His main research interests include the design of high efficiency RF power amplifier and the linearization technology.

Bao-Lei Li was born in Henan, China, in 1987. He received his Ph.D. degree in Information and Communication Engineering from Yunnan University, Kunming, China. He is currently working as a Lecturer in the Department of Physics and Electrical Engineering in Nanyang Normal University, Nanyang, China. His main research interests include intelligent optimization algorithm, path planning and so on.

Ling Xia was born in Zhejiang, China, in 1965. He received his B.E. degree in Automation and Ph.D. degree in Biomedical Engineering from Zhejiang University, Hangzhou, China. He is currently working as a Professor in the Department of Biomedical Engineering in Zhejiang University, Hangzhou, China. His main research interests include MRI key technical issues, biological effects of electromagnetic fields, Physiological simulation and modeling and so on.

Passive Fractal Chipless RFID Tags Based on Cellular Automata for Security Applications

Mohammad N. Zaqumi [1], Jawad Yousaf [2], Mohamed Zarouan [1], Mohammed A. Hussaini [3], and Hatem Rmili [1,*]

[1] King Abdulaziz University, Department of Electrical and Computer Engineering, Jeddah 21589, Saudi Arabia
*hmrmili@kau.edu.sa

[2] Department of Electrical, Computer and Biomedical Engineering, Abu Dhabi University, United Arab Emirates
jawad.yousaf@adu.ac.ae

[3] Universiti Kuala Lumpur – British Malaysian Institute, Gombak 53100, Selangor, Malaysia

Abstract — In this paper, we propose a novel design of low-profile fractal chipless tags with unique specific electromagnetic responses. The tags are designed using cellular automata (Game of Life) technique to ensure the randomness of the generated fractal tags. The tags are simulated in CST Microwave Studio for the frequency range of 2 to 10 GHz. The tags are realized on FR4 substrate and their radar cross-section (RCS) characteristics are analyzed for the nine different tags for the three different polarizations (horizontal, vertical, and oblique). Each tag shows a unique signature resonance response. The obtained results of coding capacity (16-20 bits), coding spatial capacity (1-1.25 bits/cm^2), coding spectral capacity (2.15-2.9 bits/GHz), and coding density (0.15-0.18 bits/GHz x cm^2) of realized tags are very good. The presented tags could be used for the development of secure RFID systems.

Index Terms — Cellular automata, chipless RFID, fractal tags, game of life.

I. INTRODUCTION

Radiofrequency identification (RFID) tags are the backbone of the Internet of Things (IoT). These tags are also widely used in supply chain (inventory management, shipment tracking, etc.), biomedical, document security, and various civil and military applications [1-3]. Chipless RFID tags emerged as a low-cost solution because of their miniaturized size and no need for battery-powered components. The security of the data transfer has been a vital issue in RFID. Therefore, the exchange of information using RFID must be protected from hackers to ensure the safe usage of RFID in the aforementioned applications [4, 5].

Passive fractal chipless RFID tags have gained a lot of interest recently for wireless data transmission. Fractal tags exhibit interesting characteristics of multiband operation and broadband resonances in a limited size as well as good radiation characteristics, as compared to conventional non-fractal large size chipless tags [1, 6-8]. The broadband resonance characteristics in small size enhance the surface coding density of fractal tags.

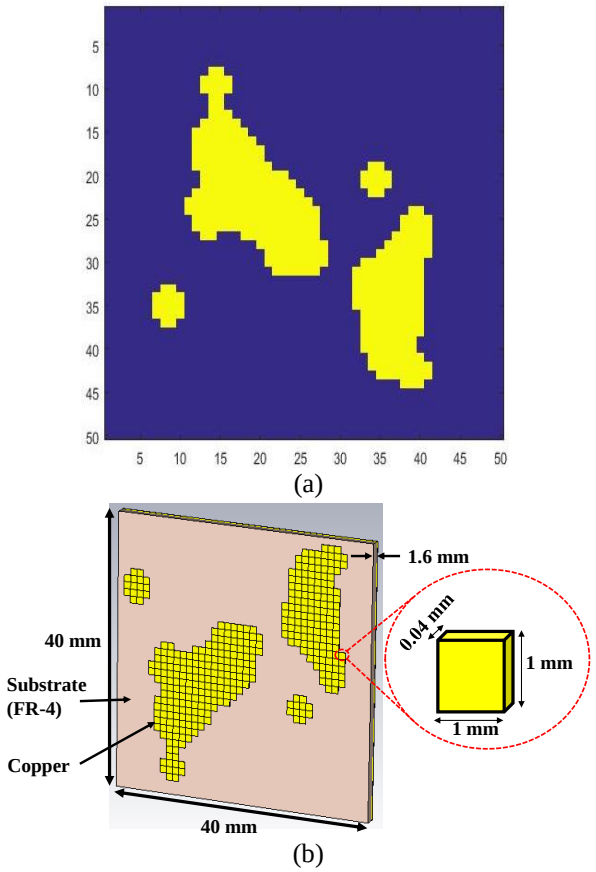

Fig. 1. (a) 2D form of game of life in Matlab; (b) CST structure of applied game of life on the chipless RFID tag.

Submitted On: April 4, 2021
Accepted On: May 16, 2021

https://doi.org/10.47037/2020.ACES.J.360510

The unique wideband resonance characteristics of irregular RFID tags which are used for the accurate detection of the tag, cannot be recognized by traditional readers. These interesting features of fractal tags make them a superior candidate for the security and safety applications such as authorized access control, counterfeiting, weapons recognition, passport system at airports, classified documents, currency notes, and cheques identifications; along with other wide range of conventional RFID applications [1, 2, 4-7].

For the non-fractal tags, the coding capacity (# of bits) and density are dependent on the number of the resonators in the tags. Although utilization of the bi-statics (dual polarization) measurements data and hybrid encoding procedure in the conventional (patch, split ring, slot, *etc*. [9-12]) resonators-based frequency domain (FD) tags could enhance their encoding capacities. However, for higher coding density, large size tags are required to increase the number of resonators in tags.

Many studies are available in the literature on the design of fractal RFID tags. Sultan implemented the polygon fractal loops for the UHF RFID applications [1]. Padmini *et al.* [7] presented the simulation-based design of Vicsek square fractal (square shape) passive tags. The findings of [7] suggested that the second iteration design of the Vicsek fractal provides better resonance characteristics for the detection of the designed tag. The authors in [8] used the micro-genetic algorithm (m-GA) for the shape optimization of the passive fractal RFID tags based on self-similar fractal line and patch. The Hilbert-curve fractal space-filling technique is used for the designing of the card-type dual-band loop tag for HF and UHF RFID applications in [9]. Rmili *et al.* [13] reported the fractal-jet fluid patch type chipless RFID-tag for security applications and suggested that encoding density of fractal tags can be enhanced by analyzing the both magnitude and phase of the reflection coefficient of the tag. Mouse *et al*. [14] proposed the simulation-based microstrip open resonator-based tags with two orthogonal fractal antennas for short-range RFID applications. The space-filling (Peano and Hilbert curved) based tags are reported in [15].

In this study, we propose a novel design of low-profile fractal chipless tags with specific electromagnetic responses that can be used for secure RFID systems. We investigate the design of new chipless tags based on the cellular automata (Game of Life) concept. We have considered a regular patch which we have modified by applying a sequence of programming procedures based on the cellular automata concept as illustrated in Fig. 1. The electromagnetic signature of RFID chipless tag and cellular automata geometries are usually self-similar and offer the possibility to increase the resonating length inside a limited area. We have obtained 100 tags with different structures of random square-shaped patches, which we have analyzed numerically by determining their radar cross-section (RCS) when illuminated with an incident electromagnetic wave within the range of 2-10 GHz. Computer Simulation Technology (CST) software was used for the numerical analysis of the tags. The selected designed structures out of 100 were then analyzed in terms of the capacity of coding by determining their coding density and RCS characteristics.

II. DESIGN OF TAGS USING CELLULAR AUTOMATA

A. Cellular automata and Game of Life (GoL)

The term cellular automata is plural and cellular automaton is its singular form. The concept was proposed by Stanislaw Ulam and John von Neumann in the 1940s [16]. The cellular automata is used in building a system of a large number of objects with varying states over time [17]. Cellular automata (cellular automaton singular) originates from automata theory in model computation, which is discrete [16]. A cellular automaton constitutes a grid of cells in which each cell exhibits a finite number of states (alive or dead). The states of each cell are changed, after defining its initial condition at time $t = 0$, depending on the characteristics of its neighboring cell through a set of rules [16].

The concept was evolved by Conway in the 1970s in terms of two-dimensional cellular automaton which was referred to as Game of Life (GoL) [18]. In GoL, the size of the neighborhood cells increases for the design of more random and complex applications. Initially, the Game of life appeared as an article in Scientific American in 1970 and soon has applied in the display of LEDs, screens, projection surfaces, and so on [18]. The main principles of the Game of life are directly related to simulation of the natural world with code such as creating a simulation that illustrates the characteristics and behaviors of biological systems of reproduction. Opposite to Von Neumann that generated an extremely complex system of states and rules, Conway wanted to get a similar “lifelike” result applying the simplest set of rules possible. The concept of Game of Life is applied in this study for the design of random fractal RFID tags.

B. Tag designs

Figure 1 shows the application of Game of life, which was firstly applied in Matlab as a 2D image. Figure 1 (a) shows a Matlab image of random cells in 2D form. The Matlab was linked to CST. Firstly, an application interface for CST-Matlab is required for applying the game of life. Once the game of life is

created as a 2D image in Matlab. Then the game of life will be executed in CST and the result will be as a 3D shape utilizing the API for CST-Matlab. The following notes are detailed steps for generating the game of life in the CST and Matlab.

- A full pack of an Application Interface (API) for CST-Matlab is available.
- Create/develop the game of life algorithm in Matlab.
- Generate/produce a 2D image of the game of life in Matlab.
- Create/develop the final sequence of code for chipless RFID tag and code for generation of the 2D image of the game of life in Matlab, then connect them with the CST in the presence of API for CST-Matlab.
- After the RFID tags are obtained in the CST thus perform simulation and further investigation in the CST for each generated tag.
- Select the best tags regarding their coding capacity or coding density.

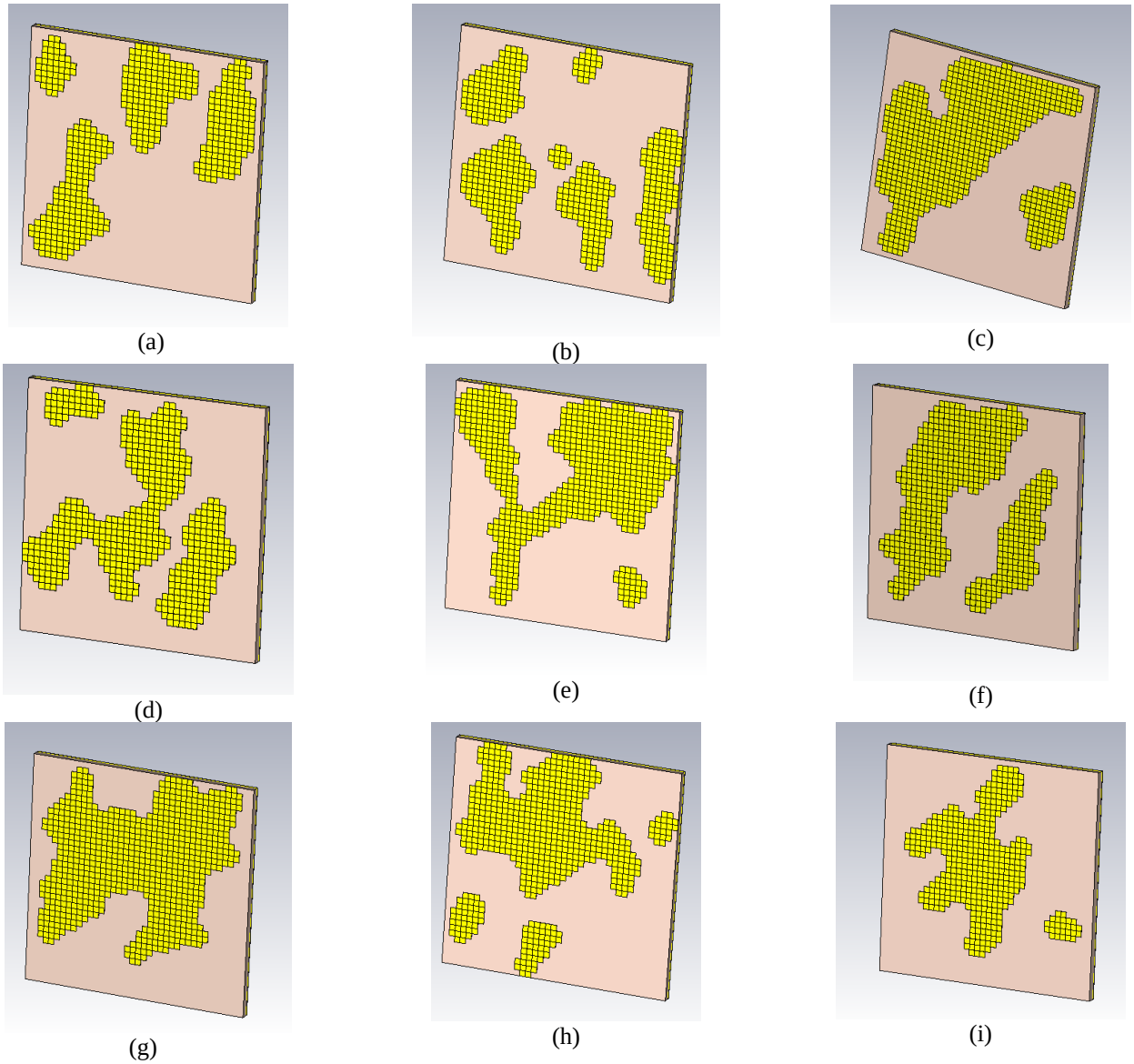

Fig. 2. CST structure of applied Game of life on the Chipless RFID tags: (a) Tag 1; (b) Tag 2; (c) Tag 3; (d) Tag 4; (e) Tag 5; (f) Tag 6; (g) Tag 7; (h) Tag 8; (i) Tag 9.

Figure 1 (b) illustrates the implementation of Game of life on the tag in CST. Each tag cell has dimensions of 1 mm x 1 mm with a thickness of 0.04 mm. The random shape of the metallic copper tag is etched on an FR4 substrate having a thickness of 1.6 m. The dimensions of the used FR4 substrate are 40 mm x 40 mm x 1.6 mm. The dimensions of all parameters of the realized tags are depicted in Table 1.

The geometries of the studied tags are illustrated in Fig. 2. The first structure (Fig. 2 (a)) is obtained next to the first iteration where the game of life is applied to the main structure. Additionally, the second, third, and fourth structure is obtained using the game of life from cellular automata. By repeating the same procedure, we obtain more structures with randomly shaped RFID tags utilizing the game of life as shown in Fig. 2. One hundred (100) such structures were realized and simulated in CST MWS. However, only a few structures of Fig. 2 are discussed here which shows good performance in terms of sensitivity and higher coding density as compared to other structures.

Table 1: Dimension of the realized tags

Parameter	Dimension
Substrate Dimensions	40 mm x 40 mm
Substrate thickness	1.6 mm
Substrate Dielectric constant	4.3 [F/m]
Conductor thickness	0.04 mm

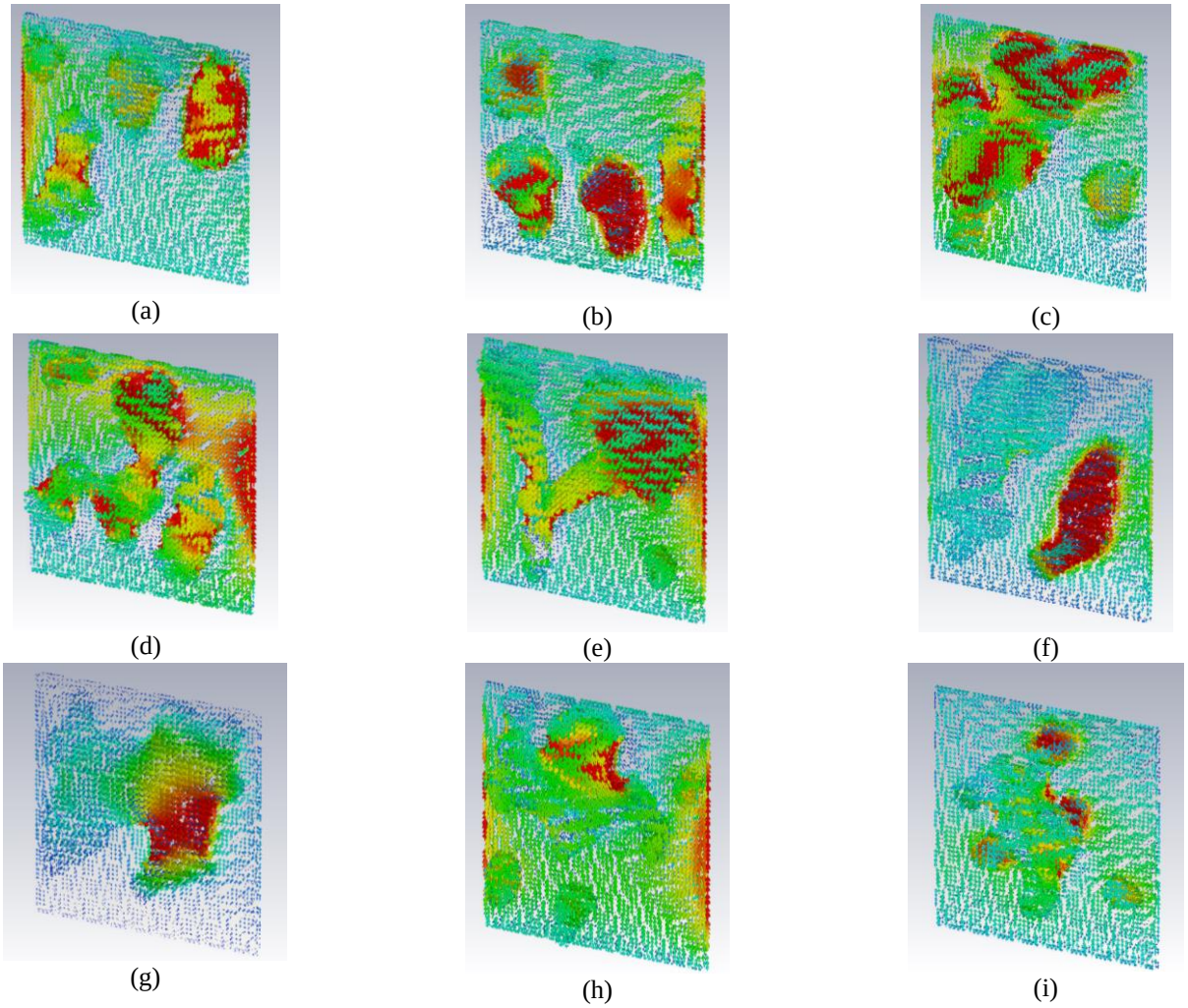

Fig. 3. Surface current distribution of realzied Chipless RFID tags in vertical polarization: (a) Tag 1 at f = 3.79 GHz, J_{max} = 0.219 A/m; (b) Tag 2 at f = 4.09 GHz, J_{max} = 0.258 A/m; (c) Tag 3 at f = 5.84 GHz, J_{max} = 0.134 A/m; (d) Tag 4 at f = 5.07 GHz, J_{max} = 0.162 A/m ; (e) Tag 5 at f = 3.42 GHz, J_{max} = 0.205 A/m; (f) Tag 6 at f = 2.72 GHz, J_{max} = 0.299 A/m; (g) Tag 7 at f = 2.25 GHz, J_{max} = 0.275 A/m; (h) Tag 8 at f = 3.34 GHz, J_{max} = 0.241 A/m; (i) Tag 9 at f = 7.9 GHz, J_{max} = 0.093 A/m.

The passive chipless RFID tag is excited with plane waves which induce the particular surface current distribution on the tag according to its structure. The analysis is performed for the frequency range of 2 to 10 GHz. The detection procedure of the passive chipless RFID tag is based on the analysis of the unique signature resonances in the received broadband backscattered signal from the designed tag at the RFID reader [7-9]. The presence of a large number of multiband resonances in the reflected signal from the fractal tag geometries provides additional security features to these tags compared to conventional chipless RFID tags [1-4]. The RCS characteristics are numerically investigated for each tag for three different polarization of horizontal, vertical, and oblique respectively.

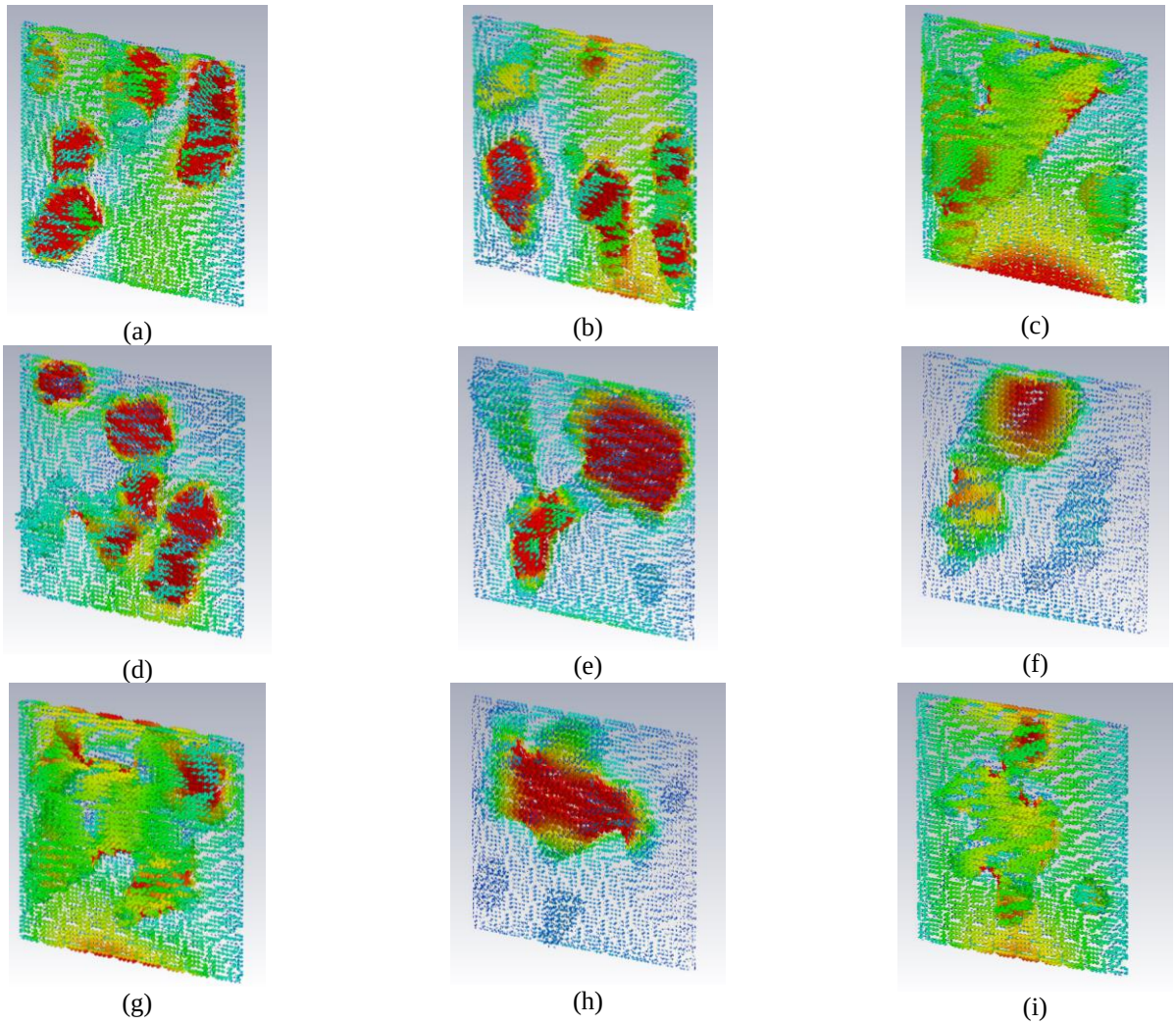

Fig. 4. Surface current distribution of realzied Chipless RFID tags in horizontal polarization: (a) Tag 1 at f = 7.26 GHz, J_{max} = 0.046 A/m; (b) Tag 2 at f = 5.79 GHz, J_{max} = 0.119 A/m; (c) Tag 3 at f = 3.94 GHz, J_{max} = 0.139 A/m; (d) Tag 4 at f = 6.03 GHz, J_{max} = 0.169 A/m; (e) Tag 5 f = 3.50 GHz, J_{max} = 0.157 A/m; (f) Tag 6 at f = 3.55 GHz, J_{max} = 0.127 A/m; (g) Tag 7 at f = 4.45 GHz, J_{max} = 0.118 A/m; (h) Tag 8 at f = 2.14 GHz, J_{max} = 0.234 A/m; (i) Tag 9 at f = 5.78 GHz, J_{max} = 0.046 A/m.

III. RESULTS AND DISCUSSION

A. Surface current distribution analysis

The surface current distributions of nine selected tags at their selected respective resonance frequencies in vertical polarization are depicted in Fig. 3. The distributions of Fig. 3 are obtained at the frequencies where the minimum RCS values were recorded for each tag. The current distribution results are plotted for the resonance frequencies of 3.79 GHz, 4.09 GHz, 5.84 GHz, 5.07 GHz, 3.42 GHz, 2.72 GHz, 2.25 GHz, 3.34 GHz, and 7.9 GHz for Tag 1, Tag 2, Tag 3, Tag 4, Tag 5, Tag 6, Tag 7, Tag 8, and Tag 9 respectively. Figures

4 and 5 illustrate the current distribution results in the horizontal and oblique polarizations. The obtained results of Figs. 4 and 5 are at their respective resonance frequencies in horizontal and oblique polarization for each tag.

The red color in Figs. 3, 4, and 5 graphs represent highly concentrated surface current areas. It shows the exciting parts of the tags at the selected frequencies. As can be noticed from Fig. 3 (a) that for Tag 1 the maximum value of surface current density at the resonance frequency of 3.79 GHz is 0.219 A/m (in the red portion) in vertical polarization. The maxim value of J_{max} for Tag 2 is 0.258 A/m which is obtained at the resonance frequency of 4.09 GHz. The metallic islands of the tags resonate at different frequencies depending on their size compared to the wavelength.

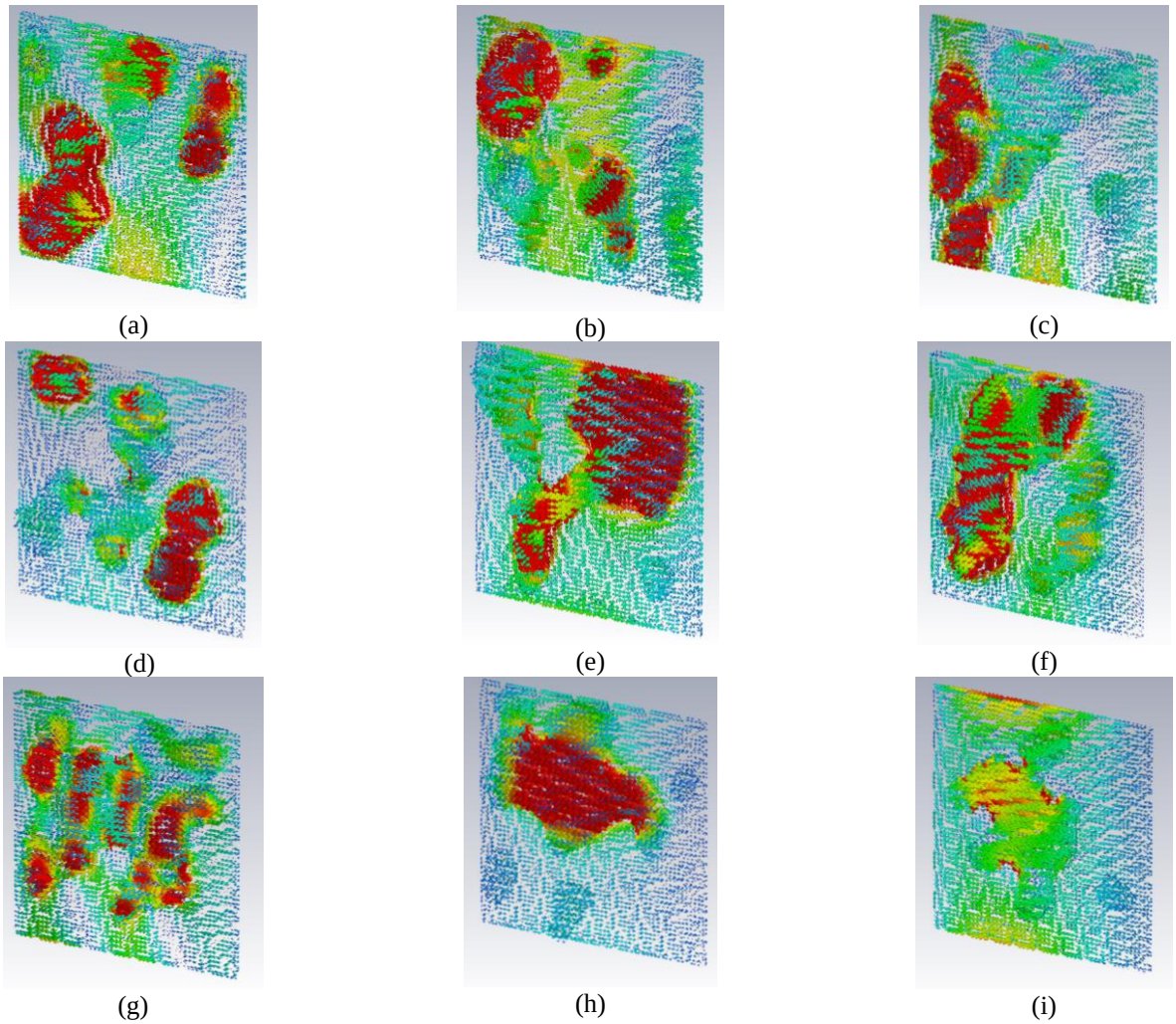

Fig. 5. Surface current distribution of realzied Chipless RFID tags in oblique polarization: (a) Tag 1 at f = 6.95 GHz, J_{max} = 0.066 A/m; (b) Tag 2 at f = 7.17 GHz, J_{max} = 0.087 A/m; (c) Tag 3 at f = 9.89 GHz, J_{max} = 0.051 A/m; (d) Tag 4 at f = 6.66 GHz, J_{max} = 0.131 A/m; (e) Tag 5 f = 3.54 GHz, J_{max} = 0.109 A/m; (f) Tag 6 at f = 5.67 GHz, J_{max} = 0.137 A/m; (g) Tag 7 at f = 9.69 GHz, J_{max} = 0.046 A/m; (h) Tag 8 at f = 2.14 GHz, J_{max} = 0.173 A/m; (i) Tag 9 at f = 3.86 GHz, J_{max} = 0.149 A/m.

The tags resonance frequency changes with the change in the polarization to horizontal and oblique. This can be noticed from the current distribution's maps of Figs. 4 and 5 for each tag. Tag 1 resonance frequency changes to 7.26 GHz and 6.95 GHz in horizontal and oblique polarization respectively. This changes the spreading of current around the metallic parts of the tag as can be noticed from Figs. 4 (a) and 5 (a) respectively for Tag 1. The current distribution of Tag 1 in horizontal and oblique polarization is quite different than its distribution in vertical polarization. Similar observations can be made for the Tags 2-9 by comparing their current distributions from Figs. 3-5 respectively.

This change in the current distribution depending on the fractal irregular shape of tags produce different unique RCS characteristics of each tag in each analyzed polarization.

B. RCS analysis

Figure 6 shows the RCS results of the nine realized tags for horizontal, vertical, and oblique polarizations. For Tag 1 from Fig. 6 (a), the resonant frequencies dips can be noticed at 4.25 GHz, 5.6 GHz, 5.84 GHz, 6.86 GHz, 7.26 GHz, and 8.67 GHz in horizontal polarization, at 2.98 GHz, 3.79 GHz, 4.27 GHz, 7.62 GHz, and 9.11 GHz in vertical polarization, and at 3.26 GHz, 4.24 GHz, 6.22 GHz, 6.95 GHz, 8.95 GHz, 9.09 GHz, and 9.58 GHz in oblique polarization respectively. Similar observations can be made for other realized tags in Fig. 2.

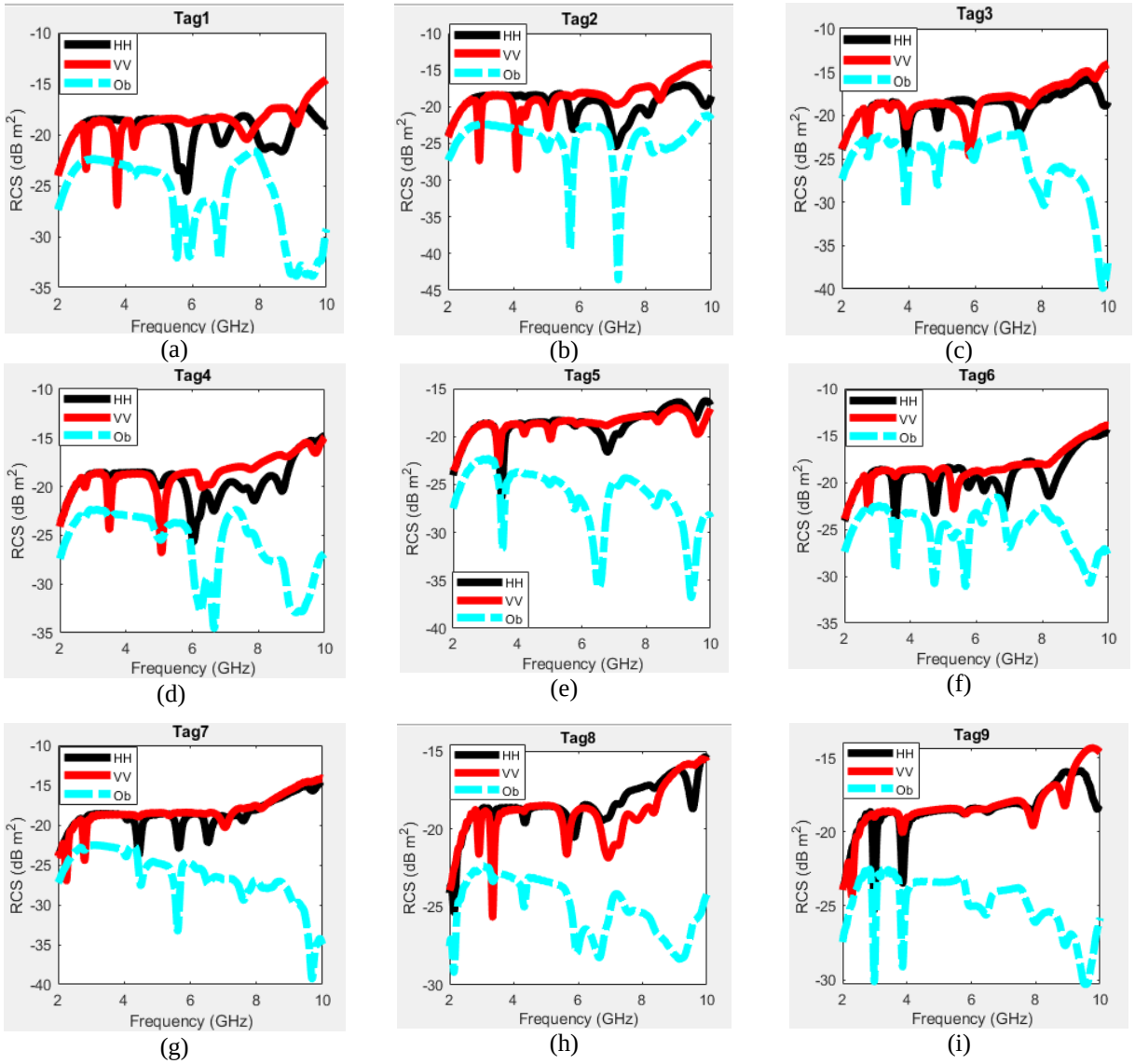

Fig. 6. RCS results of realzied Chipless RFID tags: (a) Tag 1; (b) Tag 2; (c) Tag 3; (d) Tag 4; (e) Tag 5; (f) Tag 6; (g) Tag 7; (h) Tag 8; (i) Tag 9.

Table 2 summarizes all resonance frequencies of all investigated tags of Fig. 2. We observe that each tag has its unique resonance characteristics in all three polarizations. The number of horizontal, vertical, and oblique polarization resonant frequencies changes for each realized tag. These resonance characteristics represent the different signatures of each fractal tag which can be used for its identification. The change in the fractal geometry of the tags due to the applied game of life concept ensures the randomness of the tags. This

results in unique current distribution on the metallic structure of the tag for the incident plane wave as can be noticed in Figs. 3, 4, and 5. Thus, a unique signature resonance response of each tag is obtained as can be observed from the signature resonance frequencies of each Tag in Table 2.

Table 3 compares the performance of analyzed tags in terms of the overall operating frequency range, coding capacity (bits), coding spatial capacity (bits/cm^2), coding spectral capacity (bits /GHz), and coding density (bits/GHz x cm^2). The overall operational frequency range of Tag 1 is 2.98 to 9.58 GHz (the range in which maximum resonance frequencies are recorded). There is a total of 18 resonance frequencies for these tags in three analyzed polarization which represent its 18-bit coding capacity. The observed coding spatial capacity, coding spectral capacity, and coding density for Tag 1 are 1.125 bits/ cm^2, 2.727 bits /GHz, and 0.17 bits/ GHz x cm^2 respectively. Similar observations can be made for other tags in Table 3. All investigated tags have a coding spatial capacity of more than 1 bit/cm^2 while the values of coding spectral capacity are greater than 2 bits/GHz for all tags. Among the analyzed tags, the highest coding spatial capacity (1.25 bits/cm^2) is recorded for Tags 4 and 8 respectively. The reason for these tags' superior performance is the availability of higher backscattered resonance frequencies from their randomized metallic structure based on GOL as compared to other tags. Tag 4 also outperforms all other tags in terms of coding spectral capacity (2.861 bits/GHz) and coding density (0.178 bit/GHz x cm^2). The summary of Table 3 reflects that the overall performance of the presented tags is very good in terms of the analyzed critical parameters of Table 3.

Table 2: Resonance frequency in (GHz) of characteristics of realized Chipless RFID tags of Fig. 2 and Fig. 6

	Polarization		
Tag #	**HH**	**VV**	**Oblique**
1	4.25, 5.6, 5.84, 6.86, 7.26, 8.67	2.98, 3.79, 4.27, 7.62, 9.11	3.26, 6.22, 6.95, 4.24, 8.95, 9.09, 9.58
2	5.79, 5.05, 7.11, 9.85, 8.07	2.95, 4.09, 4.33, 5.05, 7.11, 8.44	5, 5.71, 7.17, 8.22
3	2.77, 3.94, 3.42, 4.89, 6.03, 7.34, 9.88	2.78, 3.43, 3.94, 5.84, 7.65, 9.624	2.78, 3.92, 4.87, 5.99, 8.08, 9.89
4	2.76, 3.49, 5.03, 6.03, 6.65, 7.88, 8.70	2.76, 3.50, 5.07, 6.29, 7.76 8.84, 9.74	2.75, 3.50, 5.02, 6.26, 6.66, 9.14
5	3.50, 5.78, 6.78, 8.34, 9.51	3.42, 4.22, 5.03, 8.38, 9.61	3.54, 5, 5.78, 6.50, 7.14, 8.30, 9.39
6	2.71, 3.55, 4.73, 5.75, 6.23, 6.84, 8.19	2.72, 3.54, 4.70 5.33	2.74, 3.54, 4.72, 5.67, 5.29 6.18, 6.97, 9.44
7	2.78, 4.45, 5.67, 6.54, 7.62, 9.69	2.25, 2.8, 7.05, 8.14	4.06, 4.50, 5.62, 6.53, 7.61, 9.69
8	2.14, 3.33, 4.34, 5.88, 6.75, 8.38, 9.57	2.92, 3.34, 4.32, 5.65, 6.93, 7.26, 7.84, 8.35	2.14, 3.34, 4.32, 5.97, 6.66, 9.17
9	2.99, 3.86, 5.78, 6.52, 7.89, 9.91	2.29, 2.99, 3.86, 5.8, 7.90, 8.89	2.98, 3.86, 5.95, 6.45, 7.96, 8.92, 9.54

Table 3: Comparison of different characteristics of the realized nine Tags

Tag #	**Frequency Range (GHz)**	**Coding Capacity (bits)**	**Coding Spatial Capacity (bits/cm^2)**	**Coding Spectral Capacity (bits/GHz)**	**Coding Density (bits/GHz x cm^2)**
1	2.98-9.58	18	1.125	2.727	0.17
2	2.95-9.58	16	1	2.413	0.15
3	2.77-9.89	19	1.188	2.668	0.166
4	2.75-9.74	20	1.25	2.861	0.178
5	3.42-9.51	17	1.063	2.791	0.174
6	2.71-9.44	19	1.188	2.823	0.176
7	2.25-9.69	16	1	2.15	0.134
8	2.14-9.57	20	1.25	2.691	0.168
9	2.29-9.54	19	1.188	2.620	0.164

The uniqueness of the presented tags is the random fractal structure of each obtained tag. This provides additional security features to the presented tags as their characteristics cannot be decoded using a conventional RFID scanner or readers.

IV. CONCLUSION

This study has presented a novel design of fractal chipless RFID tags which were realized using the cellular automata concept for the secure RFID systems. The results of nine tags, out of realized 100 tags, are discussed. The obtained results show the unique signature random EM characteristics of each realized tag, adding additional security features to the presented chipless tags. The presented tags show good results in terms of coding capacity (16-20 bits), coding spatial capacity (1-1.25 bits/cm^2), coding spectral capacity (2.15-2.9 bits /GHz), and coding density (0.15-0.18 bits/GHz x cm^2). The presented tags could be used for potential applications in document security, bank cheques along other applications in IoT devices.

ACKNOWLEDGMENT

This project was funded by the Deanship of Scientific Research (DSR), King Abdulaziz University, under Grant No. (RG-39-135-40). The authors gratefully acknowledge technical and financial support of KAU.

REFERENCES

[1] Q. H. Sultan and A. M. Sabaawi, "Design and implementation of improved fractal loop antennas for passive UHF RFID tags based on expanding the enclosed area," *Progress In Electromagnetics Research C*, vol. 111, pp. 135-145, 2021.

[2] M. Borgese, S. Genovesi, G. Manara, and F. Costa, "Radar cross section of chipless RFID tags and BER performance," *IEEE Transactions on Antennas and Propagation*, vol. 69, no. 5, pp. 2877-2886, 2021.

[3] A. Ramos, Z. Ali, A. Vena, M. Garbati, and E. Perret, "Single-layer, flexible, and depolarizing chipless RFID tags," *IEEE Access*, vol. 8, pp. 72929-72941, 2020.

[4] V. Mulloni and M. Donelli, "Chipless RFID sensors for the internet of things: Challenges and opportunities," *Sensors*, vol. 20, no. 7, p. 2135, 2020.

[5] D. Dobrykh, I. Yusupov, S. Krasikov, A. Mikhailovskaya, D. Shakirova, A. Bogdanov, A. Slobozhanyuk, D. Filonov, and P. Ginzburg, "Long-range miniaturized ceramic RFID tags," *IEEE Transactions on Antennas and Propagation*, pp. 1-1, 2020.

[6] H. Rmili, D. Oueslati, I. B. Trad, J. M. Floch, A. Dobaie, and R. Mittra, "Investigation of a random-fractal antenna based on a natural tree-leaf geometry," *Inter. J. of Ant. and Propag.*, vol. 2017, p. 7, Art. no. 2084835, 2017.

[7] E. Pazmiño, J. Vásquez, J. Rosero, and D. Pozo, "Passive chipless RFID tag using fractals: A design based simulation," in *2017 IEEE Second Ecuador Technical Chapters Meeting (ETCM)*, pp. 1-4, 2017.

[8] Y. Watanabe, H. J. I. J. o. A. E. Igarashi, and Mechanics, "Shape optimization of chipless RFID tags comprising fractal structures," vol. 52, no. 1-2, pp. 609-616, 2016.

[9] M. Alibakhshi-Kenari, M. Naser-Moghadasi, R. A. Sadeghzadeh, B. S. Virdee, and E. Limiti, "Dual-band RFID tag antenna based on the Hilbert-curve fractal for HF and UHF applications," *IET Circuits, Devices & Systems*, vol. 10, no. 2, pp. 140-146, 2016.

[10] H. Huang and L. Su, "A compact dual-polarized chipless RFID tag by using nested concentric square loops," *IEEE Antennas and Wireless Propagation Letters*, vol. 16, pp. 1036-1039, 2017.

[11] D. Girbau, J. Lorenzo, A. Lazaro, C. Ferrater, and R. Villarino, "Frequency-coded chipless RFID tag based on dual-band resonators," *IEEE Antennas and Wireless Propagation Letters*, vol. 11, pp. 126-128, 2012.

[12] A. Ferchichi, N. Sboui, A. Gharsallah, and H. Baudrand, "New antennas based on triangular patch as a solution for RFID application," *Applied Computational Electromagnetics Society Journal*, vol. 25, no. 3, pp. 199-205, 2010.

[13] H. Rmili, D. Oueslati, L. Ladhar, and M. Sheikh, "Design of a chipless RFID tags based on natural fractal geometries for security applications," *Microwave and Optical Technology Letters*, vol. 58, no. 1, pp. 75-82, 2016/01/01 2016.

[14] M. E. Mousa, H. H. Abdullah, and M. E. d. A. El-Soud, "Compact chipless RFID tag based on fractal antennas and multiple microstrip open stub resonators," in *2018 Prog. in Elect. Res. Symp. (PIERS-Toyama)*, pp. 1332-1338, 2018.

[15] J. McVay, A. Hoorfar, and N. Engheta, "Space-filling curve RFID tags," in *2006 IEEE Radio and Wireless Symposium*, pp. 199-202, 2006.

[16] B. Chopard and M. Droz, *Cellular Automata*. Springer, 1998.

[17] S. Wolfram, "Cellular automata as models of complexity," *Nature*, vol. 311, no. 5985, pp. 419-424, 1984.

[18] J. Conway, "The game of life," *Scientific American*, vol. 223, no. 4, p. 4, 1970.

Design of Rectangular Dielectric Resonator Antenna for Mobile Wireless Application

Chaitanya Bethala and Manjunatha Chari Kamsali

EECE Department, GITAM University, Hyderabad 502329, Telangana, India
cbethala@gitam.edu, mkamsali@gitam.edu

Abstract – In this article, a pentaband rectangular DRA is explored and presented. The proposed antenna has a crescent-shaped radiating element with defected ground structure and it is feed by 50-Ω microstrip line. The RDRA invariably has two similar dielectric resonators made up of RT5870 is positioned on top of the crescent-shaped patch. With the use of a dielectric resonator, the proposed structure has good improvement in impedance bandwidth and gain. The proposed rectangular DRA has penta operating frequency bands with resonant frequency at 1.49 GHz, 2.00 GHz, 2.50 GHz, 5.49 GHz, and 7.75 GHz. The projected structure exhibits the broadside radiation pattern with the maximum gain and directivity of 4 dBi and 4.5 dBi, respectively. The gig of the projected RDRA is validated with the help of simulated results by CST software. The observed results of the proposed antenna indicate that it can be a potential candidate for GPS, PCS, UMTS, ISM, WLAN, Wi-MAX applications.

Index Terms – GPS, ISM, mobile, rectangular DRA, RT5780, wireless application, WLAN.

I. INTRODUCTION

In the last two decades, the demand for multiband antennas has increased because of the rapid increase in wireless communication and miniaturization of wireless devices [1-3]. To properly equip with the modern wireless device requirement, there is a high demand for the new antenna technology. Multiband antenna is the new antenna technology that plays a vital role in satisfying the need for modern wireless communication systems. The multiband is achieved with the needed help of a wide variety of practical techniques such as defected ground structure, meandering the patches, introduction of slots, metamaterial [4-8], and DRA [9-12]. Because of the high radiation efficiency and compactness without any losses, the Dielectric Resonator antenna (DRAs) has naturally attracted more antenna researchers.

For Modern wireless communication systems, the DRA is the Competent antenna technique because of its advantage, such as large bandwidth, decreased production cost, and fabrication difficulty. The relative dielectric permittivity used in DRA, its shape, size, and operating modes [11-13] decides the DRA's resonant frequency. It is excited by various feeding structures with the help of coupling. When low permittivity is used, the DRA will be larger, while that is not the case in high permittivity dielectric. Various shapes are reported in the literature for the DRA, like rectangular, Cylindrical, and hemispherical. Compact DRA [14-16]is designed with the help of printing the conducting material on the dielectric, but the resonant frequency and the bandwidth are highly reduced. The impedance bandwidth can be enhanced by placing the DRA on a patch [17,18]. The major challenge for design the antenna for modern wireless communication is its multiband operation along with compact size, the resonator shapes decide the reasoning band, and radiation pattern will be changed [19]. Various unique geometries [20] are proposed for the DRA, such as triangular, conical, and biconical, to enhance the antenna's bandwidth. Stacking [21-24] two DRAs results in an improvement in impedance bandwidth. In [25], cross-shaped DRA with coaxial feed and a metal strip is proposed for wideband circular polarized performance. In [26], a dual circular polarized band is achieved by incorporating the metal strip at the sides of the DRA, and the bandwidth enhancement with the help of parasitic patches on DRA is proposed in [27]. Still, the major drawback is the low-profile nature of DRA is not maintained, and there is an increase in fabrication difficulty. In [28], two layers of sapphire is used as a dielectric resonator to achieve dual-band. The gain improvement is achieved with the metamaterial superstrate, which is reported in [29]. In [30], MIMO DRA is proposed for UWB application. In [31], dual-band DRA is proposed with a ring-shaped DRA made up of alumina, and in [32], H shape DRA is proposed with microstrip feed for triple-band wireless application. In [33], a filtering feed network is proposed for single wideband operation, and in [34], with the help of metallic strips along with DR, the Penta band DRA is reported. In [35], a triple-band antenna with CPW slotted feed and foam is reported.

In this paper, a multiband Rectangular DRA (RDRA) is proposed for mobile wireless applications [36]. With the help of CST electromagnetic software, the

Submitted On: October 29, 2020
Accepted On: May 9, 2021
https://doi.org/10.47037/2020.ACES.J.360511

optimization of the RDRA is done. The structural complexity of the proposed antenna is very less. The entire structure is fed with a simple microstrip patch antenna. The dielectric resonator [37-39] improves the impedance bandwidth and gain of the proposed structure. The size of the dielectric resonator used is very small and chemical glue is used for bonding. The combination of the simple crescent shape patch along with DRA, makes the proposed DRA as a Hybrid RDRA for wireless radio communication. The anticipated structure has a dimension of 37.5 x 57 x 0.8 mm^3. The proposed rectangular DRA has operating bands 1.38 GHz to 1.70 GHz, 1.90 GHz to 2.09 GHz, 2.36 GHz to 2.87 GHz, 5.18 GHz to 5.93 GHz and 7.61 GHz to 7.88 GHz. Section 2 gives the theory regarding the Design of RDRA, Section 3 & 4 presents the geometry, and DRA experimental results and Section 5 is the conclusion.

II. THEORETICAL FACET OF RDRA

Figure 1 represents the 3-D of Rectangular DRA. The RDRA has a rectangular dielectric resonator of ε_r relative dielectric constant, presents width, b represents the length, and h represents the substantial height of the RDRA. Because of the three geometrical parameters independent of each other, the rectangular DRA offered more design suppleness than a cylindrical-shaped DRA. The Rectangular DRA [40-43] is analyzed with the needed help of a dielectric waveguide model. The $TE_{111,}$ which is the resonant frequency of RDRA, is calculated from the equations shown below [3]:

$$f_o = \frac{C}{2\Pi\sqrt{\varepsilon_r}}\sqrt{k_x^2 + k_y^2 + k_z^2}, \quad (1)$$

$$k_{z=}\frac{\Pi}{a}, \quad (2)$$

$$k_{z=}\frac{\Pi}{2b}, \quad (3)$$

$$d = \frac{2}{k_y}\tanh\left(\frac{k_{yo}}{k_y}\right), \quad (4)$$

$$k_{yo} = \sqrt{k_x^2 + k_y^2}. \quad (5)$$

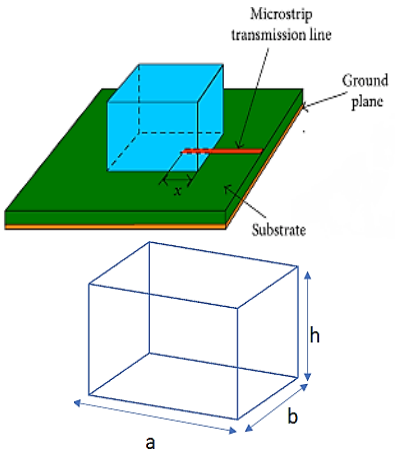

Fig. 1. 3D view of microstrip feed rectangular DRA.

III. RDRA FOR MOBILE WIRELESS APPLICATION

In this paper, a multiband DRA is proposed. In this intricate design, two similar dielectric resonators are placed on a top extreme of the Crescent-shaped patch, which is correctly fed microstrip line of 50-ohm. The various stages of Rectangular DRA are presented in Fig. 2. The proposed structure possesses a defective ground structure with the ground dimension of l_g x w_g x t mm^3. A slot of size l_s x w_s x t mm^3 is etched from the top upper left corner of the ground to make it as defective ground structure. The defective ground structure is created in order to match the impedance at the resonating bands. The Projected DRA structure has four stages of evolution, such as Antenna I, Antenna II, Antenna III, and Antenna IV. In Fig. 3, the back view of Antenna I, II, III, and IV are depicted, and a perspective view in the CST design environment is presented in Fig. 4. The final antenna design, along with its parameters, is shown in Fig. 5, and the parameter values are listed in Table 1. The antenna I is a single crescent patch antenna with microstrip feed and defected ground structure, and it resonates at dual-band from 1.34 GHz to 2.43 GHz and 5.17 GHz to 6.22 GHz. Antenna II is designed by including another crescent ring, which is electromagnetic couple to the first ring and this structure is having Penta band response from 1.40 GHz to 1.70 GHz, 2.03 GHz to 2.40 GHz, 4.24 GHz to 4.40 GHz, 5.26 GHz to 6.09 GHz and 7.01 GHz to 7.46 GHz. In Antenna III, both the crescent rings are directly connected to the feed line, and the structure operates at the Penta band from 1.42 GHz to 1.77 GHz, 2.02 GHz to 2.13 GHz, 2.42 GHz to 2.90 GHz, 5.23 GHz to 6.00 GHz and 8.14 GHz to 8.43 GHz. Antenna IV, the proposed RDRA, in which two similar dielectrics are placed on the crescent-shaped patch.

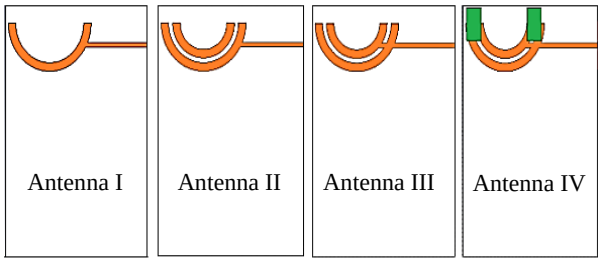

Fig. 2. Front view of Antenna I, II, III and IV.

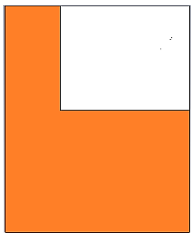

Fig. 3. Back view of Antenna I, II, III, and IV.

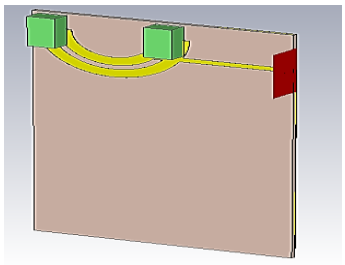

Fig. 4. Perspective view of the proposed DRA.

The dielectric resonator is made up of the material with relative permittivity of 2.33, and the size of the DR is a x b x h mm^3. The proposed Rectangular DRA operates in the Penta band from 1.38 GHz to 1.70 GHz, 1.90 GHz to 2.09 GHz, 2.36 GHz to 2.87 GHz, 5.18 GHz to 5.93 GHz, and 7.61 GHz to 7.88 GHz. The antenna geometry, along with its parameters, is presented in Fig. 5. Taking the 1.7 GHz as the base frequency, the maximum dimension of the 0.68 λ_0. The entire structure is fabricated 4.4 dielectric constant FR4 substrates. Section of two circles with different radius constitutes the radiator. A part of the ground near the feeding point is etched, which helps in tuning the multiple resonances. The outer radius is designed for the 1.7 GHz, and it can be evident from the surface current plot presented in Fig. 11 (a) with the optimized defected ground structure the 5.2GHz is achieved. Then the second ring is responsible for the 2.2 GHz band, which is proved with the help of surface current density in Fig. 11, in which it is seen that the maximum surface current is associated with the inner ring. Then the feed line is extended to the inner ring so that the coupling is increased, which results in the impedance matching and additional frequency resonance due to change in the current flow direction. Further, the performance of the antenna is enhanced with the help of DRA.

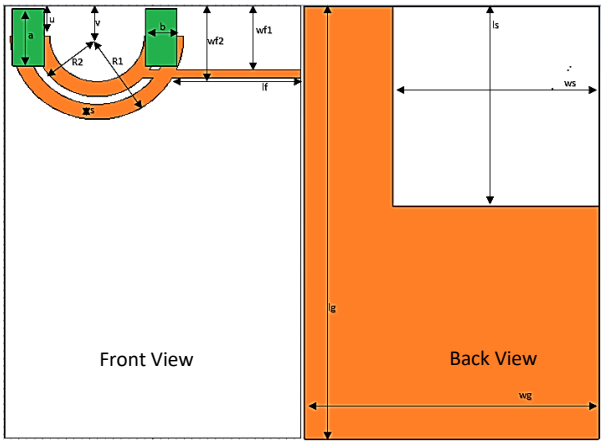

Fig. 5. Parameters of proposed RDRA for mobile wireless application.

Table 1: Antenna design parameter value in mm

Wg	lg	Ws	ls	wf_1	wf_2	l_f	R_1
37.5	57	26.25	24.75	8.5	9.5	17.9	11
R_2	a	b	u	v	s	t	h
8	7.5	4	4	5	2	0.035	1

Figure 6 depicts the S_{11} characteristics plot of Antenna I, II, III, and IV. The Antenna I is operated in two bands with a single crescent ring. The Antenna II is designed by adding another crescent ring. The inner ring and outer ring are not directly connected. This structure has an addition to resonance because of the second crescent ring. Then in Antenna III, both the rings are connected to each other through the feed line. The current is directly transferred to both the rings, and as a result, reliable impedance matching is achieved. Then the two symmetrical DRA is placed at the optimized position so that the antenna performance is slightly improved, and the DRA has a direct effect on the higher resonant frequency. The comparison of the operating frequency band with DRA and without DRA is presented in Table 2. On observing that, it is pragmatic that with the inclusion of the dielectric resonator, there is a slight increase in the bandwidth with a small reduction in the impedance matching, which is due to coupling loss.

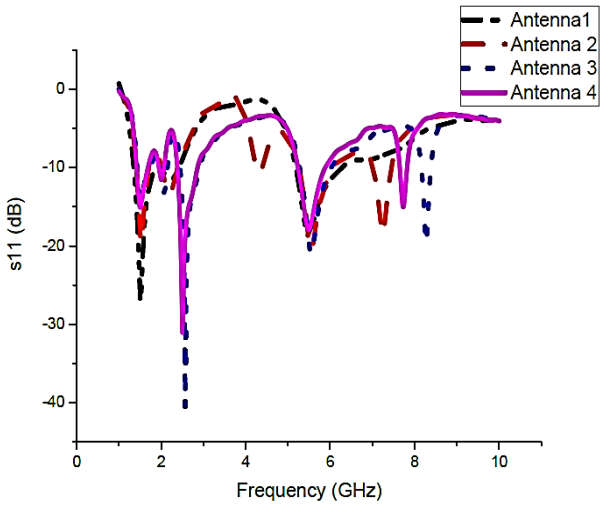

Fig. 6. S_{11} characteristics - various stages of proposed antenna.

All this analysis is depicted in Figure 7. Similarly, the parameters of the dielectric resonator are analyzed for deciding the optimum dimensions. The a, b, and h are varied, and its return loss characteristics are studied. In Fig. 8, the return loss plot for various dimensions of the dielectric resonator is presented. From which it is carefully observed that h=1mm, has an excellent performance in terms of impedance bandwidth in higher-

order resonating bands, and therefore, is chosen as the dielectric resonator height. The impedance matching gets reduced as the increase in the height of the dielectric. The reason is due to the larger ratio of volume to the surface at higher-order modes, so h = 1 mm is chosen for the final design.

Table 2: Antenna III vs Antenna IV

Band	Antenna III					Proposed RDRA (Antenna IV)				
	Fl (GHz)	Fu (GHz)	Return Loss (dB)	Bandwidth (MHz)	Gain (dBi)	Fl (GHz)	Fu (GHz)	Return Loss (dB)	Bandwidth (MHz)	Gain (dBi)
Band 1	1.42	1.77	-14.34	354	3.01	1.38	1.72	-15.32	340	4.27
Band 2	2.02	2.13	-13.4	119	1.35	1.9	2.09	-11.93	190	2.62
Band 3	2.42	2.9	-40.99	449	1.41	2.36	2.87	-31.32	510	2.66
Band 4	5.23	6	-21.19	744	2.51	5.18	5.93	-18.24	750	3.77
Band 5	8.14	8.43	-19.79	282	-0.34	7.61	7.88	-15.31	270	0.912

The dimension 'a' has a direct impact on the higher resonant frequency, and 'b' has a very profound effect on a lower frequency. The values a=4mm and b=7.5mm is chosen for the final design since it has very good impedance matching in all the resonating bands. At 7.75 GHz band alone, the impedance matching provided by a=6mm is high, for all the other bands a=4mm is providing slightly higher impedance matching. So, a=4 mm is chosen for final design.

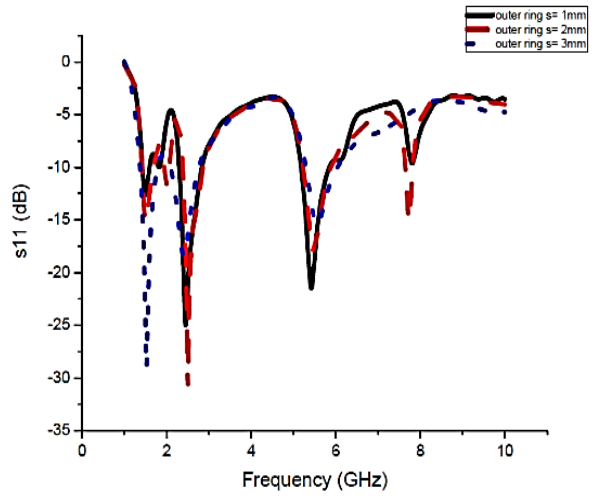

(a) S_{11} variation concerning the radius of the outer ring

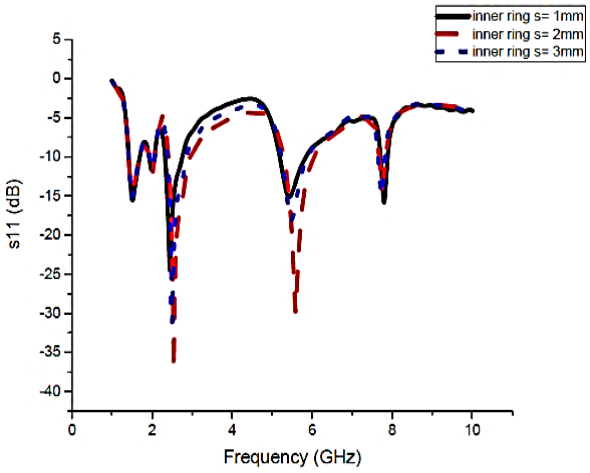

(b) S_{11} variation concerning the radius of the inner ring

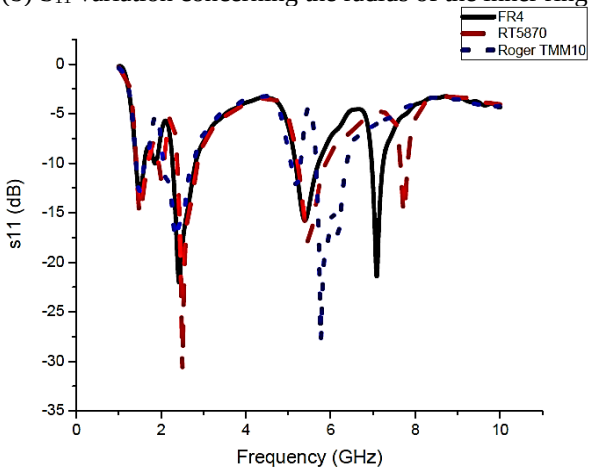

(c) S_{11} variation concerning the substrate material

Fig. 7. Parametric analysis of patch dimensions and substrate types.

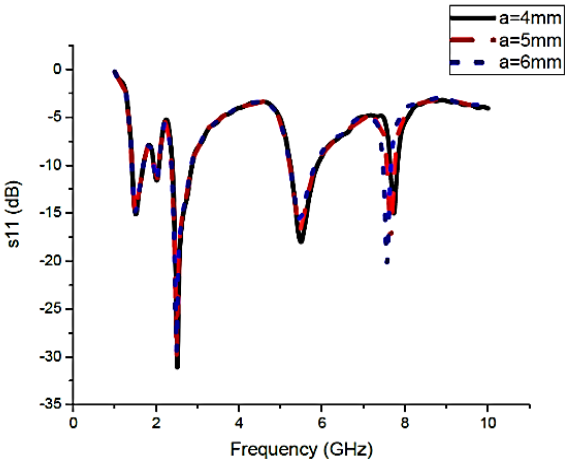

(a) S_{11} variation concerning DR dimension a

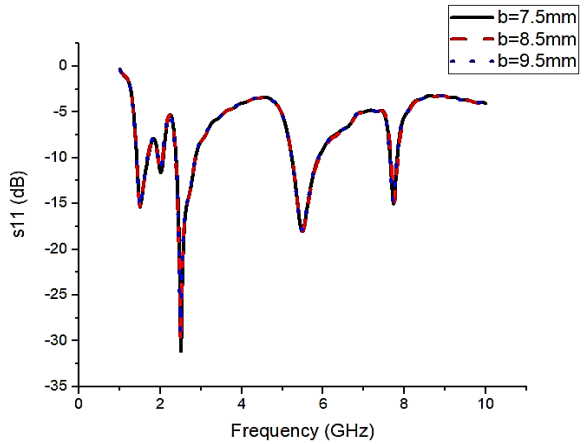

(b) S_{11} variation concerning DR dimension b

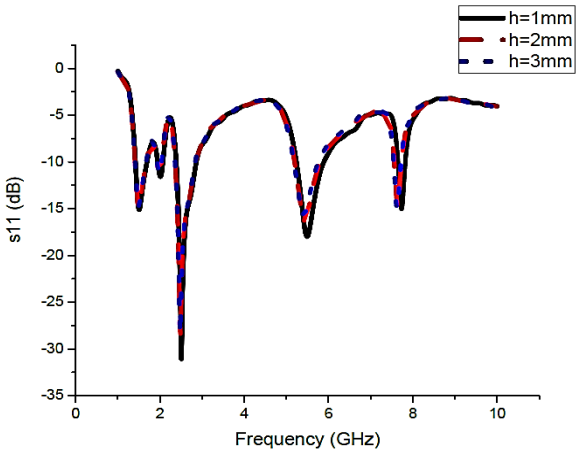

(c) S_{11} variation concerning DR dimension h

Fig. 8. S_{11} variation concerning the DR dimensions.

IV. RESULT AND DISCUSSION

In Fig. 9, the S_{11} of the RDRA is presented; from the figure, we can observe that the proposed rectangular dielectric resonator antenna is having Penta operating frequency bands with resonant frequency at 1.49 GHz, 2.00 GHz, 2.50 GHz, 5.49 GHz, and 7.75 GHz. In Figure 10, the simulated and measured VSWR of the proposed antenna is presented, which is observed from that the VSWR is lower than 2 in all the operating bands. This desired result shows that the proposed structure is having very decent impedance matching in the resonating bands.

In Fig. 11, the surface current distribution of the RDRA for mobile wireless applications at various resonating frequencies is presented. From the figure, we can see that the surface current is concentrated maximum on the crescent-shaped patch which couples with the dielectric resonator, is placed at the top of the patch. In Fig. 12, the simulated and measured radiation pattern at various frequencies is presented, from which we can observe that the proposed structure has an omnidirectional radiation pattern except at the higher mode resonant frequencies.

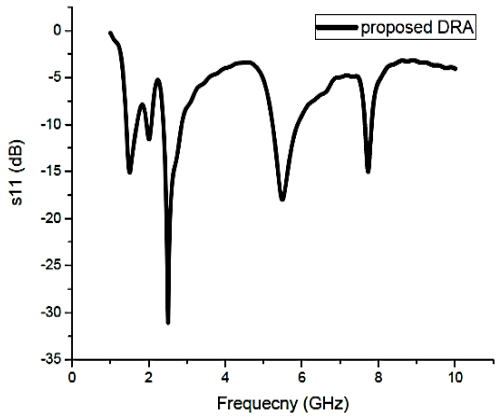

Fig. 9. S_{11} plot of proposed RDRA.

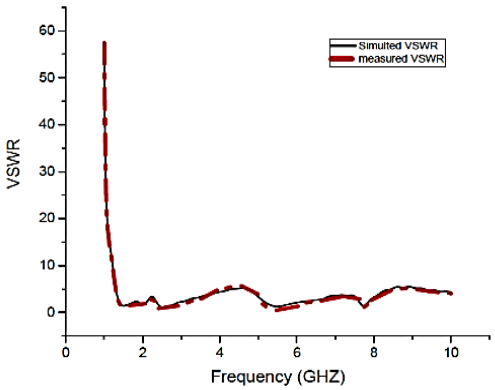

Fig. 10. VSWR of proposed RDRA.

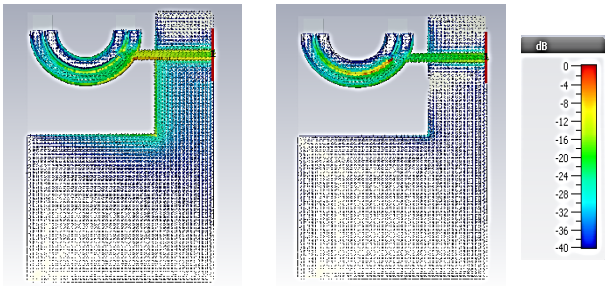

(a) 1.49 GHz (b) 2.00 GHz

(c) 2.5 GHz (d) 5.49 GHz

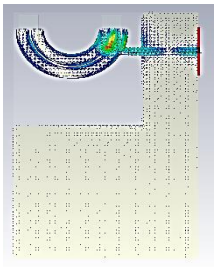

(e) 7.75 GHz

Fig. 11. Surface current of proposed antenna.

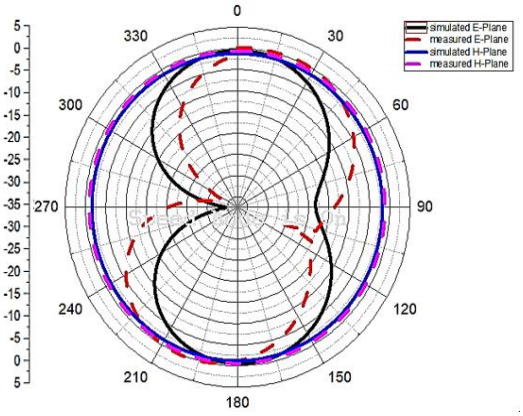

(a) 1.49 GHz

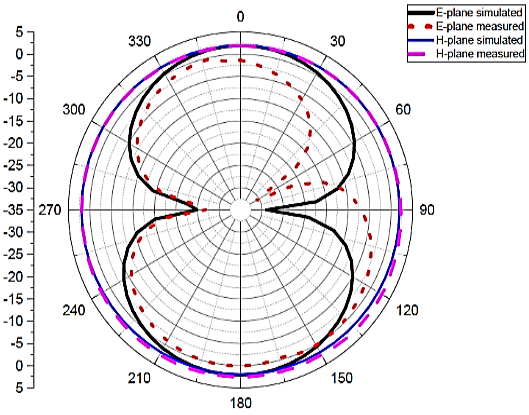

(b) 2.00GHz

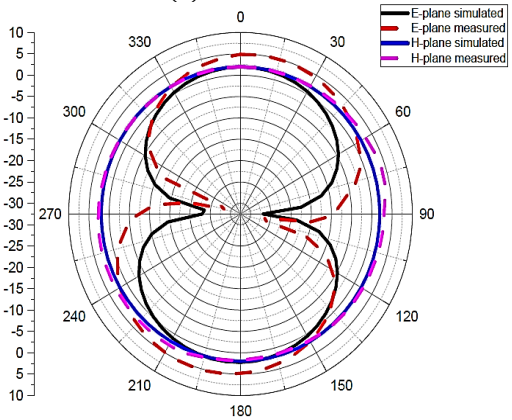

(c) 2.5 GHz

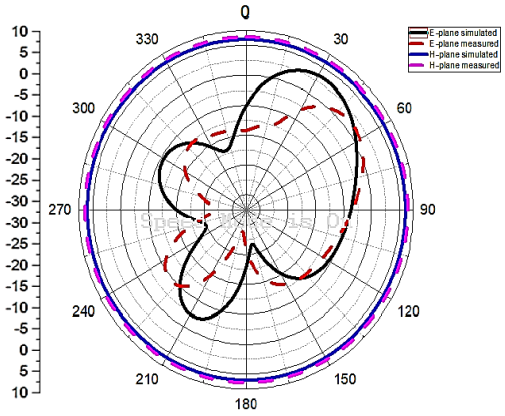

(d) 5.49 GHz

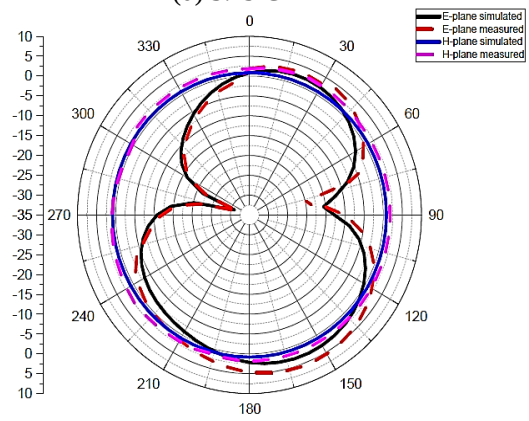

(e) 7.75 GHz

Fig. 12. E plane and H plane pattern (measured and simulated comparison).

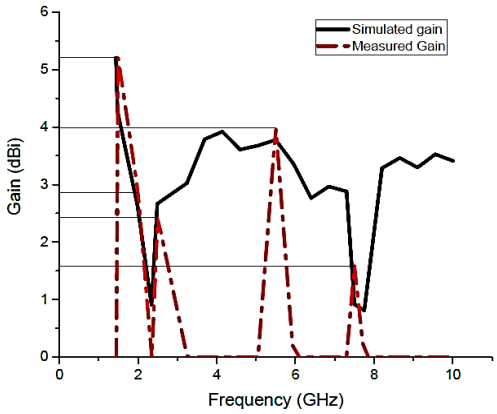

Fig. 13. Gain of the proposed RDRA.

In Fig. 13, the gain of the proposed RDRA is presented, and the measure gain is above 1.5 dBi. The measured gain is 5.216, 2.867, 2.428, 3.986, and 1.586 dBi at 1.49, 2, 2.5, 5.49, and 7.5GHz resonant frequency, respectively. In Fig. 14, the directivity of the RDRA is plotted. The proposed structure is capable of having a maximum directivity of 4.5dBi.

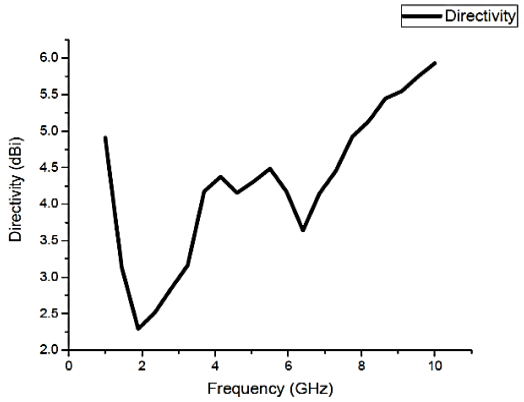

Fig. 14. Directivity plot of the proposed RDRA.

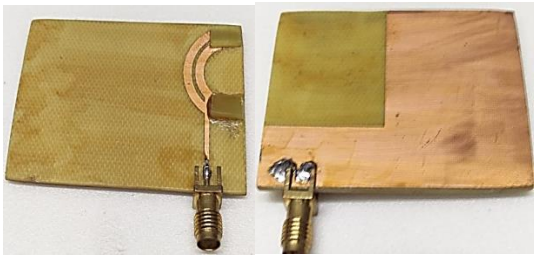

Fig. 15. Front and back view of the fabricated antenna.

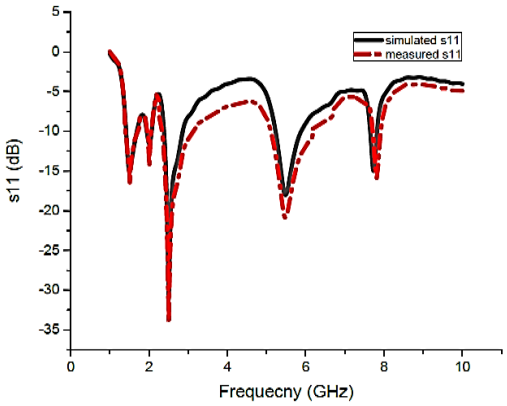

Fig. 16. Measured result vs. simulated result of proposed DRA.

In Table 3, the proposed work is compared with DRA available in the literature, and from the table, we can observe that the proposed DRA outperforms all the reported DRA. In Fig. 15, the fabricated antenna is depicted and measured using network analyzer N5230A. The simulated results are accurately related to the measured result and presented in Fig. 16. In Table 4, the measured and simulated S_{11} and bandwidth results are tabulated.

Table 3: Comparison with literature

Ref. No	No. of Bands	Feeding Method	Resonating Band (GHz)	DRA Material	DRA Size (mm)
31	Dual band	Microstrip	2.28-2.93, 4.26-4.65	Alumna	13.5 x 13
32	Triple band	Aperture couple	1.89-2.64, 4.13-5.47, 5.54-5.59	Alumna	40.5 x 31 x 19.68
33	Single band	Filter feed network	2.9-3.4	RT TMM 10	18.5 x 18.5 x 15.3
34	Penta band	Microstrip	2.38-2.42, 3.41-3.62, 3.93-4.26, 4.75-4.94, 5.01-5.39	Roger RT6010	18 x 18 x 9
35	Triple band	Slotted CPW	3.3-3.7, 4.8-5.0, 5.8-5.9	Foam	10 x 11 x 7
Proposed work	Penta band	Microstrip	1.38-1.70 GHz, 1.90-2.09, 2.36-2.87, 5.18-5.93, 7.61-7.88	RT5870	4x 7.5x1

Table 4: Simulated vs. measured results

Simulated Results					Measured Results				
Fl (GHz)	Fu (GHz)	Return Loss (dB)	Band Width (MHz)	Resonant Frequency (GHz)	Fl (GHz)	Fu (GHz)	Return Loss (dB)	Band Width (MHz)	Resonant Frequency (GHz)
1.38	**1.72**	**-15.32**	**340**	**1.50**	**1.39**	**1.74**	**-16.7**	**350**	**1.51**
1.9	**2.09**	**-11.93**	**190**	**2.00**	**1.954**	**2.053**	**-14.38**	**99**	**2.00**
2.36	**2.87**	**-31.32**	**510**	**2.50**	**2.332**	**3.142**	**-32.36**	**810**	**2.52**
5.18	**5.93**	**-18.24**	**750**	**5.42**	**5.112**	**6.17**	**-20.015**	**1058**	**5.43**
7.61	**7.88**	**-15.31**	**270**	**7.731**	**7.723**	**7.91**	**-15.77**	**187**	**7.82**

V. CONCLUSION

A rectangular DRA is proposed for the radio application. The proposed antenna is designed in four stages. Antenna I is a simple microstrip fed with a single crescent patch antenna with a defected ground structure. Antenna II is designed by including another crescent ring which is electromagnetic couple to the first ring, Antenna III both the crescent rings are directly coupled to the feed line, and Antenna IV is the proposed RDRA, in which two similar dielectric resonators made up of RT5870 is placed on a crescent-shaped patch in order to achieve multiband with good impedance bandwidth. The performance of the proposed RDRA supported by the simulated results. The proposed rectangular DRA has Penta operating frequency bands with resonant frequency at 1.49 GHz, 2.00 GHz, 2.50 GHz, 5.49 GHz, and 7.75 GHz, which covers the GPS, PCS, UMTS, ISM, WLAN, and Wi-MAX applications

REFERENCES

[1] K. M. Luk and K. W. Leung, eds., Dielectric Resonant Antenna. Research Studies Press, 2003.

[2] R. Mahmood and M. T. Beg, "Multiband dielectric resonator filter (MBDRF) with defected ground structure (DGS) for wireless application," *International Journal of Intelligent Systems and Applications (IJISA)*, vol. 6, no. 9, pp. 40-46, 2014.

[3] A. Petosa, Dielectric Resonator Antenna Handbook. Norwood MA: Artech Publication House, 2007.

[4] D. Guha, M. Biswas, and Y. M. M. Antar, "Microstrip patch antenna with a defected ground structure for cross-polarization suppression," *IEEE Antennas and Wireless Propagation Letters*, vol. 4, no. 1, pp. 455-458, 2005.

[5] D. Nesic, "A brief review of microwave photonic band-gap (PBG) structures," *Microwave Review*, vol. 7, no. 1, pp. 18-24, July 2001.

[6] Y. Qlan, "A microstrip patch antenna using novel photonic band-gap structures," *Microwave Journal*, vol. 42, no. 1, pp. 66-76, 1999.

[7] F. Yang and Y. Rahmat-Samii, "Applications of electromagnetic band-gap (EBG) structures in microwave antenna designs," in *Proceedings of the 3rd International Conference on Microwave and Millimeter-Wave Technology, IEEE*, Beijing, China, pp. 528-531, Aug. 2002.

[8] J. S. Kuo and K. L. Wong, "A compact microstrip antenna with meandering slots in the ground plane," *Microwave and Optical Technology Letters*, vol. 29, no. 2, pp. 95-97, 2001.

[9] R. D. Richtmyer, "Dielectric resonators," *Journal of Applied Physics*, vol. 10, no. 6, pp. 2391-398, 1939.

[10] S. A. Long, M. W. Mcallister, and L. C. Shen, "The resonant cylindrical dielectric cavity antenna," *IEEE Trans Antennas Propag*., vol. 31, no. 3, pp. 406-412, 1983.

[11] A. Petosa and A. Ittipiboon, "Dielectric resonator antennas: A historical review and the current state of the art," *IEEE Antennas Propag. Mag*., vol. 52, no. 5, pp. 91-116, 2010.

[12] S. K. K. Dash, T. Khan, and Y. M. M. Antar, "A state-of-art review on performance improvement of dielectric resonator antennas," *International Journal RF Microw. Comp. Aided Eng*., vol. 28, no. 6, pe.21270, 2018.

[13] R. K. Mongia and A. Ittipiboon, "Theoretical and experimental investigations on rectangular dielectric resonator antennas," *IEEE Transactions on Antennas and Propagation*, vol 45, no. 9, pp. 1348-1356, 1997.

[14] K. W. Leung, E. H. Lim, and X. S. Fang, "Dielectric resonator antennas: From the basic to the aesthetic," *Proc IEEE*, vol. 100, no. 7, pp. 2181-2193, 2012.

[15] D. Soren, R. Ghatak, R. K. Mishra, and D. R. Poddar, "Dielectric resonator antennas: Designs and advances," *Prog. Electromagn. Res. B*, vol. 60, pp. 195-213, 2014.

[16] S. Keyrouz and D. Caratelli, "Dielectric resonator antennas: Basic concepts, design guidelines, and recent developments at millimeter-wave frequencies," *International Journal of Antennas Propag*., Article ID 6075680, 2016.

[17] H. B. Basarudin, S. Ahmed, K. G. Tan, M. Y. Alias, F. Hossain, and L. C. Pao, "Dielectric resonator antenna design with high gain and wide bandwidth," *Journal of Engineering and Applied Sciences*, vol. 13, no. 19, pp. 8022-8026, 2018.

[18] H. Younesiraad, M. Bemani, and S. Nikmehr, "Small multi-band rectangular dielectric resonator antennas for personal communication devices," *International Journal of Electrical and Computer Engineering*, vol. 4, no. 1, pp. 1-6, 2014.

[19] F. Elmegri, C. H. See, R. A. Abd-Alhameed, C. Zebiri, and P. S. Excell, "Dielectric resonator antenna design for UWB applications," *2013 Loughborough Antennas & Propagation Conference (LAPC)*, Loughborough, pp. 539-542, 2013.

[20] G. Almpanis, C. Fumeaux, and R. Vahldieck, "Novel broadband dielectric resonator antenna fed through double-bowtie-slot excitation scheme," *Applied Computational Electromagnetics Society Journal*, vol. 22, no. 1, pp. 97-104, 2007.

[21] Y. M. Pan and S. Y. Zheng, "A low-profile stacked dielectric resonator antenna with high-gain and wide bandwidth," in *IEEE Antennas and Wireless Propagation Letters*, vol. 15, pp. 68-71, 2016.

[22] A. Khalajmehrabadi, M. K. A. Rahim, and M. Khalily, "Dual-band double-stacked dielectric resonator antenna with a P-parasitic shape strip for circular polarization," Presented at *IEEE International on RF and Microwave Conference* (RFM), pp. 444-447, 2011.

[23] F. Legier, P. Kennis, S. Toutain, and J. Citerne, "Resonant frequencies of rectangular dielectric resonators," *IEEE Transactions on Microwave Theory and Techniques*, vol. 28, no. 9, pp. 1031-1034, 1980.

[24] A. Gupta and R. K. Gangwar, "Hybrid rectangular dielectric resonator antenna for multiband applications," *IETE Technical Review*, vol. 37, no. 1, pe. 8390, 2020.

[25] K. Munish and V. Nath, "A circularly polarized printed elliptical wide-slot antenna with high bandwidth-dimension-ratio for wireless applications," *Wireless Networks*, vol. 26, no. 7, pp. 5485-5499, 2020.

[26] R. Kumar, G. Varshney, R. S. Yduvanshi, K. D. Dhirendra, and P. V. Shankar, "Dual-band dielectric resonator antenna with multi-frequency circular polarisation," *IET Microwaves, Antennas & Amp. Propagation*, vol. 14, no. 5, pp. 435-439, 2020.

[27] J. Iqbal, U. Illahi, M. I. Sulaiman, M. P. Alam, M. S. Mazliham, M. Najib, N. Yasin, and M. H.

Jamaluddin, "Bandwidth enhancement and generation of CP by using parasitic patch on rectangular DRA for wireless applications," in *IEEE Access*, vol. 7, pp. 94365-94372, 2019.

[28] G. Bakshi, A. Vaish, and R. S. Yaduvanshi, "Two-layer sapphire rectangular dielectric resonator antenna for rugged communications,"*Progress in Electromagnetics Research Letters*, vol. 85, pp. 73-80, 2019.

[29] A. K. Pandey, M. Chauhan, V. K. Killamsety, and B. Mukherjee, "High-gain compact rectangular dielectric resonator antenna using metamaterial as the superstrate," *International Journal RF Microw. Comput. Aided Eng.*, vol 29, p e21968, 2019.

[30] M. M. Sani, R. Chowdhury, and R. K. Chaudhary, "An ultra-wideband rectangular dielectric resonator antenna with MIMO configuration," in *IEEE Access*, vol. 8, pp. 139658-139669, 2020.

[31] A. Sharma, P. Ranjan, and Sikandar, "Dual band ring shaped dielectric resonator based radiator with left and right-handed sense circularly polarized features," *IETE Technical Review*, pp. 1-9, 2020.

[32] Chakraborty, Ujjal, A. K. Biswas, S. Maity, B. Roy, and S. Roy, "Dielectric resonator array antenna for triple band WLAN applications with enhanced gain," *International Journal of RF and Microwave Computer-Aided Engineering*, vol. 29, no. 2, e21529, 2019.

[33] S. Ballav and S. K. Parui, "Performance enhancement of dielectric resonator antenna by using cross-resonator based filtering feed-network," *AEU-International Journal of Electronics and Communications*, vol. 114, p. 152989, 2020.

[34] A. I. Afifi, A. B. Abdel Rahman, A. S. A. El-Hameed, A. Allam, and S. M. Ahmed, "Small frequency ratio multi-band dielectric resonator antenna utilizing vertical metallic strip pairs feeding structure," in *IEEE Access*, vol. 8, pp. 112840-112845, 2020.

[35] Q. Guo, J. Zhang, J. Zhu, and D. Yan, "A compact multiband dielectric resonator antenna for wireless communications," *Microw. Opt. Techno. Lett.*, vol 62, pp. 2945-2952, 2020.

[36] C. S. Prasad Jones and N. Gunavathi, "A tri-band monopole antenna loaded with circular electric–inductive–capacitive metamaterial resonator for wireless application," *Applied Physics A*, vol. 126, no. 10, pp. 1-11, 2020.

[37] M. Ojaroudi, N. Ojaroudi, and N. Ghadimi, "Enhanced bandwidth small square slot antenna with circular polarization characteristics for WLAN/WiMAX and C-band applications," *Applied Computational Electromagnetics Society Journal*, vol. 28, no. 2, Feb. 2013.

[38] S. H. Zainud-Deen, H. A. Malhat, and K. H. Awadalla, "8×8 near-field focused circularly polarized cylindrical DRA array for RFID applications," *Applied Computational Electromagnetics Society Journal*, vol. 27, no. 1, Jan. 2012.

[39] S. H. Zainud-Deen, H. A. Malhat, and K. H. Awadalla, "Mutual coupling reduction in dielectric resonator antenna arrays embedded in a circular cylindrical ground plane," *Applied Computational Electromagnetics Society Journal*, vol. 25, no. 12, Dec. 2010.

[40] Fakhte, Saeed, and HomayoonOraizi, "Derivation of the resonant frequency of rectangular dielectric resonator antenna by the perturbation theory," *Applied Computational Electromagnetics Society Journal*, vol. 31, no. 8, 2016.

[41] F. A. Abushakra, A. S. Al-Zoubi, and D. F. Hawatmeh, "Design and measurements of rectangular dielectric resonator antenna linear arrays," *Applied Computational Electromagnetics Society Journal*, vol. 33, no. 4, 2018.

[42] M. Z. Hameed, S. Majeed, R. Saleem, M. F. Shafique, and S. Rehman, "Dielectric resonator antenna based dual port multiple input multiple output antenna," *Applied Computational Electromagnetics Society Journal*, vol. 34 no. 8, pp. 1254-1257, 2019.

[43] N. A. Al-Shalaby and S. M. Gaber, "Design of dielectric resonator band stop/band pass filters," *Applied Computational Electromagnetics Society Journal*, vol. 38, no. 8, 2019.

Chaitanya Bethala, Department of Electrical, Electronics & Communication Engineering, GITAM School of Technology, Hyderabad Campus, completed M.Tech. (Microwave Engineering). Presently is working as Assistant Professor in Electrical Electronics & Communication Engineering Department, School of Technology, GITAM (Deemed to be University) Hyderabad, Telangana, Telangana.

Manjunatha Chari Kamsali received his Ph.D from JNT University, Kakinada. He has 20 years teaching experience and 3 years of industry experience. At present, is working as Professor at Department of Electrical, Electronics & Communication Engineering, School of Technology, GITAM (Deemed to be University), Hyderabad, Telangana. He has published more than 50 research articles in reputed journals.

Multifold Bandwidth Improvement in Conformal Patch Antenna for Aircraft Application Using Corrugated Edge Coupling

Jeyakumar Monica* and Paramasivam Jothilakshmi

Department of Electronics and Communication Engineering
Sri Venkateshwara College of Engineering, Anna University, Pennalur, Sriperumbudur, Chennai, India
*jkumarmonica@gmail.com, jothi@svce.ac.in

Abstract ─ In the high-speed Internet of Things (IOT) era, the aircraft on-board is one of the few places that lacks high speed network access. The speed of this communication link between the ground station and the aircraft is limited by the transmitting antenna power, cost, latency and available infrastructure. The Direct Air to Ground (DATG) is a much-guaranteed technique which can provide a high-speed link between the ground station and aircraft. This paper describes a novel conformal microstrip patch antenna design which provides fourfold increase in bandwidth. As the bandwidth of an antenna mounted on the fuselage of aircraft is crucial to achieve higher data rate, this antenna performance is promising and suits better for DATG application. The proposed antenna with a size of (6.81 X 7.21cm) achieves a bandwidth of ~700MHz (5.032GHz to 5.73GHz) and max Gain of 9.53dB with max radiation efficiency of 93%. As this antenna is to be mounted on the aircraft fuselage, a substrate material, RT duroid 5880 with a thickness of 0.787mm is selected to have better conformability, low loss and high gain. This paper explains the different performance metrics involved in the DATG system and derives the specification for the proposed antenna structure. Also, the detailed structural analysis with the support of parametric and Characteristic Mode Analysis (CMA) is provided to get the physical insight of the designed antenna.

Index Terms ─ Characteristic mode analysis, direct air to ground, internet of things.

I. INTRODUCTION

The global liberalization of trade has increased the movement of people from one continent to another, one country to another and one city to another more frequently. The major medium of transport is through air, as it is more efficient in terms of travel time. The number of passengers as well as the number of carriers also growing year by year. The statistics [1] shows that more than 4.1 Billion passengers had been travelled in the commercial aircraft in 2017. Another statistic [2] shows that it may increase to 8.2 Billion in 2037. There are total of 1303 airlines all over the world which operates approximately 32000 fleets [3] per annum. As the business have spread throughout the world due to globalization, it has become necessary for the people to be connected in order to meet the deadlines, as the competition has grown exponentially. In this competitive world when someone does a business travel from one place to another, doesn't want to miss the business updates. Another aspect of internet availability inside the aircraft is streaming the videos, movies etc. to keep the kids engaged which helps in smooth travel experience with family.

The aircraft uses an on-board radio equipment with different types of antenna operating at different frequency bands. There are two broad classification of aircraft communication with respect to the distance of communication, Short range aircraft communication systems and Long-range communication systems [4]. The short-range communication uses Very High Frequency (VHF) band of 118 to 137MHz, to communicate with the air traffic control stations. The communication is limited to a line of sight (LOS) distance within the earth curvature change. The LOS distance for these short-range communications can be calculated as shown in [4]. Also, the antenna used for this communication is usually Omni-directional and vertically polarized with approximate power rating of 5 to 30W. The long-range communication is traditionally carried out through High Frequency (HF) band of 3 to 30MHz [4]. Since this communication channel supports the distance beyond the LOS distance, the transmitted waves undergo multiple reflections from the earth surface before reaching the destination, thus requires lot of power (300 – 1000W) in the transmitter.

Another method of long-range communication is adopted along with the development in satellite communication. In satellite communication method [5], the smaller aperture antenna arrays are mounted on top of the aircraft fuselage with the ability of rotating the main lobe direction in order to keep the connection intact while the carrier is moving. This method of satellite communication uses relatively lesser power. The major

Submitted On: January 13, 2021
Accepted On: May 17, 2021

https://doi.org/10.47037/2020.ACES.J.360512

drawbacks of the system are the limited data rates, latency and the cost. This communication system uses either Geostationary or Non-Geostationary orbital satellites. The communication link through satellite is inevitable for those aircrafts flying between continents which are separated by a large ocean surface. But, for those inter-continent aircraft there is another way to communicate with the ground station which is called Direct Air to Ground (DATG). In this method, the transmitter antenna is mounted in the bottom of aircraft fuselage through which it connects to a series of ground station antennas separated by a distance of ~10 to 200km. The antenna used for DATG should also have adaptive beam-forming feature to provide the continuous network connectivity.

The Electronic Communication Committee (ECC) has recommended few frequency bands to be used in DATG communication [6], [7]. These recommendations are the result of few case studies carried out by ECC. It is also mentioned that the frequencies below 6GHz is suitable for this communication. As this technology is not widely available around the world, there is no common frequency band available for this communication. In this design the frequency band of 5 to 5.8GHz is selected for designing the antenna. Every communication channel has three bands, up-link, down-link and guard band. Usually the up-link uses the higher frequency band as this require more power because of environmental loss. As of now the data rate of this DATG communication channel is limited to 3 to 4MHz [8]. In this design the targeted data rate is ~500Mbps in order to support the future need of live cock-pit video, remote control, flight data transmission, on-board internet access etc., This paper concentrates on a unit antenna design for DATG applications. As this antenna is intended to be mounted on the fuselage of aircraft, the conformability nature of the antenna is also important. So, the designed antenna in conformed to different radius of curvatures, 20 to 30cm, during the simulation and measurement. In order to achieve the conformability, the RT Duroid 5880 with a thickness of 0.787mm is used as a substrate material.

In this proposed work a novel structure of conformal micro-strip patch antenna is designed, fabricated and tested. It achieves better bandwidth to meet the DATG system requirement. Also, the maximum antenna gain of 10dB at 5.3GHz is achieved which helps in reducing number of elements in the final phased array. The design is carried out with RT Duroid 5880 as a substrate with a thickness of 0.787mm. The system requirements, antenna geometry, structural analysis of designed antenna with the help of parametric study and Characteristic mode analysis are presented in Section II. Experimental results are discussed in Section III and finally the conclusion and future work is discussed in Section IV.

II. DESCRIPTION OF THE ANTENNA STRUCTURE

A. System requirements

In DATG communication channel, both the Ground station (GS) and the aircraft are always in the LOS region. The important parameters of a communication system are path loss, required transmitter gain, modulation scheme, Bandwidth, coverage distance and transmitter gain. The path loss or fading is the time varying attenuation of the transmitted signal before reaching the receiver. This time varying attenuation is mainly because of the changing environment. It is important to know the path loss because the transmitting power has to be derived based on the path loss calculation. The path loss is dependent on the distance between the transmitter and the receiver. The mean path loss in free space is expressed below, [9,10]:

$$L(d) = 10 * \gamma * \log_{10}(d) + (20 - 10 * \gamma) * \log_{10}(d_0) + 20 * \log_{10}(f) + 32.5dB. \quad (1)$$

Where d is the distance between aircraft and GS (km), d_0 is the reference distance for which the path loss is known, 'f' is the transmitting signal frequency (GHz), 'γ' is the propagation constant (is 2 for free space). The above equation can be used to estimate the free space path loss at different frequencies and distance. For instance, with a separation of 80km and the signal frequency of 5.2GHz the path loss can be calculated as, ~145dB. The loss due to shadowing effect is not considered for this analysis.

The required bandwidth is dependent on the modulation scheme. For the required bit rate of 500Mbps, the needed bandwidth for different modulation scheme can be calculated using equation (2). The require bandwidths are, BPSK (M = 2) is 500MHz, QPSK (M=4) is 250MHz, QAM-16 (M=8) is 166MHz and QAM-64 (M=6) is 83MHz. Though the higher order modulation seems more efficient in terms of bandwidth, it has its own limitations such that the need of higher signal to noise ratio and bit more complicated receiver design. But the higher order modulation schemes help is accommodating large number of users within the available bandwidth. For instance, with QAM-64 and 700MHz transmitter bandwidth, approximately 8 users can access a speed of 500Mbps. As per the key performance indicators proposed for 5G DATG by NGMN Alliance [11] the required internet speed per user is estimated as ~15Mbps. If the fraction of achieved bandwidth 300MHz in combination with QAM-64 modulation scheme is assumed for the download link, then 120 on-board users can enjoy the internet speed of 15Mbps:

$$B = \left(\frac{R_b(1+a)}{\log_2 M}\right). \quad (2)$$

Where B is the transmitter bandwidth, R_b is the bit rate and M is the number of symbols used or constellation

points. The estimation of the signal to noise ratio is important because it helps in calculating the minimum signal power at the receiver and the required antenna gain to achieve it:

$$\mathrm{SNR} = \frac{E_b}{N_0} + 10\log_{10}\left(\frac{R_b}{B}\right) \text{ dB}. \quad (3)$$

Where E_b is the energy per Bit, N_o is the Noise power spectral density. The minimum signal power required at receiver end can be estimated using below equation, if the receiver system noise figure (NF) is known [12]. The noise figure parameter helps in identifying the amount of noise contributed by the components present in the receiver channel:

$$P_{RX} = \mathrm{SNR} * KT_0 * \mathrm{NF} * B. \quad (4)$$

Where P_{RX} is the Receiver power, SNR is the Signal to Noise ratio of the channel, K is the Boltzmann constant, T_o is the temperature (300K). The link budget equation for a LOS communication channel can be written as,

$$P_{RX} = P_{TX} - L_{TX} + G_{TX} - L(d) + G_{RX} - L_{RX}(\mathrm{dBm}). \quad (5)$$

Where P_{TX} represents the transmitted power, L_{TX} represents the transmitter system loss, G_{TX} represents the gain of the antenna mounted on aircraft fuselage, G_{RX} represents the Gain of the ground station antenna and L_{RX} represents the receiver system loss. This equation can be re-written to calculate the required gain of the antenna mounted on aircraft. By assuming typical values for the above-mentioned parameters, NF = 2dB, G_{RX} = 10dB, Bit error rate (BER) = 10^{-6}, L_{TX} = 10dB, L_{RX} = 5dB, the calculated values are SNR = 62dB, P_{RX} = -87dbm. From these values the required gain of the antenna is calculated as 36.28dB for a 1W of transmitted power. It falls down to 26.28dB if the transmitted power is 10W. These gain values are, to be achieved using the micro-strip phased array structure. The gain value of a unit element antenna in an array that determines the number of required elements and thus decides the antenna size [13]. So, achieving higher gain in a unit antenna helps in reducing the array size. Theoretically the gain increases by 3dB for every doubling of unit antenna element in the phased array. In order to achieve the required gain of 36.28dB the total number of unit antennas, with a gain of 10dB, needed are ~512. It is approximately a phased array structure of 24 X 24. The calculation in equation (6) shows the estimated transmitter antenna gain for the assumed conditions:

$$G_{TX} = -87\mathrm{dBm} - 30\mathrm{dBm} - 5.72 + 145 + 15 = 36.28\mathrm{dB}. \quad (6)$$

B. Antenna design

The geometry and CST design model of the proposed micro-strip patch antenna is shown in Figs. 1 and 2. Alike regular patch antenna, this proposed structure also has only three layers, ground plane, substrate and the top patch. It doesn't possess any defect in the ground plane as that technique is not suitable for the aircraft mounting. It uses RT Duroid 5880 as substrate with a thickness of 0.787mm in order to support the conformability. The top layer exhibits very distinct structural changes compare to its basic single patch antenna. The proposed antennas dimension is designed as per the design equations explained in [14]. The various dimensions of this proposed structure are explained below.

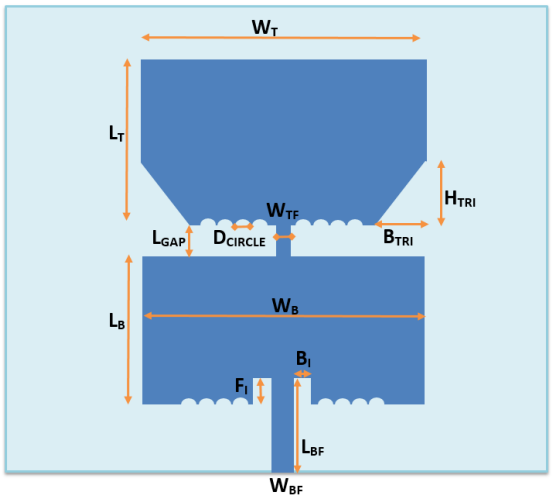

Fig. 1. Geometrical configuration of antenna structure.

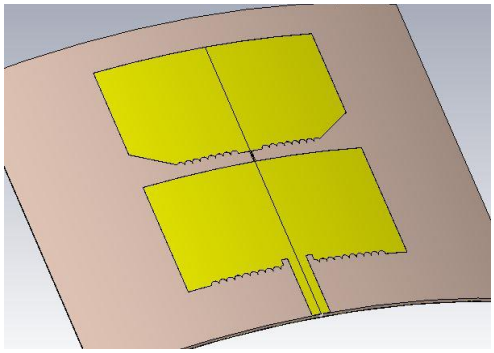

Fig. 2. CST simulation model of antenna structure.

Firstly, the bottom patch resembles the conventional single patch structure. L_B and W_B represents the length and width of the bottom patch. In this design inset feed is incorporated as it helps in easy integration with the other microwave circuitry. F_I and B_I illustrates the depth and the spacing of inset feed. W_{BF} and L_{BF} represents the width and length of the 50Ω micro-strip feed line. Secondly, there are two patches instead of one in the conventional single patch structure. The dimension of these two patches can be same or it differs slightly based on the final optimization. L_T and W_T illustrates the length and width of the top patch. The top patch is connected to the bottom patch through a small micro-strip

transmission line feed with a length L_{Gap} and width W_{TF}. Thirdly, the top patch has a triangular cut in the right and left bottom corners. The dimensions, height and breadth, of the right-angle triangular cuts are illustrated as H_{TRI} and B_{TRI}. The height and breadth of these cuts are not equal. Fourthly, the top and bottom patches exhibit multiple half circular cuts or wedges in its respective bottom edges. These circular cuts present in both the sides of the top and bottom feed line till the triangular edge. The number of cuts and its X-plane (Horizontal) location are same for both bottom and upper patches. The diameter of this circular cut is represented as D_{CIRCLE}. These circular wedges overlap with each other along its perimeter. The proposed structure is approximately double the size of single patch structure. But, this increase in size is outweighed by the benefit it provides, in terms of ~ 3dB increase in gain and approximately 4 times increase in bandwidth.

The Patch antenna is fed through a 50Ω microstrip feed to match the edge impedance. Then using the general patch antenna equations, the dimension of bottom and top patches are estimated. The feedline connecting both bottom and top patch is roughly sized as λ/20 and then optimized for better performance. The triangular cuts at the bottom has to be optimized to get dual resonance within the bandwidth. The spacing between the two patches has to be optimized for adding an additional resonance. The circular wedges are sized and spaced optimally to provide higher bandwidth.

The designed antenna measures 6.81cm (Length) * 7.21cm (Width) (inclusive of ground plane) is conformed to a curvature of 20-30cm to be placed in the aircraft fuselage.

C. Structural analysis

The bandwidth of the proposed structure is 700MHz that is approximately 13% of its center frequency, 5.4GHz. It is slightly more than four times the bandwidth of single patch antenna with same substrate thickness and material. This higher bandwidth is achieved through the structural changes mentioned above. In this section, the proposed antenna structure is disintegrated into multiple sub-structures and their return loss curve is observed for the resonance. Also, the parametric analysis is carried out for certain sub structures to get better understanding of the performance. It is also supported with the respective characteristic mode analysis results to get more physical insight of the behavior. For each sub structure the input is fed from the source with an impedance of 50Ω. These sub-structures are also conformed to a cylindrical fuselage made of Aluminum (Al) with a radius of curvature 25cm, in order to mimic the actual aircraft environment.

The first sub-structure to be analyzed is the standalone bottom patch without any circular cuts as shown in Fig. 3. This resembles the basic single patch antenna structure. The structure for analysis and its return loss curve is shown in Fig. 4. These simulation results clearly illustrate that this structure exhibits a single resonance at 5.16GHz. The return loss also has the second dip as the impedance is not properly matched with 50Ω feed. As it is a sub-structure, the impedance will change when it is integrated with other structural changes. Also, the CMA analysis is not critical for this single patch because it has a single feeding point through a micro-strip line which defines the current flow from the bottom edge to the top edge.

The second sub-structure is illustrated in Fig. 5. Structurally it exhibits a very minimal change of having small circular shape wedges at the bottom edge compared to a standalone single patch. As certain portion of copper is etched away in the bottom edge, it is expected to shift the resonant frequency upwards. Instead, it marginally reduces the resonant frequency to 5.12GHz as shown in Fig. 4.

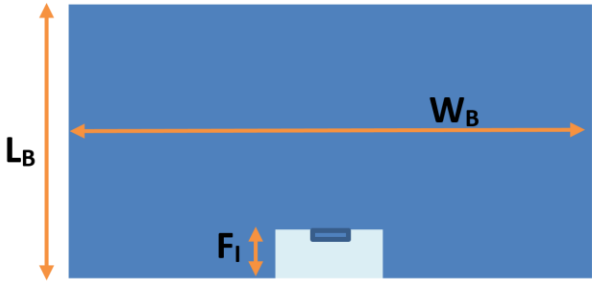

Fig. 3. Sub structure 1 - Bottom patch standalone.

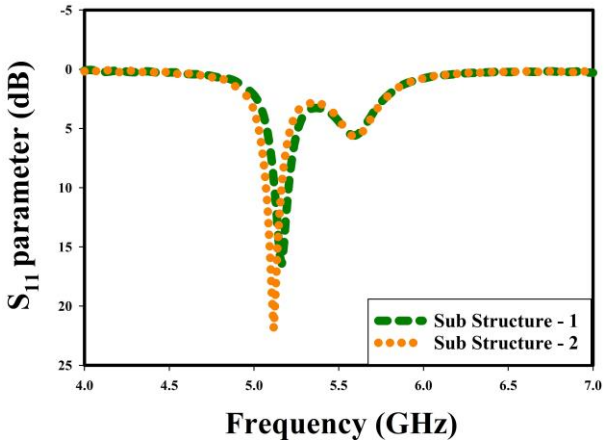

Fig. 4. Return loss curve - Structural changes in bottom patch.

The travel distance of the current in a patch decides the resonant frequency as the length of the patch is directly related to the wavelength. So, in order to reduce the resonant frequency, the current travel distance has to be longer than usual. Because of the presence of this circular wedges, certain portion of current components

travels around the perimeter of these circular wedges before resonating back. Therefore, the effective travel distance of the surface current is increased slightly. It can be clearly observed in the surface current plot shown in Fig. 6. The inclusion of this circular wedges helps in adjusting the resonant frequency slightly once this sub-structure is integrated into the proposed structure.

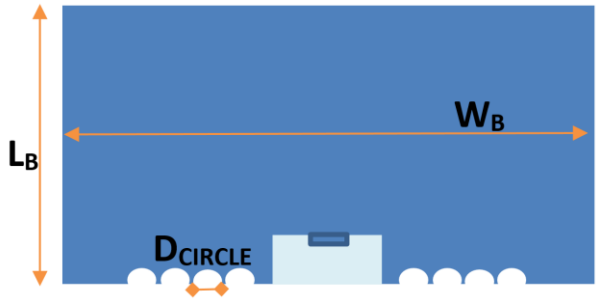

Fig. 5. Sub structure 2 - Bottom Patch with circular wedges.

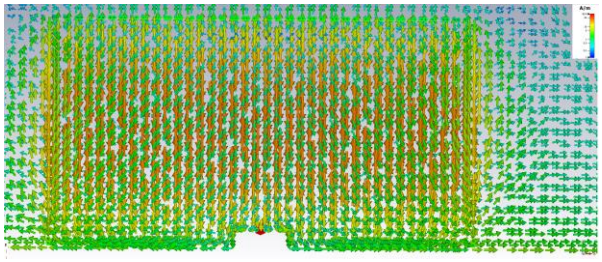

Fig. 6. Sub structure 2 - Surface current in the bottom patch with circular wedges.

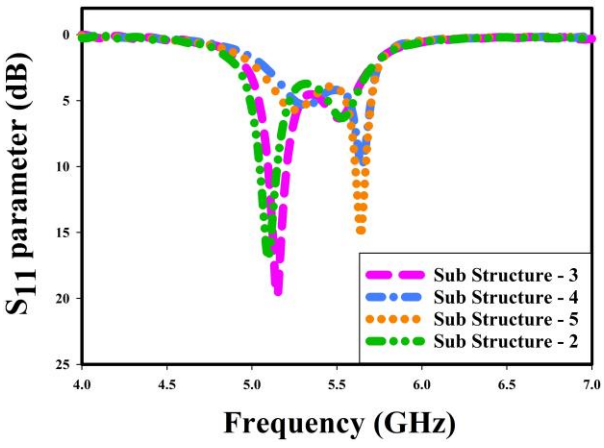

Fig. 7. Return loss curve - Structural changes in top patch.

The third sub-structure to be analyzed is the standalone top patch that has similar structure as standalone bottom patch shown in Fig. 3. The return loss curve corresponds to this structure is shown in Fig. 7. The length and width of this top patch structure matches with the standalone bottom patch dimensions. So, the resonant frequency of this structure, 5.15GHz is matching with the bottom patch. But this structure undergoes multiple structural changes unlike the bottom patch. The effect of these structural changes on top patch structure are discussed further in this section.

The fourth analysis is carried out on the sub-structure shown in Fig. 8. In this structure the rectangular patch is having a triangular cut in its bottom corners. The return loss curve corresponds to this structure is shown in Fig. 7. Though the return loss value is not higher than 10dB because of the standalone analysis, it provides information about the resonant points. The two resonant point are at 5.33GHz and 5.66GHz. The dimensions of this triangular cut also have significant impact on these resonant points. In order to understand the effect of H_{TRI} and B_{TRI}, parametric analysis is carried out and the results are shown in Fig. 9 and Fig. 10. Three major observations can be made from this parametric analysis. The first one is, the resonant point doesn't change much with both the parameters. The second observation is, as the B_{TRI} value comes closer or below the H_{TRI} value, the matching is good and the return loss curve goes above 10dB. It also indirectly means that the B_{TRI} modulates the edge impedance of the patch. The third observation is, as the H_{TRI} value moves closer or higher than B_{TRI} the resonance is lost. Based on these observations, it can be stated that the H_{TRI} has to be lesser than B_{TRI} to have a better matching with 50Ω source impedance.

So, these two parameters can be used as a trimming option in order to achieve optimized performance after the complete integration of structure. All the above observations are true only if the feed is provided at the bottom center edge and the current travels in the longitudinal direction. In the final integrated structure, this top patch is not fed directly by the source through micro-strip edge feeding instead it receives energy through the bottom patch. So, the direction of current entering into this top patch is not necessarily in longitudinal direction. So, carrying out an analysis using CMA will provide very useful insight on possible current flow directions on top patch and its corresponding resonant frequency. The details of CMA and its parameters can be found in literature [15-18]. The CMA is very useful in bringing up the hidden characteristics of patch antenna. The performance of any patch antenna has a direct relationship with the surface current flow. In CMA, different possible combinations of current flow are assumed and the corresponding parameters are estimated. These parameters are useful in fine tuning the antenna shape, size and feed location.

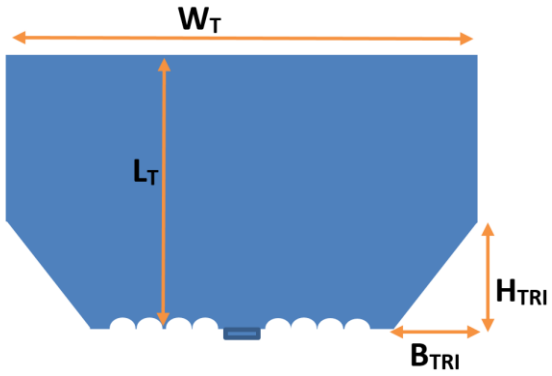

Fig. 8. Sub structure 4 - Top patch with triangular cuts.

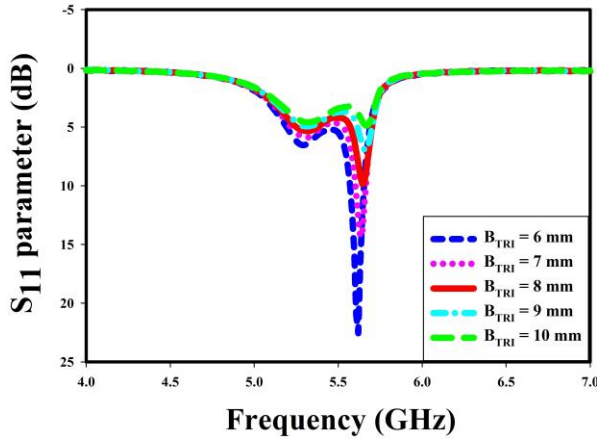

Fig. 9. Sub structure 4 - Return loss curve by sweeping B_{TRI} and H_{TRI} = 5.35 mm.

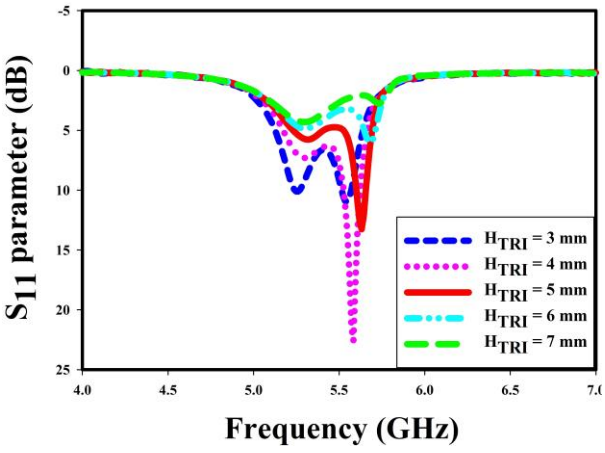

Fig. 10. Sub structure 4 - Return loss curve by sweeping H_{TRI} and B_{TRI} = 8 mm.

The vector form of characteristic mode is represented as follows,

$$X(\vec{J}_n) = \lambda_n R(\vec{J}_n). \quad (7)$$

Where $\vec{J}_n$ represents the Eigen characteristic current modes, λ_n is the eigen value, R and X are the resistive and reactive parts of impedance operator. Along with Eigen value (λ_n), the other two forms also used to estimate the characteristics of each current mode:

$$\text{Modal Significance (MS)} \; \alpha \; \frac{1}{1+j\lambda_n}, \quad (8)$$

$$\text{Characteristic Angle (CA)} = 180^{\circ} - \arctan(\lambda_n). \quad (9)$$

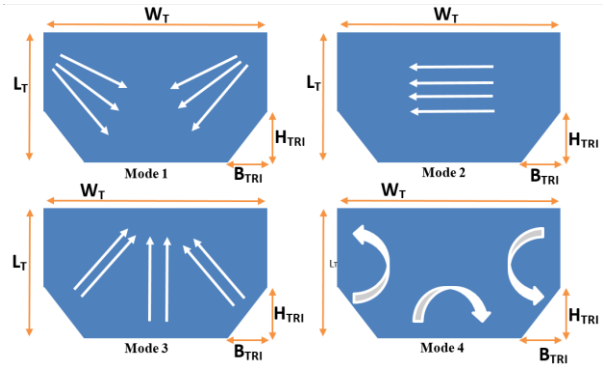

Fig. 11. Sub structure 4 - CMA current modes.

As this paper concentrates on bandwidth improvement, identifying the position of multiple resonant points are important. The resonant frequency of each current mode is represented differently by these three parameters.

1. Zero crossing frequency of Eigen value.
2. Peak frequency of Modal Significance.
3. 180˚ crossing frequency of CA.

In this paper only Modal Significance (MS) parameter and the respective surface current plots are used for analysis. Figure 11 and Fig. 12 show the different current modes and its corresponding MS curve across frequency. The frequency at which the MS curve reaches its peak value of unity depicts the resonant point of that particular current mode. The different current modes show the assumed direction of the surface current components.

This analysis clearly explains that the top patch structure can exhibit multiple resonant points depends on the direction and length of the current flow. The resonant point corresponds to mode 1 matches closely with the sub-structure of standalone edge fed top patch without any structural changes. The mode 3 exhibits matched resonant frequency with the sub-structure of standalone top patch with triangular cuts. The mode 4 resonates at much higher frequency as the current path is very short. So, it is very much clear that the top patch can have multiple resonant points depending on the direction of current injection.

The fifth sub-structure to be analyzed is the standalone top patch with both triangular cut and the circular wedges is shown in Fig. 13. The presence of

circular wedges slightly reduces the resonant frequency as shown in Fig. 7. The impact of the radius of these circular wedges are analyzed as a part of next sub structure.

The sixth structure to be analyzed is the integrated top and bottom patch without any structural modifications is shown in Fig. 14. The corresponding return loss curve is shown in Fig. 15. In this structure, the two patches with same dimensions are stitched together vertically through a narrow micro-strip line. The energy from the source has to travel through the bottom patch before exciting the top patch. So, there is a higher possibility that the top patch can receive the energy in different path and direction. One of such known paths is through the feed line connecting the two patches and another is through the overlapping edges. So, the important parameter to be analyzed in this structure is the gap between top and bottom patch and the width of the narrow feed line. The return loss graph is obtained for different gap values through simulation as shown in Fig. 16. Lowering the gap separates two resonant points and increasing the gap brings the two resonant points closer. This observation is very straightforward as the gap increases the magnitude of parasitic capacitance between the bottom and top patch reduces and thus turning this structure into a single patch. Therefore, further increase in gap merges the two resonant points into one. Another important parameter is the width of the feed line connecting two patches. The return loss curve is observed for different values of this feed line width. The parametric result is shown in Fig. 17. It can be observed that the change in width alters only the matching, i.e., the edge impedance at the input port.

The analysis of sixth sub-structure is further extended with CMA. Figure 18 shows 4 different current modes having a resonant frequency in the vicinity of expected bandwidth range. In the first current mode the current travels mostly in the lower patch and the amount of energy transferred to the upper patch is less. In the second current mode the current distribution is approximately equal in both the patches which means that there is a coupling between lower patch and the upper patch. This is directly visible from the resonant points of respective modes shown in Table 1, where the first mode possesses higher resonant frequency compare to the second mode. In third mode the current travels diagonally towards the horizontal edges, in both top and bottom patches, and thus the travel distance is less that results in little higher resonant frequency. In fourth current mode the current travels from one corner of the patch to another which results in shorter distance and thus results in higher resonant frequency. Also, the current distribution in both lower and upper patch is same in the fourth current mode. The separation between the mode 3 and mode 4 resonant point is ~280MHz in this structure. Similarly, the separation between mode 1 and mode 3 resonant point is ~290MHz. In order to keep the return loss higher than 10dB the resonant points have to be placed within a certain optimum distance. This structure tends to keep more distance between the resonant points and thus resulting in return loss below 10dB within the bandwidth. In order to improve the bandwidth, the placement of multiple resonant points has to be closer.

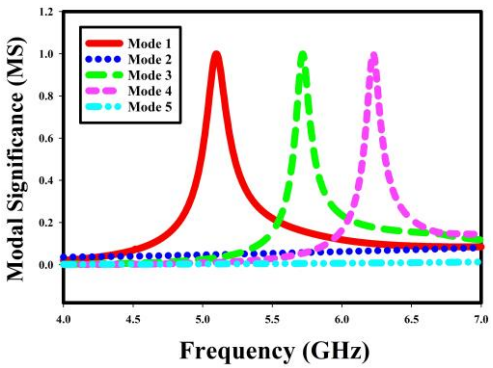

Fig. 12. Sub structure 4 - Modal significance curve.

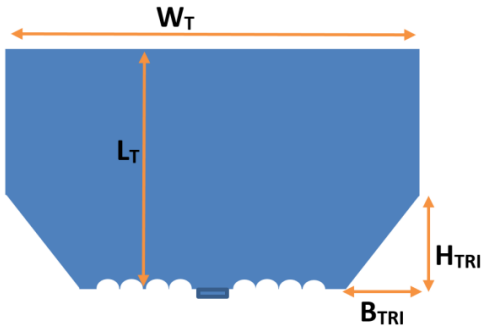

Fig. 13. Sub structure 5 - Top patch with triangular cuts and circular wedges.

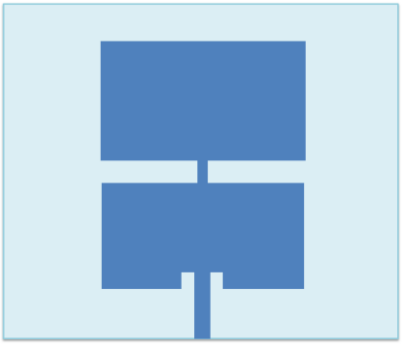

Fig. 14. Sub structure 6 - Integrated patch without any structural changes.

The seventh structure is the integrated top and bottom patch with triangular cuts on the bottom corner of top patch as shown in Fig. 19. The return loss curve

for this structure is shown in Fig. 15. This structure has slightly lesser bandwidth compare to the final structure. The respective current modes and its modal significant curves are shown in Fig. 20 and Fig. 21. The resonant points for each sub structure is listed in Table 1 and Table 2. This structure moves the mode 1 resonant point towards the mode 3 resonant point whereas the mode 3 resonant point is moved towards the mode 4 resonant point. Thus, the distance between mode 3 and mode 1 resonant point is further increased to ~330MHz. So, this structure tends to exhibit better performance but the middle portion of return loss curve bump towards 10dB point. The distance between each resonant point for all these sub-structures can be obtained from summary Table 2. Another important observation is that this structure lacks a resonant point in between and thus providing lesser bandwidth. Also, the return loss curve is hovering around the threshold point of 10dB. This is a result of widely separated resonant points. Therefore, an optimized structure should possess more resonant points spaced efficiently in order to get better bandwidth.

The next sub structure shown in Fig. 22, is the full integrated structure with only circular wedges at the bottom edge of top and bottom patch. This eighth structure exhibits similar behavior as the sixth structure except there is a little shift in the lower resonant points as shown in Table 2. The important parameter of this sub-structure is the diameter of the circular wedges. The parametric study is carried out by varying the diameter of circular wedges in this sub-structure and the corresponding return loss curve is shown in Fig. 23. The parametric study shows that the diameter of these circular wedges affects the lower resonant points and thus moves the lower resonant points towards lower frequency as the diameter increases.

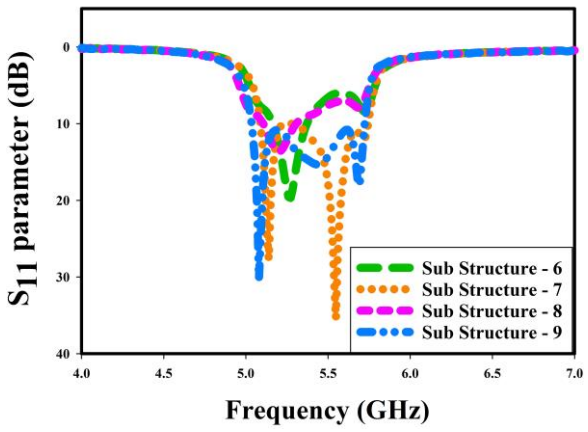

Fig. 15. Return loss curve - Integrated structure with different structural changes.

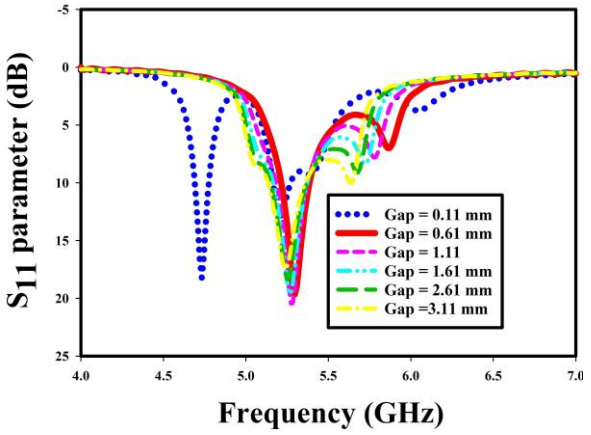

Fig. 16. Sub structure 6 - Return loss of parametric analysis L_{GAP}.

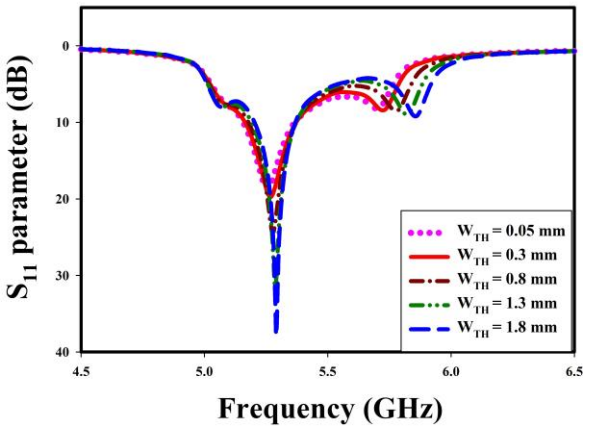

Fig. 17. Sub structure 6 - Return loss of parametric analysis W_{TF}.

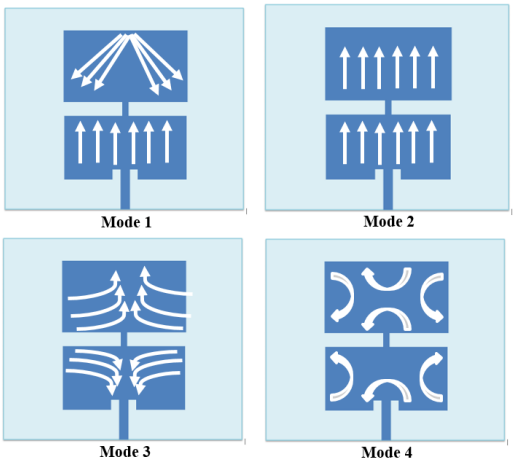

Fig. 18. Sub structure 6 - CMA current modes.

The ninth and final structure is the complete integrated structure with all the modifications as shown in Fig. 1. The return loss curve in Fig. 15, shows that this integrated structure possesses better bandwidth compare to all other sub structures. Also, the MS curve from the CMA analysis shows that the resonant points of four different current modes in Table 2 are spaced approximately at an equal distance. The distance between mode 1 and mode 2 resonant point is ~210MHz. The distance between mode 1 and mode 3 resonant point is ~270MHz. The distance between mode 3 and mode 4 resonant point is ~170MHz. This clearly explains the reason for exhibiting better performance compare to other sub structures.

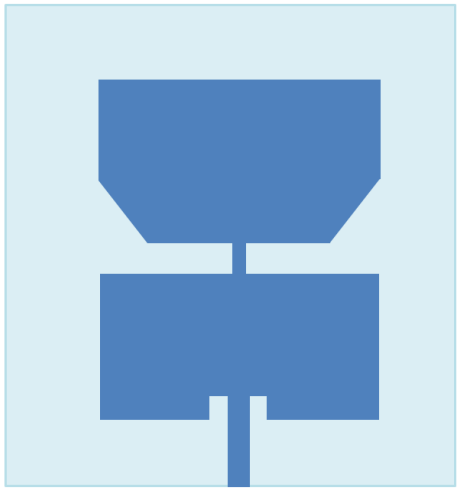

Fig. 19. Sub structure 7 - Integrated patch with only triangular cuts.

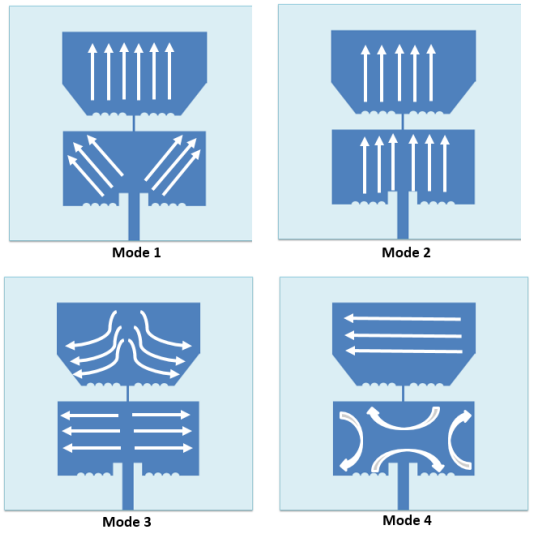

Fig. 20. CMA current modes for sub-structures 7, 8 and 9.

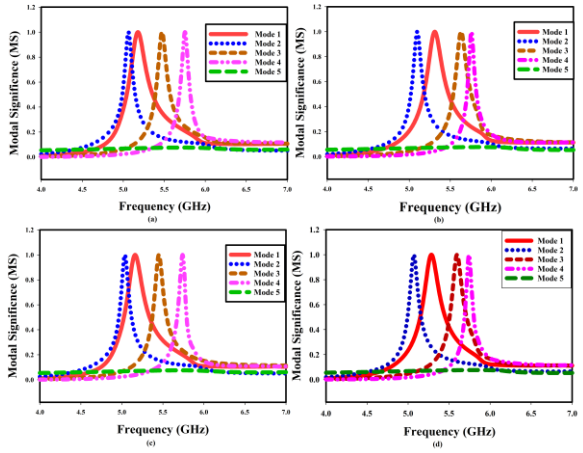

Fig. 21. CMA modal significance curve for sub-structures: (a) 6, (b) 7, (c) 8, and (d) 9.

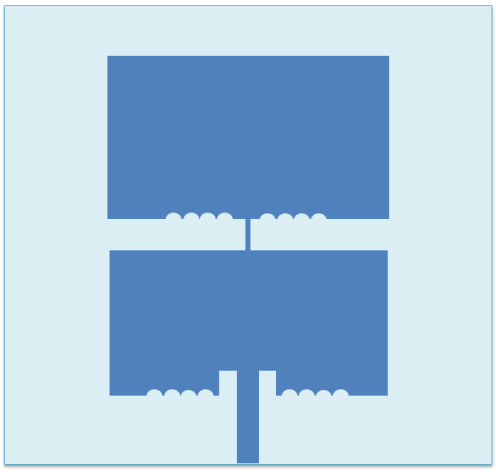

Fig. 22. Sub structure 8 - Integrated patch with only circular wedges.

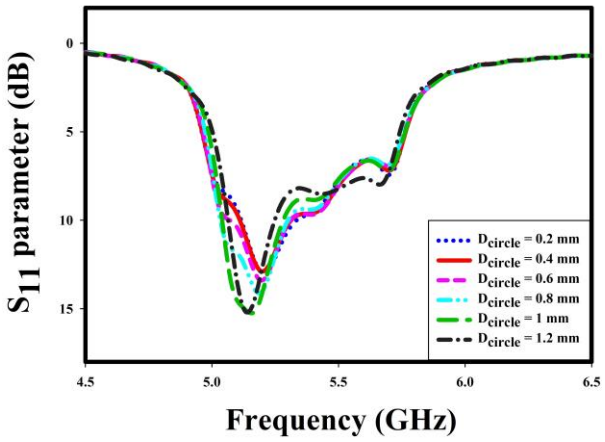

Fig. 23. Sub structure 8 - Return loss curve by sweeping D_{circle}.

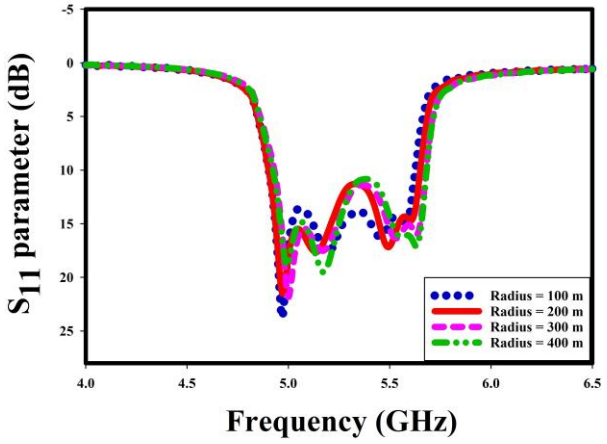

Fig. 24. Sub structure 9 - Return loss curve by sweeping the radius of curvature of fuselage.

Table 1: Resonant points of sub-structures 1 to 5

Sub Structure	1	2	3	4	5
Frequency (GHz)	5.16	5.12	5.16	5.33 & 5.66	5.08

Table 2: Resonant points of sub-structures 6 to 9 obtained through CMA

Sub Structure	6	7	8	9
Mode1 (GHz)	5.18	5.21	5.16	5.3
Mode2 (GHz)	5.063	5.1	5.035	5.074
Mode3 (GHz)	5.47	5.64	5.45	5.57
Mode4 (GHz)	5.756	5.76	5.74	5.74
Mode5 (GHz)	x	x	x	x

As this antenna is meant for aircraft application and will be mounted on the aircraft fuselage in the end application, it is important to analyze the return loss curve for different radius of curvature. The return loss curve for different radius of curvature is shown in Fig. 24. At different radius of curvature, the separation between the intermediate resonant points tend to move and bumps the return loss curve towards 10dB point. Still the return loss magnitude is kept higher than 10dB within the bandwidth. To improve the performance further across different radius of curvature, the parameters has to optimized independently for each radius of curvature.

III. RESULTS AND DISCUSSIONS

The proposed design is manufactured and tested for its performance. The manufactured antenna is conformed on top of two different cylindrical structures made of Aluminum (Al) and Carbon Fiber Composites (CFC) before taking the measurement as shown in Fig. 25. Mounting on these materials is very important because in the actual application this antenna is intended to be mounted on the aircraft fuselage. The aircraft fuselage is made of these composite materials in order to reduce the weight and thus to improve the payload [19]. The conventional techniques (e.g., increasing the thickness of substrate and Defected ground structure) used for improving micro-strip antenna bandwidth is not suitable for aircraft applications as the structure needs to support the conformability and also the fuselage is made of electrically conducting material (Al & CFC).

The return loss performance is measured with the help of network analyzer and the result is shown in Fig. 26. The measured return loss curves with both Al and CFC as fuselage, show good agreement with simulation results. This specific design achieves approximately 400% more bandwidths compare to a single patch antenna with a same substrate material and thickness. The maximum measured gain of 9.53dB is 76% more than a single patch gain of 7.1dB. It helps in reducing the transmitter power. The gain characteristics of the proposed antenna with different fuselage material mount is included in the Table 3. The measured antenna gain and the radiation efficiency at different frequency points inside the bandwidth is shown in Fig. 27. The reason for the difference in gain across frequency is the variation in current flow. The gain is more at frequencies where the current flows in both the patches and the gain is less where the current flows in only one patch. The radiation pattern of the antenna is depicted in Fig. 28 and Fig. 29.

The power requirement of the system is estimated again using the equations 1 to 6. With the proposed antenna having a gain of 9.53dB, the required transmitter power is calculated to be ~600W. Assuming a formation of 23X23 phased array structure with the proposed antenna, the estimated gain would be ~36.53dB. Therefore, it would require approximately 1W of transmitting power for this phased array structure.

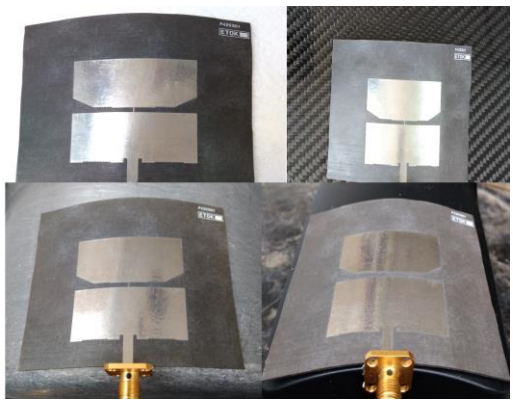

Fig. 25. Fabricated antenna conformed to aluminum and CFC cylindrical structure.

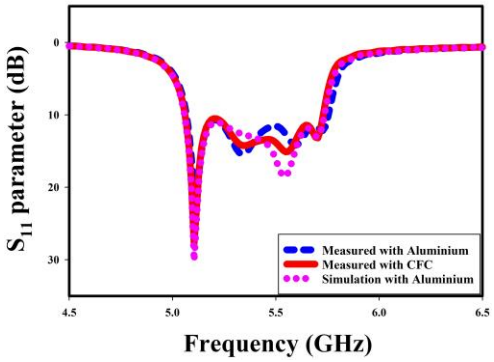

Fig. 26. The measured and simulated return loss plot of the antenna.

Table 3: Gain characteristics of proposed antenna at 5.3GHz with different substrate materials

Simulation/ Measured	Fuselage Material	Gain (dB)	Efficiency (%)
Simulation	Aluminum	9.3	92.7
Measured	Aluminum	9.15	92.5
Measured	CFC	9.53	93

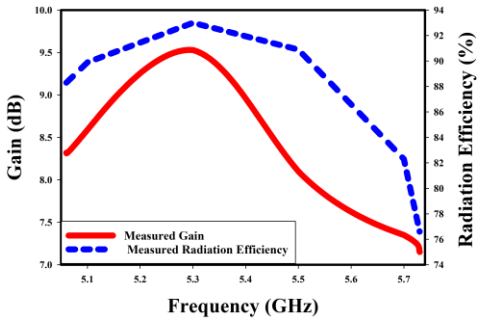

Fig. 27. Gain and efficiency curve across bandwidth.

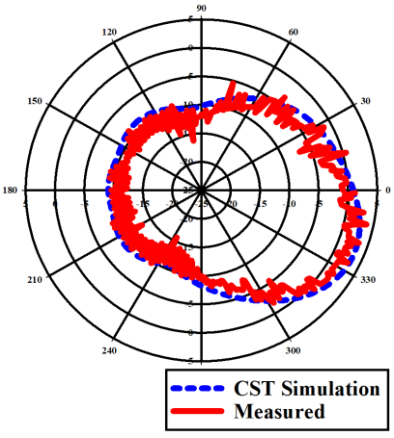

Fig. 28. Radiation pattern E-co.

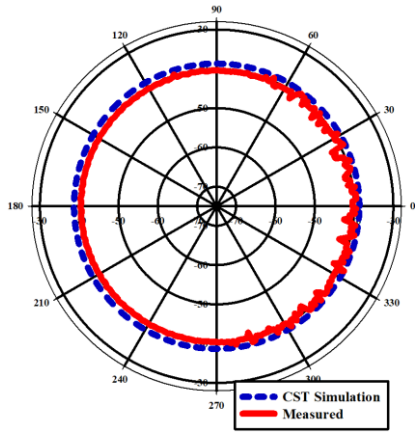

Fig. 29. Radiation pattern H-cross.

IV. CONCLUSION

A unit conformal micro-strip patch antenna is designed to provide a bandwidth of 700MHz and a gain of 9.53dB. With the increased bandwidth and conformal nature this design perfectly suits for DATG application. The achieved bandwidth helps in improving the data rate of internet connectivity inside the aircraft. The simulation results and measurement data are closely matching. In future, this work can be extended to phased array with beam steering capability. This phased array can be integrated into a DATG system to provide high speed internet or a communication link between the ground station and the aircraft. Also, this proposed structure can be analyzed further by changing the circular wedges and triangular cuts into different shapes to improve the performance.

REFERENCES

[1] D. Martinez, B. Ebenhack, and T. Wagner, *Energy Efficiency - Concepts and Calculations*, Elsevier Science Inc., May 10, 2019.

[2] S. K. Kearns, T. J. Mavin, and S. Hodge, *Engaging the Next Generation of Aviation Professionals*, Taylor and Francis Group, London, Nov. 8, 2019.

[3] T. Cooper, I. Reagan, C. Porter, and C. Precourt, *Global Fleet & MRO Market Forecast Commentary 2019–2029*, Oliver Wyman, Jan. 14, 2019.

[4] C. Binns, *Aircraft Systems: Instruments, Communications, Navigation, and Control*, John Wiley & Sons, Inc., New Jersey, Oct. 12, 2018.

[5] D. Stacey, *Aeronautical Radio Communication Systems and Networks*, John Wiley & Sons, Inc., New Jersey, Feb. 22, 2008.

[6] "Harmonised Standard for access to radio spectrum, Broadband Direct Air-to-Ground Communications; Equipment operating in the 1900 MHz to 1920 MHz and 5 855 MHz to 5 875 MHz frequency

bands; Beam-forming antennas," *Harmonised European Standard*, ETSI EN 303 316 V1.2.0 (2017-11).

[7] "Compatibility/sharing studies related to PMSE, DECT and SRD with DA2GC in the 2 GHz unpaired bands and MFCN in the adjacent 2 GHz paired band," *Electronic Communication Committee*, Approved Sep. 2014.

[8] "Systems for public mobile communications with aircraft-M Series Mobile, radio determination, amateur and related satellite service," *ITU-R M.2282-0 Electronic Publication*, Geneva, 2014.

[9] L. Ahlin and J. Zander, "Principles of Wireless Communications," *Student Litterateur*, Sweden, 1998.

[10] A. W. Graham, N. C. Kirkman, and P. M. Paul, *Mobile Radio Network Design in the VHF and UHF Bands: A Practical Approach*, John Wiley & Sons Ltd., Nov. 17, 2006.

[11] R. El Hattachi and J. Erfanian, "5G white paper," *NGMN Alliance*, ver. 1.0, Feb. 17, 2015.

[12] Avionics Department of Naval Air Warfare Center Weapons Division (NAWCWD TP 8347), *Electronic Warfare and Radar Systems Engineering Handbook*, Fourth Edition, Point Mugu, CA 93042, Oct. 2013.

[13] S. Alam, E. Wijanto, B. Harsono, F. Samandatu, M. Upa, and I. Surjati, "Design of array and circular polarization microstrip antenna for LTE communication," *MATEC Web of Conferences (ICIEE-2018)*, vol. 218, 2018.

[14] J. Monica and P. Jothilakshmi, "Gain enhanced conformal patch antenna with defected ground for aircraft applications," *IET Communications*, vol. 14, no. 2, pp. 290-299, Jan. 2020.

[15] M. Cabedo-Fabres, E. Antonino-Daviu, A. Valero-Nogueira, and M. Ferrando Bataller, "The theory of characteristic modes revisited: A contribution to the design of antennas for modern applications," *IEEE Antennas and Propagation Magazine*, vol. 49, no. 5, Oct. 2007.

[16] J. F. Liu, W. Tang, M. Wang, H. C. Zhang, H. F. Ma, X. Fu, and T. J. Cui, "A dual-mode UWB antenna for pattern diversity application," *IEEE Transactions on Antennas and Propagation*, vol. 68, no. 4, pp. 3219-3224, Apr. 2020.

[17] P. Liu, W. Jiang, S. Sun, Y. Xi, and S. Gong, "Broadband and low-profile penta-polarization reconfigurable metamaterial antenna," *IEEE Access*, vol. 8, pp. 21823-21831, 2020.

[18] G. Gao, R.-F. Zhang, W.-F. Geng, H.-J. Meng, and B. Hu, "Characteristic mode analysis of a non uniform metasurface antenna for wearable applications," *IEEE Antennas and Wireless Propagation Letters*, vol. 19, no. 8, pp. 1355-1359, Aug. 2020.

[19] A. Hiken, *Aerospace Engineering - 'The Evolution of the Composite Fuselage: A Manufacturing Perspective*, IntechOpen, Nov. 20, 2019.

J. Monica completed her B.E. degree in Electronics and Communication Engineering from Anna University in 2013 and M.E. degree in Communication Systems under Anna University in 2015. Currently pursuing her Ph.D. from Anna University, Chennai, India. Her research works is in the areas of Antennas and wireless propagations, Aircraft antennas, Microwave design and conformal antenna design. She has published papers in SCI indexed International journals and conferences.

P. Jothilakshmi completed her B.E. degree in Electronics and Communication Engineering from University of Madras, in 1996 and M.E. degree in Communication Systems from Madurai Kamaraj University, in 2000. She completed her Ph.D. degree from Anna University, Chennai, India. She is serving as a Teacher from 1996 onwards. She is currently serving as a Professor in ECE at Sri Venkateswara College of Engineering, Chennai, India. She is an active fellow in professional societies ISTE, IETE and IAENG. She lead several numbers of B.E. and M.E. and Ph.D. level project. She has published several SCI indexed; Scopus indexed International journal papers. She presented and published papers in International and National Conference. Her research area is Microwave antenna design and Wireless Communication.

A Compact Broadband Circularly Polarized Slot Antenna for Universal UHF RFID Reader and GPS

Canjie Chen and Quanyuan Feng

School of Information Science and Technology
Southwest Jiaotong University, Chengdu, 610031, China
1770371408@qq.com, fengquanyuan@163.com

Abstract ─ A novel compact printed broadband circularly polarized slot antenna is proposed in this paper. The antenna consists of an inverted L-shaped coplanar waveguide feed structure and a square ground plate loaded with three rectangular slots. The antenna achieves good impedance matching and circular polarization characteristics by adjusting the size of the L-shaped band and the rectangular slot. The simulation results show that the antenna has a 10-dB impedance bandwidth of 1360 MHz (690-2050 MHz) and a 3 dB axial ratio (AR) bandwidth of 490 MHz (770-1260 MHz). Additionally, the maximum gain reached 4.02 dBi. The antenna proposed in this paper can be applied to UHF RFID and GPS frequency bands.

Index Terms ─ Axial Ratio (AR), Coplanar Waveguide (CPW), Circularly Polarized (CP), Global Positioning System (GPS), RFID reader, Ultrahigh Frequency (UHF).

I. INTRODUCTION

Radio Frequency Identification (RFID) technology is a non-contact automatic identification technology [1], which uses the spatial coupling effect of electromagnetic waves to send and receive information between the electronic tag and the reader. RFID can be used in various harsh environments and high-speed moving objects and can identify multiple electronic tags simultaneously [2]. It has the advantages of waterproof, anti-magnetic, high-temperature resistance, and ample storage data capacity. At present, RFID technology has been widely used in supermarkets, automated production, logistics, access control, transportation, and other fields [3].

The tags and readers of the RFID system have their antennas. In actual use, the tag antenna is mostly linearly polarized (LP) [4]. While the circularly polarized antenna can receive electromagnetic waves of any polarization type signal and reduce space loss caused by multipath effects, RFID reader antennas are mostly circularly polarized (CP) antennas.

At present, the frequency bands used by RFID in each country have strict standards. For example, the UHF RFID frequency bands used in China are 840.5-844.5 MHz and 920.5-924.5 MHz, and North America are 902-928 MHz, Japan is 950-955 MHz, Europe is 866-869 MHz, and South Korea is 908.5-914 MHz [5-6], etc. Given the different frequency band standards of various countries, we need to design a reader antenna applied to all UHF frequency bands.

In recent years, people have done a lot of research on RFID reader antennas. In [7], a circularly polarized reader antenna using coaxial line feed was proposed. In [8-9], a patch antenna with an asymmetric circular slot was presented, and the size of the antenna was reduced by slotting. In [10], the air dielectric layer is used to broaden the impedance bandwidth. However, the above-mentioned antenna structure has the disadvantages of too narrow bandwidth and too large volume. To achieve full coverage of the UHF frequency band, in [11-13], a wide frequency band was achieved by using a laminated structure, while these antennas also face problems such as excessive size and complex feeding structure. The use of CPW-fed slot antennas solves the problems mentioned above to a certain extent. In [14-15], the bandwidth to cover the UHF band was obtained by using a suitable CPW feed structure and loading slots on the floor.

Global Positioning System (GPS) is a high-precision positioning system based on artificial earth satellites. In the working frequency band of the GPS, the L2 frequency band (1.215-1.237 GHz) is used for military operations, and the L1 frequency band (1.575 GHz) is used in the civil field [16], and the L5 frequency band (1176.45 MHz) is used for high-precision positioning. In recent years, there has been some research work focusing on the integration of RFID and GPS antennas. In [17-18], a dual-frequency circularly polarized antenna applied to RFID and GPS frequency bands was presented, while the AR bandwidth and impedance bandwidth of the proposed antenna only cover a part of the RFID. A planar tri-band antenna for RFID, GPS, and WLAN was proposed in [19], while the antenna did not achieve circular polarization and the bandwidth only covered part of the RFID frequency band.

In this paper, we present a compact printed

Submitted On: January 29, 2021
Accepted On: April 17, 2021

https://doi.org/10.47037/2020.ACES.J.360513

broadband circularly polarized slot antenna for universal UHF RFID readers and GPS. By adjusting the size of the L-shaped patch and the rectangular slots loaded on the floor achieves wider impedance bandwidth and good AR bandwidth. The experimental results show that the proposed antenna obtains a 10-dB return loss bandwidth of 1360 MHz (690-2050 MHz) and a 3-dB AR bandwidth of about 490 MHz (770-1260 MHz), and the impedance bandwidth and AR bandwidth of the antenna cover RFID UHF and GPS L2 and L5 frequency bands.

II. PROPOSED ANTENNA CONFIGURATION

Figure 1 shows the geometric structure of the compact printed broadband circularly polarized slot antenna proposed in this paper. The antenna is etched on an FR4 substrate with a relative dielectric constant of 4.4, loss tangent value of 0.02, and thickness of 1.6 mm. The side length of the substrate is L=120 mm, and a square groove with a side length of W=94 mm is engraved in the middle of the substrate. A rectangular slot with a size of W7 × L8 in the square ring to place the antenna's feeder, and three rectangular slots of different sizes were loaded on the right side of the square ring. The size of the proposed antenna can be roughly estimated by the following formula [6]:

$$L = \frac{c}{2f\sqrt{\frac{2}{\varepsilon_r + 1}}}, \quad (1)$$

where ε_r is the dielectric permittivity, c is the speed of light in free space, and f is the resonant frequency.

In order to understand the principle of the proposed antenna model clearly, we present the three-step design process of the antenna prototype (Ant.1, Ant.2, and Ant.3) in Fig. 2. The simulation results of impedance bandwidth and axial ratio at each stage are shown in Fig. 3. Ant.1 is the most original antenna that consists of a reverse L-shaped strip and a square floor with rectangular slots on the right. From Fig. 3 (a), we can see that the reflection coefficients S_{11} of Ant.1 near 825 MHz and 1.57 GHz is less than -10dB, while the polarization type of the antenna is linear polarization. To improve the performance of the antenna, a rectangular slot (L4 × W4) was loaded base on Ant.1 to obtain Ant.2, and then Ant.2 expands the impedance bandwidth generated by the two resonance points of Ant.1, and generates a new resonance point near 700 MHz, thereby expanding the impedance bandwidth of the antenna. It can be seen from Fig. 3 (b) that the Ant.2 achieves circular polarization around 1.25 GHz. The third step is to introduce a rectangular slot (L5× W5) on the basis of Ant.2 to obtain the final Ant.3. The Ant.3 has good impedance bandwidth and circular polarization characteristics. Table 1 lists the dimensions of the proposed antenna, and the physical diagram of the proposed antenna is shown in Fig. 1 (c).

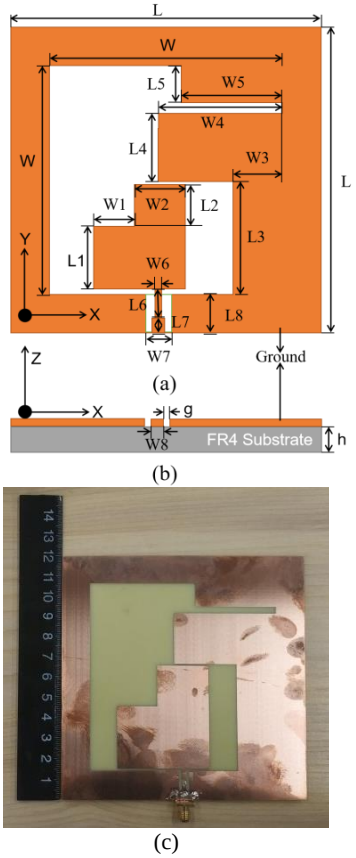

Fig. 1. The geometric structure and physical picture of the proposed antenna: (a) geometry (top view), (b) geometry (side view), and (c) physical picture.

Table 1: Parameters of the proposed antenna (unit: mm)

Parameter	Size	Parameter	Size
L	120	W	92
L1	30	W1	20
L2	20	W2	25
L3	52	W3	19.5
L4	25	W4	50
L5	11.5	W5	39.5
L6	10	W6	2
L7	5	W7	5
L8	14	W8	4
g	0.5	h	1.6

Fig. 2. Three step design process of the circularly polarized slot antenna.

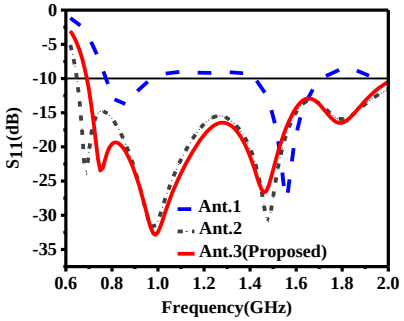

(a)

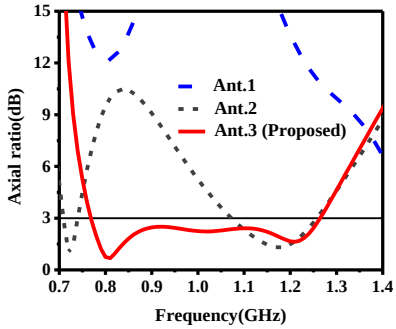

(b)

Fig. 3. Simulated reflection coefficients S_{11} (a) and axial ratio (b) for Ant 1, 2, and 3(proposed antenna).

III. PARAMETERS ANALYSIS AND DISCUSSION

In this paper, the simulation software Ansoft HFSS 18 is used to simulate the antenna. To determine the best antenna parameters, a detailed simulation analysis of each parameter is required. When analyzing the influence of a specific parameter on the antenna performance, other parameters remain unchanged.

Figure 4 shows the effect of the L1 change on impedance bandwidth. We can see that the resonance point of the antenna's low-frequency part shifts to the right when L1 increases from 25 mm to 35 mm, and the impedance matching becomes worse, on the contrary, the impedance matching of the high-frequency part becomes better. Therefore, we can adjust the value of L1 to obtain good impedance matching characteristics for the antenna.

The influence of adjusting the length of W1 on the simulated reflection coefficient S_{11} is shown in Fig. 5. When W1=16 mm, the reflection coefficient S_{11} of the antenna is only from 0.7 GHz to 1.6 GHz, and when W1 is increased to 20 mm, the antenna obtains a good impedance bandwidth. Meanwhile, we noticed that when W1 continues to increase to 24 mm, the impedance matching of the antenna will become very awful at 1.25 GHz.

The effect of changing the length of W6 on the reflection coefficient S_{11} of the antenna is shown in Fig. 6. It can be noted that changing the value of W6 has significant impact on the resonance depth of the S_{11} parameter. When W6 is increased from 1 mm to 2 mm, the impedance bandwidth of the antenna becomes more expansive. Adjusting W6 helps to broaden the impedance bandwidth of the antenna.

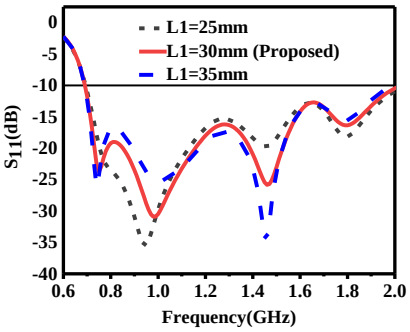

Fig. 4. Simulated reflection coefficients S_{11} with different L1.

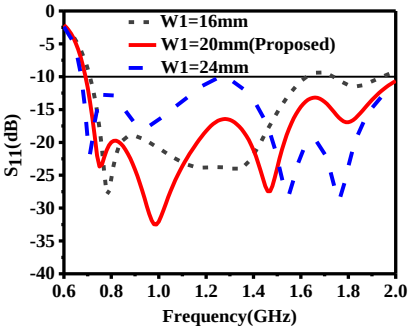

Fig. 5. Simulated reflection coefficients S_{11} with different W1.

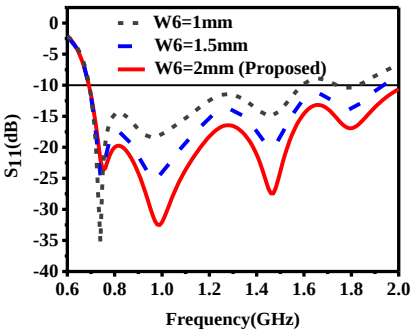

Fig. 6. Simulated reflection coefficients S_{11} with different W6.

Figure 7 shows the effect of W4 on the simulated AR bandwidth. As shown in the figure, when the value of W4 increases, it mainly affects the starting frequency of the AR bandwidth without influence the cut-off frequency of the antenna AR bandwidth. When W4=50 mm, the antenna obtains the best AR bandwidth, and

when W4 increases to 52 mm, the AR bandwidth of the antenna becomes very poor. Therefore, adjusting W4 is beneficial to control the starting frequency of the AR bandwidth.

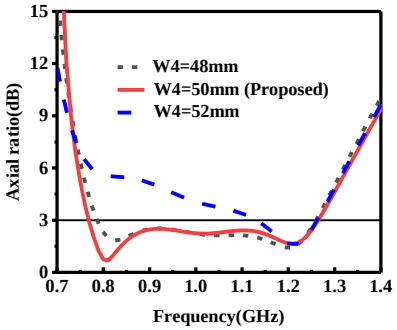

Fig. 7. Simulated results of axial ratio with different W4.

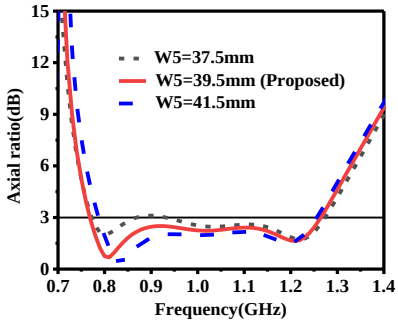

Fig. 8. Simulated results of axial ratio with different W5.

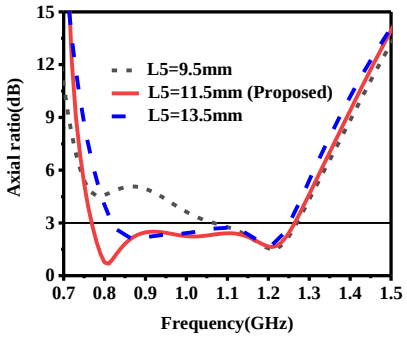

Fig. 9. Simulated results of axial ratio with different L5.

Figure 8 shows the influence of W5 on the simulated axial ratio bandwidth. It can be seen that the change in length of W5 mainly affects the low-frequency part of the axial ratio, while the impact on the axial ratio of cutoff frequency has less influence. Therefore, we can obtain the best axial ratio bandwidth by adjusting the length of W5.

As shown in Fig. 9, the value of L5 increased has a significant influence on the axial ratio between 0.77-1.1 GHz, while has a slight effect on the axial ratio after 1.1 GHz. Therefore, the starting frequency of the axial ratio bandwidth can be controlled by adjusting the value of L5.

IV. RESULTS AND DISCUSSION

Figure 10 shows the comparison between simulated and measured results of reflection coefficient and axial ratio. As shown in Fig. 10 (a), the antenna's impedance bandwidth simulated result is 1360 MHz (690-2050 MHz), and the measured result is 1420 MHz (680-2100 MHz). We notice that the simulated results of the reflection coefficient S_{11} are similar to the measured results, however, due to the differences between the simulation conditions and the measured environment, as well as the manufacturing tolerance, the resonance frequency of the reflection coefficient S_{11} shifts slightly to the right. It should be noted that the reflection coefficient S_{11} is measured by the vector network analyzer model of Agilent E5071C.

Figure 10 (b) illustrates the comparison between the simulated and measured results of the axial ratio bandwidth. As shown in the figure, the simulated axial ratio bandwidth is 490 MHz (770-1260 MHz), while the measured axial ratio bandwidth is 393 MHz (870-1263 MHz). The discrepancy between the simulated and the measured results at the starting frequency is mainly due to the antenna measuring system effect and tolerances in the manufacturing process, while the rest of the AR simulation and test results have a good consistency. It can be seen from Fig. 10 that the impedance bandwidth and axial ratio bandwidth of the proposed antenna have covered the RFID UHF frequency band and the L2 and 15 frequency bands of GPS. The far-field data of the antenna is measured in the anechoic chamber.

The simulated and measured maximum gain of the proposed antenna is shown in Fig. 11. It can be seen that the antenna gain in the entire circular polarization frequency band is greater than 2.5 dBi, and the gain in the GPS L2 and L5 frequency bands is greater than 3 dBi. The simulation and measurement results of maximum gain show good consistency.

In Table 2, we compare some antennas that work in the global UHF RFID and GPS frequency bands. As shown in Table 2, the antennas proposed in [11-12] and [15, 20, 21] use a stacked structure to obtain high gain, but there are problems of complex design and large volume. In addition, although the antenna in [22] has a small volume, its bandwidth only covers a part of the RFID UHF frequency band and GPS L5 frequency band, and it does not achieve circular polarization characteristics. Compared to above-mentioned antennas, the proposed antenna has achieved wider impedance and axial ratio bandwidth with a simpler and smaller structure.

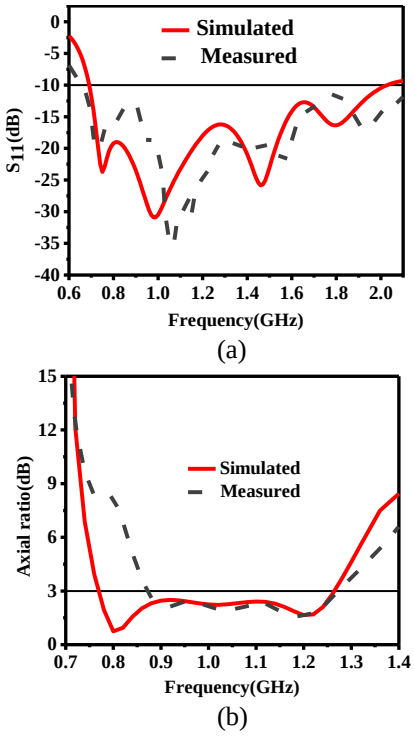

Fig. 10. Measured and Simulated results of reflection coefficients S_{11} and axial ratio of the proposed antenna. (a) Reflection coefficients and (b) axial ratio.

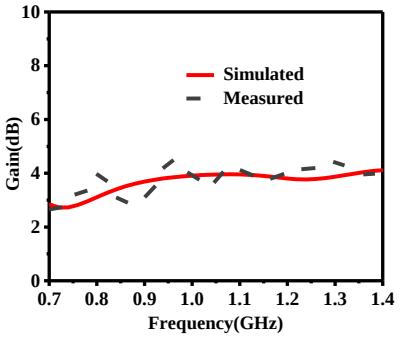

Fig. 11. Simulated and measured gain of the proposed antenna.

In order to understand the principle of circular polarization of the proposed antenna fully, Fig. 12 shows the simulated current distribution of the antenna in the four phases of 0°, 90°, 180°, and 270° at 900 MHz. As shown in the figure, with the increase of the phase angle, the current distribution on the antenna surface from the +z direction propagates in the clockwise direction. The currents at 0° and 90° have the same amplitude, but the phase is opposite, and the currents at 0° and 180° have the same amplitude and a relative phase shift of 180°, and then the antenna obtains left-handed circular polarization (LHCP) radiation in the +z direction.

Table 2: Comparison of the referenced and proposed antenna

Ref.	10-dB RL BW (MHz, %)	3-dB AR BW (MHz, %)	Gain (dBi)	Size (mm^3)
[11]	758-983 25.8	838-959 13.5	8.6	250×250 ×24.5
[12]	760-963 25.6	818-964 16.4	8.3	250×250 ×35
[15]	685-1125 48.6	836-986 16.5	8.6	250×250 ×60
[20]	833-960 14.2	846-926 9.3	7.3	150×150 ×25
[21]	730-990 30.2	760-970 24.2	5.3	150×150 ×21
[22]	900-1610 56.5	—	3.1	123×31× 1.6
Our work	690-2050 99.3	770-1260 48.3	4.02	120×120 ×1.6

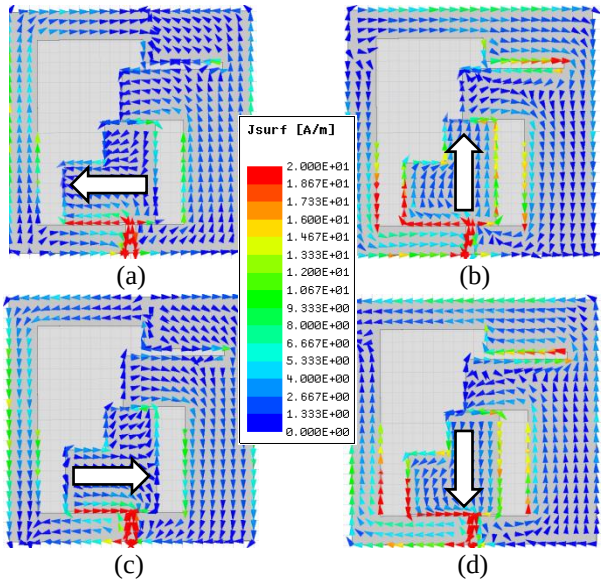

Fig. 12. Distribution of the surface current at 900 MHz with four phase angles: (a) 0°, (b) 90°, (c) 180°, and (d) 270°.

Figure 13 shows the simulated and measured radiation pattern of the proposed antenna at the XZ- plane (Phi=0°) and YZ-plane (phi=90°) at 0.9 GHz and 1.23 GHz. As shown in the figure, the simulated and measured radiation patterns are approximately equal to each other. It can be observed from Fig. 13 that the proposed antenna exhibits left-handed circular polarization (LHCP) in the +z direction and right-handed circular polarization (RHCP) in the -z direction. Therefore, the proposed antenna has good bidirectional radiation characteristics.

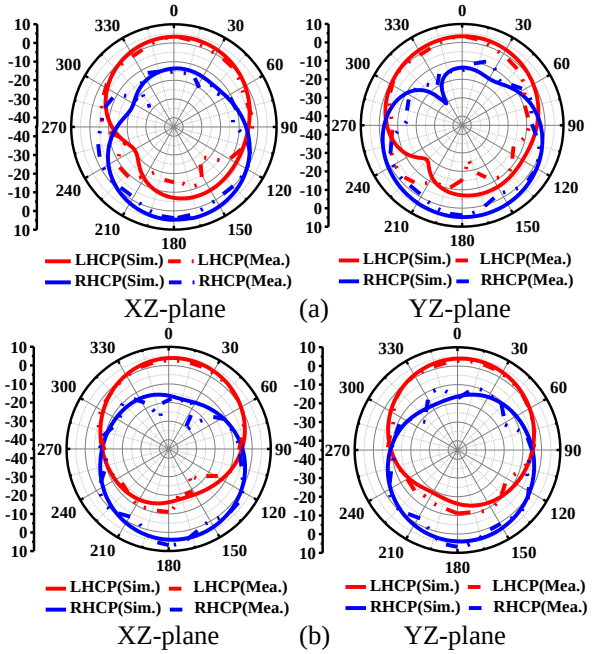

Fig. 13. Simulated and measured radiation patterns at: (a) 0.9 GHz and (b) 1.23 GHz of the proposed antenna.

V. CONCLUSION

In this paper, a compact broadband circular polarization slot antenna is proposed, which can work in RFID UHF and GPS L2 and L5 bands. The antenna consists of a reverse L-shaped CPW feeder and a square floor loaded with three rectangular slots. By adjusting the L-shaped strip and rectangular slot, the antenna can obtain good impedance matching and circular polarization characteristics. The simulation results show that the proposed antenna can achieve a 10-dB impedance bandwidth of 1360 MHz (690-2050 MHz) and a 3-dB axial ratio bandwidth of 490 MHz (770-1260 MHz), and the maximum gain reached 4.02 dBi. Compared with antennas of similar dimensions, the proposed antenna has achieved wider impedance and axial ratio bandwidth with simpler and smaller structure.

ACKNOWLEDGMENT

This work is supported by Key Project of the National Natural Science Foundation of China under Grants 62090012, 62031016 and 61831017 and the Sichuan Provincial Science and Technology Important Projects under Grants 2019YFG0498, 2020YFG0282, 2020YFG0452 and 2020YFG0028 and the Science and Technology Commission Project under Grant 19-163-21-TS-001-062-01.

REFERENCES

[1] Z. Wang, R. She, J. Han, S. Fang, and Y. Liu, "Dual-band dual-sense circularly polarized stacked patch antenna with a small frequency ratio for UHF RFID reader applications," *IEEE Access*, vol. 5, pp. 15260-15270, July 2017.

[2] M. H. Zolghadri and S. Jam, "A wideband circular polarization antenna for UHF tags," *Applied Computational Electromagnetics Society (ACES) Journal*, vol. 33, no. 3, pp. 319-324, Mar. 2018.

[3] T. Björninen, J. Virkki, and L. Ukkonen, "Small square-shaped slot antenna for wearable passive UHF RFID tags," *2017 International Applied Computational Electromagnetics Society Symposium (ACES)*, pp. 1-2. Aug. 2017.

[4] W. Luo, R. B. He, and P. Wang, "Overview of the design strategies for the circularly polarized UHF RFID tag antenna," *2019 Photonics Electromagn. Res. Symp. - Fall, PIERS - Fall 2019 – Proc.*, pp. 2683-2685, Dec. 2019.

[5] Z. Du, Z. Wu, M. Wang, J. Rao, and P. Luo, "Compact quasi-yagi antenna for handheld UHF RFID reader," *Applied Computational Electromagnetics Society (ACES) Journal*, vol. 30, no. 8, pp. 860-865, Aug. 2015.

[6] J. D. Teran Guerra, E. A. Morales Gonzalez, F. Lopez Huerta, I. Arceo Rosas, R. Lopez Leal, and J. Martinez Castillo, "Patch antenna design for UHF RFID systems," *2019 IEEE Int. Conf. Eng. Veracruz (ICEV)*, pp. 1-5,Oct. 2019.

[7] C. Yang, Y. Yao, J. Yu, and X. Chen, "Novel compact circularly polarized antenna with high front-to-back ratio for UHF RFID reader applications," *Asia-Pacific Microw. Conf.*, pp. 1358-1361, Dec. 2011.

[8] Nasimuddin, Z. N. Chen, and X. Qing, "Asymmetric-circular shaped slotted microstrip antennas for circular polarization and RFID applications," *IEEE Trans. Antennas Propag.*, vol. 58, pp. 3821-3828, Dec. 2010.

[9] E. Ghanem, E. A. Abdallah, and M. A. Aboul-Dahab, "A circularly polarized printed antenna with modified slots and slits for RFID reader," *2019 Photonics Electromagn. Res. Symp. - Fall, PIERS - Fall 2019 – Proc.*, pp. 1260-1264, Dec. 2019.

[10] Y. Zhang, B. Wang, and J. Huang, "Circularly polarized truncated microstrip antenna for UHF RFID reader," Proc. *2019 IEEE 2nd Int. Conf. Autom. Electron. Electr. Eng (AUTEEE)*, pp. 468-471, Nov. 2019.

[11] Z. Wang, S. Fang, S. Fu, and S. Jia, "Single-fed broadband circularly polarized stacked patch antenna with horizontally meandered strip for universal UHF RFID applications," *IEEE Trans. Microw. Theory Tech.*, vol. 59, no. 4, pp. 1066-1073, Apr. 2011.

[12] Z. N. Chen, X. Qing, and H. L. Chung, "A universal UHF RFID reader antenna," *IEEE Trans. Microw. Theory Tech.*, vol. 57, no. 5, pp. 1275-1282,

May 2009.
[13] C. Y. D. Sim and C. J. Chi, "A slot loaded circularly polarized patch antenna for UHF RFID reader," *IEEE Trans. Antennas Propag.*, vol. 60, no. 10, pp. 4516-4521, Oct. 2012.
[14] J. Lu and S. Wang. "Planar broadband circularly polarized antenna with square slot for UHF RFID reader," *IEEE Trans. Antennas Propag.*, vol. 61, no. 10, pp. 45-53, Sept. 2013.
[15] C. Sim, Y. Hsu, and G. Yang, "Slits loaded circularly polarized universal UHF RFID reader antenna," *IEEE Antennas Wireless Propag. Lett.*, vol. 14, pp. 827-830, Apr. 2015.
[16] C. Sun, H. Zheng, and Y. Liu, "Analysis and design of a low-cost dual-band compact circularly polarized antenna for GPS application," *IEEE Trans. Antennas Propag.*, vol. 64, no. 1, pp. 365-370, Jan. 2016.
[17] N. M. Sahar, M. T. Islam, and N. Misran, "A reconfigurable multiband antenna for RFID and GPS applications," *Elektron. ir Elektrotechnika*, vol. 21, no. 6, pp. 44-51, Oct. 2015.
[18] K. Oh, W. Son, S. Cha, M. Lee, and J. Yu, "Compact dual-band printed quadrifilar antennas for UHF RFID/GPS operations," *IEEE Antennas Wireless Propag. Lett.*, vol. 10, pp. 804-807, Aug. 2011.
[19] R. Patel, A. Desai, and T. Upadhyaya, "An electrically small antenna using defected ground structure for RFID, GPS and IEEE 802.11 a/b /g /s applications," *Prog. Electromagn. Res. Lett.*, vol. 75, pp. 75-81, Apr. 2018.
[20] J. Li, H. Liu, S. Zhang, M. Luo, Y. Zhang, and S. He, "A wideband single-fed circularly-polarized patch antenna with enhanced axial ratio bandwidth for UHF RFID reader applications," *IEEE Access*, vol. 6, pp. 529-551, Oct. 2018.
[21] J. L. Li, H. Liu, S. Zhang, Y. Zhang, and S. He. "Compact broadband circularly-polarised antenna with a backed cavity for UHF RFID applications," *IET Microw. Antennas Propag.*, vol. 13, no. 6, pp. 789-795, May 2019.
[22] Y.-Y. Lu and E. F. Lin, "Design of coplanar dipole antenna with inverted-H slot for 0.9/1.575/2.0/2.4/2.45/5.0 GHz applications," *J. Electr. Electron. Eng.*, vol. 5, no. 2, pp. 38-47, Apr. 2017.

Canjie Chen was born in Wuzhou, Guangxi, China, in 1995. He is currently working toward the Master's degree in Information and Communication Engineering at Southwest Jiaotong University, Chengdu, China. His main research content is antenna design and theory, Mainly in RFID antennas.

Quanyuan Feng (M'06–SM'08) received the M.S. degree in Microelectronics and Solid Electronics from the University of Electronic Science and Technology of China, Chengdu, China, in 1991, and the Ph.D. degree in EM Field and Microwave Technology from Southwest Jiaotong University, Chengdu, China, in 2000. He is the Head of Institute of Microelectronics, Southwest Jiaotong University, Chengdu, China. He has been honored as the "Excellent Expert" and the "Leader of Science and Technology" of Sichuan Province owing to his outstanding contribution. In recent 5 years, more than 500 papers have been published on IEEE Transactions on Antennas and Propagation, IEEE Transactions on Microwave Theory and Techniques, IEEE Antennas and Wireless Propagation Letters etc., among which more than 300 were registered by SCI and EI.

His research interests include integrated circuits design, RFID technology, embedded system, wireless communications, antennas and propagation, microwave & millimeter wave technology, smart information processing, electromagnetic compatibility and RF/microwave devices & materials etc.

GPR Pulse Propagation Topography

Veli E. Voipio

Department of Electronics and Nanoengineering, School of Electrical Engineering
Aalto University, Espoo, P.O. Box 11000, FI-00076 AALTO, FINLAND
veli-erkki.voipio@aalto.fi

Abstract — In this article, I propose a new method for calculating and visualizing the pulse radiation within the depth range commonly used by Ground Penetrating Radar (GPR). The text describes the method and illustrates the propagation with several examples. One conventional method is also applied for a quick comparison. The method can be used to optimize GPR antennas and transmit pulse shapes.

Index Terms — Antennas, FDTD, Ground Penetrating Radar (GPR), patch antenna, propagation, UWB.

I. INTRODUCTION

When using Ground Penetrating Radar (GPR), it is important to know the pulse propagation behavior in the range normally used by GPR. Both the antenna design and the excitation pulse shape affect the radar performance. The proposed method relates to recent research: [1] describes what they call "near field directivity"; [2] uses near field distribution; [3] shows single-frequency far field patterns in dielectric half-space and also discusses the antenna footprint approximation; the total (received pulse) energy concept is used in [4] and [5]; pulse radiation visualizations also exist, e.g., in [6]; ongoing pulse shape research is suggested in [7].

The GPR range is roughly twenty wavelengths downwards into the medium [1]. The radiated field behavior is not trivial that close to the antenna. The antenna and target size and the depth are all of similar magnitude. The wide spectrum means that at a specific point the reactive near field, diffractive (Fresnel) and far field (Fraunhofer) exist simultaneously at various frequencies. [3] mentions: "Near the antennas the fields are more complex and require numerical simulation". According to [7], the GPR radiation patterns do not exhibit far-field behavior. Summing up, new analysis methods should be explored.

In this article, I introduce a new method to calculate the radiation in the ground and to visualize it: the peak amplitude of the simulated pulse (maximal magnitude of the electric field passing the point/pixel/voxel) is stored. That information can be used to create a map of the radiation: a quantitative radiation topography, and it is available for various kinds of postprocessing.

No similar method exists so far to my knowledge, but my method visually resembles those where the contours show color as path loss at height and distance points in the radio propagation, revealing ducting and other possible features [8]. Simulations for the fields near the antenna in the ground have been available for decades, but this kind of calculation of the maximal field value in each point is new. It allows quick estimation of the propagation, although the time and frequency information are lost. One can expect that this calculation method adds a new variable for the research and design: it provides important information to improve the GPR antennas, optimize the transmit pulse, and for the tomography/inverse processing.

The paper is organized as follows. Section II describes the new method. In Section III, there are examples of the calculations, comparing the Gopher antenna [9] with a loaded dipole model. Section IV shows examples for a combined schematic pattern of a bistatic radar antenna. Section V illustrates the effect of the pulse width on radiation topography. Section VI presents conventional pulse radiation solutions applied to the GPR range, and Section VII the far field radiation pattern for comparison. Section VIII discusses a field measurement example. Section IX concludes the article with an evaluation.

II. THE METHOD

The Finite-Difference Time-Domain (FDTD) method with a Gaussian pulse is commonly applied to indicate the wideband spectrum and phase behavior of the electromagnetic waves. Now I am proposing a procedure that stores the highest electric field magnitude (combination of all three field components) during the FDTD simulation in each pixel in a defined plane. As time passes in the FDTD simulation with Gaussian pulse excitation, at each time step in each cell or voxel the field strength is compared to the maximum thus far encountered. If larger, then it becomes the new maximal value. The maximal field strengths in the maps do not occur at the same instant of time. One must interpret it the same way as ducting is visualized in [8]. Commercial and

Submitted On: January 15, 2021
Accepted On: April 18, 2021
https://doi.org/10.47037/2020.ACES.J.360514

academic FDTD codes are available, also for GPR, for example [10] but they cannot be modified by the users. Thus, I have modified the code in [11] for the FDTD simulation. The result can be visualized and used for postprocessing. However, this visualization method does not inform about the time, phase and propagation direction of the signal. Nevertheless, the explorative expectation is that the pulse shape stays reasonably similar in the area of interest. This expectation is evaluated in Section IX.

The Gopher antenna structure in Fig. 1 was used in the simulations. The Gopher antenna is described in [9]. The spacing between the Gopher antenna pair is 100 mm. For comparison, a loaded center-fed wire dipole is defined here as a reasonable representative corresponding to the common commercial loaded dipoles. The dipole used for the comparison is 450 mm long and the dipole pair spacing is 120 mm. The material has a conductivity of 30 S/m in order to achieve a sufficient bandwidth using the low conductivity as an evenly distributed resistive load.

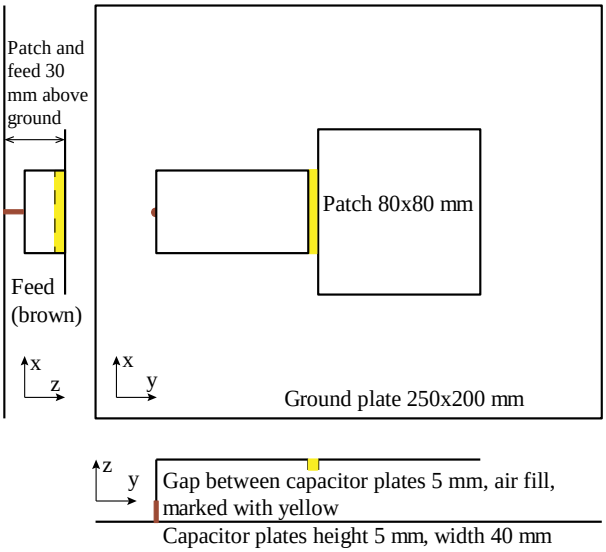

Fig. 1. Gopher antenna structure drawing with dimensions. Material is copper plate 0.5 mm. In FDTD simulations, the perfect electric conductor was used as material.

In this study, the Gopher antenna is filled with neoprene, $\varepsilon_r = 6.7$ to lower the central frequency of the antenna and to improve the matching to the ground (commonly $\varepsilon_r = 6$–8 in the ground). Both the dipole and the Gopher antennas have a wide spectrum and a good Gaussian pulse response: the central frequency of the Gopher antenna with the neoprene fill is 440 MHz, and the spectrum with the -10 dB of the maximal power limit is 220–630 MHz. The central frequency of the loaded dipole antenna is 300 MHz and the spectrum with the -10 dB of the maximal power limit is 120–630 MHz. The simulations in Sections III and IV use a Gaussian pulse. The pulse is 1.4 ns at 50% of the maximal amplitude. In order to have the same transmit power in both antennas, the excitation voltage is 1 V for the Gopher antenna, and 3.4 V for the loaded dipole.

The simulated ground volume is 600 mm deep with an 800x800 mm^2 footprint, using 5 mm voxels. Antennas are 20 mm above the ground, as [7] concurs. The permittivity $\varepsilon_r = 6.7$ is used in the ground. The simulation space above the ground is air and contains two identical antennas in each simulation: either Gopher or dipole antennas.

The absorbing boundary is convolutional perfectly matched layer (CPML) as in [11], but the simulation space is in direct contact with the CPML, without the air gap between. The time step is calculated in the code resulting $\Delta t = 8.7$ picoseconds. That is optimal for the air although oversampling in neoprene. If ten times the distance between two grid points (10·5 mm = 50 mm) is used to define the minimal wavelength in one dimension [12], then the minimal wavelength $\lambda_{min} = \sqrt{3} \cdot 50$ mm = 87 mm in a cube in air. Then the maximal frequency when the FDTD grid is valid $f_{max} = c/(\lambda_{min} \cdot \sqrt{\varepsilon_r}) = 1.3$ GHz.

All the simulations have two antennas in the simulation space, except the simulations used to create Fig. 15. The simulation spaces are shown in Fig. 3 and Fig. 4. An enlargement of the simulation space in the yz-plane is in Fig. 2. showing the antenna section and the neoprene fill in and around it.

Fig. 2. Gopher antenna in the simulation space, yz-plane, showing the neoprene fill around the antenna and in the ground in gray. The gap between the antenna and the ground is 20 mm.

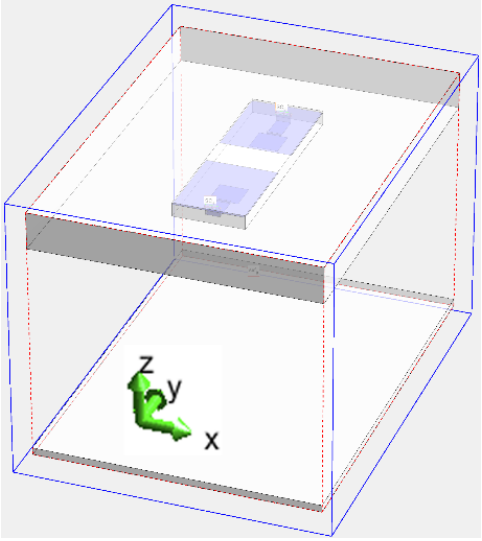

Fig. 3. Gopher antenna simulation space. Two antennas side-by-side, 100 mm gap between them. Xz-plane is in the middle of the gap parallel to the short edges of the antennas, and yz-plane goes through the centers of the antennas.

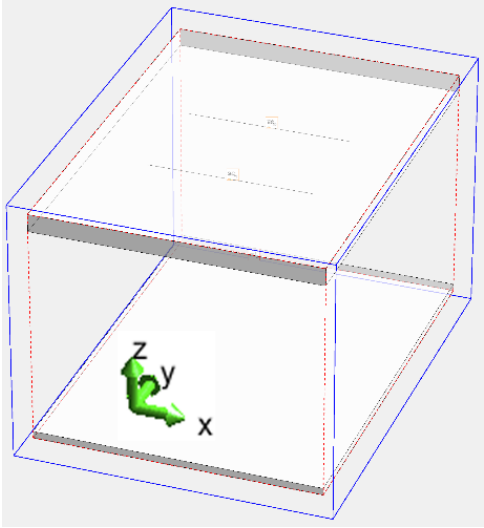

Fig. 4. Dipole antenna simulation space. Two antennas side-by-side, 120 mm gap between them. Xz-plane is in the middle of the gap parallel to the antennas, and yz-plane goes across the centers of the antennas.

III. GOPHER ANTENNA AND LOADED DIPOLE RADIATION

The calculation results illustrated in Fig. 5 and Fig. 6 show the electric field maximal magnitude with the 1.4 ns transmit pulse in the yz plane. The yz plane is electrically the E-plane for the Gopher antenna, and H-plane for the dipole. The colorbar is in dB and 0 dB is 6 V/m in all pictures 5–12.

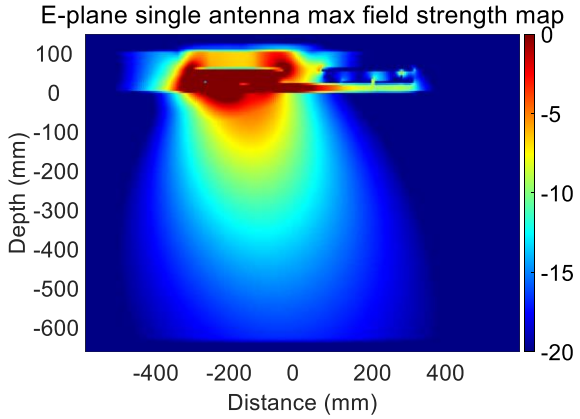

Fig. 5. Gopher antenna yz-plane (E-plane) max field strength map by a 1.4 ns transmit pulse, through the antenna centers.

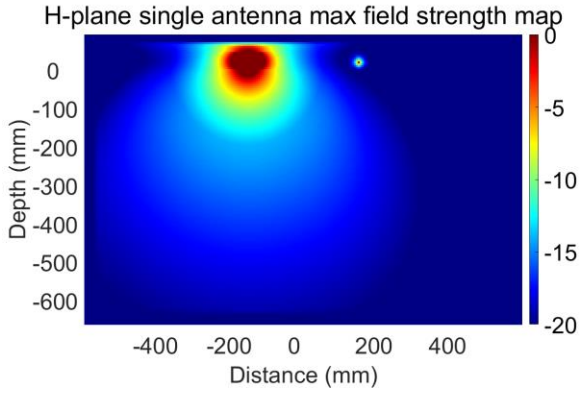

Fig. 6. Dipole antenna yz-plane (H-plane) max field strength map by a 1.4 ns transmit pulse, through the antenna centers.

Below Fig. 7 and Fig. 8 show the electric field maximal magnitude in the xz plane between the antenna pair.

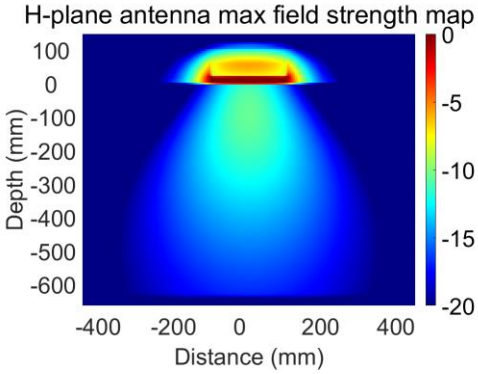

Fig. 7. Gopher antenna xz-plane (H-plane) max field strength map by a 1.4 ns transmit pulse, through the antenna centers.

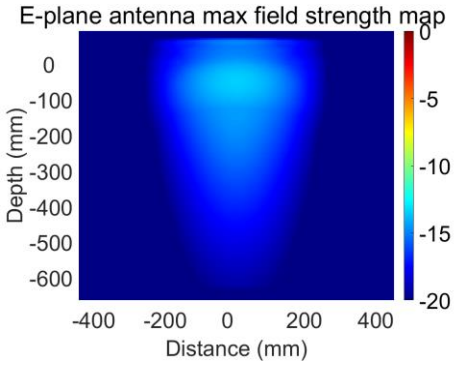

Fig. 8. Dipole antenna xz-plane (E-plane) max field strength map by a 1.4 ns transmit pulse, through the antenna centers.

IV. EXAMPLES OF A COMBINED PATTERN

In a monostatic radar, the gain is the square of the antenna gain. In a bistatic radar, the case is more complex. Here I approximate the combined radiation topography by multiplying the transmit and receiver antenna radiation values at each point (voxel). Figure 9 and Fig. 10 show the results, and they can be compared with Fig. 5 and Fig. 6, respectively.

Comparable cases are very rare in the literature. For the dipole, one comparable case is in [5] (design information in [13]), where the 6 dB beam (two-way gain, corresponds to the 3 dB beam in my simulation) is 75° wide in materials with ε_r = 5 and 10. In my simulation the dipole antenna pair 3 dB beam is 80° wide, as inferred from Fig. 10 at the 600 mm depth.

Another comparable case is in [1] where the E-plane dipole pair beam at 11 ns travel distance in oil (ε_r = 2.1) is 38° wide (my estimation from the picture, assuming the picture represents received power from two-way travel). In my simulation the corresponding beam is 32° wide.

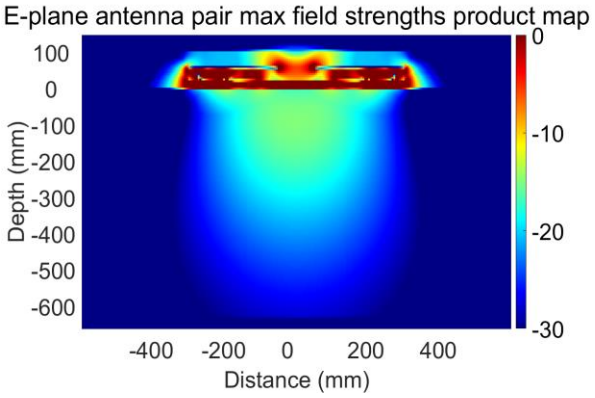

Fig. 9. Gopher antenna E-plane, combined radiation topography. Corresponds approximately to the 3dB 50° beamwidth at 0.6 m depth.

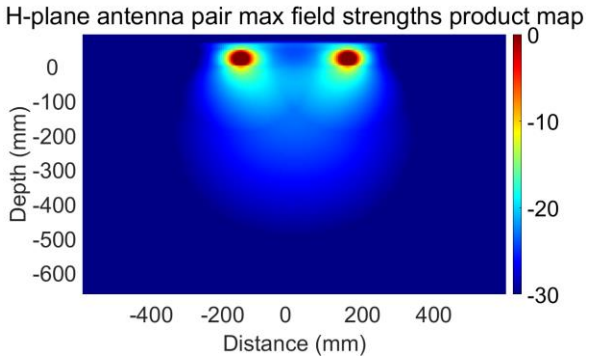

Fig. 10. Dipole antenna H-plane, combined radiation topography. Corresponds approximately to the 3dB 80° beamwidth at 0.6 m depth.

V. EFFECT OF THE PULSE WIDTH

The central frequency of these antennas in the air is below 500 MHz. Here a short Gaussian pulse of 0.47 ns is applied to see its effect to the radiation topography. The central frequency of the pulse spectrum is 1140 MHz, thus well above the central frequency of the antenna. The results are shown in Fig. 11 and Fig. 12.

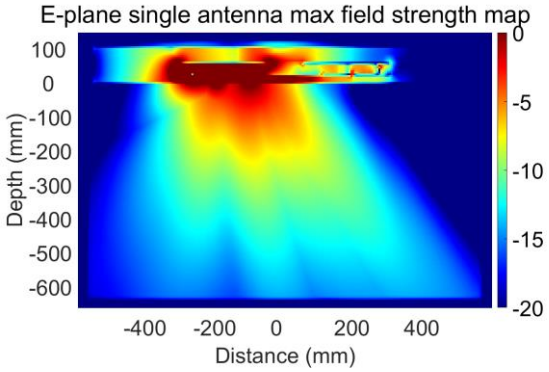

Fig. 11. A short Gaussian pulse of 0.47 ns with Gopher antenna E-plane (yz). E-Plane goes through the antenna center. Compare to 0.

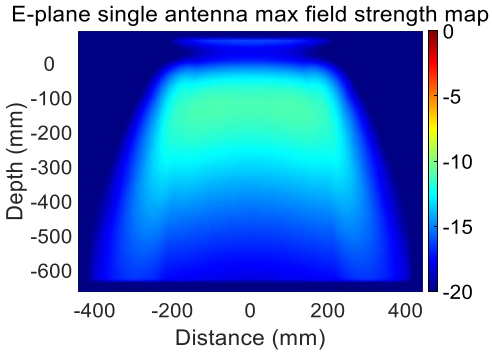

Fig. 12. A short Gaussian pulse of 0.47 ns with dipole antenna E-plane (xz). The E-plane is between antennas. Compare to Fig. 8.

The pulse pattern radiation topography visualization can be very beneficial for optimizing the pulse width for the desired purposes. A narrow beam as in Fig. 9 is good for point or line targets, like a pipeline in the sand. A reasonably wide beam is good for a synthetic aperture radar [2].

VI. CONVENTIONAL PULSE RADIATION VISUALIZATION APPLIED FOR THE GPR RANGE

In order to collect quantitative information of the radiating pulse, it is possible to record the field strength at defined points as a function of time. The pulse pattern for various angles at constant distance can be visualized using one or more of these: maximal cross-correlation (pulse fidelity factor), amplitude and spectrum. Variations of these can be seen in, e.g., [6] and [14]. Some visualization examples are further discussed below.

The amplitude of the electric field E_θ was calculated in the yz plane, perpendicular to the radius. The possible radial component was ignored as in [7]. The calculation results are shown in Table 1. It provides quantitative relative values on the pulse strength and quality in different directions at the constant distance of 300 mm.

The maximal normalized absolute cross-correlation depends on the pulse chosen for the comparison. In this case, the first derivative of the transmitted Gaussian pulse gave the highest results compared to the Gaussian or to the second derivative Gaussian pulse.

Table 1: Field values at 300 mm distance

Angle	240°	210°	180°	150°	120°
Max E field V/m	0.31	0.45	0.62	0.60	0.20
Max Cross-Correlation	0.80	0.85	0.93	0.94	0.95

Figure 13 shows the pulse versus time graphs in the same locations as in Table 1. The amplitude is easy to see, but the quality of the pulse is not easy to discern with the human eye. Figure 14 displays the same results with arrows. Line width is relative to the maximal power density at 300 mm from the antenna. Color is related to the maximal cross-correlation: lowest orange, highest cyan. One other possibility could be to show colored circles in the yz rectangular grid, the size of the circle relative to the power, and the circle color showing the quality.

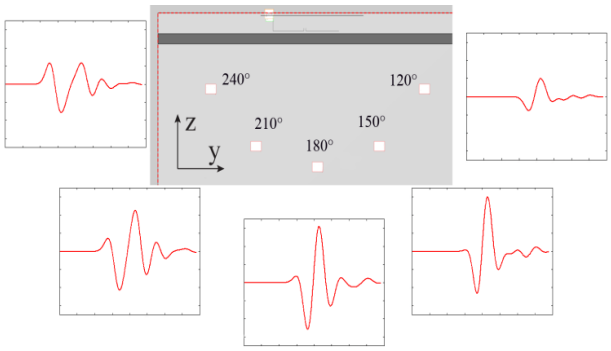

Fig. 13. Electric field versus time, yz plane, at 300 mm from the antenna. Simulation space section in the top center. Compare to 0.

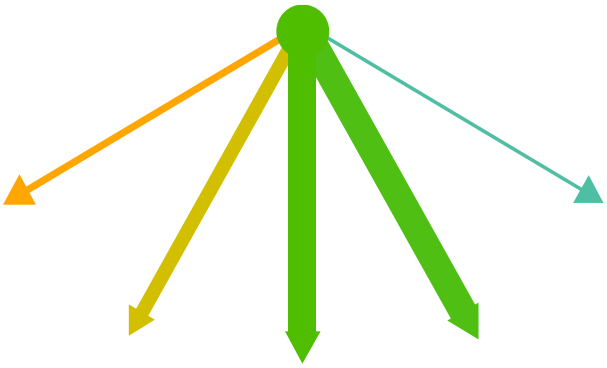

Fig. 14. Field magnitude and pulse quality combined. Line width is relative to the maximal field magnitude at 300 mm from the antenna. The arrow orientations correspond to Fig. 13. Color is related to the maximal cross-correlation: lowest orange, highest cyan. Compare to Fig. 5. Data is from Table 1.

VII. COMPARISON WITH THE FAR FIELD NARROWBAND RADIATION PATTERNS

Figure 15 shows the far field pattern of the single Gopher antenna in narrowband frequencies in neoprene. Generally, it conforms with the pulse radiation topography. The maximal directivity and gain is 9.6 dBi at 0.4 GHz. Gain drops on upper and lower frequencies while directivity can be good.

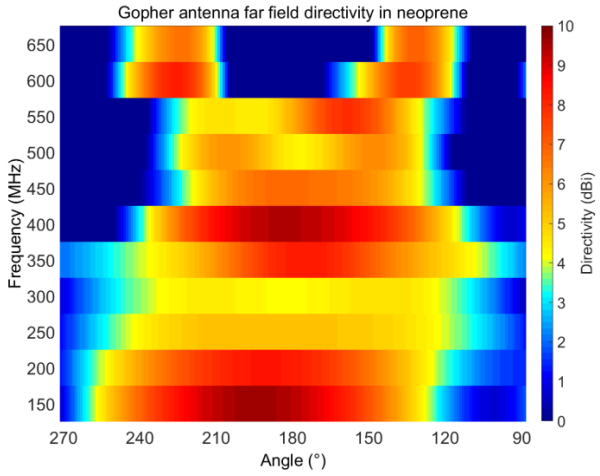

Fig. 15. Gopher antenna narrowband far field radiation pattern set: directivity D_ϑ versus frequency in the neoprene. $\varphi = 90°$, yz plane pattern. Angle ϑ corresponds to an antenna upside down towards the ground with the patch on the right side on the feed. 180° is downwards, 90° to the right, thus corresponding to the angles in Table 1 and in Figs. 13 and 14.

VIII. MEASURED PROFILE

Figure 16 is an example of a measured profile in a lake using the Gopher antenna. In the middle, there is a boat haven under the water. It is an approximately two meters wide trench where the bottom is approximately at one 0.8 m depth. Roundish stones are piled on both sides. In the profile the hyperbolas and the other artifacts are minimal, thus – although one cannot prove that – it can be considered implying a narrow beam or small radiation footprint. The radar pulse is 2 ns long and the permittivity of water $\varepsilon_r \approx 81$.

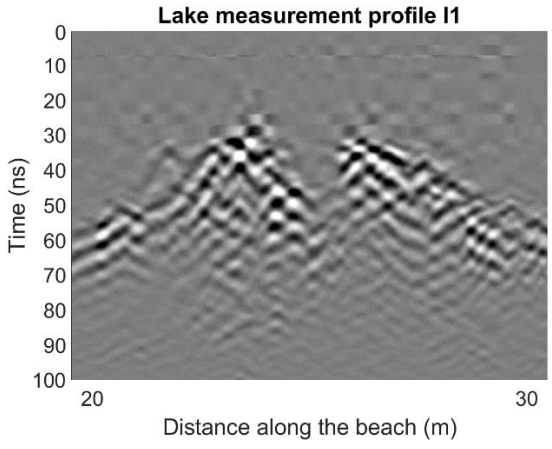

Fig. 16. Measured lake bottom profile crossing a boat haven submerged in the lake. It is an approximately two meters wide trench where the bottom is approximately at 0.8 m depth. Roundish stones are piled on both sides. Approximate horizontal distance values. 100 ns time corresponds to the depth approximately 1.6 m.

IX. EVALUATION OF THE FINDINGS AND CONCLUSION

Table 1 shows that to some directions the cross-correlation deteriorates with the strength of the pulse. It means that the explorative expectation mentioned in Section II does not strictly speaking hold. A low quality pulse shape means that the target is not recognizable even when the signal is strong. Quantifying the combination of these two properties of the pulse radiation is an important item for further study.

In this paper, I have proposed a new method to characterize GPR radiation in the ground: it stores the highest electric field magnitude during the FDTD simulation in each pixel in a defined plane. The method adds to the available tool set, although it can be utilized on its own. This visualization can be utilized effectively in the GPR antenna development. This method provides a new perspective for GPR antenna design, helps customize the transmit pulse and opens new opportunities for future research.

ACKNOWLEDGMENTS

At Aalto University: Research Engineer Matti Vaaja and Associate Professor Ville Viikari, and at Easy Radar USA Chief Engineer Karl Harrar.

REFERENCES

[1] D. Daniels, *Ground Penetrating Radar*. London: IET, 2004.

[2] D. Comite, A. Galli, I. Catapano, and F. Soldovieri, "The role of the antenna radiation pattern in the performance of a microwave tomographic approach for GPR imaging," *IEEE Journal of Selected Topics in Applied Earth Observations and Remote Sensing*, vol. 10, no. 10, pp. 4337-4347, Oct. 2017.

[3] H. Jol, *Ground Penetrating Radar: Theory and applications*. Oxford: Elsevier Science, 2009.

[4] C. Warren and A. Giannopoulos, "Characterisation of a ground penetrating radar antenna in lossless homogeneous and lossy heterogeneous environments," *Signal Processing*, vol. 132, no. Mar., pp. 221-226, Mar. 2017.

[5] C. Warren and A. Giannopoulos, "Experimental and modeled performance of a ground penetrating radar antenna in lossy dielectrics," *IEEE Journal of Selected Topics in Applied Earth Observations and Remote Sensing*, vol. 9, no. 1, pp. 29-36, Jan. 2016.

[6] H. Schantz, *The Art and Science of Ultrawideband Antennas*. 2nd edition, Boston: Artech House, 2015.

[7] N. Diamanti and A. P. Annan, "Characterizing the energy distribution around GPR antennas," *Journal of Applied Geophysics*, vol. 99, pp. 83-90, Dec.

2013.

[8] M. Hall, L. Barclay, and M. Hewitt, *Propagation of Radiowawes*. Exeter: Short Run Press, 1996.

[9] V.-E. Voipio, "The Gopher antenna - A new efficient design for ground penetrating radar," in *International Workshop on Advanced Ground Penetrating Radar*, Hague, Netherlands, pp. 1-5, Sep. 2019.

[10] L. Pajewski, A. Giannopoulos, C. Warren, S. Antonijevic, V. Doric, D. Poljac, and D. Pirrone, "Development of electromagnetic simulators for ground penetrating radar," in *2017 International Applied Computational Electromagnetics Society (ACES) Symposium*, Firenze, Italy, pp. 1-2, Mar. 2017.

[11] A. Elsherbeni and D. Veysel, *The Finite-Difference Time-Domain Method for Electromagnetics with MATLAB Simulations*. Raleigh NC: SciTech Publishing Inc., 2008.

[12] K. Holliger and T. Bergmann, "Accurate and efficient FDTD modeling of ground-penetrating radar radiation," *Geophysical Research Letters*, vol. 25, no. 20, pp. 3883-3886, Oct. 15, 1998.

[13] C. Warren and A. Giannopoulos, "Creating FDTD models of commercial GPR antennas using Taguchi's optimisation method," *Geophysics*, vol. 76, no. 2, pp. 37-47, Mar.-Apr. 2011.

[14] C. A. Balanis, *Modern Antenna Handbook*. Hoboken NJ: Wiley, 2008.

The Effect of Wi-Fi Radiation on the Mineralization and Oxidative Stress of Osteoblasts

Mengxi Wang [1], Guohui Yang [2], Yu Li [3], Qun Wu [2,*], and Yingsong Li [4]

[1] Fourth Affiliated Hospital of Harbin Medical University, Harbin 150001, China

[2] School of Electronic and Information Engineering, Harbin Institute of Technology, Harbin 150001, China

[3] Department of Life Science and Engineering, Harbin Institute of Technology, Harbin 150001, China

[4] College of Information and Communication Engineering, Harbin Engineering University, Harbin 150001, China
*qwu@hit.edu.cn

Abstract — Some articles reported that Wi-Fi radiation induced oxidative stress (OS) in cells and vital organs. However, the possible effects of Wi-Fi electromagnetic fields (EMFs) on bone cells have not yet been investigated. MC3T3-E1 cells were cultured in cell incubators during induced differentiation and placed 3 cm from Wi-Fi antenna. A 2.45-GHz Wi-Fi signal, transmitted between a Wi-Fi router and a laptop Wi-Fi antenna, radiated on cells for 30 min/day over a 7-day period. The two modes of the Wi-Fi irradiation were 100 mW and 500 mW. The specific absorption rates (SARs) in the cell layer by 100 mW and 500 mW Wi-Fi were 0.1671 W/kg and 0.8356 W/kg, respectively, represented as SARa and SARb, and the cell layer temperature increased by 0.065°C and 0.32°C, respectively, after 30 min of irradiation by finite difference-time domain (FDTD) simulation. The cell oxidative stress indexes were measured by a microplate reader, and the calcified nodules were examined by alizarin red S staining. At a 3-cm close range, 2.45-GHz Wi-Fi radiation increased Reactive oxygen species (ROS) and glutathione (GSH) levels in osteoblasts with the increase of irradiation time, and the quantity of mineralization slightly depended on the radiation intensity.

Index Terms — FDTD, GSH, in vitro, MC3T3-E1 cell, ROS, SAR, temperature.

I. INTRODUCTION

The extensive presence of Wi-Fi in domestic premises and public spaces has aroused concern among the general public, especially after 2011, when the World Health Organization (WHO) and the International Association of Research on Cancer (IARC) classified radio-frequency radiation as "possibly carcinogenic to humans" (Group 2B; limited evidence of carcinogenicity in humans and less than sufficient evidence of carcinogenicity in experimental animals) based on epidemiological evidence of a connection between brain tumors and mobile phone use [1].

The study of biological electromagnetic effect needs to reveal the electromagnetic mechanism as well as the biological mechanism. Therefore, a large number of biological experiments are required to verify the theoretical mechanism between biological response and electromagnetic parameters. For in vitro bio-electromagnetic experiments with microwave (MW), cells are usually in plastic culture containers, such as tubes [2], culture flasks [3] and Petri dishes [4], filled with a culture medium and set close to a wave source. Due to the culture medium above the cells and the high-water content of biological cells, the attenuation of MW is rapid, presenting a challenge for temperature measurements and calculations in a thin adherent cell layer at the bottom of a cell container.

Kunt [5] confirmed that long-term exposure to electromagnetic fields could affect bone metabolism and increase OS by increasing the total oxidant status and decreasing the antioxidant status. OS induced by Wi-Fi irradiation on organs in vivo, such as the uterus [6] and brain [7], and on cells in vitro [2] has also been affirmed. OS could disturb the bone remodeling process and lead to skeletal system disorders. It is reasonable to speculate that bone, as the largest organ of the body, might also be affected by Wi-Fi EMFs. Osteoblasts, the primary bone-forming cells, control the synthesis, secretion and mineralization of bone matrix and maintain the metabolism of mature bone. MC3T3-E1 cells, preosteoblastic cells derived from mice, were employed in this study, which have been used in researches of EMFs biological effects on osteoblasts [8]. This study was designed to analysis the effects of 2.45-GHz Wi-Fi on OS indexes and mineralization of osteoblasts in vitro.

Submitted On: May 19, 2020
Accepted On: March 6, 2021

https://doi.org/10.47037/2020.ACES.J.360515

II. MATERIALS AND METHODS

A. Exposure system and experimental design

MC3T3-E1 cells (iCell Bioscience Inc., Shanghai, China) of the clone-14 preosteoblastic murine cell line were induced in a Forma Series II 3110 water jacketed CO_2 incubator (Thermo Fisher Scientific Inc., Waltham, Massachusetts, USA) with 5% CO_2 at 37°C. Four milliliters of α-minimal essential medium (α-MEM; Gibco Invitrogen, Grand Island, New York, USA) containing 100 IU/mL penicillin, 100 μg/mL streptomycin, 10% fetal calf serum (α-MEM-FCS), 10 mmol/L β-phosphoglycerol, 10^{-8} mol/L dexamethasone and 50 μg/mL ascorbic acid was changed every 48 h. A Wi-Fi router, six 60-mm cell culture dishes, and a notebook with an antenna were placed in a cell incubator during the experiment (Fig. 1). The distance between the router antenna and the cell dishes was 3 cm. Both the wireless access point and the wireless network card of the notebook were connected by standard 3 dB gain antenna. The front end of the wireless access point was driven by a gain-adjustable power amplifier which transmits signals according to the IEEE 802.11b protocol, and the signals were received by the notebook computer. After the Wi-Fi connection established, Internet Control Message Protocol (ICMP) packet was sent by the notebook test program to ensure that the power of Wi-Fi was maintained at a certain power value. In the control groups, the Wi-Fi router and computer were placed in the cell incubator without data transmission.

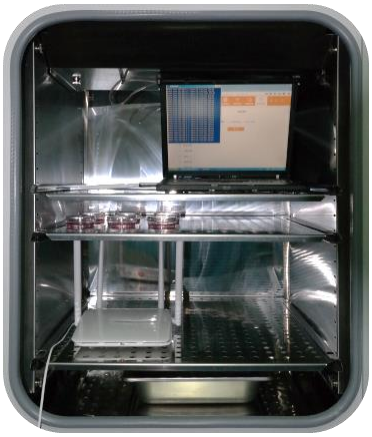

Fig. 1. Photo of the exposure system.

The metallic incubator will lead to resonances, but it could also shield the external electromagnetic interference, equivalent to the transverse electro-magnetic cells (TEM) model, which meets the requirements of the radiation environment standard of biological electromagnetic experiment.

B. FDTD simulation

The computing method of SAR and temperature rise in the cell monolayers of this model has been described in our previous article [9].

The SAR and electric field distributions in the cell layers at the bottom of 60-mm diameter Petri dishes were illustrated in Fig. 2. The mean SAR for the six dishes was 0.1671 W/kg for 100 mW Wi-Fi and 0.8356 W/kg for 500 mW Wi-Fi (Table 1). The temperature variation in the cell layers in 30 min of irradiation was shown in Fig. 3. The average temperature of the cell layer in each dish after 30 min of irradiation was shown in Table 2.

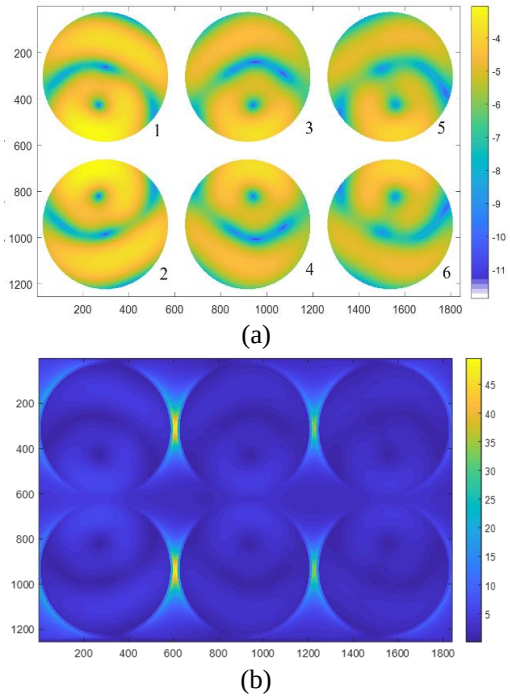

Fig. 2. SAR and electric field distributions of the cell layer plane. (a) SAR distribution and (b) electric field distribution.

Table 1: SAR of the cell monolayers

Incident Power		SAR in the Cell Layer of a Single Dish						Mean SAR of 6 Dishes
		1	2	3	4	5	6	
0.1 W	Average (W/kg)	0.2519	0.2519	0.1387	0.1387	0.1107	0.1107	0.1671
	Standard deviation	0.2081	0.2081	0.1093	0.1093	0.0866	0.0866	0.0669
0.5 W	Average (W/kg)	1.2594	1.2595	0.6936	0.6936	0.5537	0.5537	0.8356
	Standard deviation	1.0405	1.0405	0.5465	0.5465	0.4328	0.4328	0.334

Table 2: Temperature of the cell monolayers after 30 min of irradiation

Incident Power		Temperature in the Cell Layer of a Single Dish						Mean Temperature of 6 Dishes
		1	2	3	4	5	6	
0.1W	Average (°C)	0.0973	0.0973	0.0535	0.0535	0.0427	0.0428	0.0645
	Standard deviation	0.0209	0.0209	0.0118	0.0118	0.0091	0.0091	0.0279
0.5W	Average (°C)	0.4866	0.4867	0.2674	0.2674	0.2137	0.2138	0.3226
	deviation	0.1045	0.1044	0.0591	0.0590	0.0453	0.0453	0.1394

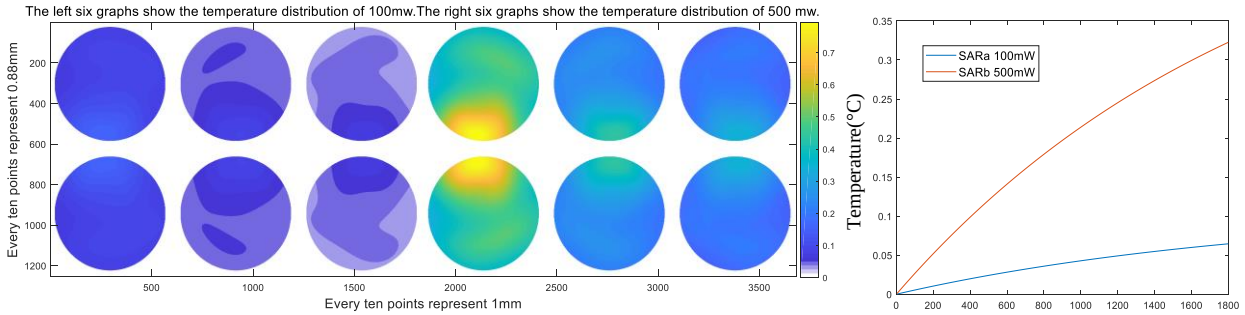

(a) (b)

Fig. 3. Temperature in the cell layers. (a) Temperature distribution of the cell layer plane in each dish after 30 min. (b) Average temperature changes in cell monolayers of 6 dishes in 30 min.

C. ROS

After 72 h of induction in osteogenic medium (50 μg/mL ascorbic acid, 10^{-8} mol/L dexamethasone, and 10 mmol/L β-glycerophosphate), the cells were digested with 0.25% Trypsin-0.53 mM EDTA and then seeded into a 96-well plate at a density of 5×10^3 cells/mL in 100 μL of osteogenic medium, which was changed every 48 h. 2',7'-Dichlorofluorescein diacetate (KeyGen Biotech Co., NanJing, Jiangsu, China) was added to each well according to the manufacturer's instructions. After 45 min of incubation in the dark, the cells were exposed to Wi-Fi radiation. The ROS levels were then determined by measuring the fluorescence intensity at 518-nm excitation and 605-nm emission using a spectrophotometer plate reader (Spectra Max M3, Molecular Devices, California, USA).

D. GSH

Cells were seeded on 60-mm culture dishes at a density of 5×10^4 cells/mL in 4 mL of osteogenic medium, which was changed every 48 h. After 72 h, the cells were exposed to Wi-Fi radiation. Then, the cells were digested with 0.25% Trypsin-0.53 mM EDTA. After centrifugation (3500 g, 10 min), the cell supernatant was added to a 96-well culture plate. Cellular GSH levels were determined using a GSH assay kit (KeyGen Biotech Co.) according to the manufacturer's instructions. The optical absorbance values were measured by a microplate reader at 405 nm (SpectraMax M3).

E. Alizarin red S staining

MC3T3-E1 cells were seeded at 3×10^3 cells/mL in 60-mm culture dishes and cultured in 4 mL of osteogenic medium in incubators. After 72 h, the cells were irradiated with Wi-Fi for 30 min/day for 7 days. On day 21, the cells were fixed with 4% paraformaldehyde for 20 min at room temperature. After being washed with 1× PBS (pH 7.2, without calcium or magnesium), the samples were covered with alizarin red S staining solution (pH 8.3, KeyGen Biotech Co.) without light exposure for 90 min at 37 °C and then rinsed with 1× PBS (pH 7.2, without calcium or magnesium). Subsequently, images were acquired by an inverted fluorescence microscope (OLYMPUS TH4-200, Tokyo, Japan).

F. Statistical analysis

The data were expressed as the mean ± standard deviation (SD) of three or more independent experiments. Significant differences were determined using factorial analysis of variance (ANOVA). Statistical analysis was performed using SPSS 13.0 software (SPSS Inc., Chicago, Illinois, USA), and a value of $P<0.05$ was considered as statistically significant.

III. RESULTS

A. Alizarin red S staining on day 21 (Fig. 4)

The calcification of the SARb group was slightly greater than that of the sham and SARa groups. However, the SARa group displayed no significant difference from

the sham group.

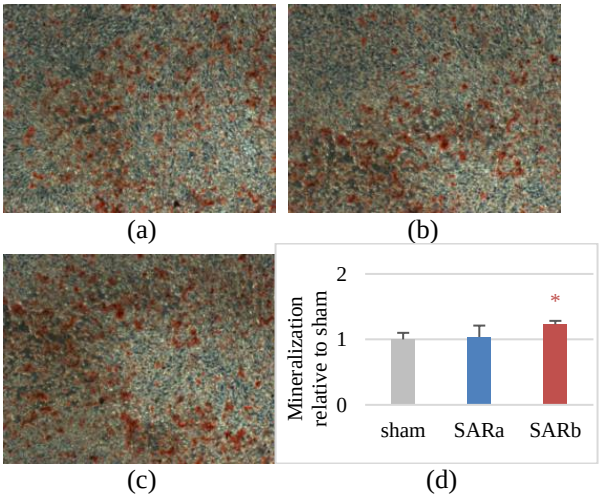

Fig. 4. Mineralized nodule analysis: (a) Sham; (b) SARa; (c) SARb; (d) mineralization relative to sham (P<0.05 *).

B. GSH and ROS (Fig. 5)

The ROS levels were elevated on day 3 and were even higher on day 6. The ROS level on the 3rd day in the SARb group was higher than that in the SARa group, but the ROS level in the SARb group on the 6th day had no significant difference with that in the SARa group. Despite the similar trends like ROS, the GSH level of the SARb group was higher than that of the SARa group on day 6, and the GSH levels of the SARa group showed no significant difference with that in the SARb group on day 3. Neither the ROS nor the GSH levels showed obvious changes on the 1st day after 30 min of Wi-Fi radiation.

IV. DISCUSSION

The cell layer temperature increases in vitro caused by the 2.45-GHz Wi-Fi EMFs generally does not exceed 1°C by simulation or actual observation [10-12]. Collin A. [11] calculated temperature rises using FDTD, and the maximum temperature rise was approximately 1°C at 2.45 GHz for a SAR of 16 W/kg. Paffi [12] calculated the maximum temperature changes for plane wave exposures (100 V/m incident electric field at 0.9, 1.8, or 2.5 GHz) by CST simulation and concluded that the temperature increased by approximately 1°C at thermal equilibrium. In our experiment, because the irradiation time was only 30 minutes, the temperature changes were small, which were 0.065°C for 100 mW incident power and 0.32°C for 500 mW incident power respectively by FDTD simulation. Consequently, the effects on OS and mineralization were more likely initiated by the non-thermal effects of Wi-Fi. Furthermore, other studies have reported adverse effects of Wi-Fi radiation within the safety threshold on biological tissue [13]. Some studies revealed that Wi-Fi radiation could impact the reproductive system [14], laryngotracheal mucosa [15], liver [16], brain [7], and fetal tissue [6], partly due to OS [15] and DNA damage [17].

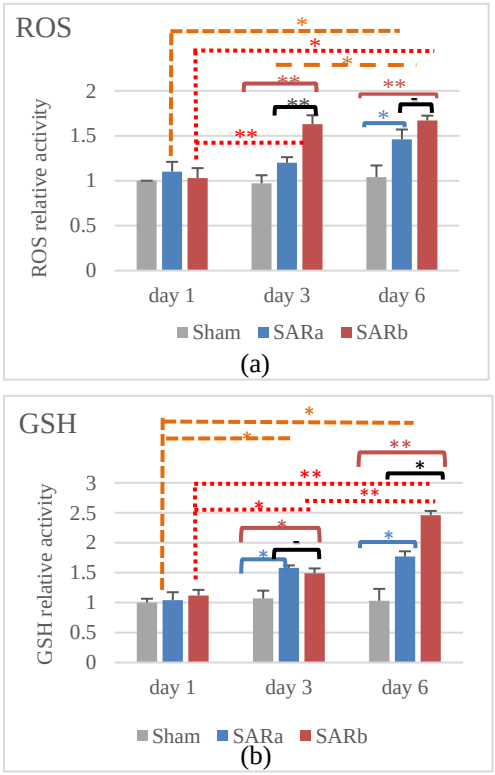

Fig. 5. ROS and GSH levels in MC3T3-E1 cells on days 1/3/6 after 30-min Wi-Fi exposure. (a) Relative OD of ROS. (b) Relative OD of GSH (P≥0.05 -, P<0.05 *, P<0.01 **).

Among all the biological effects of Wi-Fi irradiation, OS mechanisms have received the most attention. The primary cause of OS is the overproduction of ROS. ROS is the general name of a class of molecules or ions with high chemical reactivity and high oxidation activities [18]. In certain unfavorable conditions, such as hunger, nutritional deficits, drug stimulation, severe environmental changes, bacterial infections and various diseases, the ROS levels in cells would increase significantly. Elevated ROS levels could damage proteins, lipids and DNA, and eventually trigger apoptosis and lead to cell death [19]. In an in vitro experiment, Ghazizadeh [20] isolated hippocampal and dorsal root ganglion (DRG) neurons from rats and exposed the neurons to a 2.45-GHz Wi-Fi (12 μW/cm^2 SAR: 0.52±0.05 mW/kg) for 1 hr. It was found that Wi-Fi caused Ca^{2+} influx and OS-induced hippocampal and DRG death. Subsequently, to elucidate the electromagnetic effect of radiation from mobile phones (900 and 1800 MHz) and 2.45-GHz Wi-Fi on cells and the relationship between the biological

effects and distance, Çiğ B. [2] set 6 tubes of MCF-7 breast cancer cells at different distances (0 cm, 1 cm, 5 cm, 10 cm, 20 cm and 25 cm) from the radiant (the same appliance as used by Ghazizadeh V.) for 1 hr. Çiğ B. found that cytosolic ROS production, Ca^{2+} concentrations, apoptosis and caspase-3 and caspase-9 values were higher in 900 and 1800 MHz mobile phone groups as well as in 2.45-GHz Wi-Fi groups at distances less than 10 cm. In our study, the ROS levels increased in both the 100 mW and 500 mW groups after 3-6 days of Wi-Fi exposure at a distance of 3 cm. Hence, Wi-Fi radiation might be an exogenous OS stimulus to osteoblasts.

Multiple studies have shown that EMFs could rapidly induce ROS, and some even showed the time-dependent and SAR-dependent manners [21]. Similarly, we found that the ROS level increased on day 3 in the 500 mW group and rose higher on day 6 in both the 100 mW and 500 mW groups, presenting a time-dependent manner. Moreover, the ROS level of the 500 mW group was higher than that of the 100 mW group, showing a SAR-dependent trend.

Özorak [14] reported that 2.45-GHz Wi-Fi and 900- and 1800-MHz mobile phone exposure of 1 hr/day for 120-180 days induced OS in the kidneys of rats during pregnancy by reducing GSH and GSH-Px levels. In contrast, Fahmy [22] confirmed that 2.45-GHz Wi-Fi (SAR 0.01 W/kg, 24 hr/day for 40 days) emitted from an indoor Wi-Fi device increased GSH levels in kidney tissues. Similar to Fahmy, the increased GSH levels were also observed in our study, along with increased ROS levels. It was previously confirmed that EMFs could promote MC3T3-E1 cell mineralization [23]. Our results showed that the calcification of the 500 mW group was greater than that of the sham and 100 mW groups. A high level of ROS could induce apoptosis and reduce osteoblast activity, differentiation, mineralization and osteogenesis, however, antioxidants could activate the differentiation and mineralization of osteoblasts either directly or by counteracting the action of oxidants [18]. Thus, it is possible that the drastic GSH increase in the 500 mW group in the later period of this experiment might contribute to calcification, since GSH could serve as a direct ROS scavenger to restore the dynamic balance between ROS generation and elimination in cells [21].

The obvious change in ROS and GSH levels presented on day 3 and day 6, but not on day 1, which might be related to the "cumulative effects" [24] or "window effects" [25].

V. CONCLUSIONS

ROS, GSH and mineralization changes in osteoblasts were caused by non-thermal effect of 2.45-GHz Wi-Fi, and displayed a SAR-dependent trend. The cumulative effect of repeated exposure could aggravate the degree of cellular reaction. Long-time, high-intensity, close-range contact with Wi-Fi signal radiation sources and equipment should be avoided. In the future, the experiment can be predicted using adaptive algorithms under MIMO environments [26-30].

ACKNOWLEDGMENTS

This work was supported by National Natural Science Foundation of China, grant number 61571155 and the Fundamental Research Funds for the Central Universities (3072021CF0804) and Funding of Key Laboratory of Advanced Marine Communication and Information Technology, MIIT, China (AMCIT2101-03).

REFERENCES

[1] W. Iarc, "IARC Classifies Radiofrequency Electromagnetic Fields as Possibly Cancinogenic to Humans. International Agency for Research on Cancer," *Lyon, Tech. Rep*., N:208, Jan. 2011.

[2] B. Çiğ and M. Nazıroğlu, "Investigation of the effects of distance from sources on apoptosis, oxidative stress and cytosolic calcium accumulation via TRPV1 channels induced by mobile phones and Wi-Fi in breast cancer cells," *Biochimica et Biophysica Acta (BBA)-Biomembrane*s, vol. 1848, no. 10, pp. 2756-2765, Oct. 2015.

[3] J. Zhao, and H. Lu, "Meniscus effect on the in vitro dosimetry of the T25 flask under 2.45 and 5.25 GHz exposures," *IEEE Microwave and Wireless Components Letters*, vol. 23, no. 2, pp. 105-107, Feb. 2013.

[4] S. I. Alekseev, M. V. Zhadobov, E. E. Fesenkojr, and E. E. Fesenko, "Millimeter wave dosimetry at exposure of cell monolayer," *Biophysics*, vol. 62, no. 2, pp. 261-264, June 2017.

[5] H. Kunt, İ. Şentürk, Y. Gönül, M. Korkmaz, A. Ahsen, Ö. Hazman, A. Bal, A. Genç, and A. Songur, "Effects of electromagnetic radiation exposure on bone mineral density, thyroid, and oxidative stress index in electrical workers," *Onco. Targets Ther*., vol. 9, pp. 745-754, Feb. 2016.

[6] M. Yüksel, M. Nazıroğlu, and M. O. Özkaya, "Long-term exposure to electromagnetic radiation from mobile phones and Wi-Fi devices decreases plasma prolactin, progesterone, and estrogen levels but increases uterine oxidative stress in pregnant rats and their offspring," *Endocrine*, vol. 52, no. 2, pp. 352-362, Nov. 2015.

[7] H. Othman, M. Ammari, M. Sakly, and H. Abdelmelek, "Effects of repeated restraint stress and WiFi signal exposure on behavior and oxidative stress in rats," *Metab. Brain Dis*., vol. 32, no. 5, pp. 1459-1469, Oct. 2017.

[8] A. M. Bique, E. Kaivosoja, M. Mikkonen, and M. Paulasto-Kröckel, "Choice of osteoblast model critical for studying the effects of electromagnetic stimulation on osteogenesis in vitro," *Electromagn.*

Biol. Med., vol. 35, no. 4, pp. 353-64, June 2016.

[9] W. Mengxi, Y. Guohui, L. Yu, W. Qun, and L. Yingsong, "Protective Role of vitamin C in Wi-Fi-induced oxidative stress in MC3T3-E1 cells in vitro," *The Applied Computational Electromagnetics Society Journal*, vol. 35, no. 5, pp. 587-594, May 2020.

[10] A. Kuzniar, C. Laffeber, B. Eppink, K. Bezstarosti, D. Dekkers, H. Woelders, A. P. Zwamborn, J. Demmers, J. H. Lebbink, and R. Kanaar, "Semi-quantitative proteomics of mammalian cells upon short-term exposure to nonionizing electromagnetic fields," *Plos One*, vol. 2, no. 2, pp. e0170762, Feb. 2017.

[11] A. Collin, M. Cueille, A. Perrin, C. Pivain, and P. Lévêque, "Electromagnetic dosimetry and thermal analysis of a new exposure setup for in vitro studies on a large frequency band," *2007 IEEE/MTT-S International Microwave Symposium*, pp. 2221-2224, June 2007.

[12] A. Paffi, M. Liberti, F. Apollonio, A. Sheppard, and Q. Balzano, "In vitro exposure: Linear and non-linear thermodynamic events in Petri dishes," *Bioelectromagnetics*, vol. 36, no. 7, pp. 527-537, Oct. 2015.

[13] M. E. Yildirim, M. Kaynar, H. Badem, M. Cavis, O. F. Karatas, and E. Cimentepe, "What is harmful for male fertility: Cell phone or the wireless internet?," *Kaohsiung J. Med. Sci*., vol. 31, no. 9, pp. 480-484, Sep. 2015.

[14] A. Özorak, M. Nazıroğlu, Ö. Çelik, M. Yüksel, D. Özçelik, M. O. Özkaya, H. Çetin, M. C. Kahya, and S. A. Kose, "Wi-Fi (2.45 GHz)-and mobile phone (900 and 1800 MHz)-induced risks on oxidative stress and elements in kidney and testis of rats during pregnancy and the development of offspring," *Biol. Trace Elem. Res*., vol. 156, no. 1-3, pp. 221-229, Dec. 2013.

[15] G. Aynali, M. Nazıroğlu, Ö. Çelik, M. Doğan, M. Yarıktaş, and H. Yasan, "Modulation of wireless (2.45 GHz)-induced oxidative toxicity in laryngotracheal mucosa of rat by melatonin," *Eur. Arch. Otorhinolaryngol*., vol. 270, no. 5, pp. 1695-1700, May 2013.

[16] F. Shekoohi-Shooli, S. M. J. Mortazavi, M. B. Shojaei-Fard, S. Nematollahi, and M. Tayebi, "Evaluation of the protective role of vitamin C on the metabolic and enzymatic activities of the liver in the male rats after exposure to 2.45 GHz of Wi-Fi routers," *J. Biomed. Phys. Eng*., vol. 6, no. 3, pp. 157, Sep. 2016.

[17] M. Z. Akdag, S. Dasdag, F. Canturk, D. Karabulut, Y. Caner, and N. Adalier, "Does prolonged radiofrequency radiation emitted from Wi-Fi devices induce DNA damage in various tissues of rats?," J. *Chem. Neuroanat*., vol. 75, no. Pt B, pp. 116-122. Sep. 2016.

[18] V. Domazetovic, G. Marcucci, T. Iantomasi, M. L. Brandi, and M. T. Vincenzini, "Oxidative stress in bone remodeling: Role of antioxidants," *Clin. Cases Miner. Bone Metab*., vol. 14, no. 2, pp. 209-216, May-Aug. 2017.

[19] Y. Tian, X. Ma, C. Yang, P. Su, C. Yin, and A. R. Qian, "The impact of oxidative stress on the bone system in response to the space special environment," *Int. J. Mol. Sci*., vol. 18, no. 10, pp. 2132, Oct. 2017.

[20] V. Ghazizadeh and M. Naziroğlu, "Electromagnetic radiation (Wi-Fi) and epilepsy induce calcium entry and apoptosis through activation of TRPV1 channel in hippocampus and dorsal root ganglion of rats," *Metab. Brain Dis*., vol. 29, no. 3, pp. 787-799. Sep. 2014.

[21] H. Wang and X. Zhang, "Magnetic fields and reactive oxygen species," *Int. J. Mol. Sc*., vol. 18, no. 10, pp. 2175, Oct. 2017.

[22] H. M. Fahmy, F. F. Mohammed, R. T. Abdelrahman, and A. Elfetoh, "Effect of radio-frequency waves emitted from conventional WIFI devices on some oxidative stress parameters in rat kidney," *Drug Metab. Toxicol*., vol. 6, no. 5, pp. 1-6, Dec. 2016.

[23] J. L. Yan, J. Zhou, H. P. Ma, X. N. Ma, Y. H. Gao, W. G. Shi, Q. Q. Fang, Q. Ren, C. J. Xian, and K. M. Chen, "Pulsed electromagnetic fields promote osteoblast mineralization and maturation needing the existence of primary cilia," *Mol. Cell Endocrinol*., vol. 404, pp. 132-140, Mar. 2015.

[24] H. S. Kim, J. S. Park, Y. B. Jin, H. D. Choi, J. H. Kwon, J. K. Pack, N. Kim, and Y. H. Ahn, "Effects of exposure to electromagnetic field from 915 MHz radiofrequency identification system on circulating blood cells in the healthy adult rat," *Bioelectro-magnetics*, vol. 39, no. 1, pp. 68-76, Jan. 2018.

[25] J. Zhou, L. G. Ming, B. F. Ge, J. Q. Wang, R. Q. Zhu, Z. Wei, H. P. Ma, C. J. Xian, and K. M. Chen, "Effects of 50Hz sinusoidal electromagnetic fields of different intensities on proliferation, differentiation and mineralization potentials of rat osteoblasts," Bone, vol. 49, no. 4, pp. 753-761, Oct. 2011.

[26] T. Liang, Y. Li, W. Xue, Y. Li, and T. Jiang, Performance and analysis of recursive constrained least Lncosh algorithm under impulsive noises, *IEEE Transactions on Circuits and Systems II: Express Briefs*, 10.1109/TCSII.2020.3037877, 2021.

[27] X. Huang, Y. Li, Y. Zakharow, and B. Chen, "Affine projection Lorentzian algorithm for vehicle hands-free echo cancellation, *IEEE Transactions on Vehicular Technology*, 10.1109/TVT.2021. 3061126.

[28] W. Shi, Y. Li, and B. Chen, "A separable maximum

correntropy adaptive algorithm," *IEEE Transactions on Circuits and Systems II: Express Briefs*, vol. 67, no. 11, pp. 2797-2801, 2020.

[29] F. Liu, J. Guo, L. Zhao, G. L. Huang, Y. Li, and Y. Yin, "Ceramic superstrate-based decoupling method for two closely packed antennas with cross-polarization suppression," *IEEE Transactions on Antennas and Propagation*, vol. 69, no. 3, pp. 1751-1756, 2021.

[30] X. Yan, K. L. Chung, Y. Li, and Y. Li, "A Jia-shaped artistic patch antenna for dual-band circular polarization," *AEÜ - International Journal of Electronics and Communications*, vol. 120, 153207, 2020.